

**MULTISCALE DESIGN OF SUPERMATERIALS:  
FRONTIER FOR HIGH-PERFORMANCE  
ENGINEERING**

by

**JAIME ORTÚN-PALACIOS**

A thesis submitted in fulfillment of the  
requirements for the degree of  
Doctor of Philosophy  
in the  
University of Burgos

Supervisors:  
Santiago Cuesta-López  
Nicolás A. Cordero

June 2019



## **Acknowledgments**

I would like to thank my thesis supervisors, Dr. Santiago Cuesta-López and Prof. Nicolás A. Cordero, as well as Prof. Antonio M. Locci for their advice, contribution and support. I would also like to thank the latter for hosting me at the University of Cagliari during the three months I was there. I would like to thank all the people of the International Research Centre in Critical Raw Materials (ICCRAM) for their help, especially to Prof. Roberto Serrano-López. And, as could not be otherwise, I would like to express my deep gratitude to my family because what I am today I owe it to them.

This work has been supported by the European Social Fund, Operational Programme of Castilla y León, and Junta de Castilla y León, through the Ministry of Education.

## Abstract

Currently, there is a lack of computational tools to predict the damage suffered by nanostructured materials as well as their performance under severe operating conditions such as those expected in the walls of reaction chambers in nuclear fusion or the shielding of space satellites. This thesis attempts to fill this gap by developing a framework of predictive modeling to optimize the design of materials that exhibit improved resistance to damage and exceptional mechanical properties for application in advanced engineering systems. As an innovative approach, a multiscale methodology is proposed to test nanostructured materials working within realistic environments which combines techniques like density functional theory (DFT), molecular dynamics (MD) and finite element method (FEM).

Many research and innovation initiatives point to nanoscale metallic multilayer composites (NMMCs) as material systems with enhanced radiation and thermal resistance to withstand the exposure to high-radiation environments and to enable stable performances under high-temperature conditions. The high mechanical strength of these materials allows to reduce the total weight associated with the structural components keeping the mechanical performance unchanged. Moreover, graphene has emerged in the last years as a superlative material that promises to transform the future due to its many applications. Thanks to its high ratio of surface area to volume, flexibility and chemical versatility, graphene can be combined with other materials to enhance their properties.

Structural materials within first-generation fusion nuclear reactors will deal with large amounts of helium and graphene, due to its extraordinary properties, might act as a vehicle to manage it. Thus, helium diffusion on and permeation towards graphene is investigated by means of DFT calculations in this dissertation. Potential energy curves have been fitted with a Yukawa–Lennard–Jones potential providing a tool for modelling helium behavior on graphene at a larger scale. The few existing first-principles works about graphene-He interaction have been limited to the study of a single helium atom. So, the most stable atomic structures that helium forms over a graphene sheet, their energetics, as well as the electron density differences in the presence of an increasing amount of helium are investigated too.

Being able to predict the performance of Cu/Nb multilayer composites, as a potential material to be used in future nuclear reactors, at different working conditions is essential. It is

known that the enhanced radiation damage tolerance of this material resides in the energetics and atomic structure of their interfaces. Hence, a MD study of temperature effects on helium trapping and storage in Cu/Nb interface is reported in this thesis. Special attention has been paid to the mechanical and microstructural response of the material to an increasing concentration of interfacial helium.

In nuclear reactors, bombarding particles provoke atomic displacements that lead to the creation of self-interstitial atoms (SIAs) and vacancies. Unlike helium, which is insoluble in metals, a SIA and a vacancy can be removed by means of recombination. The mechanisms underlying point-defect annihilation at NMMC interfaces have been covered in detail at atomistic scale. Nevertheless, they are subject to time-scale limitations. A continuum model of point-defect evolution during irradiation of a multilayer composite material is presented in this dissertation. Numerical investigation on similarities and differences between Cu/Nb, Cu/V, and Cu/Ni systems is also performed. Atomistic simulations have revealed an unconventional behavior of point defects at interfaces found in multilayer composites synthesized by physical vapor deposition (PVD). Accordingly, boundary equations and initial conditions of the model have been adapted with the aim of comparing quantitatively model predictions in Cu/Nb and Cu/V systems with experimental results reported in the literature. Even though the investigations of this thesis have focused mainly on nuclear applications, the knowledge derived from them may be relevant and transferred to other sectors (aerospace, renewable energy, etc.).

# Contents

## Chapter 1

<b>Introduction. Motivation and objectives</b> .....	1
<b>References of Chapter 1</b> .....	7
<b>Figure of Chapter 1</b> .....	9

## Chapter 2

<b>Interaction of helium with graphene: A first-principles study</b> .....	10
<b>2.1. Introduction</b> .....	10
<b>2.2. Computational details</b> .....	13
<b>2.3. Results and discussion</b> .....	14
<b>2.4. Conclusions</b> .....	18
<b>References of Chapter 2</b> .....	19
<b>Tables and figures of Chapter 2</b> .....	28

## Chapter 3

<b>Saturation of helium on graphene: A density functional theory investigation</b> .....	32
<b>3.1. Introduction</b> .....	32
<b>3.2. Computational details</b> .....	34
<b>3.3. Results and discussion</b> .....	35
<b>3.3.1. Atomic structure</b> .....	35
<b>3.3.2. Electronic structure</b> .....	38
<b>3.4. Conclusions</b> .....	41
<b>References of Chapter 3</b> .....	42
<b>Table and figures of Chapter 3</b> .....	46

## Chapter 4

### **Molecular dynamics study of temperature effects on helium trapping and storage in**

<b>Cu/Nb interface .....</b>	<b>57</b>
<b>4.1. Introduction .....</b>	<b>57</b>
<b>4.2. Computational details .....</b>	<b>61</b>
<b>4.3. Results .....</b>	<b>63</b>
<b>4.4. Discussion .....</b>	<b>68</b>
<b>4.5. Conclusions .....</b>	<b>72</b>
<b>References of Chapter 4 .....</b>	<b>75</b>
<b>Figures of Chapter 4 .....</b>	<b>80</b>

## Chapter 5

### **Role of interface in multilayered composites under irradiation: A mathematical**

<b>investigation .....</b>	<b>88</b>
<b>5.1. Introduction .....</b>	<b>88</b>
<b>5.2. Mathematical model .....</b>	<b>91</b>
<b>5.3. Results .....</b>	<b>98</b>
<b>5.4. Discussion .....</b>	<b>101</b>
<b>5.5. Conclusions .....</b>	<b>103</b>
<b>Nomenclature of Chapter 5 .....</b>	<b>104</b>
<b>References of Chapter 5 .....</b>	<b>106</b>
<b>Tables and figures of Chapter 5 .....</b>	<b>111</b>

## Chapter 6

### **Self-healing ability assessment of irradiated multilayered composites: A continuum**

<b>approach .....</b>	<b>125</b>
<b>6.1. Introduction .....</b>	<b>125</b>
<b>6.2. Mathematical model .....</b>	<b>131</b>

<b>6.3. Results</b> .....	136
<b>6.4. Discussion</b> .....	140
<b>6.5. Conclusions</b> .....	143
<b>Nomenclature of Chapter 6</b> .....	146
<b>References of Chapter 6</b> .....	148
<b>Figures of Chapter 6</b> .....	152
<b>Chapter 7</b>	
<b>Concluding remarks</b> .....	161

# Chapter 1

## Introduction. Motivation and objectives

The progress of humankind has been closely related to the evolution of human-made materials. Such is their importance in people's life that the ages of civilizations are named by the new dominant material in each new era. Nowadays, the development of novel materials remains of paramount importance to tackle societal challenges [1].

One of the main challenges is the supply of secure, clean and efficient energy [2]. Sustainable energy sources offer one of the highest potentials to meet energy needs of future generations as well as to reach climate goals. Renewable energies contribute to the decarbonisation of the energy system and to reduce fossil fuels dependence. Nevertheless, they possess an intermittent nature. In contrast, nuclear fusion may provide continuous large-scale energy through the same process that powers the sun [3].

Other societal challenge is the development of smart, green and integrated transport [4]. Significant reductions in CO<sub>2</sub> and greenhouse gas emissions may be obtained by electrifying the transport sector and integrating sustainable energy sources in the electricity grid. Moreover, lightweight solutions in the structures and components of vehicles could improve their energy efficiency and thus reduce their impact on the environment [5].

Even though sustainable energy sources offer the possibility of obtaining a cleaner environment, they will compete with more traditional ones. Therefore, the cost of producing clean energy will remain a key element for its use. It occurs similarly with lightweight solutions whose use will depend on the additional cost to save weight while maintaining their performance. Key enabling technologies (KETs), such as advanced materials, can play an important role in making low-carbon options cost competitive compared to those currently used [6].

A particular challenge in materials science and engineering is the design and synthesis of materials that possess the desired properties for a specific application. Nanomaterials are intended to improve the performance of existing technologies, and to provide new functionalities to products, such as enhanced properties, new capabilities and increased reliability [7]. These materials are the base of several components in advanced systems and have a wide variety of potential applications in engineering.

Among the diverse human-made nanostructures, multilayer materials have been largely used in the production of semiconductor and magnetic devices [8,9]. The recognition

of the technological potential of these materials has helped to achieve rapid advances in the fields of electronics and computing.

Nuclear and aerospace materials need to perform well in severe operating conditions such as those expected in the walls of reaction chambers in nuclear fusion or the shielding of space satellites. Many research and innovation initiatives point to nanoscale metallic multilayer composites (NMMCs) as material systems with enhanced radiation and thermal resistance to withstand the exposure to high-radiation environments and to enable stable performances under high-temperature conditions [10]. In addition, the high mechanical strength of these materials allows to reduce the total weight associated with the structural components keeping the mechanical performance unchanged.

The industrial revolution of the 19th century was possible thanks to the production of energy from the burning of coal. In the 20th century, plastics revolutionized the manufacturing industry. Currently, carbon may be the driving force behind a new technological revolution again. Graphene, a two-dimensional crystal of pure carbon, has emerged in the last years as a superlative material that promises to transform the future due to its many applications (electronics, spintronics, photonics, optoelectronics, energy storage, biomedicine, etc.) [11]. Its extraordinary properties are unique and superior compared to those of other materials. Moreover, there is no such combination of properties in other materials. All this, along with the abundance of carbon on the Earth that guarantees the sustainability and economic competitiveness of carbon-based technologies, make graphene a potential candidate to become the material of the 21st century.

Although much attention has been paid to the outstanding electronic, thermal, and mechanical properties of pure graphene, its isolated use has so far been discarded for most applications. However, thanks to its high ratio of surface area to volume, flexibility and chemical versatility, graphene can be combined with metals, for example, to enhance their properties [12]. Hence, the number of possible composite systems containing graphene is practically unlimited.

The incorporation of the nanoscale to materials development may provide them advanced functionalities as self-healing ability. Thus, such materials might work within an aggressive environment without property degradation by forcing damage mechanisms to proceed along selected pathways or initiating the self-repair of damage. Nonetheless, the enhancement and optimization of material response under severe operating conditions require to capture the evolution of damage at all scales and understand how material processing, nanostructure, microstructure and properties interact [13].

The cost and time needed for materials discovery, optimization and deployment may be reduced by the use of computational modeling [14]. This powerful tool kit allows to identify and design novel multifunctional materials with a huge number of industrial possibilities. Moreover, it can help to predict trends and interpret experimental results. Therefore, industries that use materials modeling will reduce the need of massive experimental testing and, thanks to the optimal experimental design, they will obtain more robust results.

Materials development represents a multiscale problem that requires a consistent hierarchy of simulations at different levels. Depending on the time scale of the phenomena and the accuracy needed, models describing different entities (electron, atom, nanoparticle, grain and continuum cell) can be applied (see **Figure 1**). Simulations are particularly important at the smaller scales to access information that would not be available otherwise. In addition, effects and processes that originate at electronic, atomistic, or nanoparticle scale are not usually included in continuum models since they disregard small details. So, the linking of several models to cover all scales and the integration of results obtained at electronic, atomistic and mesoscopic scale into continuum models represent a big challenge in materials modeling for achieving relevant industrial results [16].

Interactions between atoms and electrons are governed by the laws of quantum mechanics. Density functional theory (DFT) [17] is a successful method to obtain an approximate solution to the Schrödinger equation of a many-atom, many-electron system (the Schrödinger equation cannot be solved exactly for many-body systems). DFT technique casts the intractable complexity of electron–electron interactions into an effective potential and transforms a N-electron equation into N one-electron equations coupled through that potential which is a functional of the electron density only.

Most atomic systems of interest in chemistry and physics are too large for quantum-mechanical simulations. Molecular dynamics (MD) [18] is a technique used to study the time evolution of a set of interacting atoms by numerical integration of Newton's equations of motion. This technique provides atomic details without explicitly considering the representation of electrons. The interactions between atoms in MD simulations are described by interatomic potentials developed from experimental data or DFT calculations results. Both techniques, DFT and MD, can be used to determine parameters that serve as inputs for larger-scale models.

At the continuum level, the discrete atomistic structure is disregarded and materials are assumed to possess continuously distributed properties. The mathematical description of

continuum problems requires constitutive equations characterizing the behavior of specific idealized materials in addition to fundamental physical laws such as the conservation of mass, momentum and energy. Most continuum problems cannot be solved analytically. The finite element method (FEM) [19] is a powerful technique that provides numerical, approximate solutions to initial- and boundary-value problems including time-dependent processes. The continuum is divided into non-overlapping subdomains, finite elements, over which equations are approximated by simple functions. This allows equations to be solved by means of numerical methods.

Currently, there is a lack of computational tools to predict the damage suffered by nanostructured materials, such as multilayer composites, as well as their performance under severe operating conditions. This thesis attempts to fill this gap by developing a framework of predictive modelling to optimize the design of materials that exhibit improved resistance to damage and exceptional mechanical properties for application in advanced engineering systems. As an innovative approach, a multiscale methodology is proposed to test nanostructured materials working within realistic environments which combines techniques such as DFT, MD and FEM. Even though the investigations of this dissertation have focused mainly on nuclear applications, the knowledge derived from them may be relevant and transferred to other sectors (aerospace, renewable energy, etc.).

The reduced thickness, high mechanical strength, stability and impermeability to helium of graphene make this material a possible vehicle to manage the large amounts of helium generated in nuclear reactors, as a constituent of nanocomposites structures. Chapter 2 reports a DFT study of helium atom permeation towards graphene over different points. In order to provide some tools for modelling helium behavior on graphene at a larger scale, potential energy curves have been fitted with a Yukawa–Lennard–Jones potential. The most favorable diffusion paths of helium atoms on graphene have been analyzed too.

The few existing first-principles works about graphene-He interaction have been limited to the study of a single helium atom. In Chapter 3, the saturation process of helium on graphene is investigated by means of DFT calculations. The procedure used allows to evaluate the weight of graphene-He and He-He interactions in the binding energy of each single helium atom to the rest of the system during helium multilayered structure formation as well as the structural and energy properties of helium on graphene. Lastly, an electronic structure analysis has been carried out to explain and understand in greater detail the results obtained.

One of the most promising strategies for avoiding the deleterious effects of helium in future nuclear systems, or at least retarding their appearance, is the introduction of heterophase interfaces as those found in Cu/Nb multilayer composites. It is known that the enhanced radiation damage tolerance of these materials resides in the energetics and atomic structure of their interfaces. Such interfaces may easily change from a metastable state to another one of almost the same energy due to tensional or thermal variations. Moreover, degradation processes caused by helium precipitates depend on their characteristics and number density, which in turn have been proven to be dependent on implantation conditions. Chapter 4 tries to elucidate the effect of temperature on the mechanisms behind helium trapping as well as helium bubbles formation and growth in Cu/Nb interfaces. To this end, MD simulations were carried out at different temperatures on Cu/Nb bilayer composites in presence of an increasing amount of helium. The eventual microstructural changes in the material and its mechanical response have also been investigated.

In nuclear reactors, bombarding particles provoke atomic displacements that lead to the creation of self-interstitial atoms (SIAs) and vacancies. Unlike helium, which is insoluble in metals, a SIA and a vacancy can be removed by means of recombination. Heterophase interfaces show an enhanced ability to annihilate point defects. Consequently, the number of point defects produced in multilayer composites containing these interfaces is much lower than in single component crystals. The mechanisms underlying point-defect annihilation at NMMC interfaces have been covered in detail at the atomistic scale. Nevertheless, they are subject to time-scale limitations. A continuum model of point-defect evolution during irradiation of a multilayer composite material is presented in Chapter 5. Non-stationary balance equations are used to describe production, recombination, transport and annihilation, or removal, of SIAs and vacancies in a  $\beta$ - $\alpha$ - $\beta$  three-layer system ( $\alpha$  = Cu and  $\beta$  = Nb, V or Ni). In addition, transport and trapping of point defects at interfaces are taken into account. Numerical investigations on similarities and differences between Cu/Nb, Cu/V, and Cu/Ni systems are also performed.

Atomistic simulations have revealed an unconventional behavior of point defects at interfaces found in multilayer composites synthesized by physical vapor deposition (PVD). Accordingly, in Chapter 6, boundary equations and initial conditions of the previous chapter have been adapted with the aim of comparing quantitatively model predictions in Cu/Nb and Cu/V systems with experimental results reported in the literature. In those experiments, both multilayer composites were synthesized by PVD. The effect of interface point-defect trapping

and recombination mechanisms, as well as interface self-interstitial atoms loading and constitutional vacancies on point-defect concentrations has been studied too.

Finally, concluding remarks of this thesis are presented in Chapter 7. Detailed introduction and conclusions sections are provided for each chapter, along with computational details, or mathematical model, as well as results and discussion sections, except for last one.

## References of Chapter 1

- [1] J. P. Holdren, "Materials Genome Initiative Strategic Plan", National Science and Technology Council, 2014,  
[https://www.mgi.gov/sites/default/files/documents/mgi\\_strategic\\_plan\\_-\\_dec\\_2014.pdf](https://www.mgi.gov/sites/default/files/documents/mgi_strategic_plan_-_dec_2014.pdf).
- [2] "Work Programme 2014-2015 in the area of Secure, Clean and Efficient Energy", Horizon 2020 - European Commission, 2013,  
[http://ec.europa.eu/research/participants/data/ref/h2020/wp/2014\\_2015/main/h2020-wp1415-energy\\_en.pdf](http://ec.europa.eu/research/participants/data/ref/h2020/wp/2014_2015/main/h2020-wp1415-energy_en.pdf).
- [3] F. Romanelli, P. Barabaschi, D. Borba, G. Federici, L. Horton, R. Neu, D. Stork, and H. Zohm, "Fusion Electricity: A roadmap to the realization of fusion energy", European Fusion Development Agreement (EFDA), 2012, [https://www.euro-fusion.org/fileadmin/user\\_upload/Archive/wp-content/uploads/2013/01/JG12.356-web.pdf](https://www.euro-fusion.org/fileadmin/user_upload/Archive/wp-content/uploads/2013/01/JG12.356-web.pdf).
- [4] "Work Programme 2014-2015 in the area of Smart, Green and Integrated Transport", Horizon 2020 - European Commission, 2013,  
[http://ec.europa.eu/research/participants/data/ref/h2020/wp/2014\\_2015/main/h2020-wp1415-transport\\_en.pdf](http://ec.europa.eu/research/participants/data/ref/h2020/wp/2014_2015/main/h2020-wp1415-transport_en.pdf).
- [5] "Call NMBP-08-2016: Affordable weight reduction of high-volume vehicles and components taking into account the entire life-cycle", Horizon 2020 - European Commission, 2015,  
<http://ec.europa.eu/research/participants/portal/desktop/en/opportunities/h2020/topics/nmbp-08-2016.html>.
- [6] "Call NMBP-17-2016: Advanced materials solutions and architectures for high efficiency solar energy harvesting", Horizon 2020 - European Commission, 2015,  
<http://ec.europa.eu/research/participants/portal/desktop/en/opportunities/h2020/topics/nmbp-17-2016.html>.
- [7] "Call NMP 2-2015: Advanced Integration of novel nanomaterials into existing production lines", Horizon 2020 - European Commission, 2013,  
<http://ec.europa.eu/research/participants/portal/desktop/en/opportunities/h2020/topics/nmp-02-2015.html>.
- [8] M. Tanaka, J. P. Harbison, T. Sands, B. Philips, T. L. Cheeks, J. De Boeck, L. T. Florez, and V. G. Keramidas, "Epitaxial MnGa/NiGa magnetic multilayers on GaAs", *Applied Physics Letters*, vol. 63, no. 5, pp. 696-698, 1993.

- [9] K. Tivakornsasithorn, T. Yoo, H. Lee, S. Lee, S. Choi, S. K. Bac, K. J. Lee, S. Lee, X. Liu, M. Dobrowolska, and J. K. Furdyna, "Magnetization reversal and interlayer exchange coupling in ferromagnetic metal/semiconductor Fe/GaMnAs hybrid bilayers", *Scientific Reports*, vol. 8, article 10570, 2018.
- [10] I. J. Beyerlein, A. Caro, M. J. Demkowicz, N. A. Mara, A. Misra, and B. P. Uberuaga, "Radiation damage tolerant nanomaterials", *Materials Today*, vol. 16, no. 11, pp. 443-449, 2013.
- [11] A. C. Ferrari *et al.*, "Science and technology roadmap for graphene, related two-dimensional crystals, and hybrid systems", *Nanoscale*, vol. 7, no. 11, pp. 4598-4810, 2015.
- [12] "Graphene Flagship - one year on. Annual report 2013-2014", Horizon 2020 - European Commission, 2015, [http://graphene-flagship.eu/SiteCollectionDocuments/Admin/Annual%20report/Graphene\\_2013\\_2014.pdf](http://graphene-flagship.eu/SiteCollectionDocuments/Admin/Annual%20report/Graphene_2013_2014.pdf).
- [13] "Call NMP 19-2015: Materials for severe operating conditions, including added-value functionalities", Horizon 2020 - European Commission, 2013, <http://ec.europa.eu/research/participants/portal/desktop/en/opportunities/h2020/topics/nmp-19-2015.html>.
- [14] L. Rosso and A. De Baas, "What makes a material function? Let me compute the ways", Seventh Framework Programme (FP7) - European Commission, 2012, [https://ec.europa.eu/research/industrial\\_technologies/pdf/modelling-brochure\\_en.pdf](https://ec.europa.eu/research/industrial_technologies/pdf/modelling-brochure_en.pdf).
- [15] B. D. Wirth, G. R. Odette, J. Marian, L. Ventelon, J. A. Young-Vandersall, and L. A. Zepeda-Ruiz, "Multiscale modeling of radiation damage in Fe-based alloys in the fusion environment", *Journal of Nuclear Materials*, vol. 329, pp. 103-111, 2004.
- [16] "Call NMP 20-2014: Widening materials models", Horizon 2020 - European Commission, 2013, <http://ec.europa.eu/research/participants/portal/desktop/en/opportunities/h2020/topics/nmp-20-2014.html>.
- [17] W. Koch and M. C. Holthausen, *A chemist's guide to density functional theory*, Wiley-VCH Verlag GmbH, 2001.
- [18] D. C. Rapaport, *The art of molecular dynamics simulation*, Cambridge University Press, 2004.
- [19] J. N. Reddy, *An introduction to the finite element method*, McGraw-Hill, 2006.

Figure of Chapter 1

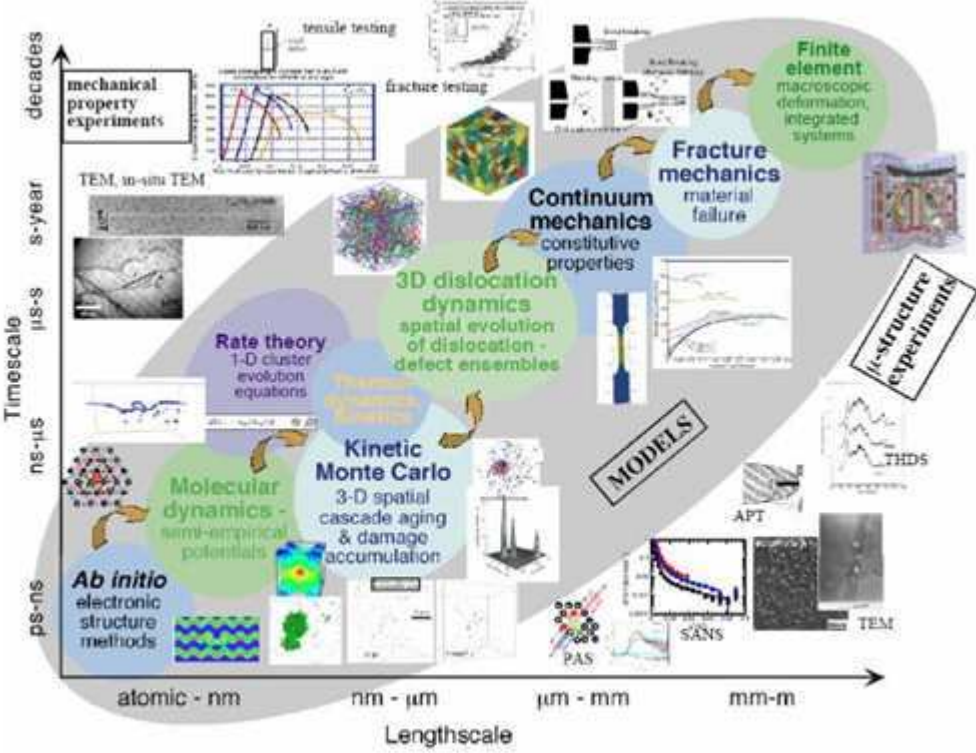


Figure 1 Scheme of multiscale materials design by a computational and experimental approach [15].

## Chapter 2

### Interaction of helium with graphene: A first-principles study

#### 2.1. Introduction

Fusion power has been presented in the last years as a trustworthy alternative to current environmentally unfriendly technologies [1] due to its many advantages in comparison to other sources [2]. International Thermonuclear Experimental Reactor (ITER) project expects to develop, implement and test fusion technology for a subsequent integration in the first commercial fusion prototype, the Demonstration Power Plant (DEMO). A huge institutional and economical effort [3] has been made to face future fusion nuclear reactors challenges: plasma confinement [4], efficient heat extraction, development of tritium breeding blankets [5] and radiation resistant materials design [6].

The main design objectives to be achieved in ITER are obtaining a pulse with a duration of 8 or 30 minutes and an amplification factor (fusion power / heating power) equal to 10 or 5 depending on the purpose—long pulse or steady-state regimen evaluation respectively—. ITER diameter is twice bigger than that of the Joint European Torus (JET), the largest tokamak built to date, which has as a consequence a plasma energy and discharge ion fluences 35 and 1000 times higher, respectively [7]. Edge localized modes (ELMs) [8,9], periodic unstable events that lead to a release of thermal energy and particles from plasma, compromise mainly the material integrity and functionality of the first wall and divertor. These instabilities help to stabilize plasma density since otherwise it would trigger a more severe instability denominated disruption with plasma control loss [10-12]. Although ELMs develop on the outermost plasma region, there is a not inconsiderable thermal energy loss in the core and consequently of magnetic confinement [13].

The first generation of fusion reactors will be based on a deuterium-tritium reaction. Deuterium can be easily obtained from water, which is not the case for tritium. By means of the interaction between neutrons produced during fusion reaction and a blanket containing lithium, tritium is supplied since its quantity in Nature would not be enough [14]. Either hydrogen isotopes or fusion reaction products, alpha particles (helium ash) and high energy neutrons, could generate very important issues. Helium ash must be removed to avoid plasma dilution [15,16] and tritium amount controlled for safety [17] because otherwise it could make necessary to stop for cleaning with the risk of unsatisfactory nuclear plant availability [18].

Some of the outstanding effects that neutron irradiation can produce are hardening, fracture toughness reduction, radiation induced precipitation, irradiation creep and volumetric swelling [19-23], depending on the combination of irradiation temperature and dose [24]. Moreover, neutron-induced transmutation leads to the formation of helium and hydrogen [25] which in case of being radioactive tritium isotope may decay into helium.

Helium atoms may diffuse reaching grain boundaries and getting trapped by sites which act like vacancies [26]. Some studies suggest, due to energetic compatibility, the possibility of helium and helium-vacancies clusters growth in grain boundaries and therefore helium bubbles formation although the binding energy of helium interstitial atoms to such clusters is usually weaker than in the matrix of the material [27]. Helium accumulation can cause grain boundary decohesion and consequently, reach the end of embrittlement-lifetime, issue that depends a lot on the component location in the nuclear reactor and the material it is made of [28]. By means of an empirical model, yield stress change and ductile-to-brittle transition temperature shift were studied as functions of irradiation dose as well as test and irradiation temperatures which allowed to elucidate some trends [29]. For irradiation temperature below 400 °C embrittlement is dominated by hardening while above this temperature it seems there is a non-hardening embrittlement contribution possibly related to a helium concentration increase that may cause the transition from transgranular cleavage to intergranular fracture. One of the main limitations is the identification and separation of helium effects from others such as damage displacement which cannot be neglected at low temperatures due to an annealing process reduction [30]. In addition to mechanical properties degradation, helium irradiation can lead to microstructural changes as phase transformation or lattice distortion, polycrystallization and amorphization [31]. Either experimental [32-35] or theoretical [36-39] investigations about metal tritides indicate the suitability of these materials to retain and release tritium considering them an exceptional solution for its storage unlike what happens with helium. For instance, the formation of helium clusters in palladium tritides increase local stresses and lattice volume and so, it could give rise to material failure due to the loss of original structural properties [40]. Moreover, in contrast to tritium, helium thermal release is difficult.

Radiation resistant materials design has been identified as the main critical point in terms of lifetime for future nuclear devices operating either in pulsed mode or in steady-state regime [41]. Therefore, finding a material capable of minimizing the damage induced by radiation is very desirable. Graphene has become one of the most important materials in the field of nanoscience due to its many applications [42,43]. The reduced thickness, the high

mechanical strength and the impermeability to helium of this material [44-46], in addition to its mechanical, thermal and chemical stability [47,48], make graphene a possible vehicle to manage the large amounts of helium generated in nuclear fusion reactors, as a constituent of nanocomposites structures.

Interaction of single atoms with graphene has attracted the attention of several researchers due to the importance that supposes tailored modifications of graphene electronic and magnetic properties for the design of high performance nanoelectronic devices [49-59]. It is worth mentioning the great number of first-principles works about interaction of hydrogen with graphene for electronic applications [60,61] and mainly for hydrogen storage [62-67]. Efforts have been made to increase the capacity of the latter through the doping of graphene [68-72], adsorbed elements [73,74] or both [75,76]. The results of these hydrogen-graphene studies contribute to increase the knowledge in the matter which allows its application in the nuclear sector. Carbon-based materials can be eroded by hydrogen through swift chemical sputtering [77] and physical one [78] depending on the ionic energy. Unlike hydrogen, there are only a few *ab initio* studies of interaction between graphene and helium [79-81].

There is an absence of appropriate neutron irradiation facilities with enough intensity for materials test in realistic conditions [82]. In addition, constitutive relations have become insufficient to analyze the technical and financial requirements of future nuclear facilities design [83]. Therefore, studying helium behavior at the electronic and atomic level is necessary. The present investigation focuses on the interaction of helium with graphene and attempts to complement previous first-principles studies giving an overall view in this regard. Burganova *et al.* [81] calculated the potential energy of a helium atom on graphene for various symmetrical points using several functionals and van der Waals corrections but only around equilibrium positions and without relaxing carbon atoms. Leenaerts *et al.* [79] do not mention any van der Waals correction and they studied the helium atom penetration only through the center of a graphene hexagon. While the energy barrier is not affected by the relaxation of carbon atoms in **Ref. (79)** because the latter is in an upper timescale than the corresponding to the interaction of helium atom with graphene, the energy barrier height varies depending on the interaction regime in **Ref. (80)**. In this last work, the authors tested two hybrid functionals and they took into account dispersion interactions. As in **Ref. (79)**, only the permeation trajectory of helium to the center of graphene hexagon was studied in the ultrafast regime. Therefore, we have employed density functional theory (DFT) to study helium atom permeation towards graphene placing the former over highly symmetric graphene points (hexagon center C, midpoint of hexagon side, or bridge B, and hexagon

vertex V). In order to provide the parameters and tools for modelling of helium behavior on graphene at a larger scale and thus elucidate the underlying mechanisms in helium diffusion and trapping as well as helium bubbles nucleation and growth, potential energy curves have been fitted with a Yukawa–Lennard–Jones form which can serve as an alternative to the widely used semiempirical potential developed by Carlos *et al.* [84]. Furthermore, the most favorable diffusion paths of helium atoms on graphene have been analyzed too but unlike in previous studies, allowing carbon atoms relaxation. The conclusions of this study raise the possibility of graphene acting as a nanomembrane, for the storage and retention of helium, which can be of importance in complex nuclear fusion systems and a solution to the material degradation caused by helium presence.

## 2.2. Computational details

To study the interaction of helium with graphene, we have employed the density functional theory (DFT). The calculations were performed using the Quantum Espresso code [85]. The valence electrons involved in the calculation were the ( $2s^2 2p^2$ ) electrons of carbon and the ( $1s^2$ ) electrons of helium, whereas the core electrons ( $1s^2$ ) of carbon were replaced by a pseudopotential. A norm-conserving pseudopotential generated with the Troullier-Martins procedure [86] was used for carbon in a semilocal form. The exchange-correlation terms were parametrized using the Perdew-Wang representation [87] within the local density approximation (LDA). Dispersion interactions were accounted for by the use of Rutgers-Chalmers van der Waals Density Functional (vdW-DF) method [88-90]. All the simulations were carried out with the periodic 4x4x1 graphene supercell shown in **Fig. 1** that was generated using the Atomic Simulation Environment (ASE) python module set with a starting carbon-carbon bond length close to 1.41 Å [91]. A separation between adjacent graphene sheets, i.e. a vacuum width in z-axis, of 16 Å was enough to give an error lower than 1 Ry in  $10^5$  atoms with respect to a single graphene layer which is in agreement with previous studies [79,62]. This distance was also enough to prevent interaction among graphene layers and consider them isolated. Moreover, as we were interested in the behavior of helium atoms not only close to the equilibrium distance to graphene, it helped us to guarantee there was sufficient space between graphene sheets to avoid the interaction of He atoms with more than a graphene layer. This supercell was used in the not-relaxed carbon atom position calculations but, before relaxed carbon atom position calculations, it was subjected to a shape optimization keeping the supercell volume fixed which caused a dimension increase in the z-axis besides a dimension decrease in xy-plane and, therefore, a carbon-carbon bond length reduction. In any

case, the variation of supercell dimensions was small. A plane-wave basis set with a kinetic energy cutoff of 70 Ry was used. The Brillouin zone was integrated with a 10x10x1 k-point grid generated using the Monkhorst-Pack scheme [92]. Minimum convergence threshold for self-consistency and ionic minimization on total energy was set to be  $10^{-8}$  Ry.

### 2.3. Results and discussion

First, we have studied the permeation of a helium atom towards the graphene sheet. In order to establish the most favorable paths for graphene penetration by helium, the energy barriers that appear because of the forces generated by the interaction of valence electrons and would have to be overcome are determined. Taking into account the shape of the supercell used, we have calculated the potential energy as a function of the distance between helium and the graphene plane placing one He atom over the following symmetric points belonging to the central hexagon of the graphene sheet (five sites in total): (i) center (one site), (ii) each of the two inequivalent carbon atoms of the unit cell (two sites), (iii) the midpoint of the perpendicular sides to the lattice vectors parallel to the graphene layer (four equivalent sites, so one site) and (iv) the midpoint of the sides parallel to the x-axis (two equivalent sites, so one site). The differences between the two inequivalent (ii) sites were negligible as well as among the (iii) and (iv) sites. In fact, they should be exactly equal for an infinite-basis calculation and with no interaction among atoms in adjacent supercells. Therefore, we are going to present the results corresponding to the following three physically inequivalent points (depicted in **Fig. 1**): hexagon center C, midpoint of hexagon side, or bridge B, and hexagon vertex V.

Here, we consider helium atom as a projectile with enough kinetic energy to not allow carbon atoms in graphene to relax and we have used the C-C distance of 1.408 Å calculated in **Ref. (91)**. Previous studies focused on permeation at the hollow site C only because this configuration leads to a much smaller barrier and a slightly bigger binding energy at the equilibrium distance [80]. However, we are interested in potential energy not only at helium equilibrium positions but also in a zone around them as we have indicated previously. Helium potential energy  $E_p$  for different distances  $d$  to the graphene plane may be expressed as:

$$E_p = E_{\text{tot}}^{\text{Gr+He}} - (E_{\text{tot}}^{\text{Gr}} + E_{\text{tot}}^{\text{He}}) \quad (1)$$

where  $E_{\text{tot}}^{\text{Gr+He}}$  is the total energy of the system formed by the graphene layer and helium atom while  $E_{\text{tot}}^{\text{Gr}}$  and  $E_{\text{tot}}^{\text{He}}$  are the total energies of isolated graphene layer and helium atom respectively with atoms occupying the same positions as in the complete system.

Potential energy results are shown in **Fig. 2** (hexagon center C, midpoint of hexagon side, or bridge B, and hexagon vertex V). We can see that all three potential energy curves are very similar when the helium atom is far from the graphene layer. As the helium atom approaches the graphene sheet, the potential energy curves decrease from zero (no interaction) and take negative values being the differences between them imperceptible until a distance close to 3.75 Å. Then, the curve corresponding to configuration C departs from the other ones. Equilibrium distances between the helium atom and graphene layer for configurations C, B and V are shown in the upper part of **Table 1** besides minimum potential energy values. Taking as a reference the most stable configuration (C), configuration B and V have a lower absolute value by 6 and 6.6 percent respectively. These values are lower than those corresponding to a hydrogen molecule but in the same order of magnitude [62]. Equilibrium potential energy and distance to graphene are determined by the electron density distribution of pure graphene above itself [62]. We can see in this reference that the isolines with the minimum electron density have a z-coordinate slightly higher above carbon atoms than on the bridge but considerable higher than over hexagon centers. Exchange-correlation contribution helps to establish an attractive interaction between the helium atom and graphene layer as it decreases more, i.e., it becomes more negative, than the sum of the remaining contributions until the equilibrium position is reached in the approach process. After the minimum, the electron cloud around the adsorbent tries to repel the  $1s^2$  electrons of helium atom and this fact increases the potential energy. This increase depends on the vertical trajectory followed and therefore, on the isolines concentration in each one. Repulsion contributions increase more between equilibrium and graphene vicinity positions in configuration V, then in configuration B and finally, in configuration C. Maximum potential energy is equal to 0.93 and 3.00 Ry for configuration C and B. For configuration V, the interaction increases very fast when the distance decreases and when  $d$  is 0.05 Å,  $E_p$  it reaches 155.33 Ry. So, considering the energy barriers that have to be surpassed, i.e., maximum potential energy plus minimum one, stable non-defective graphene penetration by helium is tremendously complicated even for the most favorable path in agreement with previous studies [79].

The interaction potential between the He atom and graphene is composed of two contributions: A screened Coulomb interaction resulting from the charge transfer between He

and C atoms and a van der Waals–type interaction. The interactions between carbon atoms in graphite can be written in the form of a simple 6-12 Lennard-Jones potential [93]. Nevertheless, when other types of atoms interact with graphene layers the interaction is more complex. For instance, for the Li case it is necessary to use a 4-6-12 Lennard-Jones potential and a Yukawa screened potential [91]. The case of He is even more subtle because the interaction close to the equilibrium configuration is much weaker than for Li. In this case it is possible to fit the interaction energy shown in **Fig. 2**, but we have to use a 4-6-8-12 Lennard-Jones potential and a Yukawa term:

$$E_p(d) = a_0 \frac{\exp(a_1 d)}{d} + \left\{ \frac{a_2}{d^4} + \frac{a_3}{d^6} + \frac{a_4}{d^8} + \frac{a_5}{d^{12}} \right\}. \quad (2)$$

The first term is a Yukawa-type screened Coulomb potential. The terms in curly brackets represent a softer and longer-ranged inverse power-law potential. The fitting parameters are listed in **Table 2**. This fit is shown in **Fig. 3** for configurations C, B and V and is valid for He-graphene distances greater than 1 Å.

The Yukawa part of the potential is always bonding since  $a_0$  is negative. The terms in the Lennard-Jones part have different signs and, therefore, bonding and non-bonding characters but the overall sum is always non-bonding. The Yukawa part is dominant at large separations and the Lennard-Jones one becomes dominant when the He atom is close to the graphene surface. The interplay between the two of them determines the equilibrium distance. Not surprisingly, considering **Fig. 2**, the coefficients for all three configurations are similar for the Yukawa part while those corresponding to the Lennard-Jones brackets are very similar for configurations B and V while those for configuration C are different. This fact is very clear in the case of  $a_3$  where there is even a reversal in sign. As can be seen in **Fig. 3**, the fitted potential reproduces accurately the calculated interaction potentials for the three configurations in the range 1–5 Å.

Next we have completed these calculations, in which the helium atom has been treated as a high energy particle, considering the opposite case. We have placed the helium atom over the symmetric points C, B and V at a distance from the graphene layer smaller than the corresponding to the minimum of the potential energy curves. Then, we have allowed the system to evolve by means of carbon atom position relaxation and thus we have determined the relaxed equilibrium configurations. Helium adsorption energy  $E_a^{He}$  is determined

similarly to Eq. (1) with the difference that total energies involved in the equation are calculated for the relaxed system.

Relaxed equilibrium distances and adsorption energies corresponding to configurations C, B and V are shown in the lower part of **Table 1**. It seems relaxation does not influence too much minimum interaction energy values as they only vary by 0.5 (C), 0.73 (B) and 0.62 percent (V) with respect to unrelaxed system results, which leaves here configuration C as the most stable too. Moreover, these values are very small which indicates that helium and graphene are in the physisorption regime and electronic states perturbation of adsorbent and adsorbate is minimal. The helium atom is not able to weaken the  $\pi$ -bonds between  $p_z$  orbitals of carbon atoms. Therefore, hybridization between helium  $s$  orbital and carbon  $p_z$  orbital is negligible in contrast to what occurs with hydrogen and rigid graphene or even the  $sp^3$ -like geometry in case of allowing carbon atoms to relax [66]. Equilibrium distances between the helium atom and graphene layer vary by 0.63 (C), 1.86 (B) and 1.09 percent (V) with respect to static calculations which is far, for instance, from results obtained for configuration V in the work mentioned just above for hydrogen. We can see that equilibrium distance decreases for configurations V and B but it increases for configuration C when cell and carbon position relaxation is allowed. Nevertheless, the length of carbon-carbon bonds surrounding the He atom decrease in the three configurations, i.e., they contract, although more slightly even than in the supercell shape optimization process described in the previous section. As a consequence, differences between not relaxed and relaxed results in **Table 1** are very small.

In addition, adsorption energy values presented in **Table 1** let us determine the activation energy barriers between configurations C, B and V that have to be overcome for the helium atom displacement parallel to the graphene sheet. The most stable site corresponds to configuration C and therefore, the most favorable diffusion paths take place from site B and V to configuration C and they could happen at any temperature like helium atom diffusion from V to B. If we consider the reverse paths, the minimum barrier to be surpassed is found between bridge and vertex sites and the maximum one between center and vertex sites corresponding to a temperature of about 5 K and 37 K respectively which allows us to conclude that helium could diffuse on any direction over graphene in almost the whole range of temperatures.

## 2.4. Conclusions

We have used density functional theory (DFT) with a van-der-Waals-corrected LDA functional to study the interaction of helium atoms with graphene. First, we have analyzed permeation towards graphene over highly symmetric graphene points (hexagon center, midpoint of hexagon side –bridge position–, and hexagon vertex). We have fitted the three potential energy curves with a Yukawa–Lennard–Jones form which can serve for larger scale calculations. Besides, we have studied the most favorable diffusion paths of helium atoms on graphene allowing carbon atoms to relax and shown that He atoms can diffuse on any direction at nearly any temperature. Therefore, our results confirm that graphene can act as a nanomembrane for the storage and retention of helium, making it suitable for the design of nanocomposite materials that integrate a possible solution to He-induced degradation observed in structural nuclear materials.

## References of Chapter 2

- [1] H. Cabal, Y. Lechón, C. Bustreo, F. Graceeva, M. Biberacher, D. Ward, D. Dongiovanni, and P.E. Grohnheit, *Fusion power in a future low carbon global electricity system*, Energy Strategy Reviews **15**, 1–8 (2017).
- [2] R.W. Conn, J.P. Holdren, S. Sharafat, D. Steiner, D.A. Ehst, W.J. Hogan, R.A. Krakowski, R.L. Miller, F. Najmabad, and K.R. Schultz, *Economic, safety and environmental prospects of fusion reactors*, Nuclear Fusion **30**, 1919–1934 (1990).
- [3] K. Ikeda, *ITER on the road to fusion energy*, Nuclear Fusion **50**, 014002 (2010).
- [4] J. Ongena, R. Koch, R. Wolf, and H. Zohm, *Magnetic-confinement fusion*, Nature Physics **12**, 398–410 (2016).
- [5] L.M. Giancarli, M. Abdou, D.J. Campbell, V.A. Chuyanoa, M.Y. Ahn, M. Enoeda, C. Pan, Y. Poitevin, E. Rajendra Kumar, I. Ricapito, Y. Strebkov, S. Suzuki, P.C. Wong, and M. Zmitko, *Overview of the ITER TBM Program*, Fusion Engineering and Design **87**, 395–402 (2012).
- [6] D. Duffy, *Modelling materials for fusion power*, International Materials Reviews **56**, 324–340 (2011).
- [7] J. Roth, E. Tsitrone, and A. Loarte, *Plasma–wall interaction: Important ion induced surface processes and strategy of the EU Task Force*, Nuclear Instruments and Methods in Physics Research B **258**, 253–263 (2007).
- [8] H. Zohm, *Edge localized modes (ELMs)*, Plasma Physics and Controlled Fusion **38**, 105–128 (1996).
- [9] K. Kamiya, N. Asakura, J. Boedo, T. Eich, G. Federici, M. Fenstermacher, K. Finken, A. Herrmann, J. Terry, A. Kirk, B. Koch, A. Loarte, R. Maingi, R. Maqueda, E. Nardon, N. Oyama, and R. Sartori, *Edge localized modes: recent experimental findings and related issues*, Plasma Physics and Controlled Fusion **49**, S43–S62 (2007).
- [10] P.C. de Vries, M.F. Johnson, B. Alper, P. Buratti, T.C. Hender, H.R. Koslowski, V. Riccardo, and JET-EFDA Contributors, *Survey of disruption causes at JET*, Nuclear Fusion **51**, 053018 (2011).
- [11] A. Cardella, H. Gorenflo, A. Lodato, K. Ioki, and R. Raffray, *Effects of plasma disruption events on ITER first wall materials*, Journal of Nuclear Materials **283–287**, 1105–1110 (2000).
- [12] T.C. Hender, J.C. Wesley, J. Bialek, A. Bondeson, A.H. Boozer, R.J. Buttery, A. Garofalo, T.P. Goodman, R.S. Granetz, Y. Gribov, O. Gruber, M. Gryaznevich, G.

- Giruzzi, S. Günter, N. Hayashi, P. Helander, C.C. Hegna, D.F. Howell, D.A. Humphreys, G.T.A. Huysmans, A.W. Hyatt, A. Isayama, S.C. Jardin, Y. Kawano, A. Kellman, C. Kessel, H.R. Koslowski, R.J. La Haye, E. Lazzaro, Y.Q. Liu, V. Lukash, J. Manickam, S. Medvedev, V. Mertens, S.V. Mirnov, Y. Nakamura, G. Navratil, M. Okabayashi, T. Ozeki, R. Paccagnella, G. Pautasso, F. Porcelli, V.D. Pustovitov, V. Riccardo, M. Sato, O. Sauter, M.J. Schaffer, M. Shimada, P. Sonato, E.J. Strait, M. Sugihara, M. Takechi, A.D. Turnbull, E. Westerhof, D.G. Whyte, R. Yoshino, H. Zohm, and the ITPA MHD, Disruption and Magnetic Control Topical Group, *MHD stability, operational limits and disruptions*, Nuclear Fusion **47**, S128–S202 (2007).
- [13] A.W. Leonard, A. Herrmann, K. Itami, J. Lingertat, A. Loarte, T.H. Osborne, W. Suttrop, the ITER Divertor Modeling and Database Expert Group, and the ITER Divertor Physics Expert Group, *The impact of ELMs on the ITER divertor*, Journal of Nuclear Materials **266–269**, 109–117 (1999).
- [14] J. Ongena and G. Van Oost, *Energy for Future Centuries: Prospects for fusion power as a future energy source*, Fusion Science and Technology **57**, 3–15 (2010).
- [15] D. Reiter, H. Keuer, G.H. Wolf, M. Baelmans, R. Behrisch, and R. Schneider, *Helium removal from tokamaks*, Plasma Physics and Controlled Fusion **33**, 1579–1600 (1991).
- [16] G. Federici, C.H. Skinner, J.N. Brooks, J.P. Coad, C. Grisolia, A.A. Haasz, A. Hassanein, V. Philipps, C.S. Pitcher, J. Roth, W.R. Wampler, and D.G. Whyte, *Plasma-material interactions in current tokamaks and their implications for next step fusion reactors*, Nuclear Fusion **41**, 1967–2137 (2001).
- [17] M. Shimada, R.A. Pitts, S. Ciattaglia, S. Carpentier, C.H. Choi, G. Dell Orco, T. Hirai, A. Kukushkin, S. Lisgo, J. Palmer, W. Shu, and E. Veshchev, *In-vessel dust and tritium control strategy in ITER*, Journal of Nuclear Materials **438**, S996–S1000 (2013).
- [18] U. Samm, *Plasma-wall interactions in magnetically confined fusion plasmas*, Fusion Science and Technology **53**, 223–228 (2008).
- [19] E. Gaganidze and J. Aktaa, *Assessment of neutron irradiation effects on RAFM steels*, Fusion Engineering and Design **88**, 118–128 (2013).
- [20] E. Gaganidze, *Assessment of Fracture Mechanical Experiments on Irradiated EUROFER97 and F82H Specimens*, Final Report for Task TW5-TTMS, 001–D14 (2007).
- [21] P.J. Maziasz, *Formation and stability of radiation-induced phases in neutron-irradiated austenitic and ferritic steels*, Journal of Nuclear Materials **169**, 95–115 (1989).

- [22] F.A. Garner and M.B. Toloczko, *High dose effects in neutron irradiated face-centered cubic metals*, Journal of Nuclear Materials **206**, 230–248 (1993).
- [23] J. Chen and W. Hoffelner, *Irradiation creep of oxide dispersion strengthened (ODS) steels for advanced nuclear applications*, Journal of Nuclear Materials **392**, 360–363 (2009).
- [24] S.J. Zinkle and J.T. Busby, *Structural materials for fission & fusion energy*, Materials Today **12**, 12–19 (2009).
- [25] M.R. Gilbert and J.-Ch. Sublet, *Neutron-induced transmutation effects in W and W-alloys in a fusion environment*, Nuclear Fusion **51**, 043005 (2011).
- [26] S.L. Dudarev, *Density Functional Theory Models for Radiation Damage*, Annual Review of Materials Research **43**, 35–61 (2013).
- [27] L. Zhang, Y. Zhang, and G.H. Lu, *Structure and stability of He and He–vacancy clusters at a  $\Sigma 5(310)/[001]$  grain boundary in bcc Fe from first-principles*, Journal of Physics: Condensed Matter **25**, 095001 (2013).
- [28] M.R. Gilbert, S.L. Dudarev, S. Zheng, L.W. Packer and J.-Ch. Sublet, *An integrated model for materials in a fusion power plant: transmutation, gas production, and helium embrittlement under neutron irradiation*, Nuclear Fusion **52**, 083019 (2012).
- [29] T. Yamamoto, G.R. Odette, H. Kishimoto, J.W. Rensman, and P. Miao, *On the effects of irradiation and helium on the yield stress changes and hardening and non-hardening embrittlement of  $\sim 8\text{Cr}$  tempered martensitic steels: Compilation and analysis of existing data*, Journal of Nuclear Materials **356**, 27–49 (2006).
- [30] H. Trinkaus and B.N. Singh, *Helium accumulation in metals during irradiation – where do we stand?*, Journal of Nuclear Materials **323**, 229–242 (2003).
- [31] X. Tan, L. Luo, H. Chen, X. Zhu, X. Zan, G. Luo, J. Chen, P. Li, J. Cheng, D. Liu, and Y. Wu, *Mechanical properties and microstructural change of W–Y<sub>2</sub>O<sub>3</sub> alloy under helium irradiation*, Scientific Reports **5**, 12755 (2015).
- [32] B.Y. Ao, X.L. Wang, Y.Z. Zhang, and Y.J. Wei, *X-ray diffraction analysis of uranium tritide after aging for 420 days*, Journal of Nuclear Materials **384**, 311–314 (2009).
- [33] Z. Xiaosong, L. Xinggui, Z. Lin, P. Shuming, and L. Shunzhong, *X-ray diffraction analysis of titanium tritide film during 1600 days*, Journal of Nuclear Materials **396**, 223–227 (2010).
- [34] T. Hayashi, T. Suzuki, and K. Okuno, *Long-term measurement of helium-3 release behaviour from zirconium-cobalt tritide*, Journal of Nuclear Materials **212–215**, 1431–1435 (1994).

- [35] S. Thiébaud, M. Douilly, S. Contreras, B. Limacher, V. Paul-Boncour, B. Décamps, and A. Percheron-Guégan, *<sup>3</sup>He retention in LaNi<sub>5</sub> and Pd tritides: Dependence on stoichiometry, <sup>3</sup>He distribution and aging effects*, Journal of Alloys and Compounds **446–447**, 660–669 (2007).
- [36] D. Chattaraj, S.C. Parida, and C. Majumder, *Structural and electronic properties of U<sub>2</sub>Ti: A first principles study*, Physica B **406**, 4317–4321(2011).
- [37] J.H. Liang, Y.Y. Dai, L. Yang, S.M. Peng, K.M. Fan, X.G. Long, X.S. Zhou, X.T. Zu, and F. Gao, *Ab initio study of helium behavior in titanium tritides*, Computational Materials Science **69**, 107–112 (2013).
- [38] D. Chattaraj, S.C. Parida, S. Dash, and C. Majumder, *Structural, electronic and thermodynamic properties of ZrCo and ZrCoH<sub>3</sub>: A first-principles study*, International Journal of Hydrogen Energy **37**, 18952–18958 (2012).
- [39] G. Liu, D. Chen, Y. Wang, and K. Yang, *First-principles calculations of crystal and electronic structures and thermodynamic stabilities of La-Ni-H, La-Ni-Al-H and La-Ni-Al-Mn-H hydrogen storage compounds*, International Journal of Hydrogen Energy **41**, 12194–12204 (2016).
- [40] N.K. Das, K. Rigby, and N.H. de Leeuw, *The effect of helium nano-bubbles on the structures stability and electronic properties of palladium tritides: a density functional theory study*, Proceedings of the Royal Society of London A: Mathematical, Physical and Engineering Sciences **470**, 20140357 (2014).
- [41] V. Philipps, *Plasma–wall interaction, a key issue on the way to a steady state burning fusion device*, Physica Scripta **T123**, 24–32 (2006).
- [42] A. K. Geim, *Graphene: Status and Prospects*, Science **324**, 1530–1534 (2009).
- [43] J.H. Warner, F. Schäffel, A. Bachmatiuk, and M.H. Rummeli, *Graphene: Fundamentals and Emergent Applications*, Newnes, (2012).
- [44] J.S. Bunch, S.S. Verbridge, J.S. Alden, A.M. van der Zande, J.M. Parpia, H.G. Craighead, and P.L. McEuen, *Impermeable Atomic Membranes from Graphene Sheets*, Nano letters **8**, 2458–2462 (2008).
- [45] J. Schrier, *Helium Separation Using Porous Graphene Membranes*, The Journal of Physical Chemistry Letters **1**, 2284–2287 (2010).
- [46] R.R. Nair, H.A. Wu, P.N. Jayaram, I.V. Grigorieva, and A.K. Geim, *Unimpeded Permeation of Water Through Helium-Leak-Tight Graphene-Based Membranes*, Science **335**, 442–444 (2012).

- [47] M.I. Katsnelson, *Graphene: carbon in two dimensions*, *Materials Today* **10**, 20–27 (2007).
- [48] A.E. Galashev and O.R. Rakhmanova, *Mechanical and thermal stability of graphene and graphene-based materials*, *Physics-Uspekhi* **57**, 970–989 (2014).
- [49] M. Alemani, A. Barfuss, B. Geng, C. Girit, P. Reisenauer, M.F. Crommie, F. Wang, A. Zettl, and F. Hellman, *Effect of gadolinium adatoms on the transport properties of graphene*, *Physical Review B* **86**, 075433 (2012).
- [50] M.T. Hershberger, M. Hupalo, P.A. Thiel, and M.C. Tringides, *Growth of fcc(111) Dy multi-height islands on 6H-SiC(0001) graphene*, *Journal of Physics: Condensed Matter* **25**, 225005 (2013).
- [51] A. Ishii, M. Yamamoto, H. Asano, and K. Fujiwara, *DFT calculation for adatom adsorption on graphene sheet as a prototype of carbon nano tube functionalization*, *Journal of Physics: Conference Series* **100**, 052087 (2008).
- [52] L. Li, Y. Wang, L. Meng, R.T. Wu, and H.J. Gao, *Hafnium intercalation between epitaxial graphene and Ir(111) substrate*, *Applied Physics Letters* **102**, 093106 (2013).
- [53] Y.J. Li, M. Wang, M.Y. Tang, X. Tian, S. Gao, Z. He, Y. Li, and T.G. Zhou, *Spin and orbital magnetic moments and spin anisotropy energies of light rare earth atoms embedded in graphene: A first-principles study*, *Physica E: Low-dimensional Systems and Nanostructures* **75**, 169–173 (2016).
- [54] X. Liu, C.Z. Wang, M. Hupalo, Y.X. Yao, M.C. Tringides, W.C. Lu, and K.M. Ho, *Adsorption and growth morphology of rare-earth metals on graphene studied by ab initio calculations and scanning tunneling microscopy*, *Physical Review B* **82**, 245408 (2010).
- [55] P. Medeiros, A.J.S. Mascarenhas, F. de Brito Mota, and C.M.C. de Castilho, *A DFT study of halogen atoms adsorbed on graphene layers*, *Nanotechnology* **21**, 485701 (2010).
- [56] L. Sheng, Y. Ono, and T. Taketsugu, *Ab Initio Study of Xe Adsorption on Graphene*, *The Journal of Physical Chemistry C* **114**, 3544–3548 (2010).
- [57] C.L. Song, B. Sun, Y.L. Wang, Y.P. Jiang, L. Wang, K. He, X. Chen, P. Zhang, X.C. Ma, and Q.K. Xue, *Charge-Transfer-Induced Cesium Superlattices on Graphene*, *Physical Review Letters* **108**, 156803 (2012).
- [58] Z. Xu and M.J. Buehler, *Interface structure and mechanics between graphene and metal substrates: a first-principles study*, *Journal of Physics: Condensed Matter* **22**, 485301 (2010).

- [59] L.J. Zhou, Z.F. Hou, and L.M. Wu, *First-Principles Study of Lithium Adsorption and Diffusion on Graphene with Point Defects*, The Journal of Physical Chemistry C **116**, 21780–21787 (2012).
- [60] Z.M. Ao, A.D. Hernández-Nieves, F.M. Peeters, and S. Li, *Enhanced stability of hydrogen atoms at the graphene/graphane interface of nanoribbons*, Applied Physics Letters **97**, 233109 (2010).
- [61] Y. Ferro, D. Teillet-Billy, N. Rougeau, V. Sidis, S. Morisset, and A. Allouche, *Stability and magnetism of hydrogen dimers on graphene*, Physical Review B **78**, 085417 (2008).
- [62] J.S. Arellano, L.M. Molina, A. Rubio, and J.A. Alonso, *Density functional study of adsorption of molecular hydrogen on graphene layers*, The Journal of Chemical Physics **112**, 8114 (2000).
- [63] D. Henwood and J.D. Carey, *Ab initio investigation of molecular hydrogen physisorption on graphene and carbon nanotubes*, Physical Review B **75**, 245413 (2007).
- [64] V.V. Ivanovskaya, A. Zobelli, D. Teillet-Billy, N. Rougeau, V. Sidis, and P.R. Briddon, *Hydrogen adsorption on graphene: a first principles study*, The European Physical Journal B **76**, 481–486 (2010).
- [65] Y. Miura, H. Kasai, W. Diño, H. Nakanishi, and T. Sugimoto, *First principles studies for the dissociative adsorption of H<sub>2</sub> on graphene*, Journal of Applied Physics **93**, 3395–3400 (2003).
- [66] Y. Miura, H. Kasai, W.A. Diño, H. Nakanishi, and T. Sugimoto, *Effective Pathway for Hydrogen Atom Adsorption on Graphene*, Journal of the Physical Society of Japan **72**, 995–997 (2003).
- [67] Y. Okamoto and Y. Miyamoto, *Ab Initio Investigation of Physisorption of Molecular Hydrogen on Planar and Curved Graphenes*, The Journal of Physical Chemistry B **105**, 3470–3474 (2001).
- [68] Z.M. Ao, Q. Jiang, R.Q. Zhang, T.T. Tan, and S. Li, *Al doped graphene: A promising material for hydrogen storage at room temperature*, Journal of Applied Physics **105**, 074307 (2009).
- [69] Z.M. Ao and F.M. Peeters, *Electric Field Activated Hydrogen Dissociative Adsorption to Nitrogen-Doped Graphene*, The Journal of Physical Chemistry C **114**, 14503–14509 (2010).

- [70] Z.M. Ao, A.D. Hernández-Nieves, F.M. Peeters, and S. Lia, *The electric field as a novel switch for uptake/release of hydrogen for storage in nitrogen doped graphene*, Physical Chemistry Chemical Physics **14**, 1463–1467 (2012).
- [71] I. Cabria, M.J. López, and J.A. Alonso, *Enhancement of hydrogen physisorption on graphene and carbon nanotubes by Li doping*, The Journal of Chemical Physics **123**, 204721 (2005).
- [72] R.H. Miwa, T.B. Martins, and A. Fazzio, *Hydrogen adsorption on boron doped graphene: an ab initio study*, Nanotechnology **19**, 155708 (2008).
- [73] Z.M. Ao and F.M. Peeters, *High-capacity hydrogen storage in Al-adsorbed graphene*, Physical Review B **81**, 205406 (2010).
- [74] Y. Liu, L. Ren, Y. He, and H.P. Cheng, *Titanium-decorated graphene for high-capacity hydrogen storage studied by density functional simulations*, Journal of Physics: Condensed Matter **22**, 445301 (2010).
- [75] E. Beheshti, A. Nojeh, and P. Servati, *A first-principles study of calcium-decorated, boron-doped graphene for high capacity hydrogen storage*, Carbon **49**, 1561–1567 (2011).
- [76] H. Lee, J. Ihm, M.L. Cohen, and S.G. Louie, *Calcium-Decorated Graphene-Based Nanostructures for Hydrogen Storage*, Nano letters **10**, 793–798 (2010).
- [77] A. Ito and H. Nakamura, *Molecular Dynamics Simulation of Bombardment of Hydrogen Atoms on Graphite Surface*, Communications in Computational Physics **4**, 592–610 (2008).
- [78] J. Marian, L.A. Zepeda-Ruiz, G.H. Gilmer, E.M. Bringa, and T. Rognlien, *Simulations of carbon sputtering in amorphous hydrogenated samples*, Physica Scripta **T124**, 65–69 (2006).
- [79] O. Leenaerts, B. Partoens, and F.M. Peeters, *Graphene: A perfect nanoballoon*, Applied Physics Letters **93**, 193107 (2008).
- [80] S.E. Huber, A. Mauracher, and M. Probst, *Permeation of low-Z atoms through carbon sheets: Density functional theory study on energy barriers and deformation effects*, AIP Advances **3**, 122104 (2013).
- [81] R. Burganova, Y. Lysogorskiy, O. Nedopekin, and D. Tayurskii, *Adsorption of Helium Atoms on Two-Dimensional Substrates*, Journal of Low Temperature Physics **185**, 392–398 (2016).

- [82] S.J. Zinkle, A. Möslan, T. Muroga, and H. Tanigawa, *Multimodal options for materials research to advance the basis for fusion energy in the ITER era*, Nuclear Fusion **53**, 104024 (2013).
- [83] M. Samaras, *Multiscale modelling: the role of helium in iron*, Materials Today **12**, 46–53 (2009).
- [84] W.E. Carlos and M.W. Cole, *Interaction between a He atom and a graphite surface*, Surface Science **91**, 339–357 (1980).
- [85] P. Giannozzi, S. Baroni, N. Bonini, M. Calandra, R. Car, C. Cavazzoni, D. Ceresoli, G.L. Chiarotti, M. Cococcioni, I. Dabo, A. Dal Corso, S. de Gironcoli, S. Fabris, G. Fratesi, R. Gebauer, U. Gerstmann, C. Gougoussis, A. Kokalj, M. Lazzeri, L. Martin-Samos, N. Marzari, F. Mauri, R. Mazzarello, S. Paolini, A. Pasquarello, L. Paulatto, C. Sbraccia, S. Scandolo, G. Sclauzero, A.P. Seitsonen, A. Smogunov, P. Umari, and R.M. Wentzcovitch, *QUANTUM ESPRESSO: a modular and open-source software project for quantum simulations of materials*, Journal of Physics: Condensed Matter **21**, 395502 (2009).
- [86] N. Troullier and J.L. Martins, *Efficient pseudopotentials for plane-wave calculations*, Physical Review B **43**, 1993–2006 (1991).
- [87] J.P. Perdew and Y. Wang, *Accurate and simple analytic representation of the electron-gas correlation energy*, Physical Review B **45**, 13244–13249 (1992).
- [88] M. Dion, H. Rydberg, E. Schröder, D.C. Langreth, and B.I. Lundqvist, *Van der Waals Density Functional for General Geometries*, Physical Review Letters **92**, 246401 (2004).
- [89] T. Thonhauser, V.R. Cooper, S. Li, A. Puzder, P. Hyldgaard, and D.C. Langreth, *Van der Waals density functional: Self-consistent potential and the nature of the van der Waals bond*, Physical Review B **76**, 125112 (2007).
- [90] G. Román-Pérez and J.M. Soler, *Efficient implementation of a van der Waals density functional: Application to double-wall carbon nanotubes*, Physical Review Letters **103**, 096102 (2009).
- [91] M. Khantha, N.A. Cordero, L.M. Molina, J.A. Alonso, and L.A. Girifalco, *Interaction of lithium with graphene: An ab initio study*, Physical Review B **70**, 125422 (2004).
- [92] H.J. Monkhorst and J.D. Pack, *Special points for Brillouin-zone integrations*, Physical Review B **13**, 5188–5192 (1976).

- [93] L.A. Girifalco and R.A. Lad, *Energy of Cohesion, Compressibility, and the Potential Energy Functions of the Graphite System*, The Journal of Chemical Physics **25**, 693–697 (1956).

## Tables and figures of Chapter 2

**Table 1** Equilibrium distances and interaction energies between a helium atom and a graphene layer for configurations C, B and V. Results are shown for two different cases: when cell size as well as carbon atoms position relaxation is allowed and when it is not.

<b>Not relaxed</b>	<b>configuration C</b>	<b>configuration B</b>	<b>configuration V</b>
$E_p$ (mRy)	- 3.541	- 3.330	- 3.306
$d$ (Å)	3.07	3.16	3.17
<b>Relaxed</b>	<b>configuration C</b>	<b>configuration B</b>	<b>configuration V</b>
$E_a$ (mRy)	- 3.558	- 3.355	- 3.327
$d$ (Å)	3.09	3.10	3.14

**Table 2** Fitted parameters of He-graphene interaction potential for configurations C, B and V. Values are calculated for energies expressed in Ry and distances measured in Å.

<b>Configuration</b>	$a_0$	$a_1$	$a_2$	$a_3$	$a_4$	$a_5$
<b>C</b>	- 0.7660	- 0.73343	2.2232	- 1.9092	- 0.3343	1.0812
<b>B</b>	- 0.7592	- 0.80014	1.2704	3.7742	- 7.0495	3.9993
<b>V</b>	- 0.8313	- 0.80092	1.4724	3.5208	- 6.9986	3.8577

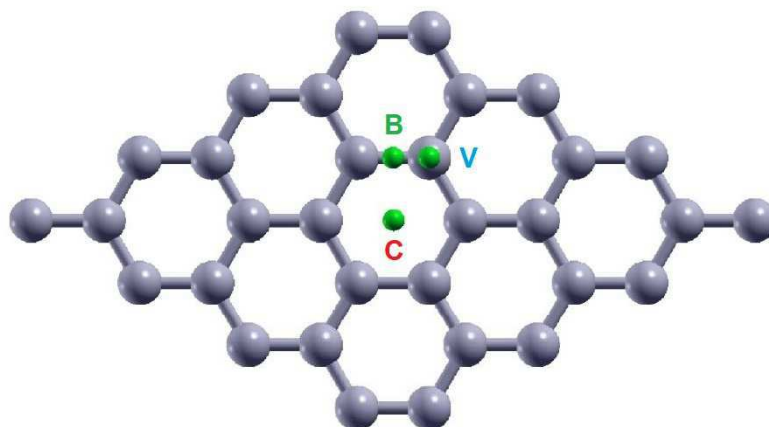


**Figure 1** Supercell used to study the interaction of helium with graphene. The three configurations considered (hexagon center C, midpoint of hexagon side, or bridge B, and hexagon vertex V) are shown.

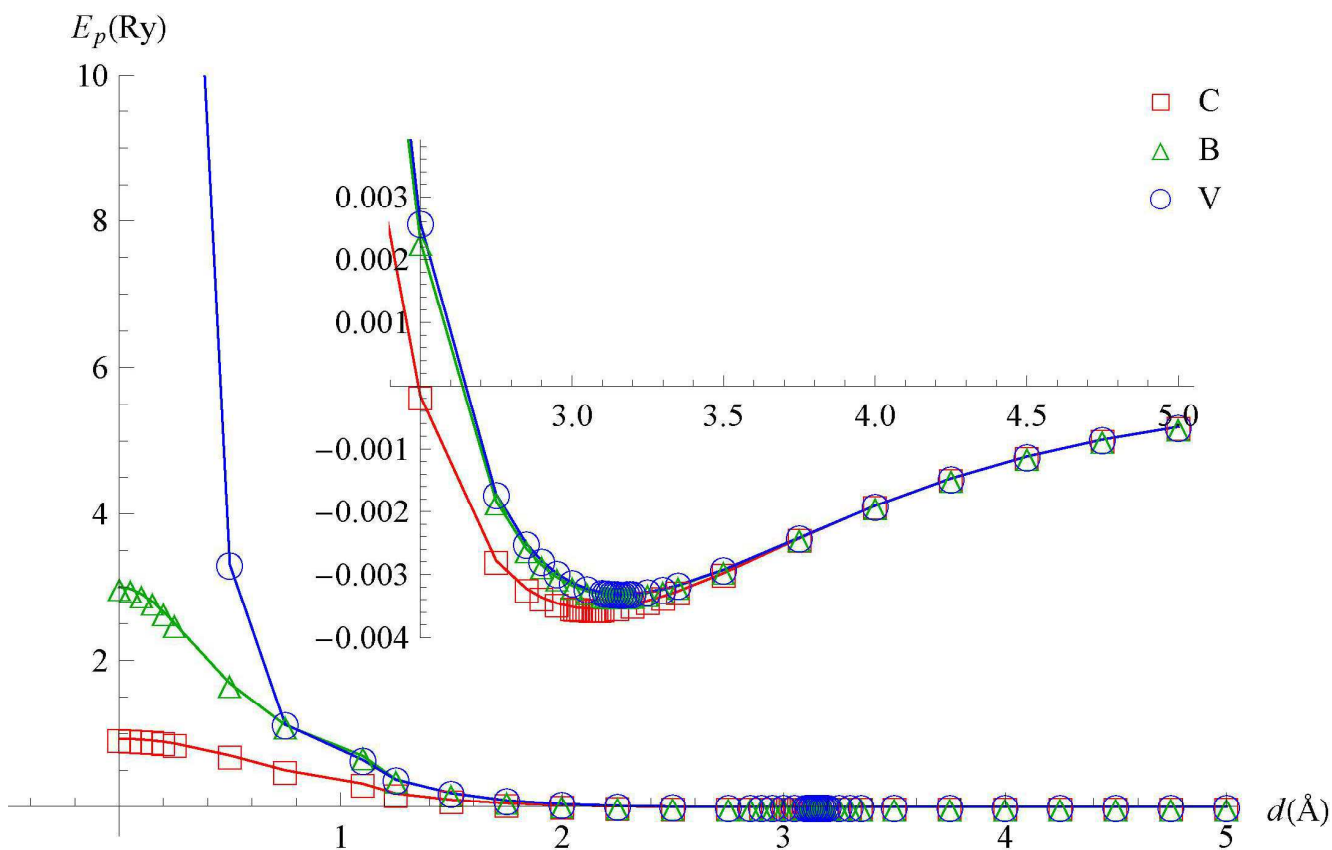


**Figure 2** Potential energy curves for the perpendicular approach of a helium atom to a graphene layer along the three trajectories studied (hexagon center C, midpoint of hexagon side, or bridge B, and hexagon vertex V). The inset shows in detail the region close to the equilibrium distance. The lines are merely guides for the eye.

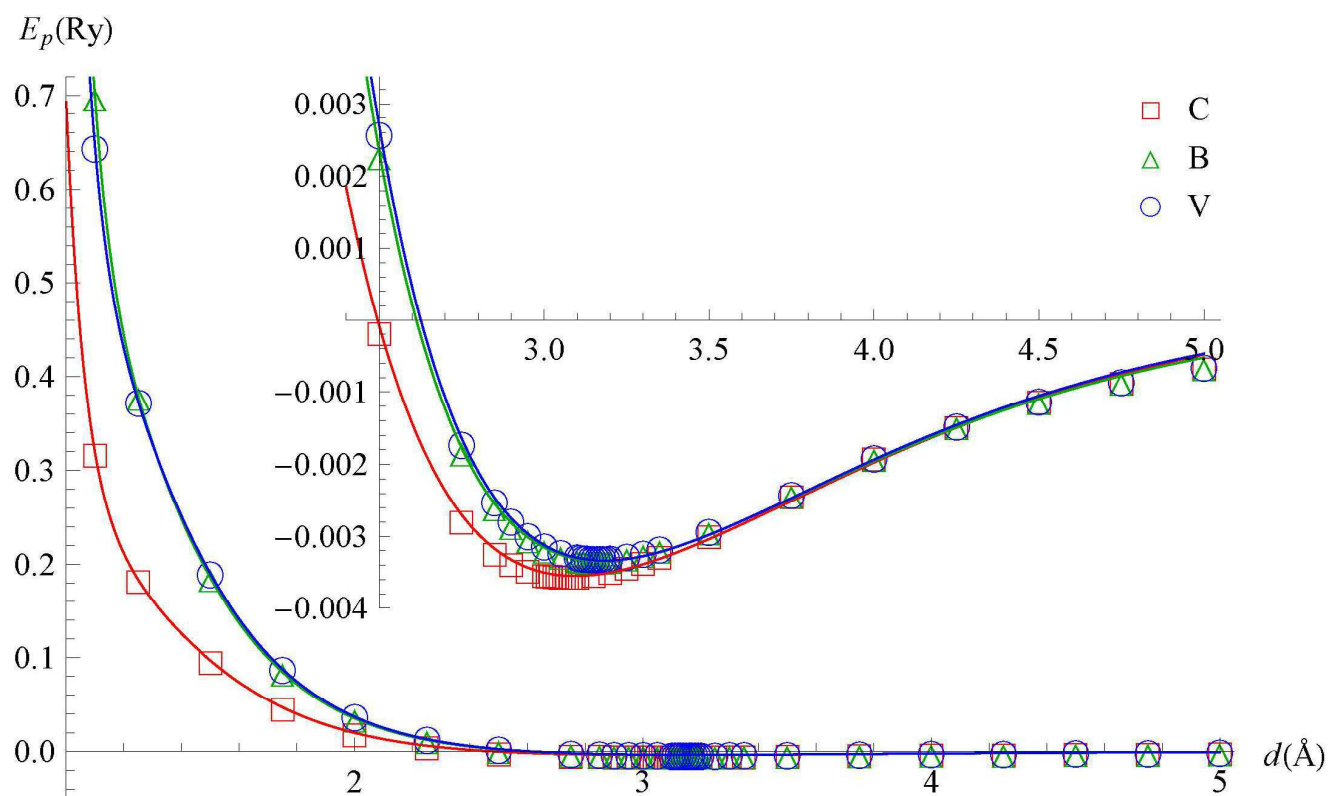


**Figure 3** Fitted energy curves for the three configurations studied (hexagon center C, midpoint of hexagon side, or bridge B, and hexagon vertex V). The inset shows in detail the region close to the equilibrium distance.

## Chapter 3

### Saturation of helium on graphene: A density functional theory investigation

#### 3.1. Introduction

One of the most plentiful chemical elements in the universe is helium alongside hydrogen [1]. Helium exceptional properties under extreme conditions of temperature and pressure have attracted the attention of the scientific community for several decades. Due to the small interatomic van der Waals forces and the high zero-point energy, helium phase diagram shows extraordinary features [2,3]. Helium is an inert gas at room temperature but nearby absolute zero it can solidify only if an external pressure is applied. In addition, liquid-solid interface experiments can be carried out more easily than in other systems as the melting curve is practically pressure-independent for very low temperatures [4]. There is no triple point so gas, liquid and solid phases do not coexist.

A macroscopic quantum effect of helium to highlight is superfluidity in which the liquid loses its viscosity and flows without friction [5]. Another one is supersolidity, concept that was introduced theoretically by Andreev and Lifshitz in 1969 [6] and has come to the fore recently although there have been some relevant events in between not exempt of controversy. Kim and Chan [7] claimed that the rotational inertia loss measured in the torsional oscillator experiment could be due to the formation of a supersolid phase. This means that zero-point vacancies, which may exist even at zero temperature, move unimpeded through solid helium. Then, it was reported in other study [8] an increase of the shear modulus as temperature decreases besides a very likely relationship between the frequency changes and the movement of dislocations present in helium crystals which may soften. This last behaviour was termed quantum plasticity [9]. Due to the uncertainty generated about the supersolid interpretation [7], the torsional oscillator was redesigned [10]. Results showed no loss of rotational inertia in this case and hence, no evidence of supersolidity. However, two research groups claim to have produced supersolid helium by different methods [11,12]. The authors have started from a Bose-Einstein condensate in both works unlike previous studies in which solid helium was used.

Crystal growth dynamics and purity of helium allow some phenomena to be seen more readily and precisely what makes it a model system. This provides the opportunity to apply some inferences thoroughly in material science [13]. The rapidity with which helium crystals

grow and melt makes possible to observe crystallization waves. This is due to the reduced dissipation of energy in the growing process. Among the most important aspects in the formation process of helium crystals are nucleation and surface roughening. The former, which represents a liquid-solid transition, is determined by different parameters depending on the scale considered [14]. At macroscopic level, nucleation depends on the interfacial tensions between the substrate and the different adsorbate phases present besides adsorbate contact angle, while microscopically it depends on the adsorbate ground state energy, substrate van der Waals field besides the atomic structure symmetries of the substrate and the adsorbate. Balibar *et al.* found out that the crystal nucleation barrier at the melting pressure is not equivalent to the necessary energy for the liquid-solid interface creation but the pinning energy [15]. The nucleation can be homogeneous or heterogeneous although intermediate situations have also been reported [16]. On the other hand, the roughness transition refers to the temperature at which step free energy vanishes [4]. As temperature increases, smooth surfaces commence showing terraces bonded by steps with increasing size and average length respectively.

Before it was proposed that helium crystal nucleates more easily in the presence of graphite particles inside the cell [15], a considerable effort had been dedicated to the experimental study of the numerous phases that can be found in helium films formed on graphite. In parallel to heat-capacity measurements [17,18] and neutron-diffraction experiments [14,19], some theories were also developed [20-22] but a breakthrough was achieved some years later due to the application of Monte Carlo techniques. Pierce *et al.* simulated helium layers adsorbed on graphite [23,24] while Gordillo *et al.* besides Happacher *et al.* did it on graphene [25,26]. Then, quantum zero-point motion of helium atoms in the case of graphite and carbon atoms in graphene were included in the calculations of latter works [27,28]. Similar studies were carried out to determine the phase diagram of molecular hydrogen on graphene [29,30]. In addition, vacancy influence on the superfluid fraction in He and H<sub>2</sub> films on graphite and graphene was analyzed [31]. The potentials used in all above Monte Carlo simulations to describe He-He, H<sub>2</sub>-H<sub>2</sub> and C-H<sub>2</sub> interactions were taken from Refs. (32), (33) and (34) respectively while for C-He ones, the potential was taken from two different references [35,36] depending on the study considered. In the previous chapter, the curves corresponding to the potential energy of a helium atom placed at different distances and positions from and over the graphene plane respectively were fitted with a Yukawa–Lennard–Jones form. This potential could be used as an alternative to above C-He ones since it was reported that the results obtained depend on which one of them is used [37].

In the previous chapter, it was commented the large number of first-principles studies about the interaction of hydrogen with graphene and the use of doped graphene and adsorbed atoms with the aim of increasing its storage capacity. In addition, the physisorption and chemisorption of several hydrogen molecules [38] and atoms [39] respectively were investigated too. Nevertheless, the few first-principles works about graphene-He interaction were limited to the study of a single helium atom [40-42]. Hauser *et al.* analyzed the helium density distribution inside and outside a carbon nanotube depending on its diameter [43]. Besides being a carbon nanotube and not a graphene sheet, they were trying to give an explanation to experimental results of other investigation [44] so no detailed helium atom positions or electron density distribution were provided. In this chapter, we intend to study the helium saturation process as close as possible to reality by means of density functional theory (DFT) calculations. In order to achieve this, we have successively added helium atoms over highly symmetric graphene points and relaxed the system which allows finding out the atom arrangements with the minimum energy. The procedure used in this study allows to evaluate the weight of graphene-He and He-He interactions in the binding energy of each single helium atom to the rest of the system during helium multilayered structure formation as well as the structural and energy properties of helium on graphene. It is known that hcp helium crystals grow epitaxially on graphite substrates [45], a fact that has been verified here with graphene as substrate. Despite different techniques have been employed, the coverage estimation of this study at which helium layers are saturated and a layer promotion begins to occur may be compared with the results of existing theoretical or experimental investigations. Lastly, an electronic structure analysis has been carried out to explain and understand more in detail the results obtained. Hence, this study provides a new insight from an atomic and electronic point of view to the existing knowledge about helium films adsorbed on graphene.

### 3.2. Computational details

The methods described in this section are very similar to those reported in the previous chapter. To study the saturation of helium on graphene, we have employed the density functional theory (DFT). The calculations were performed using the Quantum Espresso code [46]. The valence electrons involved in the calculation were the ( $2s^22p^2$ ) electrons of carbon and the ( $1s^2$ ) electrons of helium, whereas the core electrons ( $1s^2$ ) of carbon were replaced by a pseudopotential. A norm-conserving pseudopotential generated with the Troullier-Martins procedure [47] was used for carbon in a semilocal form. The exchange-correlation terms were parametrized using the Perdew-Wang representation [48] within the local density

approximation (LDA). Dispersion interactions were accounted for by the use of Rutgers-Chalmers van der Waals Density Functional (vdW-DF) method [49-51]. All the simulations were carried out with a periodic 4x4x1 graphene supercell. For its generation, a starting carbon-carbon bond length close to 1.41 Å [52] and a separation between adjacent graphene sheets of 16 Å [40] were used. Then, the supercell was subjected to a shape optimization keeping the supercell volume fixed. A plane-wave basis set with a kinetic energy cutoff of 70 Ry was used. The Brillouin zone was integrated with a 10x10x1 k-point grid generated using the Monkhorst-Pack scheme [53]. Minimum convergence threshold for self-consistency and ionic minimization on total energy were set to  $10^{-6}$  Ry.

### 3.3. Results and discussion

#### 3.3.1. Atomic structure

Due to the fact that helium atoms are physisorbed at a quite similar distance from the graphene sheet and the small gap in adsorption energy values for the different positions of helium above graphene (see previous chapter), it was very likely that helium atoms could form a multilayered structure under appropriate conditions. Therefore, with the aim of determining the most stable systems as the amount of helium atoms increases over graphene, the next procedure has been followed: (i) use the 4x4x1 graphene supercell described in the previous section, (ii) add helium atoms above hexagons centers (C), midpoint of hexagons sides, or bridge (B), and hexagons vertexes (V) belonging to the graphene sheet with the purpose of finding out the atom arrangement with the lowest total energy (see **Figure 1**), (iii) perform a self-consistent calculation for electrons and an ionic relaxation, (iv) use the ionic positions of the most stable structure in the immediately next calculation in which we have added more helium atoms. As we were studying a saturation process that involves a lot of possibilities without considerable energetic differences, allowing ionic relaxation and using periodic boundary conditions, we considered four quasi-equivalent cells of 2x2x1 size. Thus, four atoms have been added in each step, each located at the equivalent position of 2x2x1 cells (see atom arrangement at the end of each step in **Figure 2**). The atoms are denominated StepN where N makes reference to the moment in which each four atoms have been added to the system. The binding energy of each helium atom in the system at the end of step N ( ${}^N E_b^{1He}$ ,  ${}^N E_b^{2He}$  ...  ${}^N E_b^{NHe}$ ) may be expressed as:

$$\begin{aligned}
{}^N E_b^1\text{He} &= {}^N E_{tot}^{all} - \left( {}^N E_{tot}^{all-1\text{He}} + {}^N E_{tot}^{1\text{He}} \right) \\
{}^N E_b^2\text{He} &= {}^N E_{tot}^{all} - \left( {}^N E_{tot}^{all-2\text{He}} + {}^N E_{tot}^{2\text{He}} \right) \\
&\dots \\
{}^N E_b^N\text{He} &= {}^N E_{tot}^{all} - \left( {}^N E_{tot}^{all-N\text{He}} + {}^N E_{tot}^{N\text{He}} \right)
\end{aligned} \tag{1}$$

where  ${}^N E_{tot}^{all}$  is the total energy of the system formed by all carbon and helium atoms that intervene in the calculation. On the other hand, first and second terms inside the parentheses are the total energy of the system except the helium atom for which we are calculating its binding energy ( ${}^N E_{tot}^{all-1\text{He}}$ ,  ${}^N E_{tot}^{all-2\text{He}}$  ...  ${}^N E_{tot}^{all-N\text{He}}$ ) and the total energy of such helium atom ( ${}^N E_{tot}^{1\text{He}}$ ,  ${}^N E_{tot}^{2\text{He}}$  ...  ${}^N E_{tot}^{N\text{He}}$ ) respectively. In the last case, the total energy does not depend on the step number or the position of the helium atom since it is isolated. Hence, the second term inside the parentheses of Eq. (1) can be represented more generally by  $E_{tot}^{He}$ .

**Figure 3** shows the binding energy evolution of one helium atom in each four-atoms group as their values are practically the same or totally equal. Previous chapter calculations established configuration C as the most energetically stable one for the helium atom, but not the hexagon over which it is placed. Differences are practically nil so, exceptionally, convergence threshold for self-consistency and ionic minimization on total energy have been reduced to  $10^{-8}$  Ry. The site with the lowest total energy value has determined the positions of the other three atoms in Step1-atoms group. In step 2, the binding energy of Step1 and Step2 atoms to the rest of the system is higher than for the case in which helium atoms are sufficiently separated so as not to interact (Step1 atoms in step 1) because the binding energy between adsorbate atoms grows. Before analyzing this rise of binding energy, we have calculated the binding energy of the helium dimer which is around 0.5 mRy. As each Step1 or Step2 atom is surrounded by three helium atoms, taking into account the ones in adjacent periodic cells, the increase of binding energy should be roughly 1.5 mRy. However, it is lower. This may happen in part because there is an increase in the interaction between helium atoms to the detriment of the interaction of helium atoms with the graphene layer. The same occurs when Step3 atoms are added. With these last four atoms the first layer formed by twelve helium atoms is completed. If we focus on each quasi-equivalent cell of  $2 \times 2 \times 1$ , there is a helium atom occupying the V sites that are further to the left and the right besides the C site that is in between. Helium atoms form a network of equilateral triangles with a side length similar to that of the helium dimer bond which is close to 2.9 Å in our static

calculations and about twice carbon-carbon bond length in graphene. We therefore find in our DFT calculations that the coverage of a completed helium first layer is  $\sim 0.14$  atom/ $\text{\AA}^2$ . This value is slightly higher than those obtained in heat-capacity measurements [17,18] and neutron-diffraction experiments [14,19] as well as in Monte Carlo simulations [23,24,26,27]. All these investigations, either experimental or theoretical, gave similar results and were performed with graphite as substrate except in **Ref. (26)**, where the substrate was graphene. Nevertheless, as in the other Monte Carlo works, the potential used in this reference to describe C-He interactions was taken from **Ref. (35)** where the interaction between a helium atom and a graphite surface was studied. The He-He potential was also taken from the same reference in all above Monte Carlo investigations, that is, **Ref. (32)**.

In order to check if this first physisorbed layer of helium atoms can be dismantled or not, we have carried out tests in which a helium atom has been introduced very close to the graphene sheet in the C, B and V sites indicated in **Figure 1**. Then, the system has been let to evolve through an ionic relaxation. The helium atom placed in C is repelled from graphene until being at a distance quite similar to that of the first layer at the end of step 3. During the process, the helium atoms on the right and left vertexes of the central hexagon seen from above are displaced upwards and outwards. In case of placing the helium atom in B, first-layer atom occupying the nearest center position is expelled taking the atom repelled from graphene that site. Finally, the repulsion of the helium atom placed in V causes the displacement of three helium atoms in the first layer, the two that are closer to it and the one on the left of the central hexagon. In all the cases, the rest of helium atoms keep their configurations and they are just a little moved. The upward displacement of moved atoms from first layer depends on the number of displaced helium atoms indicated above since the repulsion forces are shared. If only one atom is displaced, the distance between it and the graphene layer is similar to that between the second layer of helium atoms (see below) and graphene. Nevertheless, when more than one atom is displaced, it is smaller.

After previous tests, we continue with the saturation process. As we add Step4, Step5 and Step6 atoms, i.e., second layer of helium atoms, helium atoms in the first layer have a new bond between helium atoms in each step. Like before, the increase of binding energy is lower than 1.5 mRy. However, the difference with this value is smaller in this case. Second-layer helium atoms also form a network of equilateral triangles in such a way that these atoms occupy positions over alternating triangles of first-layer network near their gravity center. In step 4, last added atoms have three first-layer helium atoms around each of them forming triangles but there should be secondary interactions too with the three non-nearest first-layer

helium atoms that are found drawing a perpendicular line to the sides of above-mentioned triangles from the position of each Step4 atom projected on the first helium layer. This causes that the Step4 binding energy is higher than three times the binding energy of the helium dimer. However, the excess of binding energy is compensated in step 5 and step 6 as the first layer helium atoms that cause these secondary interactions have nearer helium atoms to interact (Step5 and Step6 atoms). Step4-5-6 atoms, i.e., second layer of helium atoms, have a binding energy close to 4.5 mRy at the end of step 6 that corresponds with the nine bonds formed between themselves and adjacent helium atoms, six with helium atoms in the same layer and three with helium atoms that belong to the layer immediately below.

Step7-8-9 atoms, i.e., third layer of helium atoms, have practically the same configuration as those of the first layer when seen from above. This means that hcp helium crystals grow epitaxially on graphene in the same way as they do on graphite substrates [4,15,45]. There is another option in which third-layer helium atoms occupy positions over gravity centers of the second-layer network triangles that third-layer atoms do not. Differences between both options in terms of total energy are small. Step7-8-9 atoms have a binding energy at the end of step 9 a bit smaller than that of Step4-5-6 atoms at the end of step 6. Furthermore, the binding energy of first-layer helium atoms increases slightly when Step7-8-9 atoms are added. From this we can deduce that the interactions of the helium atoms in second and third layer with the graphene sheet are very small and negligible respectively as well as that the interactions between first- and third-layer helium atoms are small. Lastly, the evolution of the distance from graphene to first helium layer and the separation between helium layers are shown in **Table 1**. These distances correspond to the differences between layers of the mean z-coordinate of the atoms in each layer.

### 3.3.2. Electronic structure

An electronic structure analysis has been carried out to explain and understand more in detail the atomic structure results obtained. We have checked some changes in graphene structure as the corrugation or bond elongation between carbon atoms. The former has been analyzed considering the difference in z-coordinate between the two carbon atoms that are above and below as ripples height would be equal or smaller. Either the variation of bond length or the height of ripples formed in the graphene layer take values in the order of some  $10^{-3}$  Å at most. So, as we commented in the previous chapter, the perturbation of graphene electronic states due to corrugation and bond elongation could be considered negligible and no more detailed study has been performed on this. However, the electron density difference

at the end of each step  ${}^N \rho_{diff}$  has been calculated. It should be noted that it corresponds to the difference between the total electron density of the entire system and the total electron density of the new helium four-atom group added plus the total electron density of the rest of the system separately. Perpendicular planes to the graphene sheet contain the longest diagonal of lozenge-shape graphene layer except the one corresponding to step 7 that passes through the carbon atom with the highest x-coordinate and the one with the highest y-coordinate on the right, i.e., it is parallel to one of the lattice vectors. On the other hand, parallel planes contain helium layers and are located at the mean z-coordinate of the helium atoms in the corresponding layer. In the last planes, there are triangular areas in the corners that correspond to adjacent cells. Only the most representative results of electron density differences are shown here.

Firstly, we study the electron density changes during the formation of the first helium layer. This case is the most comprehensive since graphene interacts more with this first helium layer than with the second and third ones. In step 1, there is a transfer of electron charge from helium atoms to the regions around them (see **Figure 4a**). The electron density gain around helium atoms is greater in the part closest to graphene. Furthermore, the electrons very close to helium nuclei push the electron charge towards graphene which increases the electron density above and below carbon atoms surrounding Step1 atoms. As we can see in **Figure 4b**, there are zones among Step1 atoms with no gain of electron density and Step2 atoms are placed there at a distance similar to the helium dimer bond length from three Step1 atoms. Like in helium dimer formation, electron density loss regions appear between helium atoms (see **Figure 5b**). These straight regions point to the position of Step3 atoms. Similar to Step2 atoms, Step3 ones are placed in zones with negligible variations of charge density. Electron density loss regions between helium atoms define a triangular voronoi tessellation at the end of step 2, while at the end of step 3, the geometric pattern is hexagonal (see **Figure 6b**). The last atoms added are the ones that loss electron charge in step 1, 2 and 3. On the other hand, helium atoms added in a previous step gain electron charge except Step1 atoms that show small zones of electron density loss when Step2 atoms are inserted. Either for atoms added in a previous step or the last, there is a gain of electron density around them. As we have commented previously, the binding energy increase of each Step1 atom should be roughly 1.5 mRy when Step2 atoms are inserted. Nevertheless, it is lower because there is an increase of electron density in the region between Step1 atoms and the graphene sheet (see **Figure 5a**). This occurs too when Step3 (see **Figure 6a**) and second-layer helium atoms (not

shown here) are added. The maximum values of electron density loss in the nucleus region of Step1, Step2 and Step3 atoms are similar at the end of step 1, 2 and 3 respectively. However, the maximum values of electron density gain over carbon atoms show differences. The electron charge pushed by helium atoms, when they are added, is shared by more nearest carbon atoms if they are Step1 atoms (configuration C) than if they are Step2 and Step3 atoms (configuration V). Consequently, the maximum value of electron density gain is lower in the first case (see **Figure 4a**) than in the last two (see **Figures 5a** and **6a**). According to the difference of magnitude order between maximum values, electron density loss regions are smaller than electron density gain ones.

The distribution of the electron density difference in second or third helium atoms layers (not shown here) is very similar to that in first helium atoms layer (see **Figures 4b**, **5b** and **6b**) for equivalent steps, i.e., comparing step 4, 5 and 6 or step 7, 8 and 9 with step 1, 2 and 3 respectively. Only maximum values of electron density gain and loss show differences. The former is slightly smaller. On the other hand, the latter is about half of the values corresponding to step 1, 2 and 3. This may be due to the drastic reduction of the interaction between graphene and helium atoms in the second and third layers with respect to helium atoms in the first layer.

Previously, we have mentioned the possibility that there are also secondary interactions between last added atoms and not nearest atoms in the helium layer immediately below before upper layer is completed. Thanks to the results shown in **Figure 7a**, which correspond to step 7, we can confirm the existence of these interactions. They are named secondary only to distinguish them from those with nearest helium atoms below because, despite being smaller, they are in the same magnitude order. Moreover, in this figure, we can see that the interaction of third-layer helium atoms with the first helium layer is small. The addition of Step7 atoms to the system causes an electron density loss and gain in the regions where first-layer helium atoms are placed and between them respectively (see **Figure 7b**). This happens too in the second helium layer (see **Figure 7c**). However, second-layer results also show electron density loss areas just below Step7 atoms. To finish, and reinforcing the conclusions obtained from the energy results, the interactions between graphene and helium atoms in the third layer can be considered negligible according to the electron density changes seen around carbon atoms in **Figure 7a**.

### 3.4. Conclusions

We have used the density functional theory (DFT) with a van-der-Waals-corrected LDA functional to study the most stable atomic structures that helium forms over a graphene sheet, as well as the electron density differences in the presence of an increasing amount of helium. Helium atoms form a multilayered system with hcp structure that grows epitaxially on graphene. This structure consists of a network of equilateral triangles with a side length close to a helium dimer bond one which is around twice carbon-carbon bond length in graphene.

The atoms of the first helium layer are physisorbed on graphene. There is a transfer of electron charge from last added helium atoms to the regions around them. Thus, the electrons very close to helium nuclei push the electron charge towards graphene creating electron density loss regions between helium atoms and graphene, and increasing the electron density above and below carbon atoms surrounding helium ones. On the other hand, the interactions of helium atoms in the second and third layers with the graphene sheet are very small and negligible, respectively.

The coverage of a complete helium layer on graphene is slightly higher than that obtained in other theoretical or experimental investigations performed with graphite as substrate. First helium atoms were added over graphene hexagon centers as separate as possible to avoid interaction. The electronic structure analysis has revealed that the following atoms added to complete the helium layer were located in zones with negligible variations of charge density, forming bonds with previously added helium atoms.

For a system consisting of two or more layers of helium fully formed on a graphene sheet, the binding energy of each single helium atom in the second layer or successive ones to the rest of the system might be approximated as the binding energy of the helium dimer multiplied by the number of nearest neighboring helium atoms. In the case of a first helium layer atom, the binding energy might be estimated as the sum of two terms: previous approximate value and its adsorption energy to graphene. Unlike the first term, the adsorption energy to graphene decreases as the number of nearest neighboring helium atoms increases.

The atomic structures with the lowest total energy have been demonstrated to be determined by the electron density distribution corresponding to the preceding system. In addition, the energetics of those structures and the atoms that compose them can be easily estimated from basic first-principles calculations. Therefore, insight gained from this study may be useful to develop new predictive models that allow to study the growth of thin films on different substrates and the evolution of their properties. These conclusions may also be of importance for cases in which helium accumulates in other materials, particularly in metals.

### References of Chapter 3

- [1] J. M. McMahon, M. A. Morales, C. Pierleoni, and D. M. Ceperley, "The properties of hydrogen and helium under extreme conditions", *Reviews of Modern Physics*, vol. 84, no. 4, pp. 1607-1653, 2012.
- [2] O. V. Lounasmaa, "The superfluid phases of liquid  $^3\text{He}$ ", *Contemporary Physics*, vol. 15, no. 4, pp. 353-374, 1974.
- [3] J. K. Hoffer, W. R. Gardner, C. G. Waterfield, and N. E. Phillips, "Thermodynamic properties of  $^4\text{He}$ . II. The bcc phase and the P-T and V-T phase diagrams below 2 K", *Journal of Low Temperature Physics*, vol. 23, no. 1-2, pp. 63-102, 1976.
- [4] S. Balibar, H. Alles, and A. Y. Parshin, "The surface of helium crystals", *Reviews of Modern Physics*, vol. 77, no. 1, pp. 317-370, 2005.
- [5] J. D. Reppy, "Superfluid helium in Porous Media", *Journal of Low Temperature Physics*, vol. 87, no. 3-4, pp. 205-245, 1992.
- [6] A. F. Andreev and I. M. Lifshitz, "Quantum theory of defects in crystals", *Soviet Physics JETP*, vol. 29, no. 6, pp. 1107-1113, 2007.
- [7] E. Kim and M. H. W. Chan, "Probable observation of a supersolid helium phase", *Nature*, vol. 427, no. 6971, pp. 225-227, 2004.
- [8] J. Day and J. Beamish, "Low-temperature shear modulus changes in solid  $^4\text{He}$  and connection to supersolidity", *Nature*, vol. 450, no. 7171, pp. 853-856, 2007.
- [9] J. Beamish, "Supersolidity or quantum plasticity?", *Physics*, vol. 3, article 51, 2010.
- [10] D. Y. Kim and M. H. W. Chan, "Absence of supersolidity in solid helium in porous vycor glass", *Physical Review Letters*, vol. 109, no. 15, article 155301, 2012.
- [11] J. R. Li, J. Lee, W. Huang, S. Burchesky, B. Shteynas, F. Ç. Top, A. O. Jamison, and W. Ketterle, "A stripe phase with supersolid properties in spin-orbit-coupled Bose-Einstein condensates", *Nature*, vol. 543, no. 7643, pp. 91-95, 2017.
- [12] J. Léonard, A. Morales, P. Zupancic, T. Esslinger, and T. Donner, "Supersolid formation in a quantum gas breaking a continuous translational symmetry", *Nature*, vol. 543, no. 7643, pp. 87-90, 2017.
- [13] S. Balibar and P. Nozières, "Helium crystals as a probe in materials science", *Solid State Communications*, vol. 92, no. 1-2, pp. 19-29, 1994.
- [14] H. Wiechert, H. J. Lauter, and B. Stuehn, "Thermodynamic and neutron diffraction studies of the nucleation of solid  $^4\text{He}$  on graphite", *Journal of Low Temperature Physics*, vol. 48, no. 3-4, pp. 209-239, 1982.

- [15] S. Balibar, T. Mizusaki, and Y. Sasaki, "Comments on heterogeneous nucleation in helium", *Journal of Low Temperature Physics*, vol. 120, no. 5-6, pp. 293-314, 2000.
- [16] X. Chavanne, S. Balibar, and F. Caupin, "Acoustic crystallization and heterogeneous nucleation", *Physical Review Letters*, vol. 86, no. 24, pp. 5506, 2001.
- [17] M. Bretz, J. G. Dash, D. C. Hickernell, E. O. McLean, and O. E. Vilches, "Phases of He<sup>3</sup> and He<sup>4</sup> monolayer films adsorbed on basal-plane oriented graphite", *Physical Review A*, vol. 8, no. 3, pp. 1589-1615, 1973.
- [18] D. S. Greywall, "Heat capacity and the commensurate-incommensurate transition of He<sup>4</sup> adsorbed on graphite", *Physical Review B*, vol. 47, no. 1, pp. 309-318, 1993.
- [19] K. Carneiro, L. Passell, W. Thomlinson, and H. Taub, "Neutron-diffraction study of the solid layers at the liquid-solid boundary in He<sup>4</sup> films adsorbed on graphite", *Physical Review B*, vol. 24, no. 3, pp. 1170-1176, 1981.
- [20] J. G. Dash, "Clustering and percolation transitions in helium and other thin films", *Physical Review B*, vol. 15, no. 6, pp. 3136-3146, 1977.
- [21] R. Peierls, "Clustering in adsorbed films", *Physical Review B*, vol. 18, no. 4, pp. 2013-2015, 1978.
- [22] T. Halpin-Healy and M. Kardar, "Observation of striped phases in adsorbed helium monolayers", *Physical Review B*, vol. 34, no. 1, pp. 318-324, 1986.
- [23] M. Pierce and E. Manousakis, "Phase diagram of second layer of <sup>4</sup>He adsorbed on graphite", *Physical Review Letters*, vol. 81, no. 1, pp. 156-159, 1998.
- [24] M. Pierce and E. Manousakis, "Path-integral Monte Carlo simulation of the second layer of <sup>4</sup>He adsorbed on graphite", *Physical Review B*, vol. 59, no. 5, pp. 3802-3814, 1999.
- [25] M. C. Gordillo and J. Boronat, "<sup>4</sup>He on a Single Graphene Sheet", *Physical Review Letters*, vol. 102, no. 8, article 085303, 2009.
- [26] J. Happacher, P. Corboz, M. Boninsegni, and L. Pollet, "Phase diagram of <sup>4</sup>He on graphene", *Physical Review B*, vol. 87, no. 9, article 094514, 2013.
- [27] P. Corboz, M. Boninsegni, L. Pollet, and M. Troyer, "Phase diagram of <sup>4</sup>He adsorbed on graphite", *Physical Review B*, vol. 78, no. 24, article 245414, 2008.
- [28] M. C. Gordillo, "Diffusion Monte Carlo calculation of the phase diagram of <sup>4</sup>He on corrugated graphene", *Physical Review B*, vol. 89, no. 15, article 155401, 2014.
- [29] M. C. Gordillo and J. Boronat, "Phase diagram of H<sub>2</sub> adsorbed on graphene", *Physical Review B*, vol. 81, no. 15, article 155435, 2010.
- [30] M. C. Gordillo, "H<sub>2</sub> on corrugated graphene: Diffusion Monte Carlo calculations", *Physical Review B*, vol. 88, no. 4, article 041406, 2013.

- [31] M. C. Gordillo, C. Cazorla, and J. Boronat, "Supersolidity in quantum films adsorbed on graphene and graphite", *Physical Review B*, vol. 83, no. 12, article 121406, 2011.
- [32] R. A. Aziz, V. P. S. Nain, J. S. Carley, W. L. Taylor, and G. T. McConville, "An accurate intermolecular potential for helium", *The Journal of Chemical Physics*, vol. 70, no. 9, pp. 4330-4342, 1979.
- [33] I. F. Silvera and V. V. Goldman, "The isotropic intermolecular potential for H<sub>2</sub> and D<sub>2</sub> in the solid and gas phases", *The Journal of Chemical Physics*, vol. 69, no. 9, pp. 4209-4213, 1978.
- [34] G. Stan and M. W. Cole, "Hydrogen adsorption in nanotubes", *Journal of Low Temperature Physics*, vol. 110, no. 1-2, pp. 539-544, 1998.
- [35] W. E. Carlos and M. W. Cole, "Interaction between a He atom and a graphite surface", *Surface Science*, vol. 91, no. 1, pp. 339-357, 1980.
- [36] G. Stan and M. W. Cole, "Low coverage adsorption in cylindrical pores", *Surface Science*, vol. 395, no. 2-3, pp. 280-291, 1998.
- [37] Y. Kwon and D. M. Ceperley, "<sup>4</sup>He adsorption on a single graphene sheet: Path-integral Monte Carlo study", *Physical Review B*, vol. 85, no. 22, article 224501, 2012.
- [38] T. Heine, L. Zhechkov, and G. Seifert, "Hydrogen storage by physisorption on nanostructured graphite platelets", *Physical Chemistry Chemical Physics*, vol. 6, no. 5, pp. 980-984, 2004.
- [39] A. A. Dzhurakhalov and F. M. Peeters, "Structure and energetics of hydrogen chemisorbed on a single graphene layer to produce graphane", *Carbon*, vol. 49, no. 10, pp. 3258-3266, 2011.
- [40] O. Leenaerts, B. Partoens, and F. M. Peeters, "Graphene: A perfect nanoballoon", *Applied Physics Letters*, vol. 93, no. 19, article 193107, 2008.
- [41] S. E. Huber, A. Mauracher, and M. Probst, "Permeation of low-Z atoms through carbon sheets: Density functional theory study on energy barriers and deformation effects", *AIP Advances*, vol. 3, no. 12, article 122104, 2013.
- [42] R. Burganova, Y. Lysogorskiy, O. Nedopekin, and D. Tayurskii, "Adsorption of helium atoms on two-dimensional substrates", *Journal of Low Temperature Physics*, vol. 185, no. 5-6, pp. 392-398, 2016.
- [43] A. W. Hauser and M. P. de Lara-Castells, "Carbon nanotubes immersed in superfluid helium: the impact of quantum confinement on wetting and capillary action", *The Journal of Physical Chemistry Letters*, vol. 7, no. 23, pp. 4929-4935, 2016.

- [44] T. Ohba, "Limited quantum helium transportation through nano-channels by quantum fluctuation", *Scientific Reports*, vol. 6, article 28992, 2016.
- [45] S. Sasaki, F. Caupin, and S. Balibar, "Optical observations of disorder in solid helium 4", *Journal of Low Temperature Physics*, vol. 153, no. 3-4, pp. 43-76, 2008.
- [46] P. Giannozzi, S. Baroni, N. Bonini, M. Calandra, R. Car, C. Cavazzoni, D. Ceresoli, G. L. Chiarotti, M. Cococcioni, I. Dabo, A. Dal Corso, S. de Gironcoli, S. Fabris, G. Fratesi, R. Gebauer, U. Gerstmann, C. Gougoussis, A. Kokalj, M. Lazzeri, L. Martin-Samos, N. Marzari, F. Mauri, R. Mazzarello, S. Paolini, A. Pasquarello, L. Paulatto, C. Sbraccia, S. Scandolo, G. Sclauzero, A. P. Seitsonen, A. Smogunov, P. Umari, and R. M. Wentzcovitch, "QUANTUM ESPRESSO: a modular and open-source software project for quantum simulations of materials", *Journal of Physics: Condensed Matter*, vol. 21, no. 9, article 395502, 2009.
- [47] N. Troullier and J. L. Martins, "Efficient pseudopotentials for plane-wave calculations", *Physical Review B*, vol. 43, no. 3, pp. 1993–2006, 1991.
- [48] J. P. Perdew and Y. Wang, "Accurate and simple analytic representation of the electron-gas correlation energy", *Physical Review B*, vol. 45, no. 23, pp. 13244-13249, 1992.
- [49] M. Dion, H. Rydberg, E. Schröder, D. C. Langreth, and B. I. Lundqvist, "Van der Waals Density Functional for General Geometries", *Physical Review Letters*, vol. 92, no. 24, article 246401, 2004.
- [50] T. Thonhauser, V. R. Cooper, S. Li, A. Puzder, P. Hyldgaard, and D. C. Langreth, "Van der Waals density functional: Self-consistent potential and the nature of the van der Waals bond", *Physical Review B*, vol. 76, no. 12, article 125112, 2007.
- [51] G. Román-Pérez and J. M. Soler, "Efficient implementation of a van der Waals density functional: Application to double-wall carbon nanotubes", *Physical Review Letters*, vol. 103, no. 9, article 096102, 2009.
- [52] M. Khantha, N. A. Cordero, L. M. Molina, J. A. Alonso, and L. A. Girifalco, "Interaction of lithium with graphene: An ab initio study", *Physical Review B*, vol. 70, no. 12, article 125422, 2004.
- [53] H. J. Monkhorst and J. D. Pack, "Special points for Brillouin-zone integrations", *Physical Review B*, vol. 13, no. 12, pp. 5188–5192, 1976.

### Table and figures of Chapter 3

**Table 1** Evolution of the distance from graphene to the first helium layer, and between helium layers, calculated as the difference in z-coordinate. The z-coordinate of graphene and helium layers correspond to the mean coordinate of carbon or helium atoms in each layer.

<b>Distances (Å)</b>	<b>step 1</b>	<b>step 2</b>	<b>step 3</b>	<b>step 4</b>	<b>step 5</b>	<b>step 6</b>	<b>step 7</b>	<b>step 8</b>	<b>step 9</b>
graphene/first helium layer	3.070	3.180	3.202	3.163	3.168	3.120	3.122	3.158	3.134
first/second helium layer	-	-	-	2.174	2.267	2.312	2.286	2.275	2.270
second/third helium layer	-	-	-	-	-	-	2.189	2.296	2.352

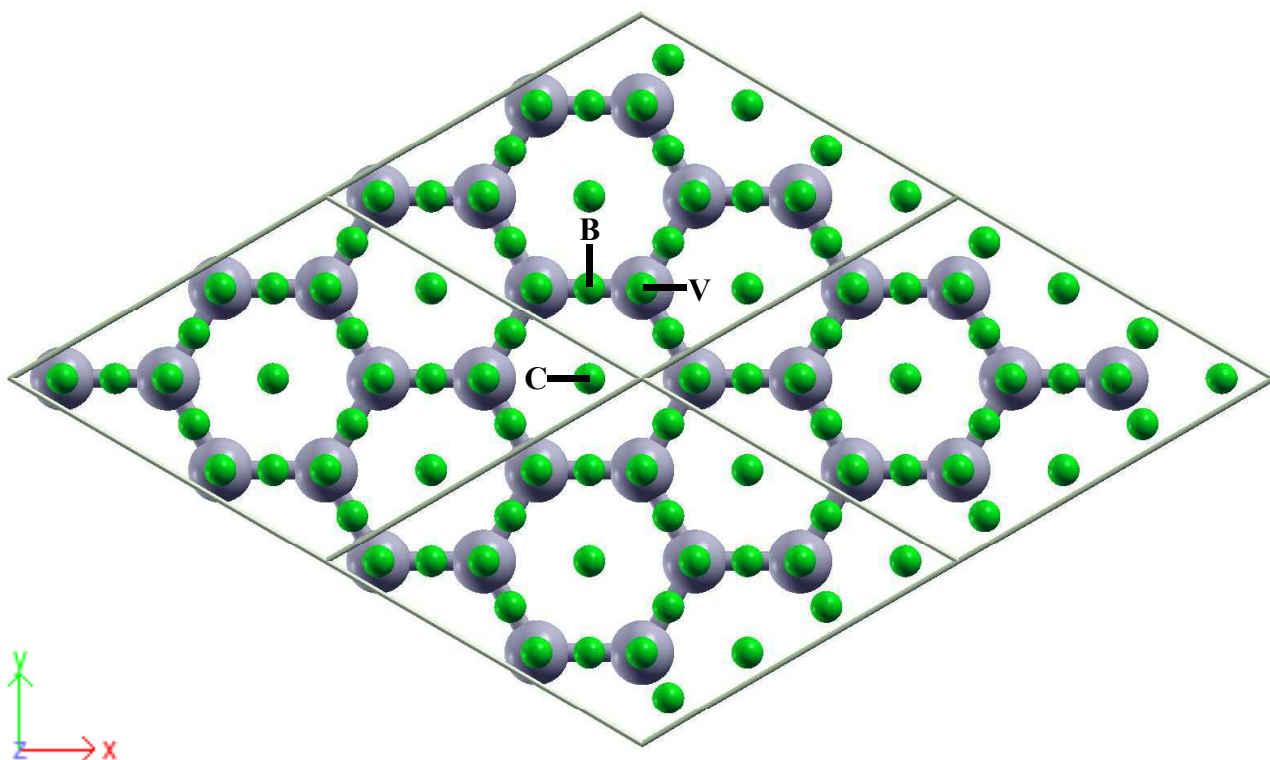
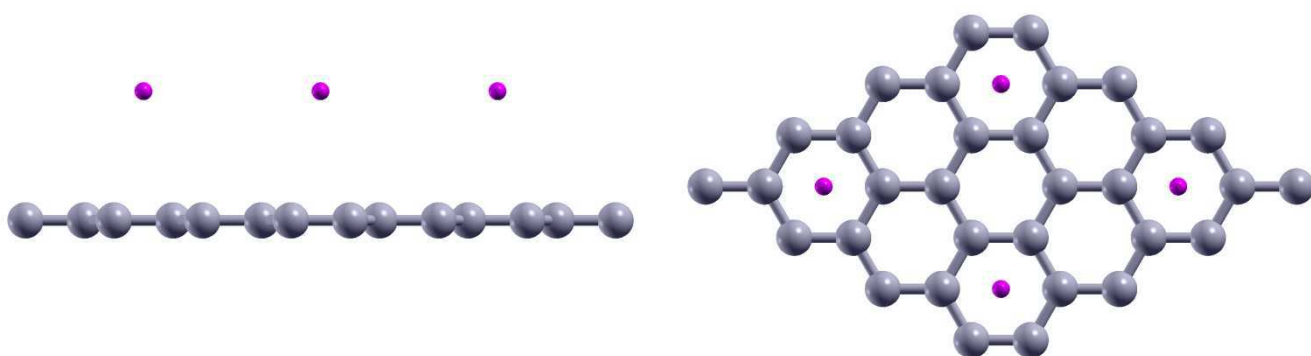
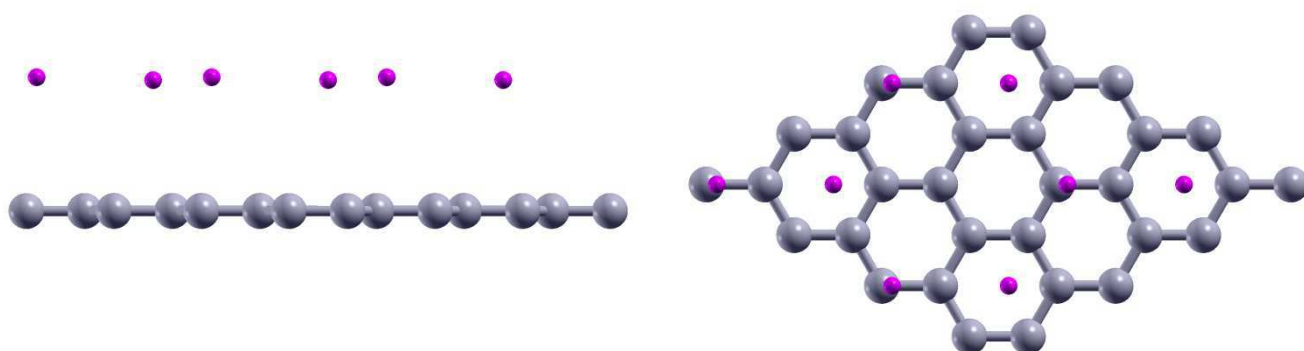


**Figure 1** Arrangement of a helium atom in all possible positions (three inequivalent configurations are considered: hexagon center C, midpoint of hexagon side, or bridge B, and hexagon vertex V) in which it can be added over the graphene sheet (helium and carbon atoms are colored in green and grey respectively). Four atoms have been incorporated to the system at the beginning of the different steps, each placed at the same position of the four  $2 \times 2 \times 1$  quasi-equivalent cells.

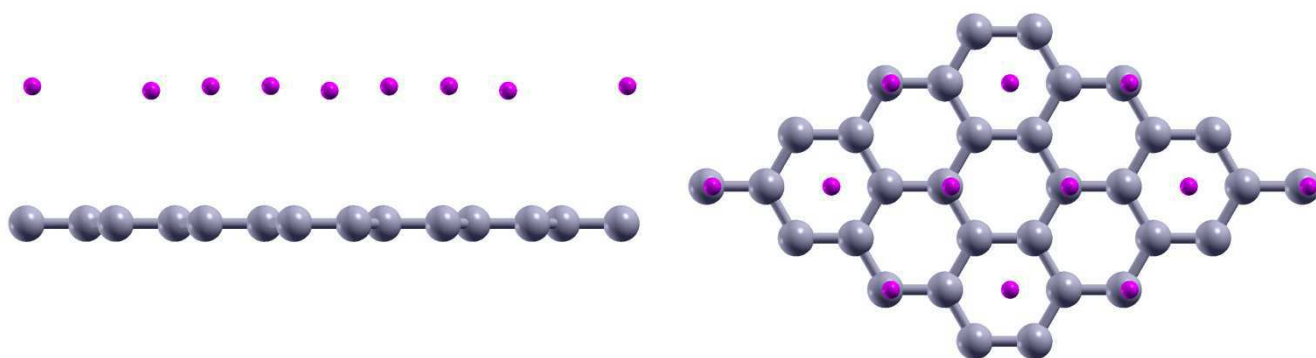
(a) step 1



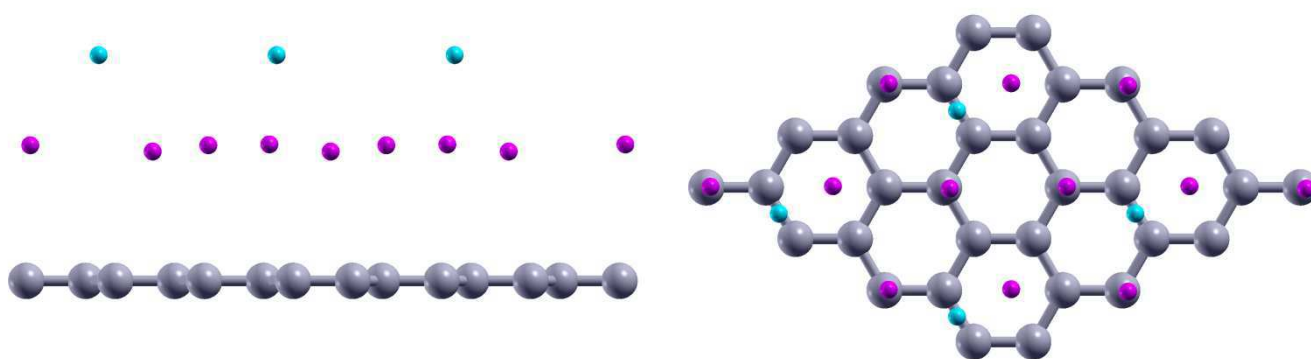
(b) step 2



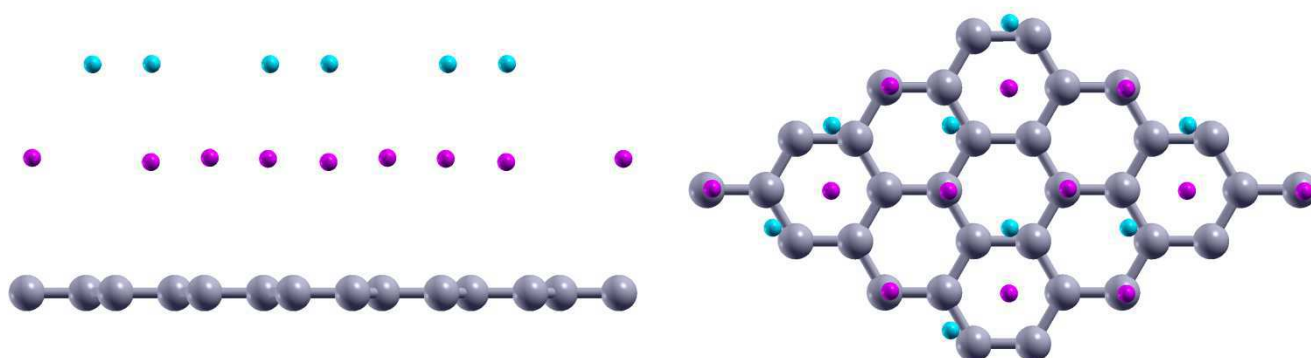
(c) step 3



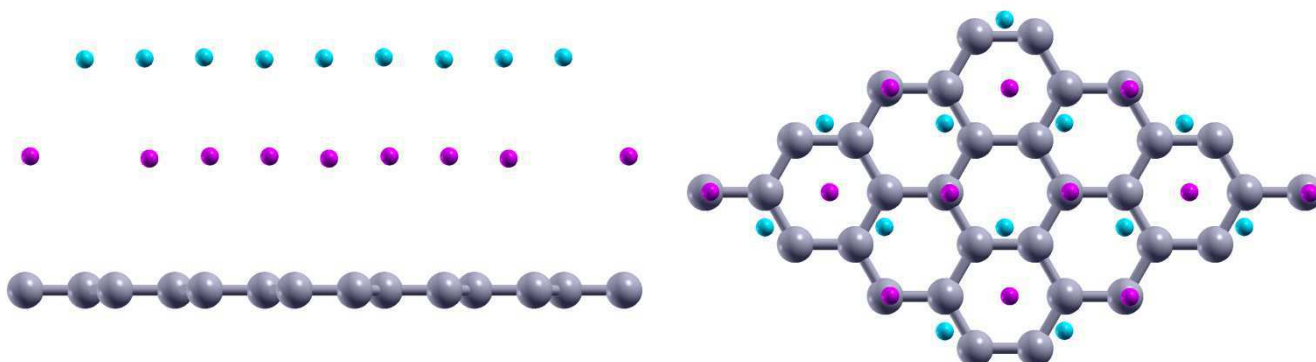
(d) step 4



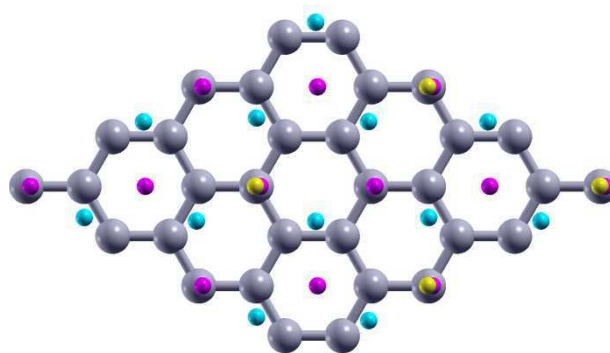
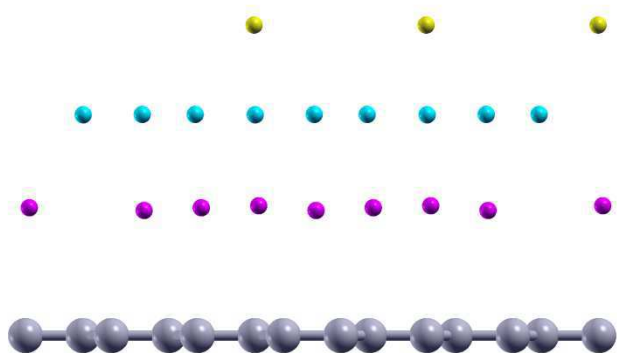
(e) step 5



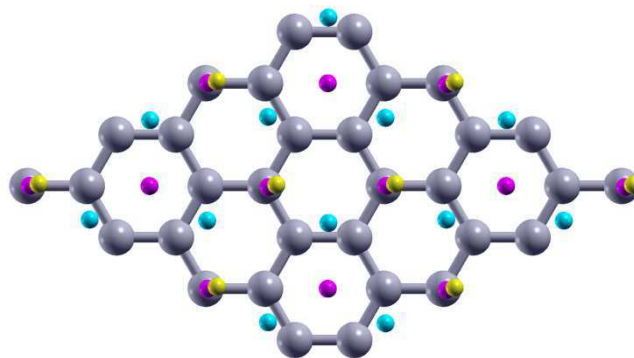
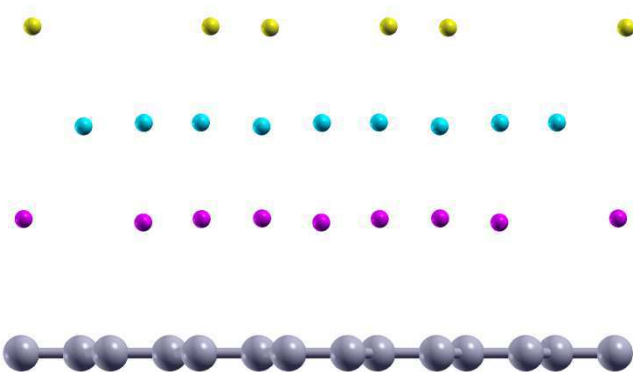
(f) step 6



(g) step 7



(h) step 8



(i) step 9

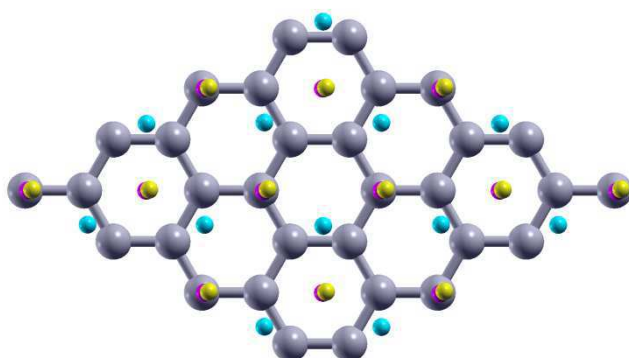
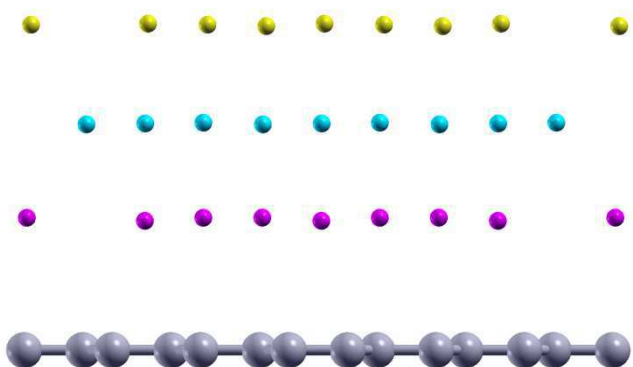


**Figure 2** Arrangement of helium atoms on graphene at the end of each step. The atomic structures shown correspond to those with the lowest total energy. We can observe how the different helium layers get saturated (first, second and third layer helium atoms are colored in purple, blue and yellow respectively).

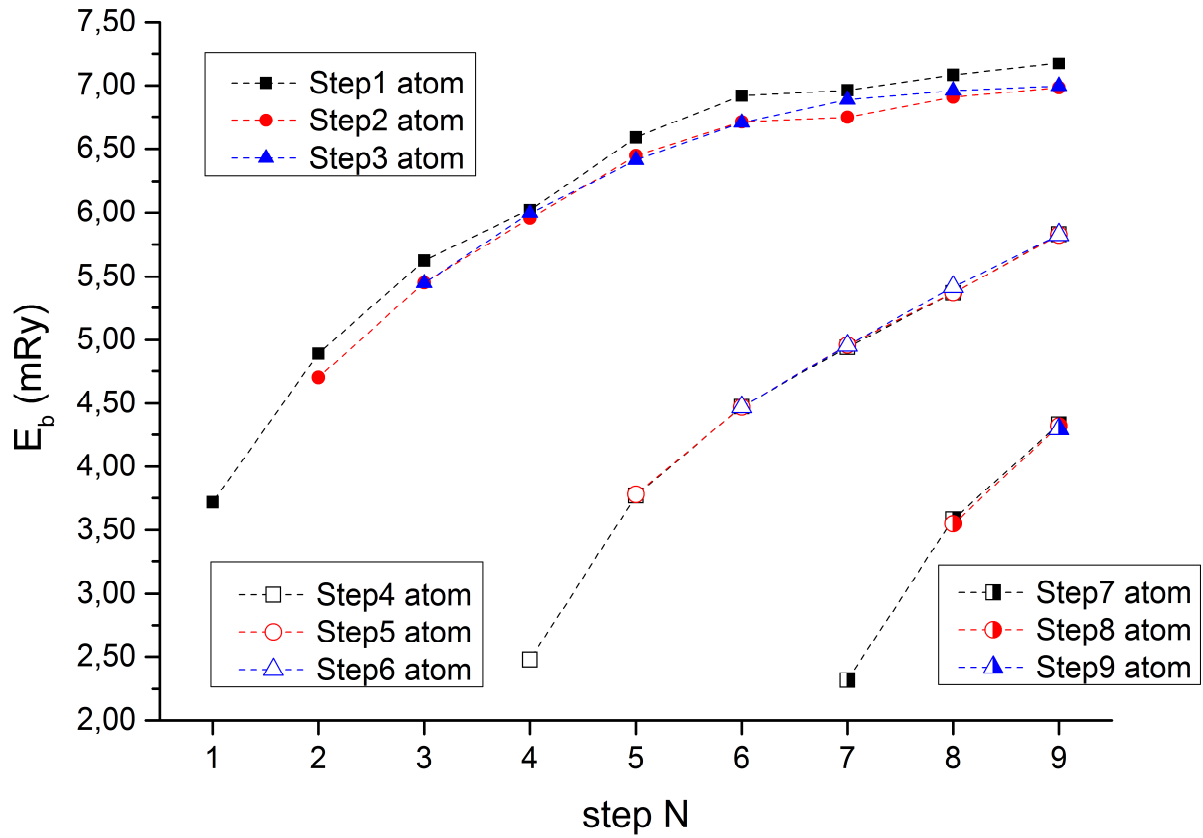


**Figure 3** Binding energy of one helium atom in each four-atom group to the rest of the system at the end of step N. The atoms are denominated StepN where N makes reference to the moment in which each four atoms have been added to the system.

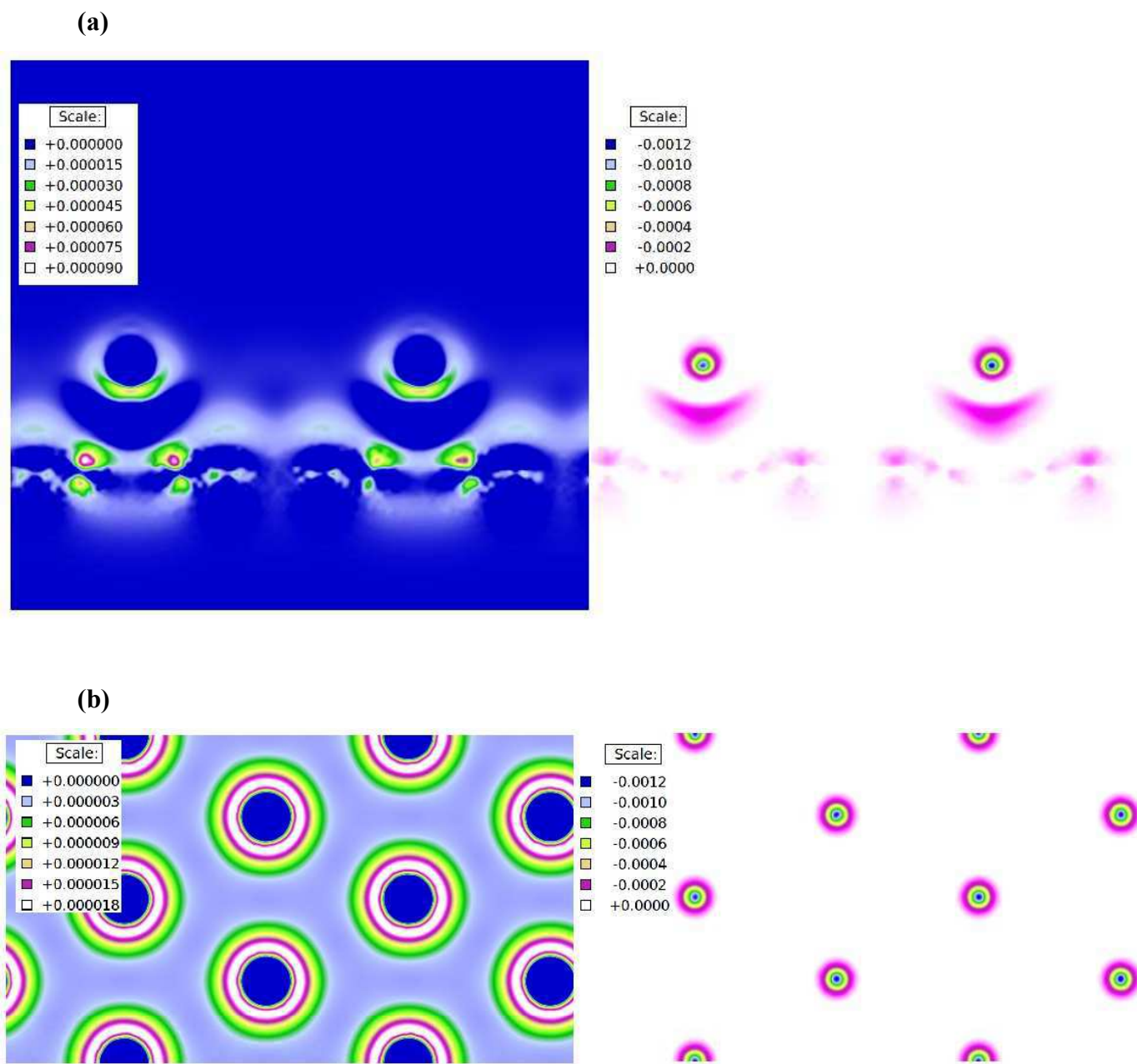


**Figure 4** Distribution of the electron density difference (units:  $e/a. u.^3$ ) corresponding to the structure of Figure 2a, i.e., the one at the end of step 1. The planes shown are **(a)** perpendicular and **(b)** parallel to the graphene sheet and contain the longest diagonal of lozenge-shape supercell and the first helium atoms layer respectively.

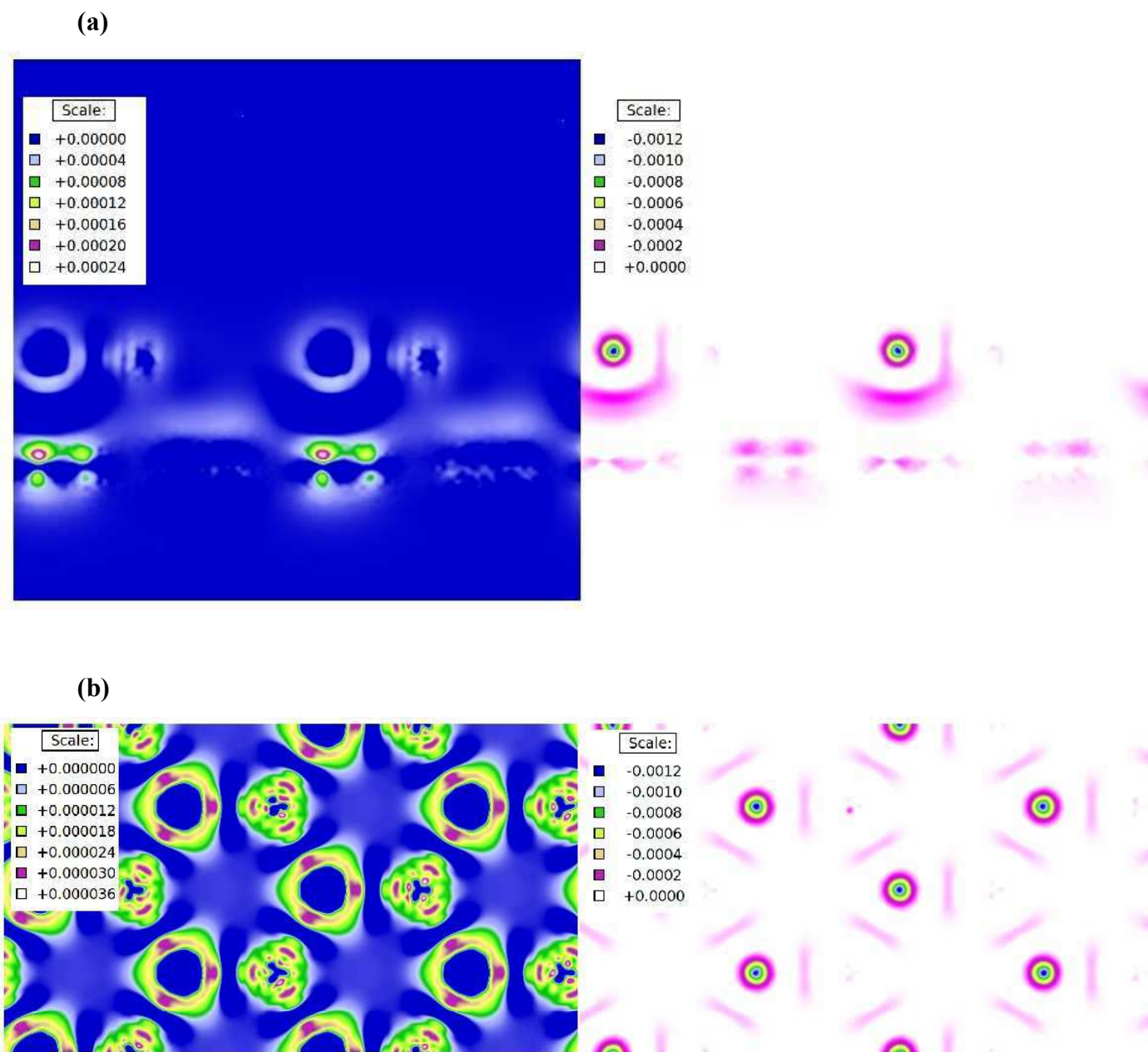


**Figure 5** Distribution of the electron density difference (units:  $e/a.u.^3$ ) corresponding to the structure of Figure 2b, i.e., the one at the end of step 2. The planes shown are **(a)** perpendicular and **(b)** parallel to the graphene sheet and contain the longest diagonal of lozenge-shape supercell and the first helium atoms layer respectively.

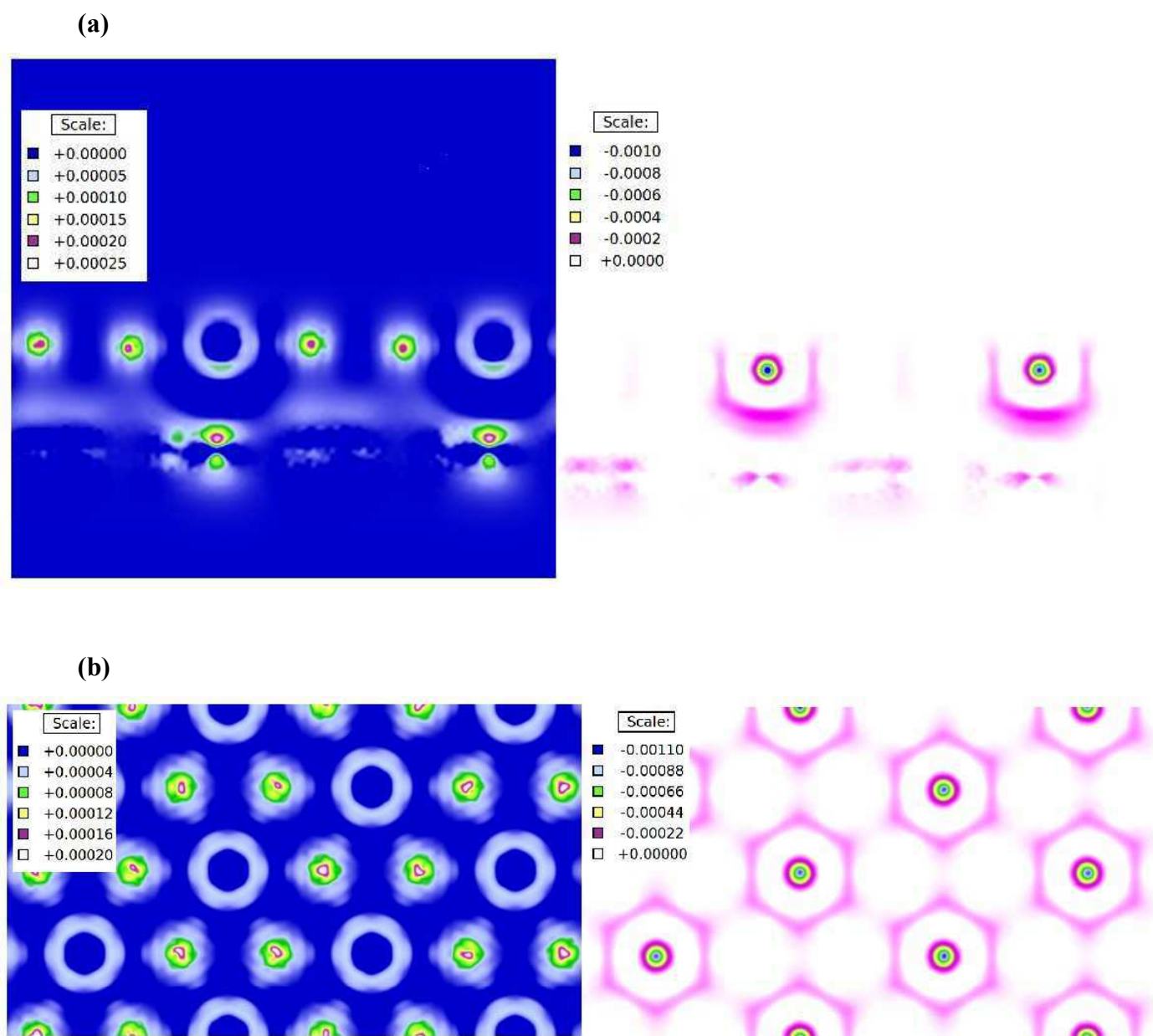
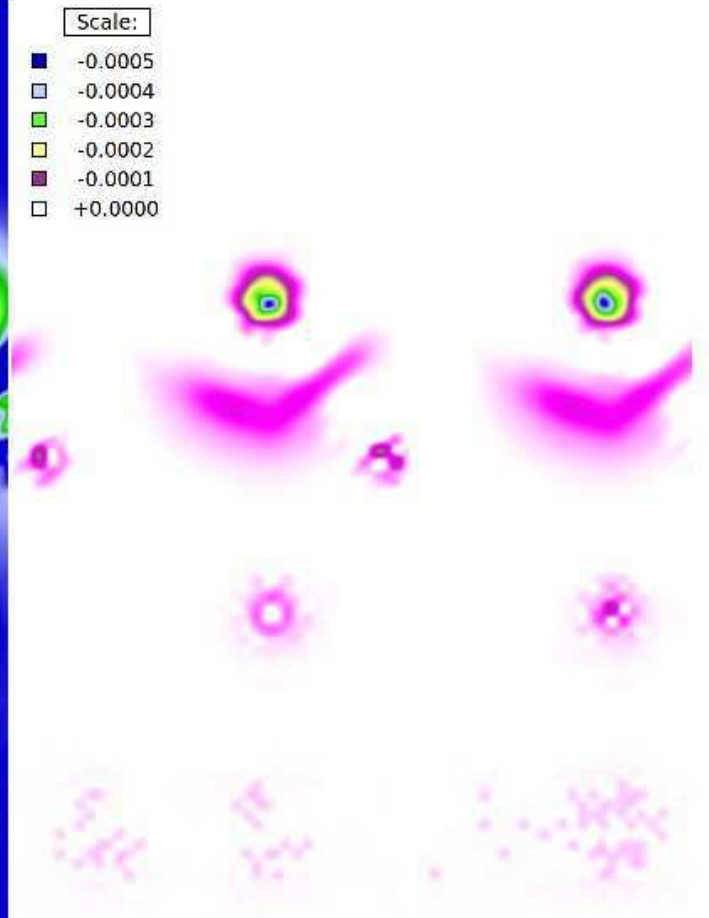
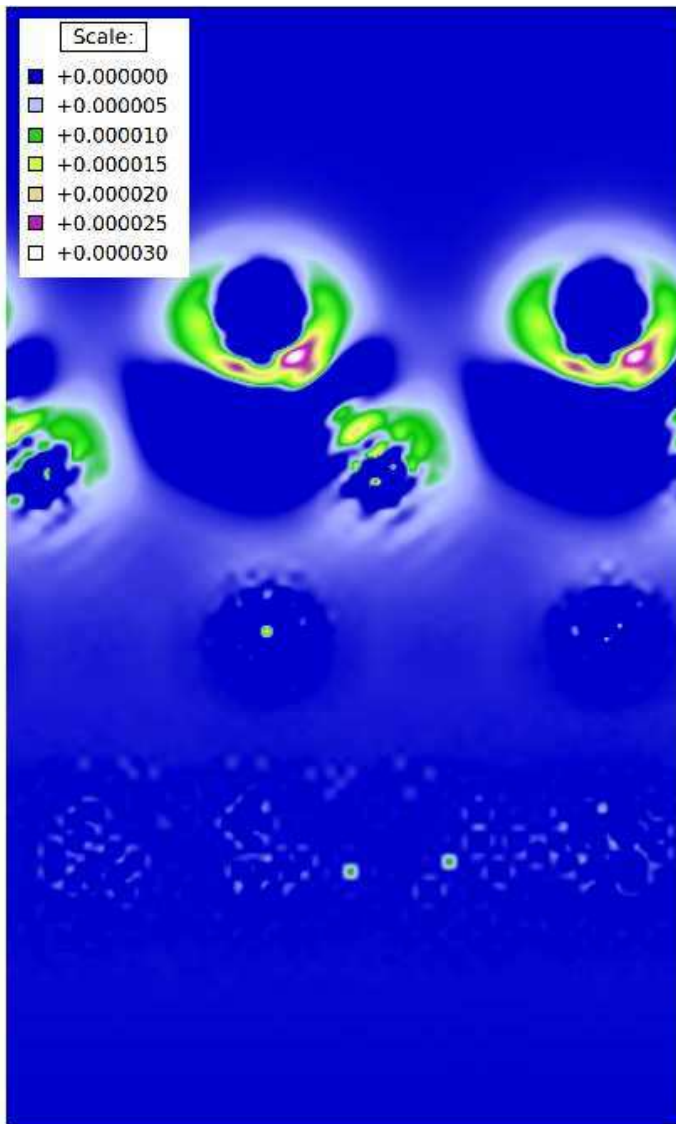
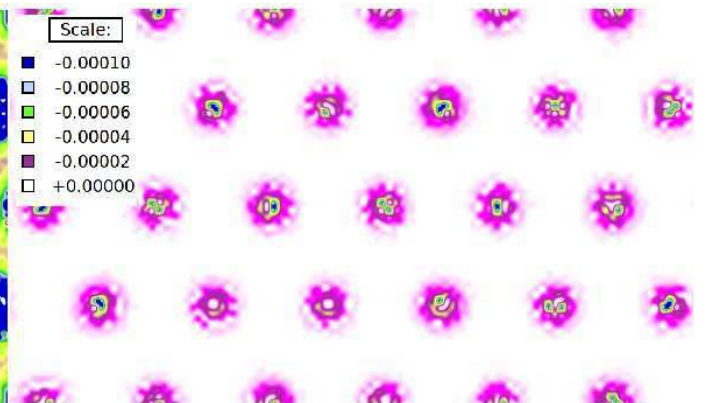
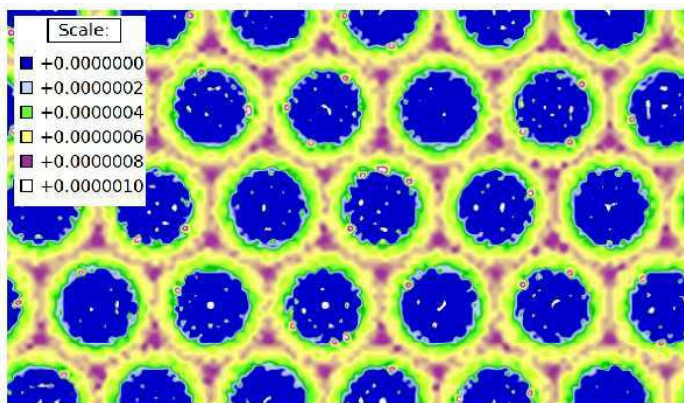


**Figure 6** Distribution of the electron density difference (units:  $e/a. u.^3$ ) corresponding to the structure of Figure 2c, i.e., the one at the end of step 3. The planes shown are (a) perpendicular and (b) parallel to the graphene sheet and contain the longest diagonal of lozenge-shape supercell and the first helium atoms layer respectively.

(a)



(b)



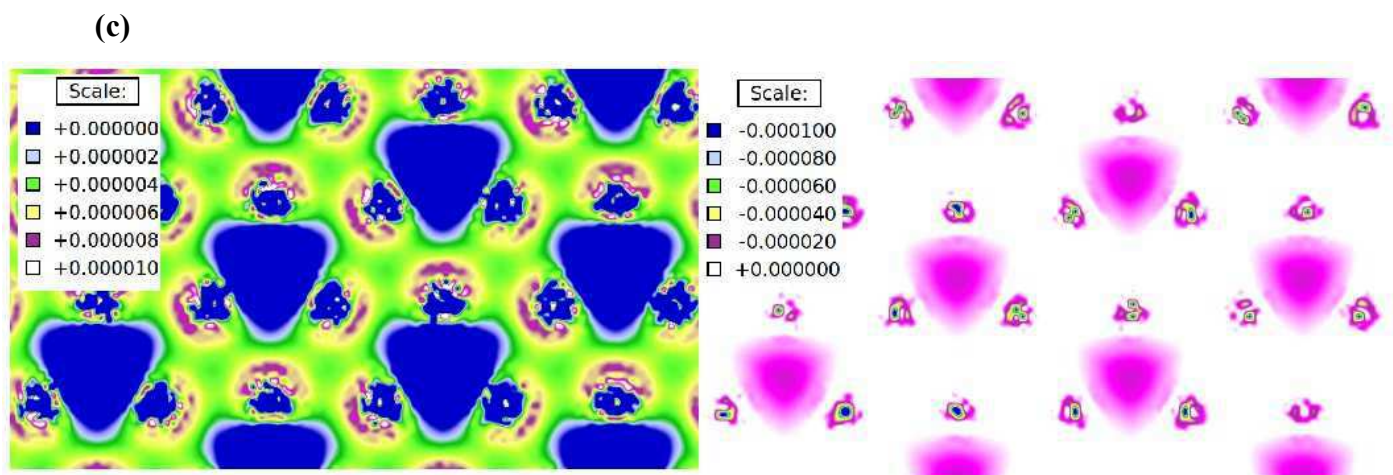


**Figure 7** Distribution of the electron density difference (units:  $e/a. u.^3$ ) corresponding to the structure of Figure 2g, i.e., the one at the end of step 7. The planes shown are (a) perpendicular and (b)-(c) parallel to the graphene sheet and contain the carbon atom with the highest x-coordinate besides the one with the highest y-coordinate on the right and the first-second helium atoms layer respectively.

## Chapter 4

### Molecular dynamics study of temperature effects on helium trapping and storage in Cu/Nb interface

#### 4.1. Introduction

Radiation damage of structural materials in nuclear reactors is mainly caused by the impact of ions and neutrons [1]. Bombarding particles provoke atomic displacements that lead to the creation of self-interstitial atoms (SIAs) and vacancies. In addition, neutrons initiate (n, alpha) reactions which may produce a considerable amount of helium [2-4]. A SIA and a vacancy can be annihilated by means of recombination while helium, which is insoluble in metals, tends to form helium and helium-vacancies clusters. As nuclear reactions increases with neutron flux and energy, the production of helium is a more significant issue in nuclear fusion reactors than in fission ones [5].

The design of materials that initially possess improved mechanical properties is not enough in the nuclear field, they must resist radiation and maintain these properties as unaltered as possible to extend the reliability, lifetime and efficiency of nuclear reactors [6]. One of the most promising strategies in the mitigation of radiation damage is the introduction of heterophase interfaces with enhanced ability to annihilate point defects and that control helium bubble nucleation and growth. Nanoscale metallic multilayer composites (NMMCs) have attracted much attention since it was proposed a strength enhancement in thin-layered two-metal laminates with respect to homogeneous alloys almost five decades ago [7,8]. Moreover, the layered structure with flat interfaces improves their coarsening resistance due to the absence of necks connecting layers of the same metal especially if immiscible elements are used [9].

The strengthening of layered metallic composites is determined by the deformation mechanism that shifts depending on the length scale [10]. For small layer thickness, heterophase interfaces can play an important role hindering slip transmission across them. This is the case of the interface atomic configuration termed  $KS_1$  in Cu/Nb multilayer composites [11].  $KS_1$  is obtained by joining Cu and Nb layers with the Kurdjumov–Sachs (KS) orientation relation [12]. Dislocation loops nucleate in the interfaces first when sliding start. Afterward, they expand, coalesce and glide as the shear increases. If a glide dislocation enters the interface, its core spreads differently depending on the dislocation type [13] and nonuniformly due to the direction dependence of the shear resistance [11].  $KS_1$  shows a very

anisotropic shear strength in Cu/Nb multilayer composites which is lower than in glide planes of single Cu and Nb crystals. The lower the shear resistance of the interface, the higher the core spreading and yield strength [10].

Cu/Nb-KS<sub>1</sub> interface contains patches where Cu and Nb atoms have a coordination number lower than inside single crystals of Cu and Nb respectively [14]. He atoms are trapped preferentially at the misfit dislocation intersections (MDIs) where above patches of undercoordination are located [11]. According to density-functional-theory (DFT) calculations [15], the formation energy of an interstitial He atom at the most stable site of KS<sub>1</sub> and the migration energy along the interface are lower and much higher respectively than the values obtained in single crystals of Cu and Nb. Therefore, a remarkable trapping effect of interstitial He atoms is expected at MDIs of Cu/Nb-KS<sub>1</sub> interface. González *et al.* also found that the formation energy of a substitutional He atom at the first interfacial Cu plane is even lower than the formation energy of an interstitial He atom at the most stable interface site which may suggest an enhancement of the trapping effect. For most of the cases studied, molecular-dynamics (MD) simulations revealed that the He atom, which is unstable in Cu side, was trapped in Cu/Nb-KS<sub>1</sub> interface by means of a self-trapping mechanism [16]. This mechanism consists on the formation of a substitutional He atom in the second or third interfacial Cu plane and the consequent emission of a self-interstitial atom (SIA) that is absorbed in the first interfacial Cu plane forming a delocalized point defect [17]. Nevertheless, for the rest of the cases studied, the He atom was absorbed as an interstitial in the first interfacial Cu plane. No migration of the He atom along the interface was observed. Helium not only clusters and precipitates in the form of bubbles that may transform to voids as in bulk metals, but also may form flat platelets at MDIs due to the higher interface energy at these regions [18]. Once all the wettable interface area at a MDI is occupied by a platelet, the growth mode of the cluster changes and its thickness increases. It was seen that He clusters grew exclusively into the Cu side of Cu/Nb interface. Finite-element-method (FEM) calculations performed also by Kashinath *et al.* showed that platelets in Cu/Nb interfaces became unstable under irradiation when they were composed of 21 He atoms and after that, the volume cluster increased until an approximately spherical bubble forms.

Top-down approaches based on O-lattice theory may be very useful for designing interfaces that reduce He-induced damage [19]. Indeed, He removal could be enhanced by promoting He precipitation into linear channels that outgas helium at free surfaces. With the aim of understanding the evolution of helium precipitate morphology, Yuryev and Demkowicz applied a phase field model to an interface containing aligned circular He-

wettable patches within a nonwettable area [20]. They found that the coalescence of helium precipitates into elongated and nearly spherical formations occurred for lower and higher wetting angles respectively. Nonetheless, to take advantage of interfaces with tailored energetics and structures, small layer thicknesses are required to ensure that helium reaches one of them before forming immobile clusters in the bulk [21]. In addition, for a given grain size, an optimal layer thickness exists which maximizes helium release from grain boundaries according to the rate-theory-based model predictions of above work. Below this thickness, helium release decrease due to increased clustering and trapping of helium on grain boundaries.

Ion beams are frequently used to study the effects of radiation on materials properties. Besides being a simple technique, helium implantation [22] creates a more realistic environment than with other techniques as tritium decay [23] where no displacement damage is expected to occur. Thus, three regions of interest can be found in He-irradiated materials depending on the depth [24]: a first region close to the surface where point defects predominate, an intermediate region that contains the peaks of point defect and helium concentrations, and the last region with a significant concentration of helium but negligible amount of point defects. Combination of different helium implantation energies and doses may produce peaks in the concentration profile with the same value but at different depths [6].

The resistant to blistering of Cu/Nb multilayer composites was analyzed after He-ion implantation at room temperature as well as after post-implantation annealing at 600 °C [25]. After annealing, no surface blistering was observed for layer thickness of 4 nm but, for layer thickness of 40 nm, Cu/Nb multilayer composites exhibited a high density of surface blisters that contained cracks. Consequently, ~10 and ~50 % of implanted helium was released from the sample in the first and last case respectively. On the contrary, only a few surface blisters, all of them without signs of having burst, were found in He-implanted Cu/Nb samples at temperatures ranging from 490 °C to 660 °C [26]. Furthermore, it was shown that the amount of helium released in Cu/Nb multilayer composites increases as the layer thickness and temperature decreases and increases respectively. For the lower temperature analyzed in above work, a detailed investigation of He-bubble distribution in He-implanted Cu/Nb multilayer composites was provided [27]. Transmission electron microscopy (TEM) imaging showed that, in Cu layer, elongated He bubbles 28-43 nm long formed along Cu grain boundaries and Cu/Nb interfaces while away from them equiaxed He bubbles with diameter of 4.5-24 nm were observed. Asymmetrically with respect to Cu/Nb interface, only He bubbles with a diameter of 1-2 nm were observed in the Nb layer. These results correspond to

layer thickness of 120 nm, the larger one analyzed in **Ref. (26)**. He bubbles with diameter of 1-2 nm were seen in Nb layers too for the smaller layer thickness investigated, that is, 5 nm. However, oblong He bubbles 7-11 nm long and confined between Cu/Nb interfaces were observed in Cu layers. These results contrast with the ones of **Ref. (25)** in which helium bubbles with a diameter of 1-2 nm formed either in Cu or Nb layers at room temperature. After annealing these helium bubbles coarsened in both layers without showing the asymmetry seen in **Ref. (27)**. Therefore, He bubble distribution may be controlled by means of the implantation conditions and multilayer composite morphology.

The analysis of transmission electron microscope (TEM) images showed that the threshold He concentration for the formation of observable bubbles in Cu/Nb multilayer composites is much higher than that in single Cu and Nb crystals [28]. Moreover, the threshold He concentration is approximately proportional to the number of interfaces per unit thickness. It was demonstrated that the introduction of Cu vacancies in appropriate sites of the first interfacial plane, that is, at MDIs, is energetically favorable [11]. Thus, the first interfacial Cu plane in the lowest energy interface configuration has 5 % less atoms than in  $KS_1$ . Therefore, Cu/Nb interfaces may exhibit a higher He solubility than single Cu and Nb crystals due to the high excess atomic volume that they possess. Similarly, Demkowicz *et al.* hypothesized that threshold He concentration differences between Cu/Nb and Cu/V multilayer composites arise from their differences of areal MDI density since either Cu/Nb or Cu/V interface contain the same number of Cu vacancies per MDI in the lowest energy interface configuration [29,30]. Neutron reflectometry (NR) is sensitive to interface He-induced density changes. Platelets store helium nearly three times more efficiently than bubbles [18]. Thus, NR technique allows to find the critical He fluence at which platelet-to-bubble transition occurs [31]. The critical He fluence is approximately proportional to the areal MDI density as the threshold He concentration. Hence, multilayer composites that contain interfaces with a high areal MDI density could increase the He concentration required to nucleate bubbles. According to the results of the experiments performed by Kashinath *et al.*, platelets transform to bubbles when there are 25 He atoms per MDI.

X-ray reflectivity (XRR) measurements demonstrated that, once the platelet-to-bubble transition occurred, the swelling of the sample increased one atomic volume per each He atom [32]. However, the morphology of Cu/Nb multilayer composites was not significantly altered by He implementation. A swelling reduction can be achieved by decreasing layer thickness. This happens too with radiation hardening, usually accompanied by embrittlement, which consists in the enhancement of hardness due to the interactions of glide dislocations with

different types of defects that act as weak or strong obstacles [33]. Hardening is not directly proportional to the areal MDI density, in contrast with the threshold He concentration for the formation of observable bubbles via TEM, but it is proportional to the hardness of unimplanted samples [34].

Experimental studies on the deleterious effects of high helium concentrations in multilayer composites have provided useful information. Nevertheless, the methods used in these studies show some limitations to determine in detail the characteristics of He precipitates, which have proven to be dependent on implantation conditions [35,36], and to correlate them with the material behavior at atomic level. It is known that the enhanced radiation damage tolerance of Cu/Nb multilayer composites resides in the energetics and atomic structure of their interfaces. Furthermore, Vattré *et al.* demonstrated that the sink strength for point defects is highly sensitive to interface stress fields [37]. So, as Cu/Nb interfaces may easily change from a metastable state to another one of almost the same energy due to tensional or thermal variations [11], atomistic modeling may help to elucidate the effect of temperature on the mechanisms that are behind helium trapping as well as helium bubbles formation and growth in Cu/Nb interfaces which remains somehow misunderstood.

Therefore, in this study, we carried out MD simulations at different temperatures on Cu/Nb bilayer composites in the presence of an increasing amount of helium. The progressive introduction of new He atoms in each simulation may be seen as an increasing He fluence. Special attention has been paid to He-atoms trapping in Cu/Nb interface, as well as their distribution and clustering. The mechanical and microstructural response of the material to an increasing concentration of interfacial helium has been investigated too. Degradation processes caused by helium precipitates depend on their characteristics and number density, so insight gained from this study is essential to be able to predict the performance of Cu/Nb multilayer composites, as a potential material to be used in future nuclear reactors, at different working conditions.

## 4.2. Computational details

To study the performance of Cu/Nb multilayer composites in the presence of an increasing amount of helium at different temperatures, we have employed molecular dynamics (MD) simulations. The calculations were performed using the Large-scale Atomic/Molecular Massively Parallel Simulator (LAMMPS) code [38]. Cu-Nb-He interactions were described by the resulting potential [39] of combining two-body (He–Cu, He–Nb and He–He) energies obtained from lattice expansion simulations, and optimized base

on first-principles calculations, with an existing embedded atom method (EAM) Cu–Nb potential [40].

All the simulations were carried out with the periodic cell shown in **Figure 1a** that was generated using the Atomic Simulation Environment (ASE) python module set. The cell contained a layer of Cu formed by 21  $\{111\}$  planes and a layer of Nb formed by 26  $\{110\}$  planes joined with the Kurdjumov–Sachs (KS) orientation relation, i.e.,  $\langle 110 \rangle$  direction in Cu  $\{111\}$  planes parallel to  $\langle 111 \rangle$  direction in Nb  $\{110\}$  planes [11]. The initial dimensions of the simulation cell in x, y, and z directions were 101.84 x 71.58 x 104.52 Å and, the total number of Cu and Nb atoms therein was equal to 52398. The cell created underwent a thermalization process at temperatures of 300, 500 and 700 K. Firstly, an energy minimization of the system was performed. Then, thermalization continued under the microcanonical (NVE) ensemble. Lastly, the isothermal-isobaric (NPT) ensemble was applied, followed by the canonical (NVT), before introducing helium atoms into the cell.

Three sets of MD simulations were performed at each of the three temperatures studied. These sets consisted of 33 steps in which 200 He atoms were randomly added to a central region of the Nb layer each time. After that, several cycles under the NVE, NPT and NVT ensemble were carried out to equilibrate the system again and adapt it to the new situation. Overlapping of He atoms was not allowed with the aim of avoiding bubble formation in the bulk and thus favoring the diffusion of He toward the interface. For the same reason, He atoms remaining in the insertion region from the previous step were deleted prior to introducing new ones. The equilibration process was followed by 7.5 ns of MD simulation under the NVT ensemble whose beginning corresponds to time  $t = 0$  ns. Each step took as a starting point the snapshot of the previous step at  $t = 2.5$  ns. The amount of helium trapped at the interface barely changes after that time, however, the simulation continued until  $t = 7.5$  ns to allow its accommodation.

Defects in Nb layer were identified using the bbc defect analysis (BDA) method which was implemented as a python script [41] for being used with the open visualization tool (OVITO) software [42]. It is worth highlighting that He and Cu atoms are not considered in the analysis. The BDA method uses several techniques as coordination number (CN), common neighbor analysis (CNA), and centro-symmetry parameter (CSP) that combined allow to classify the defects uniquely. For most of the cases, this would not be possible using the techniques separately. All particle images shown in this chapter were generated with OVITO.

### 4.3. Results

We have studied the effect of temperature on helium trapping and storage in Cu/Nb interface. Numerical graphics show the average results of the three MD sets performed at each of the temperatures studied and the corresponding error bar. The analysis of simulation results revealed that the interface, which had a similar  $z$  coordinate ( $\sim 42.8$  Å) for all the MD sets after the thermalization process, varied its position from one step to another. A specific methodology was developed to detect exactly where the interface was located in each step of each set, and thus perform the analysis in the correct region. In spite of this, no overlapping occurred between the widest interface region in which the number of He atoms has been counted and He insertion one that is between  $z = 50$  Å and  $z = 88$  Å. This means that no He atom already trapped in the interface was erroneously removed along with previous step He atoms remaining in the insertion region.

First, we focus on the interface, specifically at MDIs, where He atoms are supposed to be trapped preferentially due to the excess of atomic volume in these regions. With the aim of clarifying their location, bottom views of the relaxed  $KS_1$  interface at 300, 500 and 700 K are shown in **Figures 1b**, **1c** and **1d** respectively with the first interfacial plane atoms of the Nb layer colored in blue and Cu ones colored according to their centro-symmetry parameter value. There are two sets of parallel strips with Cu atoms colored in green. The intersections of these strips coincide with patches of undercoordination where a Cu atom, in red or orange color, is nearly on top of a Nb atom. A collection of spheres, whose centers have the same  $x$  and  $y$  coordinates that above Cu and Nb atoms and the  $z$  coordinate of the interface, are used to study the helium trapping at MDIs. The radius of the spheres has been set equal to 4 Å, that is, between 1.5 times the lattice spacing of copper and niobium (see next chapter).

The percentage of occupied spheres by He atoms at the end of each step (7.5 ns) is shown in **Figure 2a** for a temperature of 300, 500 and 700 K. It can be seen a rapid increase in the first steps that is greater for 300 K than for 500 and 700 K. Then, the percentage of occupied spheres approaches an asymptotic value in step 8 around which it oscillates. Although Cu/Nb interface shows a similar behavior at the two higher temperatures studied, the percentage of occupied spheres is higher until step 4 and usually lower from step 21 for 500 K than for 700 K. Additionally, the number of He atoms inside the spheres at the end of each step has been calculated (**Figure 2b**). It can be seen that the amount of helium grows linearly until step 8 for 300 K, and step 12 for 500 and 700 K. Then, this value is kept approximately constant at 500 K until the last step. It occurs similarly at 300 K from step 21 but, before, the number of He atoms inside the spheres still increases although slower than in

the first steps. There is also a slope reduction between steps 12 and 21 at 700 K, however, the amount of helium inside the spheres increases again considerably in the last steps which reduces and increases the differences with 300 and 500 K results respectively. The higher values correspond to 300 K at any step. On the other hand, the lower values correspond to 700 and 500 K in the first and second half of the steps respectively.

Additional information about helium distribution in Cu/Nb interface is needed to complete the results depicted in the previous figure. Thus, the total number of He atoms in the interface at the end of each step is shown in **Figure 3** for a temperature of 300, 500 and 700 K. Three widths of the interface region are considered: 4, 6 and 8 Å (**Figures 3a, 3b and 3c** respectively). A width of 4 Å includes the first interfacial plane of Cu and Nb layers. For a width of 8 Å, which is equal to the diameter of previous spheres, the second interfacial plane of Cu and Nb layers are also included. A width of 6 Å includes the first Cu and Nb interfacial plane besides the space between first and second interfacial planes in Cu layer and most of it in Nb. It can be seen that in all cases the number of He atoms in the interface increases with increasing number of steps. Negligible differences are observed between the three temperatures results until step 8 for 4 Å and, step 21 for 6 and 8 Å. For 4 Å, the absence of differences between 500 and 700 K continues too until step 21. Next, some differences appear that are smaller for wider interfaces. The higher values correspond to 500 K, the intermediate to 700 K and the lower to 300 K for any of the widths considered. Furthermore, the number of He atoms in an interface 4, 6 and 8 Å wide are compared in **Figure 3d** for 500 K. Value differences between the three widths increases with increasing number of steps. There is a slope decrease in step 8 which is quite similar for these three cases. All things said relative to previously mentioned figure can be applied too for the other two temperatures.

Up to now, the corresponding results to helium amount evolution in Cu/Nb interfaces refer to single atoms. The joint analysis of occupied spheres by helium and He atoms inside them may allow to obtain some information about helium clustering but only in the central part of MDIs. Therefore, top views of He-atoms arrangement in the interface are shown in **Figure 4** for the three temperatures studied at the end of most singular steps, that is, steps 8, 12, 21 and 33 (**Figures 4a-4c, 4d-4f, 4g-4i and 4j-4l** respectively). Although the images correspond to an interface region 8 Å wide, only Cu and Nb atoms in an interface region 4.5 Å wide are represented, i.e., first interfacial plane atoms. This means that if they move more than a few tenths of an ångström toward the interior of the corresponding layer, these atoms do not appear in the image as they leave the interface region considered. In this way, not only helium is observed more clearly but also the deterioration of the interface caused by

it is appreciated. The area occupied by the spheres used in previous analysis is represented by black circles. Moreover, it should be noted that the images correspond to the MD simulation set with closer values to the average in previous figures. Thus, visual inspection of the images reveals that most of the helium in the interface is forming clusters and that the number of single He atoms is always less than 20 at 300 K, and 5 for 500 and 700 K. The number of He dimers is also very small. In addition, it can be seen that the location of the clusters formed until step 8 varies very little in subsequent steps for the three temperatures studied, conditioning the trapping of incoming He atoms. In step 8, the number of clusters is very similar in all the cases. This value is maintained approximately constant until the last step for 700 K. For the other two temperatures, the number of clusters still increases but much slower than before step 8. So, incoming He atoms after step 8 contribute mainly to increase the size of the clusters formed in the interface for the three temperatures studied causing a significant growth of the cavities volume as it can be observed in the images. Besides this common observation, there is a notable difference. For 500 and 700 K, zones among He clusters where Cu or Nb atoms disappear from the image are seen in step 8 while for 300 K, this happens latter.

By increasing the Cu/Nb interface width considered, the amount of helium increases too. As each half of these widths corresponds to each of the two layers, this means that He clusters may grow in thickness toward the interior of copper, niobium, or both. Therefore, front views of Cu/Nb interface with He atoms at the end of step 33 are shown in **Figures 5a, 5b** and **5c** for a temperature of 300, 500 and 700 K, respectively (same MD simulation sets as in Figure 4 and with the same Cu, Nb and He atoms represented). It can be observed that most of the helium is concentrated into first interfacial Cu and Nb planes, and between them. Despite this, there is helium throughout all the interface region thickness for any temperature and MD simulation set except the one corresponding to **Figure 5a**, where there are not He atoms beyond the first interfacial plane in Cu side.

In addition to the number of He atoms and their distribution in Cu/Nb interface, the material response to thermal and mechanical solicitations associated to the temperature and He-cluster pressure respectively has been investigated too. Thus, the average stress tensor trace of all Cu and Nb atoms in an interface region 10 Å wide at the end of each step is shown in **Figure 6** for a temperature of 300, 500 and 700 K. It is worth noting again that plotted results correspond to the average of the three MD simulation sets performed for each temperature. A width of 10 Å also includes the space between second and third interfacial planes of Cu and Nb layers, or most of it. In this way, the stress tensor trace of Cu and Nb

atoms in the third interfacial plane is not considered. However, the stress tensor trace of first and second interfacial plane atoms is considered as long as they are displaced toward the interior of the corresponding layer less than two and one interplane distance, respectively, as a consequence of He-cluster growth. It can be observed that the higher the temperature, the higher the average stress tensor trace (more negative) at any step. Initially, the values increase almost linearly until step 21 for 300 K and, step 12 for 500 and 700 K. Next, the average stress tensor trace keeps nearly constant until the last step for the three temperatures studied. The relationship between these plateau values and temperature is logarithmic.

Helium in sufficient quantities leads to microstructural changes in Cu/Nb interface. In order to quantify them, the BDA method has been applied to the Nb side of the interface region. It should be noted that this method is valid only for bcc crystals. First, the total number of Nb atoms belonging to any defect structure in an interface region 10 Å wide has been computed at the end of each step for a temperature of 300, 500 and 700 K (**Figure 7a**). A rapid increase can be seen in the first steps that is greater for 300 K, then for 500 K, and lastly for 700 K. Next, the number of all defect structure atoms seems to approach an asymptotic value but it stops increasing in a somewhat abrupt way in step 21 for 300 K, and step 12 for 500 and 700 K. Plateau values are also logarithmically correlated to temperature here as in the case of average stress tensor trace. Since all or most of these atoms are identified as part of a surface structure, it is necessary to analyze the details of these results to evaluate the lattice distortion of the interface. Hence, the average CSP of all defect structure atoms in an interface region 10 Å wide at the end of each step is shown in **Figure 7b** for a temperature of 300, 500 and 700 K. Initially, the values decrease almost linearly until step 8. The lower the temperature, the greater this decrease. Then, the average defect CSP increases almost linearly and similarly for the three temperatures studied until last step although, before this, it barely varies during a few steps for 300 K. It can be observed that the higher the temperature, the higher the average defect CSP except between steps 1 and 4.

The addition of He atoms to clusters increases their pressure and part of it may be released by producing defects. Furthermore, thermal emission of defects from the cavities may also occur. Despite this, the identification of defects in the Nb side of the interface region has been reduced basically to only one type, surface structure. Many of these surface atoms would have been identified as part of other defect structures in case of being in the bulk. The defects are not emitted only to the intercluster region but also to the lower and upper region. Thus, the application of the BDA method to a region close enough to the interface and, comparable for all sets of MD simulations, may provide insight on this matter. So, lastly, the

number of Nb atoms belonging to the most relevant defect structures (vacancy, non-screw dislocation and twin/screw dislocation) in the He insertion region at the beginning and end of each step is shown in **Figure 8** for a temperature of 300, 500 and 700 K. It is worth pointing out that results are also shown at the beginning of each step in order not to merge the defects coming from the interface with the ones produced by the formation and growth of clusters in He insertion region during the 7.5 ns that each step lasts. There are another two structures in which defective Nb atoms can be classified (results not shown here). One is planar fault, and a negligible or nil number of atoms belongs to this defect structure in all steps. The other is surface structure. The number of surface atoms increases with increasing number of steps which confirms the possibility that the interface state influences helium trapping in the interface. Unidentified defect structure atoms have not been considered since their number is very low at the end of any step. Thus, continuing with the analysis of the most relevant defect structures in the He insertion region, it can be seen either in **Figure 8a** (0 ns) or **8b** (7.5 ns) that vacancy structure atoms increases linearly from the first step until the last one for 300 K. On the other hand, a rapid increase can be seen at 0 and 7.5 ns in the first steps for the other two temperatures studied that is slightly greater for 700 K. Then, the number of vacancy structure atoms for 500 and 700 K, which is much higher in any step than for 300 K, seems to approach an asymptotic value. The differences between 500 and 700 K are reduced in the last steps. In contrast with vacancy structure, the evolution of non-screw dislocation atoms in the He insertion region from the first step until the last one is different at 0 (**Figure 8c**) and 7.5 ns (**Figure 8d**) for 300 K. The number of non-screw dislocation atoms tends to increase with increasing number of steps either at 0 or 7.5 ns, nevertheless, it does so at a lower rate and from a much higher first step value in the last case. It occurs similarly at 0 ns for 500 and 700 K. However, there is a decrease in the first steps at 7.5 ns. After that, and until last step, the number of non-screw dislocation atoms is quite similar to the corresponding one at 0 ns for these two temperatures. There are not significant differences at 0 ns between the three temperatures studied although the values are higher for 500 and 300 K in the first and last half of steps respectively. The higher number of non-screw dislocation atoms at 7.5 ns corresponds to 300 K in most of the steps. The intermediate values correspond to 500 K but only in the first half of the steps since the differences with 700 K vanish in the second half. Finally, the evolution of twin/screw dislocation atoms in the He insertion region at 0 (**Figure 8e**) and 7.5 ns (**Figure 8f**) is commented. The number of atoms belonging to this last defect structure at 0 ns oscillates around first step value until last step for the three temperatures studied. Usually, the higher the temperature, the higher the number of twin/screw dislocation

atoms even though the differences are small. On the contrary, the number of twin/screw dislocation atoms at 7.5 ns is higher for 300 K than for 500 and 700 K. In these last two cases, very few or no atoms are identified as part of a twin/screw dislocation while for 300 K, the number of atoms belonging to this defect structure tends to decrease slowly from first step until last one.

#### 4.4. Discussion

One of the most promising strategies for avoiding the deleterious effects of helium in future nuclear systems or, at least retarding their appearance, is the introduction of heterophase interfaces. It is known that a decrease of layer thickness in multilayer composites causes a decrease of average He-bubble size and number density [27,35] and, therefore, a reduction of swelling [32] and hardening [43]. Helium precipitates, before forming bubbles, may form platelets at MDIs which are not detectable in TEM images due to their high efficiency to storage helium [18]. Moreover, helium release in multilayer composites increases with decreasing layer thickness [26].

The morphology of the multilayer composite is an important factor in He-bubble morphology and distribution but not the only one. Implantation conditions, such as He fluence and temperature, also play a relevant role. The introduction of the same number of He atoms at the beginning of each step may be seen as a progressive increase of He fluence. Despite the amount of helium retained in Cu/Nb multilayer composites is lower for higher temperatures [26], this effect of the temperature is avoided since periodic boundary conditions have been used here. Thus, the results of previous section are comparable and allow to investigate the effect of temperature on helium trapping and storage in Cu/Nb interface over a wide range of He concentrations.

Our results show that a similar number of He atoms are trapped in Cu/Nb interface at the end of each step for 300, 500 and 700 K (cf. **Figure 3**). This suggests that, due to the absence of displacement damage in this study, interstitial diffusion is the dominant migration mechanism of He atoms which is less sensitive to temperature [24]. The small differences between the three temperatures may originate as a consequence of the removal of He atoms randomly introduced in a central region of the Nb layer at the beginning of the steps to prevent their overlap. Most of the trapped He atoms are located into first interfacial Cu and Nb planes and between them, i.e., in an interface region 4 Å wide. Thus, the number of He atoms in an interface region 6 Å wide at step 33 is 27.8, 16.0 and 25.2 % higher than in an interface region 4 Å wide for 300, 500 and 700 K respectively. For a width of 8 Å, these

values are 12.1, 9.2 and 8.6 % higher than for 6 Å. Above results contrast in part with the trajectories followed by single He atoms initially placed 10 Å from Cu/Nb-KS<sub>1</sub> interface in Nb side [16]. He atoms ended up absorbed in a substitutional or interstitial site of the second or first interfacial Cu plane respectively, but never in the Nb side of the interface. The latter does not happen in our case where several He atoms are involved in the simulations (cf. **Figure 5**).

Incoming He atoms contribute to increase the number of clusters in the interface and their size until step 8 but, after this step, they basically contribute to increase interfacial He-clusters size (cf. **Figure 4**). Many of these clusters partially occupy some of the spheres located in the central part of MDIs or are near them. The percentage of spheres occupied by He atoms at the end of each step is higher for 300 K than for 500 and 700 K (cf. **Figure 2a**) although error bars point to a greater variability for lower temperatures. The location of the clusters formed until step 8 condition the trapping of incoming He atoms. So, until this step, the difference of occupied spheres percentage may arise from a temperature effect or the randomness with which He atoms are introduced at the beginning of each step. The rate at which He atoms are trapped in the interface region decreases in step 8 (cf. **Figure 3**). This slope decrease seems to be due to the stabilization of He cluster number.

The percentage of occupied spheres increases until step 8 and then oscillates around this step value for the three temperatures studied. On the other hand, the number of He atoms inside the spheres at the end of each step grows longer, until step 21 and 12 for 300 and 500 K respectively (cf. **Figure 2b**). Next, this value is maintained approximately constant until the last step. The number of He atoms inside the spheres for 500 and 700 K evolves somewhat similarly until last steps in which it increases again noticeably for the higher temperature. Likewise, the average stress tensor trace of all Cu and Nb atoms in an interface region 10 Å wide at the end of each step also increases (it becomes more negative) until step 21 for 300 K and, step 12 for 500 and 700 K (cf. **Figure 6**). Then, these values are kept approximately constant until the last step. Above results may suggest that the location of the clusters is important if they are related to the response of the material in the interface except in the last steps for 700 K. The deterioration shown in these steps by the interface (cf. **Figure 4**), which has lost much of the initial structure, could be the cause of that correlation discrepancy. However, intercluster ligament fracture is discarded as there is no He release [44] but quite the opposite according to the evolution of He amount in the interface region (cf. **Figure 3c**).

In addition, due to the excess of atomic volume at MDIs, the above concordance between clusters location and average stress tensor trace is very unlikely. The average CSP of

surface Nb atoms has the same value initially for the three temperatures studied but then this changes once He atoms start to get to the interface. It can be seen in **Figure 7b** that He clusters formation or growth of existing ones decreases the average CSP until step 8 to a greater extent for 300 K, then for 500 K, and lastly for 700 K. After that, the growth of existing He clusters increases the lattice distortion of the interface and, hence, the average CSP until the last step. Since it does not decrease again for 700 K despite the significant increase of He atoms inside the spheres in the last steps, the different material response seems to be a temperature effect.

The evolution of atoms belonging to the most relevant defect structures in the He insertion region has revealed that thermal emission of vacancies from the cavities may be behind the subsequent increase of the average stress tensor trace in the interface for the three temperatures studied. In order to isolate the vacancies originating from the interface as much as possible, we focus now on the defect results at the beginning of each step. It can be observed in **Figure 8a** that the number of vacancy structure atoms increases up to about step 12 similarly to the average stress tensor trace for 500 and 700 K. Thus, the pressure exerted by He clusters on Cu and Nb atoms may increase as long as vacancies are emitted. Nevertheless, vacancy emission rate decreases with increasing number of He atoms forming the cluster and cavity size [28,45]. The latter could be also related to the great difference in the number of vacancy structure atoms between 300 K and the other two temperatures studied. Initially, Cu and Nb atoms are less compressed for lower temperatures (cf. **Figure 6**) allowing He clusters to expand more and occupy a greater volume. For most of the steps, the lower the temperature, the higher the number of surface Nb atoms (cf. **Figure 7a**). However, this does not happen in the first steps and, therefore, such a low number of vacancy structure atoms for 300 K is not explained by itself by the difference of the volume occupied by He clusters alone. The vacancy concentration at thermodynamic equilibrium increases for higher temperatures (see next chapter). This means that vacancies are more easily formed at high temperatures. The vacancy diffusivity also increases with the temperature which in turn rises the vacancy emission rate [45]. As a consequence of all this, the increase of the average stress tensor trace is a little slower for 300 K than for 500 and 700 K.

The results have shown a similar behavior of Cu/Nb multilayer composite for the two higher temperatures studied and usually smaller differences between 500 and 700 K than between any of them and 300 K. One of these dissimilarities has to do with the phenomenon of vacancy emission whose rate does not decrease with increasing number of steps for 300 K (cf. **Figure 8a**). Nonetheless, the average stress tensor trace stops increasing in step 21 (cf.

**Figure 6).** This suggests the existence of a temperature between 300 and 500 K at which the material behavior changes since intercluster ligament fracture is discarded also here. The cavity growth is determined by a competition between the fluxes of radiation-induced point defects into the cavity and the thermal and He-induced emission of vacancies and SIAs, respectively, out of the cavity [46]. Thermal emission of SIAs is negligible compared to vacancies one due to their high formation energy [18]. Here, point-defect fluxes into the cavity are negligible too since only individual He atoms are added at the beginning of each step without displacement damage. So, small clusters may grow by the emission of a SIA but, if they are large, an entire dislocation loop may be emitted when the number of He atoms forming the clusters increases [44,47]. The number of twin/screw dislocation atoms in the He insertion region at 0 ns barely varies from the first step until the last one for 300, 500 and 700 K (cf. **Figure 8e**). Therefore, these defects are formed as a consequence of the equilibration process to which the system is subjected just after the introduction of new He atoms in each of the steps. On the other hand, the number of non-screw dislocation atoms at 0 ns tends to increase from a nil value with increasing number of steps for the three temperatures studied (cf. **Figure 8c**). This confirms that SIAs emission and dislocation loop punching are the mechanisms responsible for the growth of He cluster.

To conclude this section, the effect of implantation conditions on the characteristics of interfacial helium precipitates, in addition to eventual material degradation processes caused by them, is discussed. A greater He fluence implies an increase in the helium amount in the different layers, which in turn increases the average size and number density of the bubbles [35], as well as swelling and hardening [43]. The average size of He bubbles is also larger for higher temperatures [25,27,36], however, their number density is lower since the amount of helium retained in the multilayer composite is lower too [26]. It occurs similarly here with He-cluster size and number for increasing He fluence. Moreover, after step 8, the number of He clusters increases much slower than in the first steps for 300 and 500 K, or does not even do it for 700 K (cf. **Figure 4**), in agreement with the results reported in **Ref. (43)**. The increase of temperature also means a lower number of He clusters but only after step 8. Even so, the differences between 300 and 500 K are very small. In contrast, the effect of temperature on the size of He precipitates requires a more detailed analysis. In the first steps, the higher the temperature, the greater the volume occupied by He clusters (cf. **Figure 7a**). Then, this changes to the opposite case until at least step 12. After this step, an increase in the thickness of He clusters or their expansion parallel to the interface produce new surface atoms for 500 and 700 K but outside the interface region considered. It occurs analogously for

300 K after step 21. According to non-screw dislocation atoms at 0 ns (cf. **Figure 8c**), a similar number of Nb atoms are emitted from the interface for the three temperatures studied. Nevertheless, vacancies are still emitted after step 12 for 300 K whereas for 500 and 700 K this happens no longer (cf. **Figure 8a**). Thus, the volume occupied by He clusters may grow faster for the two higher temperatures than for the lower one. However, even if this happened, the size of He precipitates would still be higher for 300 K because there are generally more surface atoms in the He insertion region for this temperature than for 500 and 700 K (results not shown here). So, according to the above, an increase in swelling is also expected here with the increase of He fluence for the three temperatures studied. A higher temperature seems to imply a lower degree of swelling except in the first steps, i.e., for low He concentrations. This occurs despite the fact that, in this study, there is no helium release which increases with increasing temperature [26]. The hardening induced by He bubbles increases with their number density and size [48]. Hence, it is very likely that there is an increase in hardening with the increase of He fluence, which moderates after step 8 once the number of He clusters is stabilized [43]. In addition to He-bubble number density and size, the ratio of He atoms to vacancies in each bubble is important too [35]. A higher ratio implies an increase of the barrier strength to the glide of dislocations [48]. Here, higher temperatures result in greater He atoms/vacancies ratios except for low He concentrations. Nonetheless, He bubbles are weaker obstacles than dislocation loops. These stronger defects are emitted as a consequence of interfacial He-clusters growth. So, an increase in hardening due to dislocation loops is expected with the increase of He fluence for the three temperatures studied. Moreover, the number of non-screw dislocation atoms in the He insertion region at the beginning of each step suggests that the degree of hardening due to dislocation loops may be similar for 300, 500 and 700 K.

#### 4.5. Conclusions

The effect of temperature on the formation of He clusters and their subsequent growth in Cu/Nb-KS<sub>1</sub> interface, as well as the mechanical response and eventual microstructural changes thereof, has been investigated by means of atomistic simulations. Three MD sets composed of 33 steps were performed with a periodic cell containing a bilayer of Cu and Nb for each of the temperatures studied (300, 500 and 700 K). In order to simulate a progressive increase in He fluence, the same number of He atoms were randomly introduced in the central region of the Nb layer at the beginning of each step. Overlapping was not allowed, so some of them were deleted. Moreover, He atoms remaining in the insertion region from the previous

step were removed. These two measures aimed at preventing the formation of He bubbles in that region and thus favor the diffusion of He atoms to the interface.

Interstitial diffusion is the dominant migration mechanism of He atoms which is less sensitive to temperature. Consequently, a similar number of He atoms are trapped in Cu/Nb interface at the end of each step for 300, 500 and 700 K. Incoming He atoms contribute to increase the number of interfacial clusters and their size until step 8 but, after this step, they basically contribute to increase interfacial He-clusters size. Many of these clusters, that grow on both sides of Cu/Nb interface, partially occupy some of the spheres located in the central part of MDIs or are near them. The differences of occupied spheres percentage at the end of each step, which is higher for 300 K than for 500 and 700 K, may arise from a temperature effect or the randomness with which He atoms are added.

Initially, the average CSP of surface Nb atoms has the same value for the three temperatures studied. Due to the excess atomic volume of the interface, this value decreases until step 8 despite the formation of He clusters or growth of existing ones. Cu and Nb atoms are less compressed for lower temperatures so the decrease is greater for 300 K, then for 500 K, and lastly for 700 K. Next, the average CSP increases until last step for the three temperatures studied as lattice distortion becomes more significant. Therefore, the capacity to accommodate helium in Cu/Nb interface is enhanced for lower temperatures.

The application of the BDA method to the He insertion region has confirmed that interfacial He clusters grow by SIAs emission and dislocation loop punching in the absence of displacement damage, and has also revealed that thermal emission of vacancies from the cavities increases the pressure exerted by these clusters on Cu and Nb atoms. The average stress tensor trace of Cu and Nb atoms in the interface increases as long as vacancies are emitted for 500 and 700 K, that is, until step 12. Nevertheless, the emission of vacancies ceases to be effective in step 21 for 300 K. Even though the rate of vacancy emission does not decrease with increasing number of steps, the average stress tensor trace stops increasing in the above-mentioned step. Therefore, the growth of He clusters may be contained by the thermal emission of vacancies, or as long as this mechanism is effective, delaying the formation of bubbles. As expected, there is a greater number of thermally emitted vacancies for higher temperatures.

The number density and size of interfacial helium precipitates depend on the implantation conditions, so material degradation processes caused by them also do so. According to the results obtained in this study, higher He fluences imply a greater degree of swelling and hardening for the three temperatures studied. A moderation of the increase in

hardening is expected after step 8 once the number of interfacial He cluster is stabilized. On the other hand, a lower degree of swelling could be anticipated for higher temperatures. The higher He atoms/vacancies ratio obtained in interfacial precipitates for higher temperatures should result in a greater degree of hardening since the differences in the number of He clusters between the three temperatures studied are negligible or small. Previous statements about temperature dependence of swelling and hardening are true except for low He concentrations, i.e., in the first steps. Dislocation loops are stronger obstacles to the glide of dislocations than He bubbles. The contribution of dislocation loops to hardening is expected to increase similarly with the increase of He concentration for 300, 500 and 700 K. So, as a concluding remark and for comparable amounts of interfacial helium, a decrease in swelling may be achieved in Cu/Nb multilayer composites by increasing the temperature at the expense of increasing the lattice distortion and reducing the margin to mechanical failure once a certain value of He concentration is exceeded.

## References of Chapter 4

- [1] H. Ullmaier, "The influence of helium on the bulk properties of fusion reactor structural materials", *Nuclear Fusion*, vol. 24, no. 8, pp. 1039-1083, 1984.
- [2] G. L. Kulcinski, D. G. Doran, and M. A. Abdou, "Comparison of displacement and gas production rates in current fission and future fusion reactors", *Properties of Reactor Structural Alloys After Neutron or Particle Irradiation*, ASTM International, 1975.
- [3] H. R. Brager, H. L. Heinisch, and F. A. Garner, "Effects of neutron irradiation at 450 °C and 16 dpa on the properties of various commercial copper alloys", *Journal of Nuclear Materials*, vol. 133, pp. 676-679, 1985.
- [4] Q. Xu, T. Yoshiie, and K. Sato, "Effects of hydrogen and helium produced by transmutation reactions on void formation in copper isotopic alloys irradiated with neutrons", *Journal of Nuclear Materials*, vol. 386, pp. 363-366, 2009.
- [5] M. R. Gilbert, S. L. Dudarev, S. Zheng, L. W. Packer, and J. Ch. Sublet, "An integrated model for materials in a fusion power plant: transmutation, gas production, and helium embrittlement under neutron irradiation", *Nuclear Fusion*, vol. 52, no. 8, article 083019, 2012.
- [6] A. Misra, M. J. Demkowicz, X. Zhang, and R. G. Hoagland, "The radiation damage tolerance of ultra-high strength nanolayered composites", *JOM: Journal of the Minerals, Metals and Materials Society*, vol. 59, no. 9, pp. 62-65, 2007.
- [7] J. S. Koehler, "Attempt to design a strong solid", *Physical Review B*, vol. 2, no. 2, pp. 547-551, 1970.
- [8] S. L. Lehoczky, "Strength enhancement in thin-layered Al-Cu laminates", *Journal of Applied Physics*, vol. 49, no. 11, pp. 5479-5485, 1978.
- [9] M. J. Demkowicz, P. Bellon, and B. D. Wirth, "Atomic-scale design of radiation-tolerant nanocomposites", *MRS bulletin*, vol. 35, no. 12, pp. 992-998, 2010.
- [10] A. Misra, M. J. Demkowicz, J. Wang, and R. G. Hoagland, "The multiscale modeling of plastic deformation in metallic nanolayered composites", *JOM: Journal of the Minerals, Metals and Materials Society*, vol. 60, no. 4, pp. 39-42, 2008.
- [11] M. J. Demkowicz, J. I. A. N. Wang, and R. G. Hoagland, "Interfaces between dissimilar crystalline solids", *Dislocations in solids*, vol. 14, pp. 141-207, 2008.
- [12] G. Kurdjumow and G. Sachs, "Über den mechanismus der stahlhärtung", *Zeitschrift für Physik*, vol. 64, no. 5-6, pp. 325-343, 1930.

- [13] R. G. Hoagland, J. P. Hirth, and A. Misra, "On the role of weak interfaces in blocking slip in nanoscale layered composites", *Philosophical Magazine*, vol. 86, no. 23, pp. 3537-3558, 2006.
- [14] M. J. Demkowicz and R. G. Hoagland, "Structure of Kurdjumov–Sachs interfaces in simulations of a copper–niobium bilayer", *Journal of Nuclear Materials*, vol. 372, no. 1, pp. 45-52, 2008.
- [15] C. González, R. Iglesias, and M. J. Demkowicz, "Point defect stability in a semicoherent metallic interface", *Physical Review B*, vol. 91, no. 6, article 064103, 2015.
- [16] M. G. McPhie, L. Capolungo, A. Y. Dunn, and M. Cherkaoui, "Interfacial trapping mechanism of He in Cu–Nb multilayer materials", *Journal of Nuclear Materials*, vol. 437, no. 1-3, pp. 222-228, 2013.
- [17] M. J. Demkowicz, R. G. Hoagland, and J. P. Hirth, "Interface structure and radiation damage resistance in Cu-Nb multilayer nanocomposites", *Physical Review Letters*, vol. 100, no. 13, article 136102, 2008.
- [18] A. Kashinath, A. Misra, and M. J. Demkowicz, "Stable storage of helium in nanoscale platelets at semicoherent interfaces", *Physical Review Letters*, vol. 110, no. 8, article 086101, 2013.
- [19] D. V. Yuryev and M. J. Demkowicz, "Computational design of solid-state interfaces using O-lattice theory: An application to mitigating helium-induced damage", *Applied Physics Letters*, vol. 105, no. 22, article 221601, 2014.
- [20] D. V. Yuryev and M. J. Demkowicz, "Modeling growth, coalescence, and stability of helium precipitates on patterned interfaces", *Modelling and Simulation in Materials Science and Engineering*, vol. 25, no. 1, article 015003, 2017.
- [21] A. Y. Dunn, M. G. McPhie, L. Capolungo, E. Martinez, and M. Cherkaoui, "A rate theory study of helium bubble formation and retention in Cu–Nb nanocomposites", *Journal of Nuclear Materials*, vol. 435, no. 1-3, pp. 141-152, 2013.
- [22] A. A. Sagüés and J. Auer, "Mechanical behavior of Nb-1% Zr implanted with He at various temperatures", *International Conference on Radiation Effects and Tritium Technology for Fusion Reactors*, CONF-750989, vol. 2, pp. 331-343, 1976.
- [23] J. A. Donovan, R. J. Burger, and R. J. Arsenault, "The effect of helium on the strength and microstructure of niobium", *Metallurgical Transactions A*, vol. 12, no. 11, 1917-1922, 1981.
- [24] N. Li, M. J. Demkowicz, and N. A. Mara, "Microstructure Evolution and Mechanical Response of Nanolaminate Composites Irradiated with Helium at Elevated

- Temperatures", *JOM: Journal of the Minerals, Metals and Materials Society*, vol. 69, no. 11, pp. 2206-2213, 2017.
- [25] T. Höchbauer, A. Misra, K. Hattar, and R. G. Hoagland, "Influence of interfaces on the storage of ion-implanted He in multilayered metallic composites", *Journal of Applied Physics*, vol. 98, no. 12, article 123516, 2005.
- [26] M. J. Demkowicz, Y. Q. Wang, R. G. Hoagland, and O. Anderoglu, "Mechanisms of He escape during implantation in CuNb multilayer composites", *Nuclear Instruments and Methods in Physics Research Section B: Beam Interactions with Materials and Atoms*, vol. 261, no. 1-2, pp. 524-528, 2007.
- [27] K. Hattar, M. J. Demkowicz, A. Misra, I. M. Robertson, and R. G. Hoagland, "Arrest of He bubble growth in Cu–Nb multilayer nanocomposites", *Scripta Materialia*, vol. 58, no. 7, 541-544, 2008.
- [28] D. Bhattacharyya, M. J. Demkowicz, Y. Q. Wang, R. E. Baumer, M. Nastasi, and A. Misra, "A transmission electron microscopy study of the effect of interfaces on bubble formation in He-implanted Cu-Nb multilayers", *Microscopy and Microanalysis*, vol. 18, no. 1, pp. 152-161, 2012.
- [29] M. J. Demkowicz, D. Bhattacharyya, I. Usov, Y. Q. Wang, M. Nastasi, and A. Misra, "The effect of excess atomic volume on He bubble formation at fcc–bcc interfaces", *Applied Physics Letters*, vol. 97, no. 16, article 161903, 2010.
- [30] M. J. Demkowicz, A. Misra, and A. Caro, "The role of interface structure in controlling high helium concentrations", *Current Opinion in Solid State and Materials Science*, vol. 16, no. 3, pp. 101-108, 2012.
- [31] A. Kashinath, P. Wang, J. Majewski, J. K. Baldwin, Y. Q. Wang, and M. J. Demkowicz, "Detection of helium bubble formation at fcc-bcc interfaces using neutron reflectometry", *Journal of Applied Physics*, vol. 114, no. 4, article 043505, 2013.
- [32] M. Zhernenkov, S. Gill, V. Stanic, E. DiMasi, K. Kisslinger, J. K. Baldwin, A. Misra, M. J. Demkowicz, and L. Ecker, "Design of radiation resistant metallic multilayers for advanced nuclear systems", *Applied Physics Letters*, vol. 104, no. 24, article 241906, 2014.
- [33] E. G. Fu, J. Carter, G. Swadener, A. Misra, L. Shao, H. Wang, and X. Zhang, "Size dependent enhancement of helium ion irradiation tolerance in sputtered Cu/V nanolaminates", *Journal of Nuclear Materials*, vol. 385, no. 3, pp. 629-632, 2009.

- [34] N. Li, M. Demkowicz, N. Mara, Y. Wang, and A. Misra, "Hardening due to interfacial He bubbles in nanolayered composites", *Materials Research Letters*, vol. 4, no. 2, pp. 75-82, 2016.
- [35] N. Li, M. Nastasi, and A. Misra, "Defect structures and hardening mechanisms in high dose helium ion implanted Cu and Cu/Nb multilayer thin films", *International Journal of Plasticity*, vol. 32, pp. 1-16, 2012.
- [36] W. Z. Han, N. A. Mara, Y. Q. Wang, A. Misra, and M. J. Demkowicz, "He implantation of bulk Cu–Nb nanocomposites fabricated by accumulated roll bonding", *Journal of Nuclear Materials*, vol. 452, no. 1-3, pp. 57-60, 2014.
- [37] A. Vattré, T. Jourdan, H. Ding, M. C. Marinica, and M. J. Demkowicz, "Non-random walk diffusion enhances the sink strength of semicoherent interfaces", *Nature communications*, vol. 7, article 10424, 2016.
- [38] S. Plimpton, "Fast parallel algorithms for short-range molecular dynamics", *Journal of Computational Physics*, vol. 117, no. 1, pp. 1-19, 1995.
- [39] A. Kashinath and Michael J. Demkowicz, "A predictive interatomic potential for He in Cu and Nb", *Modelling and Simulation in Materials Science and Engineering*, vol. 19, no. 3, article 035007, 2011.
- [40] M. J. Demkowicz and R. G. Hoagland, "Simulations of collision cascades in Cu–Nb layered composites using an EAM interatomic potential", *International Journal of Applied Mechanics*, vol. 1, no. 3, pp. 421-442, 2009.
- [41] J. J. Möller and E. Bitzek, "BDA: A novel method for identifying defects in body-centered cubic crystals", *MethodsX*, vol. 3, pp. 279-288, 2016.
- [42] A. Stukowski, "Visualization and analysis of atomistic simulation data with OVITO—the Open Visualization Tool", *Modelling and Simulation in Materials Science and Engineering*, vol. 18, no. 1, article 015012, 2010.
- [43] E. G. Fu, H. Wang, J. Carter, L. Shao, Y. Q. Wang, and X. Zhang, "Fluence-dependent radiation damage in helium (He) ion-irradiated Cu/V multilayers", *Philosophical Magazine*, vol. 93, no. 8, pp. 883-898, 2013.
- [44] W. G. Wolfer, "Dislocation loop punching in bubble arrays", *Philosophical Magazine A*, vol. 59, no. 1, pp. 87-103, 1989.
- [45] R. E. Stoller and G. R. Odette, "Analytical solutions for helium bubble and critical radius parameters using a hard sphere equation of state", *Journal of Nuclear Materials*, vol. 131, no. 2-3, pp. 118-125, 1985.

- [46] L. K. Mansur and W. A. Coghlan, "Mechanisms of helium interaction with radiation effects in metals and alloys: A review", *Journal of Nuclear Materials*, vol. 119, no. 1, pp. 1-25, 1983.
- [47] W. Jäger, R. Manzke, H. Trinkaus, R. Zeller, J. Fink, and G. Crecelius, "The density and pressure of helium in bubbles in metals", *Radiation Effects*, vol. 78, no. 1-4, pp. 315-325, 1983.
- [48] E. G. Fu, A. Misra, H. Wang, Lin Shao, and X. Zhang, "Interface enabled defects reduction in helium ion irradiated Cu/V nanolayers", *Journal of Nuclear Materials*, vol. 407, no. 3, pp. 178-188, 2010.

## Figures of Chapter 4

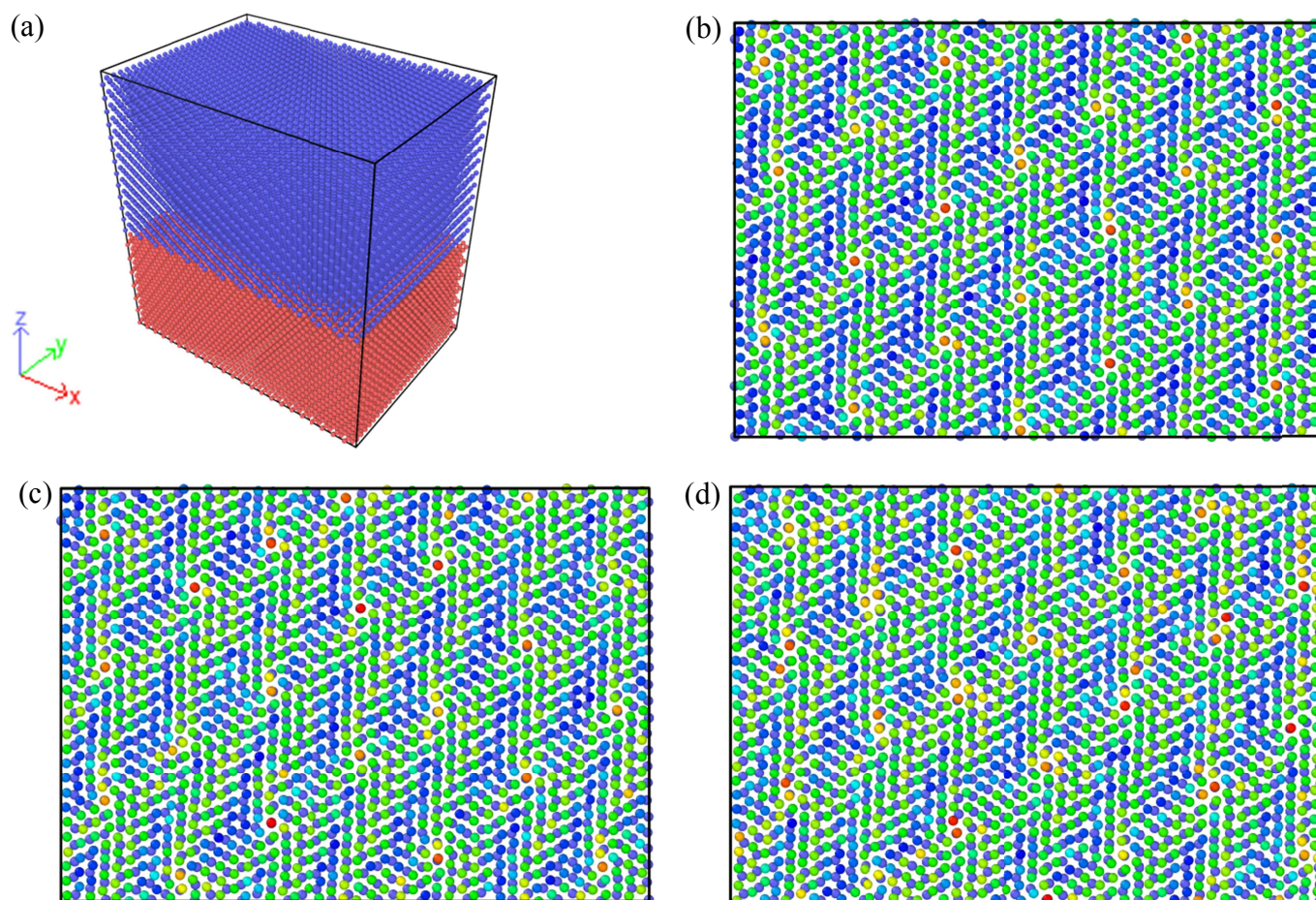


**Figure 1** (a) Perspective view of the periodic simulation cell containing Cu and Nb layers joined with the KS orientation relation (Cu and Nb atoms are colored in red and blue respectively). (b)-(d) Bottom views of the relaxed  $KS_1$  interface containing first interfacial Cu and Nb planes at 300, 500 and 700 K respectively (Nb atoms are colored in blue whereas Cu ones are colored according to their centro-symmetry parameter value). The MDIs coincide with the patches of undercoordination where a Cu atom, in red or orange color, is nearly on top of a Nb atom.

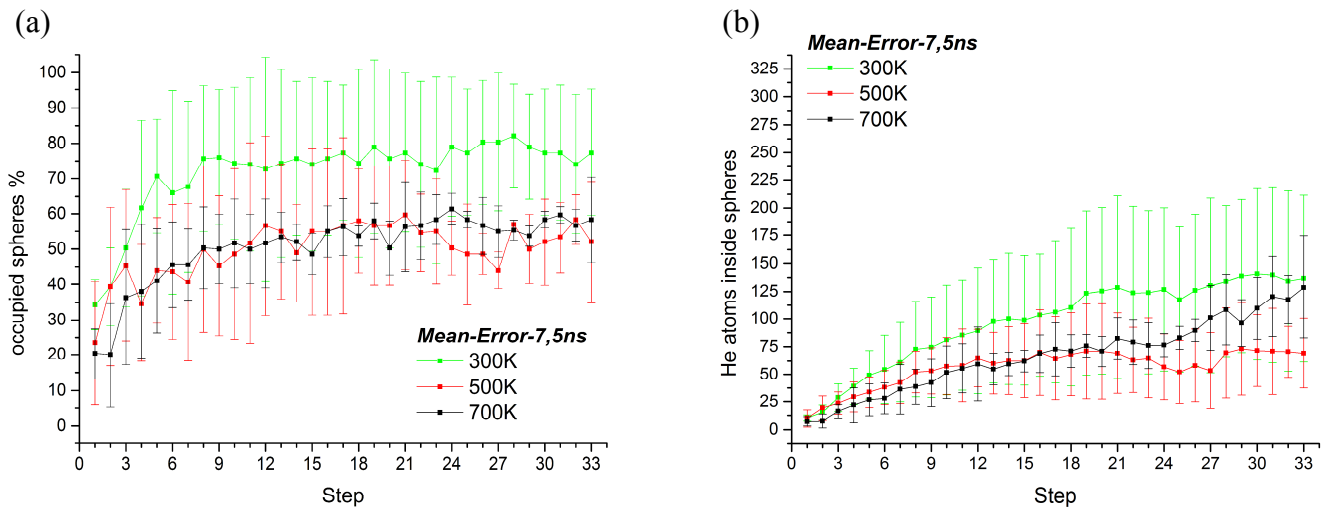


**Figure 2** (a) Percentage of occupied spheres by He atoms and (b) number of He atoms inside the spheres at the end of each step (7.5 ns) for a temperature of 300, 500 and 700 K (the spheres have a radius equal to 4 Å and are located in the central part of the MDIs).

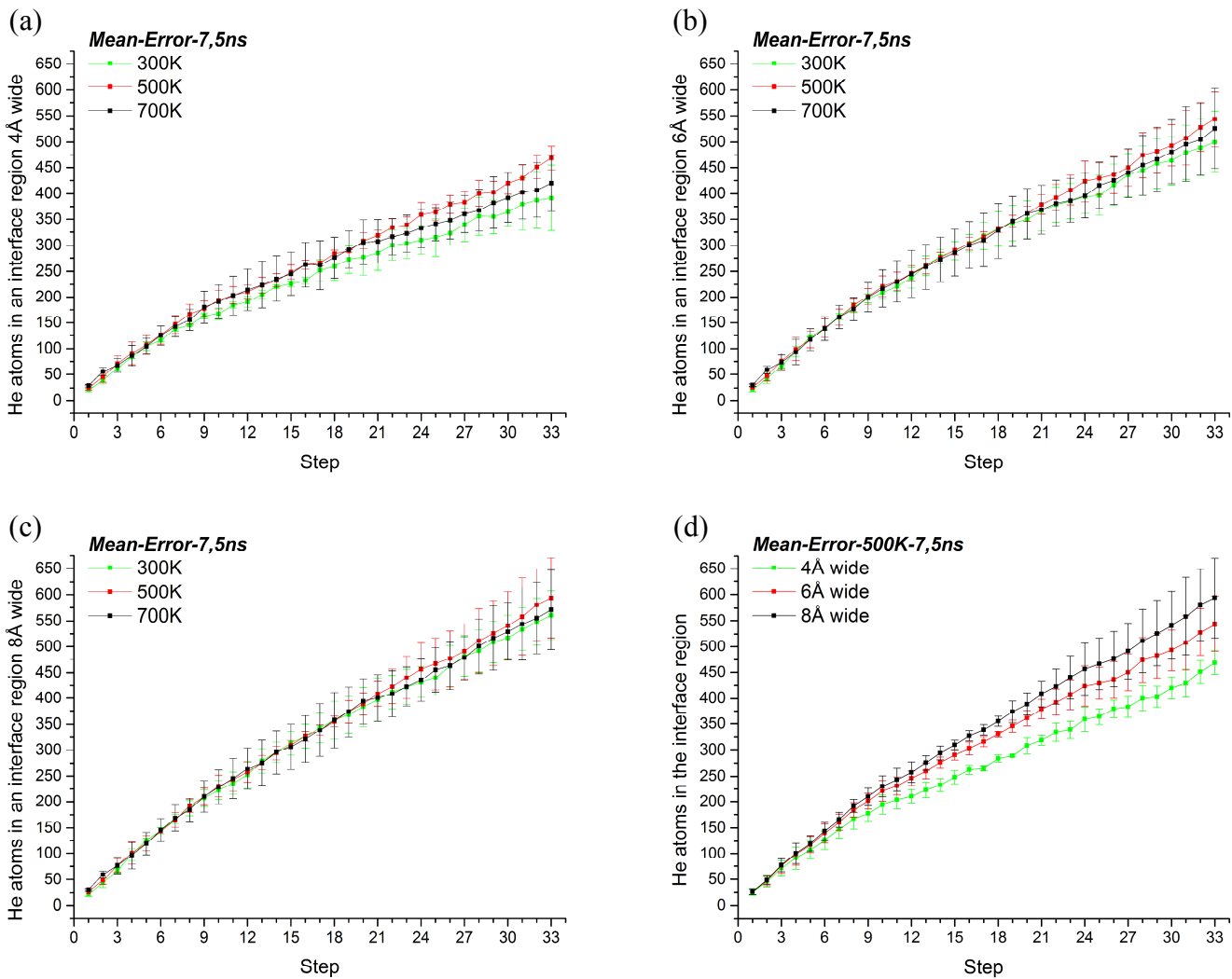


**Figure 3** Number of He atoms in an interface region (a) 4, (b) 6 and (c) 8 Å wide at the end of each step for a temperature of 300, 500 and 700 K. (d) Results in (a)-(c) are compared for 500 K. The comparison of the results for the other two temperatures is not shown here since the corresponding graphs are very similar to (d).

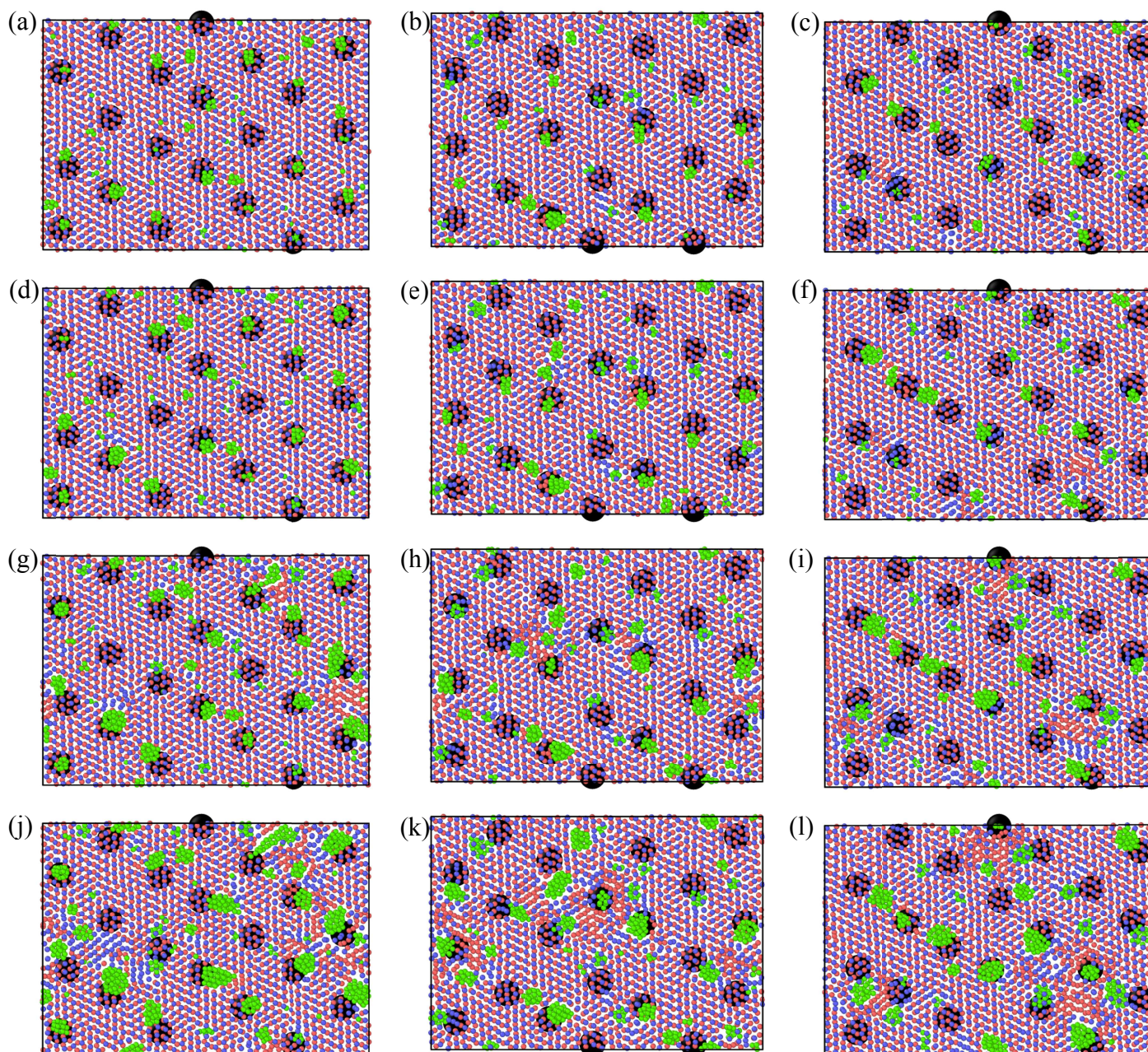


**Figure 4** Top views of He-atoms arrangement in an interface region 8 Å wide at the end of steps (a)-(c) 8, (d)-(f) 12, (g)-(i) 21 and (j)-(l) 33 for a temperature of 300, 500 and 700 K respectively (Cu, Nb and He atoms are colored in red, blue and green respectively). The area occupied by the spheres used in the analysis of Figure 2 is represented by black circles. To appreciate helium and the interface deterioration caused by it more clearly, only atoms of first interfacial Cu and Nb planes are depicted (interface region 4.5 Å wide) as long as they move less than a few tenths of an Å toward the interior of the corresponding layer.

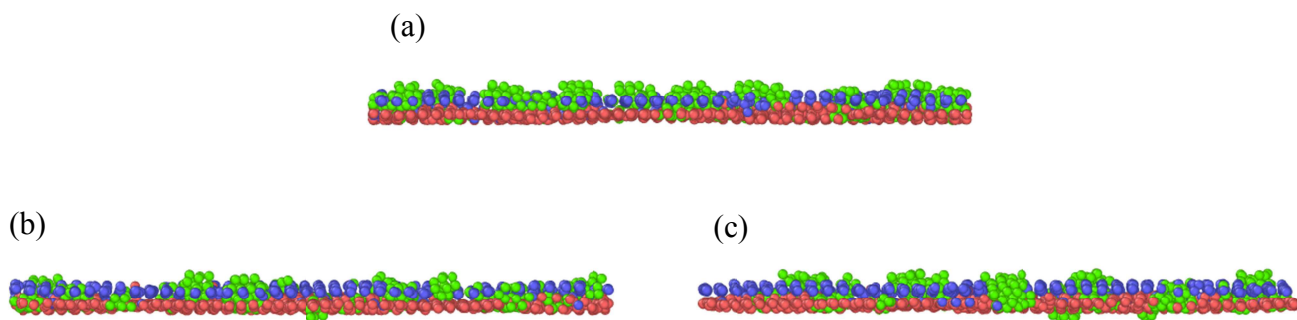


**Figure 5** Front views of He-atoms arrangement in an interface region 8 Å wide at the end of step 33 for a temperature of (a) 300, (b) 500 and (c) 700 K respectively (Cu, Nb and He atoms are colored in red, blue and green respectively). The images correspond to the same MD simulation sets of Figure 4 and contain the same Cu, Nb and He atoms.

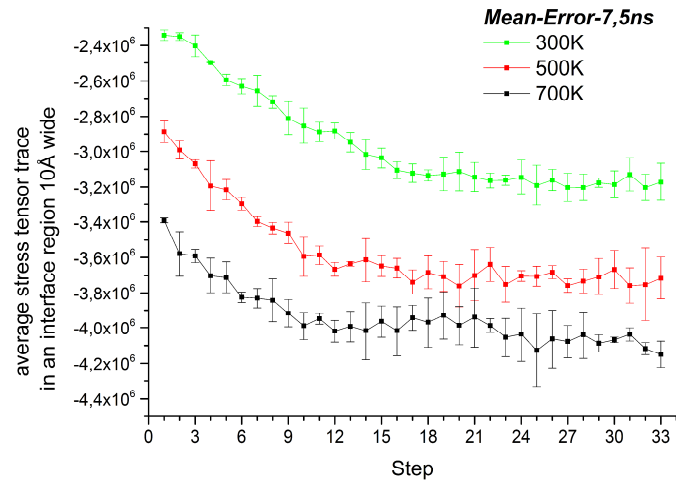


**Figure 6** Average stress tensor trace of all Cu and Nb atoms in an interface region 10 Å wide at the end of each step for a temperature of 300, 500 and 700 K.

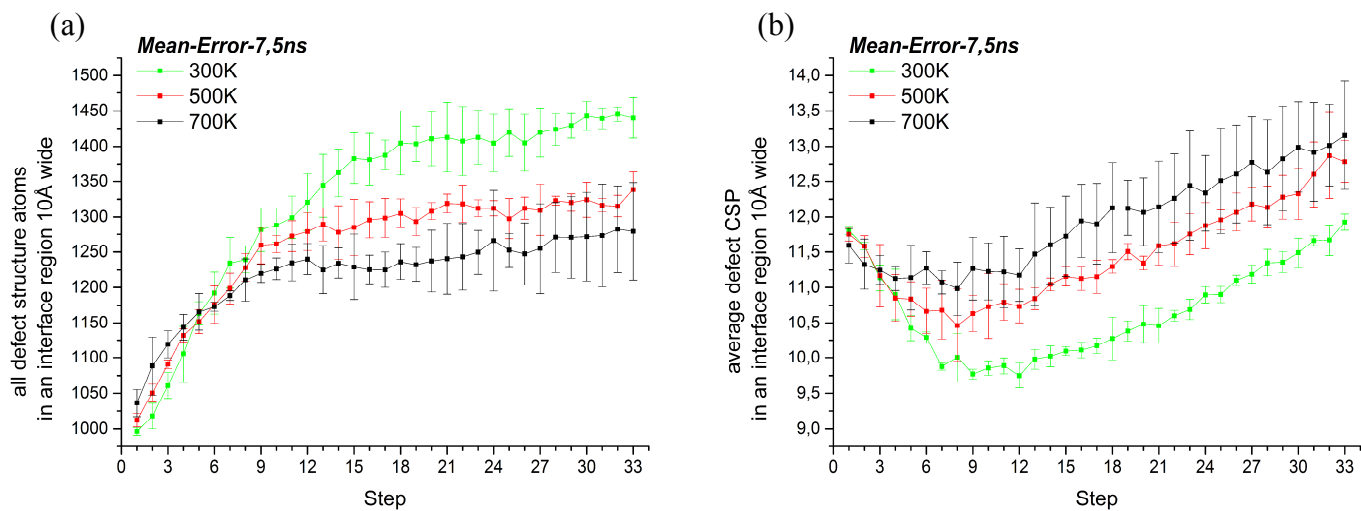


**Figure 7** (a) Number of Nb atoms belonging to any defect structure in an interface region 10 Å wide at the end of each step for a temperature of 300, 500 and 700 K and (b) average centro-symmetry parameter value of all of them. The BDA method identified all or most of these atoms as part of a surface structure.

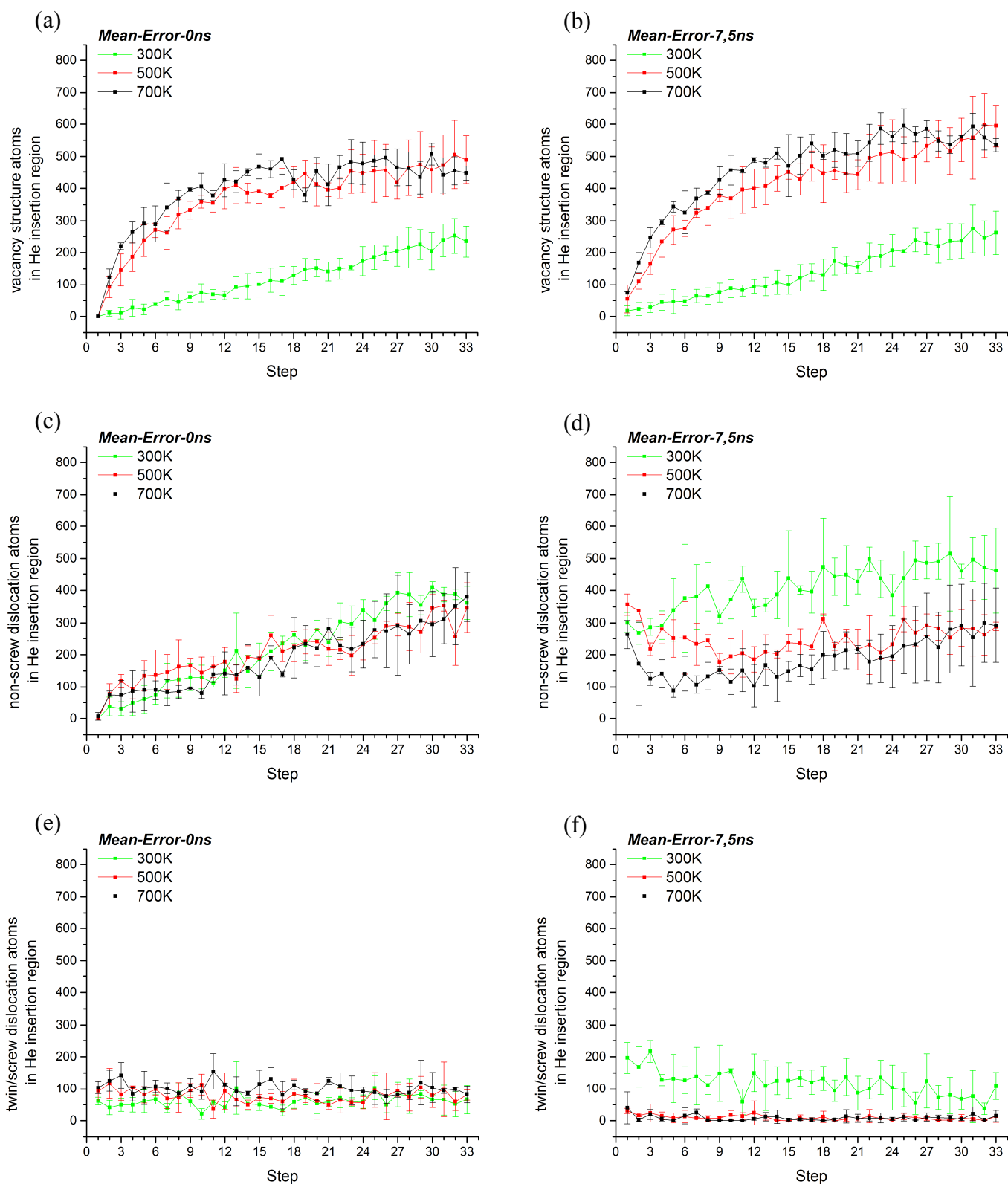


**Figure 8** Number of Nb atoms belonging to the most relevant defect structures in the He insertion region at the beginning and end of each step for a temperature of 300, 500 and 700 K: (a)-(b) vacancy, (c)-(d) non-screw dislocation and (e)-(f) twin/screw dislocation.

## Chapter 5

### Role of interface in multilayered composites under irradiation:

#### A mathematical investigation

##### 5.1. Introduction

Components of nuclear power systems will be exposed to aggressive environments of unprecedented magnitude consisting of irradiation, high temperatures and corrosive fluids [1,2]. Therefore, the performance of materials in these conditions must be significantly improved to extend reliability, lifetime, and efficiency of future nuclear reactors [3] such as fast fission reactors [4,5] and fusion reactors [6,7]. In fact, materials degradation during exposure to irradiation environments imposes substantial safety and economic impediments to the development of nuclear reactors [8]. This is true also for the core of the actual nuclear reactors generation, which presents exceptionally stringent requirements for structural materials due to the combination of high temperature, high stresses, a chemically aggressive coolant and intense radiation fluxes as well as its need for unfailing mechanical integrity [3,9].

Detrimental long-term evolution of materials under particle irradiation is largely due to the production of sustained net fluxes of point defects (i.e., vacancies and interstitials) [3,10]. The origin of these fluxes is the supersaturation of point defects produced by irradiation, which is only partially diminished by recombination. Moreover, both the production and elimination of freely migrating point defects are spatially biased so that vacancies and interstitials become separated [10]. In nuclear reactor environments, damage is also produced by helium from transmutation reactions during high-energy neutron irradiation [11,12]. In particular, helium is a byproduct of nuclear reactions that create  $\alpha$  particles (He nuclei) [13,14]. Due to extremely low solubility and fast diffusion in metals, He atoms can easily migrate and combine with radiation-induced vacancies to precipitate into clusters or bubbles [15]. Moreover, He-ion irradiation into metals will generate vacancies and nearby self-interstitial defects [16].

The damaging effects on the mechanical and thermal properties of materials by the formation of He bubbles and point-defect clusters (e.g., voids) have received considerable attention in structural materials working in high radiation environments [16,17]. Indeed, these non-equilibrium defects frequently lead to undesirable microstructural evolutions such as embrittlement, hardening, and dimensional as well as chemical instability of both structural

and fuel components [11,14]. Furthermore, swelling, solute redistribution, and creep are particularly troublesome in reactor materials subjected to neutron bombardment [18,19]. Eventually, surface deterioration phenomena such as spallation [20], swelling [2,21], blistering, which may cause wall erosion [15,22], flaking of metal surfaces [23], and corrosion [8] may be observed [14,21].

Extending performance, operating limit, reliability, efficiency and lifetime of present and future nuclear reactors thus requires the ability to remove radiation-induced point defects and to mitigate the effects of He implantation on irradiated-material properties [11,12]. Furthermore, candidate materials for nuclear applications must possess high strength, and thermal stability in addition to excellent irradiation tolerance. However, these properties are difficult to realize simultaneously in one material because of apparently intrinsic tradeoffs between them [24]. This challenge calls then for novel approaches to design materials or special structures that resist radiation damage while maintaining high strength and toughness [3,17].

In principle, a simple and direct approach to avoid the above deleterious microstructural changes can be realized if a high density of unbiased irradiation-induced point-defect sinks or traps can be introduced into the specimen [10]. This way, point defects are absorbed and annihilated by enhanced Frenkel-pair recombination [8,25] before they aggregate into clusters [17,26]. This approach includes controlling the volume fraction and size distribution of solutes, precipitates and interfaces with emphasis on optimizing both Frenkel-pair recombination rate and stability of the microstructure [10,19]. Indeed, surfaces, grain boundaries, and interphase boundaries are sinks for radiation-induced point defects and traps for implanted species such as helium [27,28].

Nanostructured materials have recently gained much attention for these purposes as they present high densities of interphase or grain boundaries as sinks [19,29]. Due to a large excess free volume of interface (and grain boundaries) and higher diffusivity of defects along interfaces [11], vacancies and interstitials are likely to be annihilated after being attracted to the interfaces. It also appears that reducing microstructural dimensions increases radiation resistance because it shortens the average diffusion distance of point defects to interfaces. Indeed, several types of nanocomposites have exhibited remarkable resistance to radiation and promise to offer high resistance to radiation damage accumulation [28,30], motivating research into potential uses of nanocomposite structural materials in future fission and fusion reactors [2].

One of the difficulties with this strategy has been maintaining the high densities of these traps/sinks during prolonged irradiation, particularly at very high temperatures, owing to processes such as radiation-induced (or enhanced) segregation, precipitation and grain growth. [31]. In fact, nanocrystalline materials have high strength and improved radiation resistance [32] because of their high density of grain boundaries, which are sinks for irradiation-induced defects [24]. Nevertheless, most nanocrystalline materials are not thermally stable and coarsen rapidly even at modest temperatures [24,33].

Efforts to engineer alloys tolerant to prolonged exposure to energetic particle irradiation have focused in recent years on multilayer films as a new concept of high densities of interfaces to provide sinks for point-defect annihilation and external species traps. Indeed, multiphase nanostructured materials such as nanolaminates could provide advanced radiation tolerance in comparison to traditional single-phase bulk materials [8,34].

Multilayer or nanolamellar composites have attracted much attention over the past decades due to their improved mechanical properties [35,36]. Nanolayered composites can also be designed to produce ultra-high strengths and enhanced radiation damage tolerance via tailoring of length scales to take advantage of the atomic structure and energetics of interfaces in order to provide the most effective sites for point-defect trapping and annihilation [3]. Indeed, the layered geometry with flat interfaces extending throughout the sample thickness may provide a benefit in this regard as compared to equiaxed-grain metals that may rapidly coarsen under irradiation at elevated temperatures [3]. Studies have shown that certain multilayer systems may significantly reduce radiation-induced damage in metallic materials [7,34]. Moreover, heterophase interfaces in multilayer systems have also been shown to be effective sinks for radiation-induced defects with respect to grain boundaries [34,37].

Therefore, multilayers with enhanced resistance to radiation can be potentially used in nuclear reactors as radiation protective coatings or fuel pin clad [37]. They may also provide additional parameters for materials design, beyond grain size and composition alone, which may be used to obtain properties that are not simultaneously achievable in a single material otherwise [34]. However, the advantages for radiation tolerance are not realized until the relevant length scale, such as the layer thickness, is reduced to the nanometer range. It appears then that the enhanced radiation damage tolerance in nanocomposites is a consequence of a short diffusion distance to the nearest sink. At the smallest sizes in the layered composites of a few nanometers, diffusion distances to sinks are short enough, due to the huge interface area in the material, to enable rapid removal of point defects before they can form into relatively stable aggregates [28]. Of course, the geometry of the nanolayered composite materials must

be stable under the extreme irradiation conditions [3]. Moreover, chemical and microstructural stability of interfaces are also necessary factors. On the other hand, energy deposited by incoming neutrons or ions may lead to extensive intermixing across interfaces, promoting morphological instabilities in these materials [28].

Several techniques such as density functional theory (DFT), molecular dynamics and phase field calculations were used to study the mechanisms underlying point-defect annihilation at interfaces of nanostructured metallic multilayer composites (NMMCs). This covered atomistic scale in enough detail. However, the overall mechanistic situation remained largely unknown. In this context, it is highly desirable to develop a continuum approach that describes long-term evolution of point defects in NMMCs subjected to irradiation.

In order to provide a contribution along this line, Fadda *et al.* [38] modeled the dynamic behavior of vacancies and interstitials at the continuum scale. They used nanostructured metallic monolayers of Cu and Nb as case study. A continuum spatial distribution of sinks either neutral or variable-biased was used to describe interfaces. This enables modeling grain boundaries and incoherent precipitates, i.e., non-coherent interfaces, as neutral sinks, and coherent precipitates, i.e., coherent interfaces, as variable-biased sinks [39]. Production, recombination, transport and annihilation of point defects at interfaces were defined by means of non-stationary balance equations. The effect of variation in layer thickness, temperature, production rate of point defects and surface recombination coefficient on annihilation processes at interfaces was studied. The present study focuses on modifying the model mentioned above to take into account surface characteristics deriving from coupling different metals. To this end, boundary equations have been modified according to  $\beta$ - $\alpha$ - $\beta$  NMMC scheme ( $\alpha = \text{Cu}$  and  $\beta = \text{Nb, Ni or V}$ ) and the temporal evolution of point-defect concentration investigated. Numerical investigations on similarities and differences between Cu/Nb, Cu/Ni, and Cu/V systems have been also performed.

## 5.2. Mathematical model

Let us consider the system depicted in **Figure 1a** where a layer of metal  $\alpha$  is in between two layers of metal  $\beta$  [40]. The evolution of point-defect, i.e., vacancy ( $v$ ) and self-interstitial atom (SIA) ( $i$ ) concentrations in layers  $\alpha$  and  $\beta$  is described by the following one-dimensional spatial reaction-diffusion equations:

$$\frac{\partial C_j^{(\gamma)}}{\partial t} - D_j^{(\gamma)} \frac{\partial^2 C_j^{(\gamma)}}{\partial x^2} = K_0^{(\gamma)} - R_C^{(\gamma)} \quad j = i, v; \quad \gamma = \alpha, \beta; \quad (1)$$

along with their initial conditions

$$t = 0; \forall x \quad C_j^{(\gamma)} = {}^*C_j^{(\gamma)} \quad j = i, v; \quad \gamma = \alpha, \beta. \quad (2)$$

Eqs. (1) represent the material balance of point defects in each layer, where  $C_j^{(\gamma)}$  is the concentration of the point defect of type  $j$  in layer  $\gamma$ ,  $D_j^{(\gamma)}$  is the diffusion coefficient of the point defect of type  $j$  in layer  $\gamma$ , while  $K_0^{(\gamma)}$  and  $R_C^{(\gamma)}$  are the production and the recombination rates of Frenkel pairs per unit volume in layer  $\gamma$ , respectively.  ${}^*C_j^{(\gamma)}$  is the concentration of the point defect of type  $j$  in layer  $\gamma$  at thermodynamic equilibrium, i.e., the concentration value at a given temperature in absence of radiation. The reader should refer to the Nomenclature section at the end of the chapter for the significance of other symbols.

Diffusion coefficients are expressed in terms of Arrhenius form for thermally activated events as follows [41]:

$$D_j^{(\gamma)} = (\alpha^{(\gamma)})^2 ({}^M v_j^{(\gamma)}) \exp\left(-\frac{{}^M E_j^{(\gamma)}}{k_B T}\right) \quad j = i, v; \quad \gamma = \alpha, \beta; \quad (3)$$

where

$${}^M v_j^{(\gamma)} = \alpha_j^{(\gamma)} v_D \exp\left(-\frac{{}^M S_j^{(\gamma)}}{k_B}\right) \quad j = i, v; \quad \gamma = \alpha, \beta. \quad (4)$$

In this study, the production rate of point defects is assumed time and spatial independent. It has been calculated using Transport of Ions in Matter (TRIM) [42], which is a Monte Carlo computer program that calculates the damage associated with the ion's energy loss in a material by means of efficient statistical algorithms. The recombination rate of point defects is expressed as a second order reaction [39]:

$$R_C^{(\gamma)} = K_{iv}^{(\gamma)} (C_i^{(\gamma)} - {}^*C_i^{(\gamma)})(C_v^{(\gamma)} - {}^*C_v^{(\gamma)}) \quad \gamma = \alpha, \beta; \quad (5)$$

where the kinetic constant is given by:

$$K_{iv}^{(\gamma)} = \frac{\alpha_{iv}^{(\gamma)} \Omega^{(\gamma)}}{(a^{(\gamma)})^2} (D_i^{(\gamma)} + D_v^{(\gamma)}) \quad \gamma = \alpha, \beta. \quad (6)$$

The concentrations at thermodynamic equilibrium depend on temperature according to the following equations [39]:

$${}^*C_j^{(\gamma)} = \frac{1}{\Omega^{(\gamma)}} \exp\left(\frac{F S_j^{(\gamma)}}{k_B}\right) \exp\left(-\frac{F E_j^{(\gamma)}}{k_B T}\right) \quad j = i, v; \quad \gamma = \alpha, \beta. \quad (7)$$

Boundary conditions for Eqs. (1) (see **Figure 1**) should take into account the characteristics of the interfaces composing the system. Specifically, interfaces between metals  $\alpha$  and  $\beta$  are modelled as variable-biased sinks considering a surface concentration of traps for interstitials,  ${}^{tot}S_i^{(\alpha-\beta)}$ , and a surface concentration of traps for vacancies,  ${}^{tot}S_v^{(\alpha-\beta)}$ . It is worth highlighting that these parameters values depend upon the metal couple  $\alpha$ - $\beta$  under investigation. The occupation probability of traps for each point-defect type is taken to be  $f_i$  and  $f_v$ , respectively. An interstitial atom adjacent to the interface is assumed to be able to enter an unoccupied interstitial trap site or to recombine with the nearest neighbor trapped vacancy, jumping there from  $z$  possible adjacent sites in the matrix. In this study,  $z$  is set equal to 4 for any material structure [43]. Similar processes are possible for vacancies. Moreover, trapped interstitials and vacancies may recombine on the interface. Accordingly to this picture, boundary conditions at the interface between metals  $\alpha$  and  $\beta$  may be expressed as [43]:

$$x = \frac{L}{2}; \quad \forall t \quad D_j^{(\gamma)} \frac{\partial C_j^{(\gamma)}}{\partial x} = (1 - f_j + z f_k) K_j^{(\gamma)} (C_j^{(\gamma)} - {}^*C_j^{(\gamma)}) \quad (8)$$

$$j = i, v; \quad k \neq j = i, v; \quad \gamma = \alpha, \beta;$$

where  $L$  is the thickness of layer  $\gamma$ . Boundary conditions (8) state that SIAs can reach the interface only if, in addition to a concentration gradient, there are unoccupied SIA traps

$(1 - f_i > 0)$  or trapped vacancies to annihilate with  $(f_v > 0)$ . Analogous considerations can be made for vacancies. Under the assumption that the lattice is not severely distorted over the final jump region, the transfer velocities are equal to

$$K_j^{(\gamma)} = \frac{D_j^{(\gamma)}}{b^{(\gamma)}} \quad j = i, v; \quad \gamma = \alpha, \beta; \quad (9)$$

where  $b^{(\gamma)}$  is the lattice spacing.

Trap occupation probabilities are obtained by solving the following balance equations:

$$\begin{aligned} \frac{df_j}{dt} = & (1 - f_j) \frac{K_j^{(\alpha)}}{{}_{tot}S_j^{(\alpha-\beta)}} (C_j^{(\alpha)} - {}^*C_j^{(\alpha)}) + (1 - f_j) \frac{K_j^{(\beta)}}{{}_{tot}S_j^{(\alpha-\beta)}} (C_j^{(\beta)} - {}^*C_j^{(\beta)}) \\ & - z f_j \frac{K_k^{(\alpha)}}{{}_{tot}S_j^{(\alpha-\beta)}} (C_k^{(\alpha)} - {}^*C_k^{(\alpha)}) - z f_j \frac{K_k^{(\beta)}}{{}_{tot}S_j^{(\alpha-\beta)}} (C_k^{(\beta)} - {}^*C_k^{(\beta)}) - \frac{\alpha_s}{{}_{tot}S_j^{(\alpha-\beta)}} f_j f_k \end{aligned} \quad (10)$$

$$j = i, v; \quad k \neq j = i, v;$$

along with their initial conditions

$$t = 0, \quad f_j = 0 \quad j = i, v. \quad (11)$$

Temporal evolution of trap occupation probability by point defects of type  $j$  depends upon fluxes to the interface arriving from both metal layers,  $\alpha$  and  $\beta$ , and the recombination mechanisms occurring at the interface. Specifically, first and second terms on the right-hand side of Eqs. (10) represent the flux of point defects of type  $j$  arriving from layer  $\alpha$  and  $\beta$ , respectively, to occupy available traps at the interface. Moreover, third and fourth terms are the flux of point defects of type  $k$  coming from layer  $\alpha$  and  $\beta$ , respectively, to recombine with trapped point defects of the type  $j$ . Last term quantifies the recombination of trapped SIAs with trapped vacancies. The positive or negative sign preceding the terms indicates if the associate mechanism causes an increase or a decrease of trap occupation probability. It should be noted that Eqs. (10) allow introducing interface structure features by means of trap concentration for point defects,  ${}_{tot}S_j^{(\alpha-\beta)}$ , and the surface recombination coefficient,  $\alpha_s$ . However, it was demonstrated in a previous study [38] that point-defect annihilation at the

interfaces is a diffusion-limited process and that point-defect evolution is not affected by the  $\alpha_s$  value. Hence,  $\alpha_s$  has been set equal to zero in this study, which means that there is no surface recombination between trapped point defects.

By referring to **Figure 1b**, boundary conditions set can be completed by the following ones:

$$x = 0; \quad \forall t \quad \frac{\partial C_j^{(\alpha)}}{\partial x} = 0 \quad j = i, v; \quad (12)$$

$$x = \frac{3L}{2}; \quad \forall t \quad \frac{\partial C_j^{(\beta)}}{\partial x} = 0 \quad j = i, v. \quad (13)$$

Boundary conditions (12) express the symmetry of the system, while Eqs. (13) state that the right end of layer  $\beta$  is treated as a free surface.

The model is given by the balance Eqs. (1) along with their initial conditions, Eqs. (2), and their boundary conditions, i.e., Eqs. (8) in the case of the interface between metals  $\alpha$  and  $\beta$  modelled as variable-biased sinks, Eqs. (12) in the case of the symmetric surface of the entire system, or Eqs. (13) in the case of the free surface. It allows to describe the spatial-temporal evolution of point-defect concentrations inside layers  $\alpha$  and  $\beta$  undergoing radiation.

It is worth mentioning that in this study it was assumed that point defects produced inside a layer cannot be transferred to the adjacent ones. Indeed, point defects generated within each layer may be annihilated by recombination inside the layer or they can migrate to the interface. There, each point defect is trapped or annihilated by surface recombination. With the aim to explain why point defects cannot cross the interface let us consider, as an example, a vacancy diffusing from inside the layer toward the interface. At this point, the vacancy can be trapped if unoccupied vacancy traps are available ( $f_v < 1$ ), or can react with a trapped interstitial if present ( $f_i > 0$ ). Even in the worst case scenario, i.e., no availability of both unoccupied vacancy traps and trapped interstitials at the interface, a vacancy cannot cross the interface since under these conditions its flux decreases to zero (cf. Eq. (8)). It should be also considered that the point-defect concentration at the interface is always lower than the one inside the layer [38]. This means that if a point defect, coming for instance from layer  $\alpha$ , would cross the interface, the same defect should then diffuse counter-gradient (i.e., from low concentration regions to high concentration ones) inside the layer  $\beta$ . Latter event is

not physically possible and then, crossing the interface by point defects is not allowed. On the other hand, metal layers influence each other through the evolution of the point-defect trap occupation probability fractions. Indeed, it can be seen (cf. Eq.(10)) that these variables behavior is affected by point-defect fluxes coming from both layers.

A change of variables was used in this study in order to obtain dimensionless and normalized equations and parameters by following the same procedure reported in **Ref. (38)**. Dimensionless variables and parameters, as well as scaling and reference values are summarized in **Table 1**. It may be worth noting that  ${}^s t$  can be also regarded as the characteristic time of interstitial diffusion along layer  $\alpha$ , while the dimensionless diffusion coefficient  $\delta_j^{(\gamma)}$  is defined with respect to the diffusion coefficient of SIAs in layer  $\alpha$ . According to this change of variables, the evolution of dimensionless point-defect concentrations in layer  $\gamma$  as a function of the dimensionless time is described by the following equations:

$$\frac{\partial \chi_j^{(\gamma)}}{\partial \tau} - \delta_j^{(\gamma)} \frac{\partial^2 \chi_j^{(\gamma)}}{\partial \xi^2} = A^{(\gamma)} (1 - \chi_i^{(\gamma)} \chi_v^{(\gamma)}) \quad j = i, v; \quad \gamma = \alpha, \beta; \quad (14)$$

along with the initial conditions

$$\tau = 0; \quad \forall \xi \quad \chi_j^{(\gamma)} = 0 \quad j = i, v; \quad \gamma = \alpha, \beta. \quad (15)$$

At the interface between metals  $\alpha$  and  $\beta$  modelled as variable biased sinks, dimensionless boundary conditions may be expressed as:

$$\xi = \frac{1}{3}; \quad \forall \tau \quad \delta_j^{(\gamma)} \frac{\partial \chi_j^{(\gamma)}}{\partial \xi} = \frac{3}{2} (1 - f_j + z f_k) \frac{\delta_j^{(\gamma)}}{\varpi^{(\gamma)}} \chi_j^{(\gamma)} \quad j = i, v; \quad k \neq j = i, v; \quad \gamma = \alpha, \beta. \quad (16)$$

The dimensionless balance equations of trap occupation probabilities appear as follows:

$$\begin{aligned}
\frac{df_j}{d\tau} = E_j^{(\alpha)} & \left[ (1-f_j) \frac{\delta_j^{(\alpha)}}{\overline{\omega}^{(\alpha)}} \chi_j^{(\alpha)} - z f_j \frac{\delta_k^{(\alpha)}}{\overline{\omega}^{(\alpha)}} \chi_k^{(\alpha)} \right] \\
& + E_j^{(\beta)} \left[ (1-f_j) \frac{\delta_j^{(\beta)}}{\overline{\omega}^{(\beta)}} \chi_j^{(\beta)} - z f_j \frac{\delta_k^{(\beta)}}{\overline{\omega}^{(\beta)}} \chi_k^{(\beta)} \right] \\
& - F_j f_j f_k
\end{aligned} \quad j = i, v; \quad k \neq j = i, v; \quad (17)$$

along with their initial conditions

$$\tau = 0, \quad f_j = 0 \quad j = i, v. \quad (18)$$

Dimensionless boundary conditions for the symmetric surface of the entire system may be expressed as:

$$\xi = 0; \quad \forall \tau \quad \frac{\partial \chi_j^{(\alpha)}}{\partial \xi} = 0 \quad j = i, v; \quad (19)$$

while dimensionless boundary conditions representing the free surface on layer  $\beta$  as:

$$\xi = 1; \quad \forall \tau \quad \frac{\partial \chi_j^{(\beta)}}{\partial \xi} = 0 \quad j = i, v. \quad (20)$$

With the aim of illustrating and discussing model results, additional auxiliary quantities needed to be introduced. Specifically, let us define the average point-defect concentration in layer  $\alpha$  and in layer  $\beta$  as

$$\overline{\chi}_j^{(\alpha)} = 3 \int_0^{1/3} \chi_j^{(\alpha)}(\xi) d\xi \quad j = i, v; \quad (21)$$

and

$$\overline{\chi}_j^{(\beta)} = \frac{3}{2} \int_{1/3}^1 \chi_j^{(\beta)}(\xi) d\xi \quad j = i, v; \quad (22)$$

respectively. The average dimensionless point-defect net-production rates are also introduced:

$$\bar{\Pi}^{(\alpha)} = 3 \int_0^{1/3} A^{(\alpha)} (1 - \chi_i^{(\alpha)} \chi_v^{(\alpha)}) d\xi; \quad (23)$$

and

$$\bar{\Pi}^{(\beta)} = \frac{3}{2} \int_{1/3}^1 A^{(\beta)} (1 - \chi_i^{(\beta)} \chi_v^{(\beta)}) d\xi. \quad (24)$$

The dimensionless point-defect fluxes are expressed as

$$J_j^{(\gamma)} = \delta_j^{(\gamma)} \frac{\partial \chi_j^{(\gamma)}}{\partial \xi} \quad j = i, v; \quad \gamma = \alpha, \beta. \quad (25)$$

Model equations are solved by using the commercial software COMSOL Multiphysics 3.4, along with the parameters reported in **Tables 2-5**.

### 5.3. Results

In what follows, copper is represented by metal  $\alpha$  while metal  $\beta$  is nickel, niobium, or vanadium. Results are shown in a double-log plot (**Figures 2-9**) and they are obtained by solving the dimensionless version of the model illustrated in the previous section. All the results belong to the half-symmetric part of the layered system depicted in **Figure 1**.

Temporal profiles of average point-defect concentrations in layers  $\alpha$  (Cu) and  $\beta$  (V, Ni, Nb) are shown in **Figures 2** and **3**, respectively. Total irradiation time is around 90.5 s [19], which corresponds to a dimensionless time ( $\tau$ ) of  $5 \cdot 10^9$ . It can be seen in **Figure 2a** that  $\bar{\chi}_i^{(\alpha)}$  constantly increases from the equilibrium concentration until  $\tau \approx 0.2$ . Then, average concentration of SIAs in layer  $\alpha$  remains constant up to  $\tau \approx 10^6$ . This behavior can be observed for all the systems investigated. However, there is a different evolution in Cu/Ni system for later times. Indeed, in this case,  $\bar{\chi}_i^{(\alpha)}$  abruptly increases to reach a higher stationary SIA average concentration with respect to Cu/V and Cu/Nb systems. **Figure 2b** shows the

temporal evolution of the vacancy average concentration in layer  $\alpha$ ,  $\bar{\chi}_v^{(\alpha)}$ . Significant differences can be observed with respect to the behavior of  $\bar{\chi}_i^{(\alpha)}$ . First, it can be seen that the  $\bar{\chi}_v^{(\alpha)}$  stationary state is reached at later times ( $\tau \approx 10^4$ ) and, secondly, the stationary value of  $\bar{\chi}_v^{(\alpha)}$  is higher compared to the steady-state  $\bar{\chi}_i^{(\alpha)}$  value. The overall evolution of  $\bar{\chi}_v^{(\alpha)}$  appears quite similar for all the systems investigated, even if the Cu/Ni system shows a slightly lower stationary value of the vacancy average concentration.

The corresponding temporal profiles of SIA and vacancy average concentrations in layer  $\beta$  are shown in **Figures 3a** and **3b**, respectively. It can be seen that  $\bar{\chi}_i^{(\beta)}$  reaches a stationary value at approximately the same time in Cu/V and Cu/Nb systems, while a little longer is needed for the Cu/Ni one. However,  $\bar{\chi}_i^{(\beta)}$  maintains this value in V layer during the whole irradiation exposure, while it can be observed an increase and a decrease in Ni and Nb layers, respectively, at longer times. Then, a new stationary state is reached in these two layers. **Figure 3b** reveals that the average concentration of vacancies in layer  $\beta$ ,  $\bar{\chi}_v^{(\beta)}$  at steady state is higher in Nb and Ni layers than in V one. It can be also observed that stationary state is reached earlier in the Cu/V system with respect to Cu/Ni and Cu/Nb ones.

In order to explain differences and similarities in the temporal evolution of point-defect average concentrations shown so far, it can be useful to investigate the time variation of all relevant phenomena concurring to produce, annihilate, and transport point defects inside the systems. Point-defect production rate is temporal- and spatially-constant (cf. Eq. (1)) but it depends upon the metal layers are made of. Specifically, the dimensionless point-defect production rate has the following values,  $0.40 \cdot 10^{-3}$ ,  $2.88 \cdot 10^{-3}$ ,  $0.73 \cdot 10^{-3}$  and  $2.18 \cdot 10^{-3}$  for Cu, Nb, Ni, and V, respectively. On the other hand, point-defect recombination rate depends upon their concentration. This means that the net-production rate of point defects is time and spatial dependent. The combined effects of these two phenomena are shown in **Figures 4a** and **4b**, where the temporal profiles of the average point-defect net-production rate in layer  $\alpha$ ,  $\bar{\Pi}^{(\alpha)}$  and layer  $\beta$ ,  $\bar{\Pi}^{(\beta)}$  are reported, respectively. It can be clearly seen in **Figure 4a** that  $\bar{\Pi}^{(\alpha)}$  does not significantly vary up to  $\tau \approx 10^6$ , for all the systems investigated. Then, a decrease down to a new stationary state is observed in the Cu/Ni systems. On the other hand, average point-defect net-production rate in layer  $\alpha$  does not show any significant variation in the Cu/V and Cu/Nb systems all along the irradiation period. A different time evolution of average point-defect net-production rate may be observed in layer  $\beta$ . Indeed, **Figure 4b** shows that  $\bar{\Pi}^{(\beta)}$

remains constant for all the systems studied only until  $\tau \approx 10^4$ . Then, it keeps its initial stationary value in V layer while a significant decrease occurs in Ni and Nb layers.

Besides recombination in the bulk, there is another mechanism affecting point-defect annihilation, which is point-defect flux to the interface between the two metals. Temporal profiles of point-defect fluxes from layer  $\alpha$  and layer  $\beta$  to the interface between the two metals are depicted in **Figures 5** and **6**, respectively. SIAs diffuse much faster than vacancies (cf. **Figures 5a** and **5b**), then SIA flux reaches its maximum earlier than vacancy one. It should be also noted that SIA and vacancy fluxes from layer  $\alpha$  to the interface have the same value for all systems once the steady state is reached. Moreover, it can be seen that only point-defect fluxes from layer  $\alpha$  in Cu/Ni system present differences, even though small, with respect to the other systems investigated. On the other hand, **Figure 6** shows that point-defect fluxes from layer  $\beta$  strongly depend upon the system investigated. SIA flux from layer  $\beta$  to the interface (cf. **Figure 6a**),  $J_i^{(\beta)}$ , is much lower in the Cu/Ni system. It can be also observed in this system an abrupt decrease of  $J_i^{(\beta)}$  at  $\tau \approx 10^6$ . Temporal profiles of  $J_i^{(\beta)}$  in the other two systems are quite similar, even if a slight decrease can be seen in the Cu/Nb system at longer dimensionless times. Concerning  $J_v^{(\beta)}$ , it can be seen (cf. **Figure 6b**) that Cu/Ni system presents the lowest values also in this case, but there is a slight decrease instead of an abrupt one. Vice versa, the highest vacancy flux occurs in Cu/V system at any dimensionless time, even if its steady-state value is closer to the one pertaining the Cu/Nb system. In addition,  $J_v^{(\beta)}$  does not show a decrease in Cu/Nb system as in the case of  $J_i^{(\beta)}$ .

It should be pointed out that point-defect production and bulk recombination phenomena are only dependent on the properties of the layer where they are taking place. On the other hand, point-defect flux to the interface depends upon the properties of the two adjacent layers (recall boundary condition (16)). Therefore, we should study in detail what point-defect flux to the interface depends on. Besides point-defect diffusion coefficient and lattice spacing, which do not generate differences in layer  $\alpha$  since it is the same metal (Cu) for all the systems, flux relies on point-defect concentration at the interface and trap occupation probabilities. Time evolution of point-defect concentrations at the interface located at  $\xi=1/3$  for both layers  $\alpha$  and  $\beta$  are shown in **Figures 7** and **8**, respectively. It can be seen that time evolution of SIA (cf. **Figure 7a**) and vacancy (**Figure 7b**) interface concentration in the copper layer is approximately the same for all systems investigated up to  $\tau$  equal about  $10^4$ . Then, we can observe an abrupt increase of the SIA concentration in the Cu/Ni system and a slight decrease of vacancy concentration for the same system. Similar behavior can be seen in

**Figure 8a**, where the concentration of SIAs at the interface in layer  $\beta$  is reported. A different evolution can be observed in **Figure 8b**, where it clearly appears that the lower steady-state concentration of vacancies occurs for the Cu/V system.

Lastly, temporal profiles of trap occupation probabilities by point defects are shown in **Figure 9**. Trap occupation probability by SIAs (**Figure 9a**) increases and then it reaches a stationary state for all the systems investigated. It can be also seen that the stationary value is higher in the Cu/Ni system and lower for the cases of Cu/Nb and Cu/V, which behave similarly, even if steady state is reached by Cu/V system sooner than by Cu/Nb one. A different behavior is shown by vacancy trap occupation probability (cf. **Figure 9b**). It can be observed a similar behavior of Cu/V and Cu/Nb systems. Instead,  $f_v$  in Cu/Ni system reaches a maximum followed by a decrease down to a stationary state. It should be noted that  $f_i$  and  $f_v$  have similar values at steady state in Cu/Nb and Cu/V systems, being their temporal evolution very different than Cu/Ni coupled layers.

#### 5.4. Discussion

Before starting to discuss the results shown in the previous section, it is worth recalling that thin layered systems are designed with the aim to increase interfaces density. This way, surface available for point-defect annihilation increases and their concentration within the system consequently decreases. Indeed, the technological goal is to maintain the concentration of SIAs and vacancies as low as possible, in order to limit clustering and then material damage induced by irradiation. Therefore, discussion of numerical simulation results should begin by commenting and comparing point-defect concentration within the systems investigated. It is also worth highlighting the behavior of the same metal Cu (layer  $\alpha$ ), when surrounded by diverse metals  $\beta$ .

Temporal profiles of average SIA and vacancy concentrations in layer  $\alpha$  and layer  $\beta$  are shown in **Figures 2** and **3**, respectively. A general comparison reveals that vacancy average concentration is typically higher than SIA one in both layers for all the systems investigated. This is a consequence of the higher diffusion rate of SIAs with respect to vacancies. Moreover, stationary state is reached by all systems investigated. It can be also seen that Cu/Nb and Cu/V systems have a very similar behavior regarding point-defect temporal evolution in layer  $\alpha$  (cf. **Figure 2**), while different profiles are shown at longer times by the Cu/Ni system. Specifically, latter system reaches a higher  $\bar{\chi}_i^{(\alpha)}$  with respect to the other systems investigated, along with a lower steady-state vacancy average concentration. It is

worth analyzing the mechanisms giving rise to the different behaviors underlined above.

First result, i.e., higher  $\bar{\chi}_i^{(\alpha)}$  should be due to higher net-production rate of SIAs and/or lower SIA flux to the  $\alpha$ - $\beta$  metals interface. Inset in **Figure 5a** confirms this explanation with respect to  $J_i^{(\alpha)}$ . On the other hand, lower value of  $\bar{\Pi}^{(\alpha)}$  at longer time of Cu/Ni system (cf. **Figure 4a**) may be explained as an effect of the higher recombination rate generated by the higher value of  $\bar{\chi}_i^{(\alpha)}$  (see Eq. (23)). It is now worth enlightening the lower SIA flux shown by the Cu/Ni system. Examination of Eq. (16) reveals that  $J_i^{(\alpha)}$  depends on a proportionality constant, SIA concentration at the interface, which shows a higher value accordingly to  $\bar{\chi}_i^{(\alpha)}$  (see **Figure 7a**), and trap occupation probabilities. Specifically,  $J_i^{(\alpha)}$  decreases as  $f_i$  increases. **Figure 9a** indeed shows that  $f_i$  reaches its maximum value, i.e.,  $f_i = 1$ , only in the case of Cu/Ni system. This finding may then explain the lower value of  $J_i^{(\alpha)}$  for this system and its peculiar behavior shown in **Figure 2a**. Saturation of SIA traps at Cu/Ni interface can also clarify the lower steady-state vacancy concentration  $\bar{\chi}_v^{(\alpha)}$  shown by the same system (cf. **Figure 2b**). In fact, as explained above, the higher value of  $\bar{\chi}_i^{(\alpha)}$  decreases the point-defect net-production rate, which, in turn, decreases  $\bar{\chi}_v^{(\alpha)}$ . The lower level of this variable may also explain the lower value of  $J_v^{(\alpha)}$  (cf. **Figure 5b**) through the lower value of vacancy concentration at the interface (cf. **Figure 7b**). Finally, the decrease of  $f_v$  shown in **Figure 9b** may be also elucidated as an effect of the reduced vacancy flux to the interface. Mechanisms illustrated above are also responsible of point-defect average concentration in nickel layer (cf. **Figure 3**).

It was stated that Cu/Nb and Cu/V systems show a very similar behavior, being the only significant difference the vacancy average concentration in vanadium layer (metal  $\beta$ ). Specifically, Cu/V system presents a lower steady-state value of  $\bar{\chi}_v^{(\beta)}$ , which cannot be explained because of vacancy net-production rate. Indeed, **Figure 4b** reveals that  $\bar{\Pi}^{(\beta)}$  of the Cu/V system is similar to Cu/Nb and higher than Cu/Ni even if latter ones both show a higher stationary value of  $\bar{\chi}_v^{(\beta)}$ . On the other hand, **Figure 6b** shows a constantly higher vacancy flux from layer  $\beta$  to the interface between metals  $\alpha$  and  $\beta$  in the case of Cu/V system. This finding may instead explain the lower stationary average vacancy concentration characterizing V layer.

To conclude, differences in the irradiation behavior shown by the systems investigated may be explained on the basis of both surface characteristics and bulk layer properties.

Specifically, the peculiar behavior of the Cu/Ni system is due to the lower value of the parameter  $^{tot}S_i^{(Cu-Ni)}$  (see **Tables 2-5**), which induces a faster saturation of SIA traps occupation probability. Instead, higher diffusivity of vacancy in vanadium layer causes the lower stationary value of  $\bar{\chi}_v^{(\beta)}$  in Cu/V system.

## 5.5. Conclusions

In the present study, a continuum model of point-defect evolution in multilayer composites was developed. Numerical investigation on similarities and differences between Cu/Nb, Cu/V, and Cu/Ni systems were also performed. A general comparison of model results reveals that average vacancy concentration is typically higher than SIA one in both layers for all the system investigated. This is a consequence of the higher diffusion rate of SIAs with respect to vacancies. Stationary state is reached without saturating interface point-defect traps by all systems but Cu/Ni for the case of SIAs. It can be also seen that Cu/Nb and Cu/V systems have a very similar behavior regarding point-defect temporal evolution in Copper (layer  $\alpha$ ), while higher SIA concentration at steady state is shown therein by Cu/Ni. Moreover, Cu/V system displays the lower stationary vacancy concentration in layer  $\beta$ .

Differences in the irradiation behavior shown by the systems investigated may be explained on the base of both surface characteristics and bulk layer properties. Specifically, the peculiar behavior of Cu/Ni layers is due to the lower value of the interface concentration of traps for point defects characterizing this system, which leads to the saturation of SIA traps. Instead, higher diffusivity of vacancies in V layer causes the lower stationary value of vacancy concentration in layer  $\beta$  of Cu/V systems.

As a concluding remark, model results reveal variations in interfacial Cu vacancy sink efficacy as a function of interface type. Specifically, while Cu/Nb and Cu/V interfaces are comparable in terms of point-defect absorption, Cu/Ni system turns out to be much less effective. These findings are qualitatively in agreement with the results reported by Mao *et al.* [19]. Indeed, they indicate that the average point-defect absorption probability should be highest for Cu–Nb interfaces and lowest for Cu–Ni interfaces with a moderate sink strength associated to Cu–V interfaces in between the two other systems. A study on quantitative comparison between model predictions and Mao *et al.* experimental results can be found in the next chapter.

## Nomenclature of Chapter 5

$a$	lattice constant, m;
$A$	dimensionless production rate of point defects, -;
$b$	lattice spacing, m;
$C$	concentration of point defects, $\text{m}^{-3}$ ;
$D$	diffusivity, $\text{m}^2 \text{s}^{-1}$ ;
$E$	dimensionless parameter of point-defect jumps from the matrix, -;
$F$	dimensionless parameter of point-defect surface recombination, -;
${}^F E$	activation energy for formation of point defects, J;
${}^M E$	activation energy for mobility of point defects, J;
$f$	trap occupation probability, -;
$k_B$	Boltzmann constant, $\text{J K}^{-1}$ ;
$K$	transfer velocity, $\text{m s}^{-1}$ ;
$K_{iv}$	recombination factor of the antidefects, $\text{m}^3 \text{s}^{-1}$ ;
$K_0$	production rate of point defects, $\text{m}^{-3} \text{s}^{-1}$ ;
$L$	layer thickness, m;
$R_C$	removal rate of point defects due to recombination, $\text{m}^{-3} \text{s}^{-1}$ ;
${}^F S$	entropy for formation of point defects, $\text{J K}^{-1}$ ;
${}^M S$	entropy for mobility of point defects, $\text{J K}^{-1}$ ;
${}^{tot} S$	concentration of traps for point defects, $\text{m}^{-2}$ ;
$T$	temperature, K;
$t$	time, s;
$x$	spatial coordinate, m;
$z$	number of jumps, -;

### *Greek letters*

$\alpha$	diffusion parameter of point defects, -;
$\alpha_{iv}$	combinatorial factor, -;
$\alpha_s$	surface recombination coefficient, $\text{m}^{-2} \text{s}^{-1}$ ;
$\chi$	dimensionless concentration of point defects, -;
$\delta$	dimensionless diffusivity, -;
$\nu_D$	Debye frequency, $\text{s}^{-1}$ ;

$M_V$	migration attempt frequency, $s^{-1}$ ;
$\tau$	dimensionless time, -;
$\varpi$	dimensionless lattice spacing, -;
$\Omega$	atomic volume, $m^3$ ;
$\xi$	dimensionless spatial coordinate, -;

### *Superscripts*

*	equilibrium;
$r$	reference;
$s$	scaling;
$(\alpha)$	layer of element $\alpha$ ;
$(\gamma)$	layer of element $\gamma$ ;
$(\beta)$	layer of element $\beta$ ;
$(\alpha-\beta)$	system formed by elements $\alpha$ and $\beta$ ;

### *Subscripts*

$i$	self-interstitial atom;
$j$	point defect of the type $j$ ;
$v$	vacancy.

## References of Chapter 5

- [1] Demkowicz M.J., Wang Y.Q., Hoagland R.G., Anderoglu O., Mechanisms of He escape during implantation in CuNb multilayer composites, *Nuclear Instruments and Methods in Physics Research B*, 261, (2007), 524-528.
- [2] Zinkle S.J., Busby J.T Structural materials for fission & fusion energy, *Materials Today*, 12, (2009), 12-19.
- [3] Misra A., Demkowicz M.J., Zhang X., Hoagland R.G., The radiation damage tolerance of ultra-high strength nanolayered composites, *JOM*, 59(9), (2007), 62-65.
- [4] Zinkle S.J., Ghoniem N.M., Operating temperature windows for fusion reactor structural materials, *Fusion Engineering and Design*, 51-52, (2000), 55-71.
- [5] Demkowicz M.J., Misra A., Caro A., The role of interface structure in controlling high helium concentrations, *Current Opinion in Solid State and Materials Science*, 16, (2012), 101-108.
- [6] Zinkle S.J., Fusion materials science: overview of challenges and recent progress, *Physics of Plasmas*, 12, (2005), 058101.
- [7] Zhernenkov M., Jablin M.S., Misra A., Nastasi M., Wang Y., Demkowicz M.J., Baldwin J.K., Majewski J., Trapping of implanted He at Cu/Nb interfaces measured by neutron reflectometry, *Applied Physics Letters*, 98, (2011), 241913.
- [8] Mao S., Dillon S., Averback R.S., The influence of Cu-Nb interfaces on local vacancy concentration in Cu, *Scripta Materialia*, 69, (2013), 21-24.
- [9] Zinkle S.J., Was G.S., Materials challenges in nuclear energy, *Acta Materialia*, 61, (2013), 735-758.
- [10] Chee S.W., Stumphy B., Vo N.Q., Averback R.S., Bellon P., Dynamic self-organization in Cu alloys under ion irradiation, *Acta Materialia*, 58, (2010), 4088-4099.
- [11] Trinkaus H., Singh B.N., Helium accumulation in metals during irradiation - where do we stand?, *Journal of Nuclear Materials*, 323, (2003), 229-242.
- [12] Li N., Mara N.A., Wang Y.Q., Nastasi M., Misra A., Compressive flow behavior of Cu thin films and Cu/Nb multilayers containing nanometer-scale helium bubbles, *Scripta Materialia*, 64, (2011), 974-977.
- [13] Ullmaier H., The influence of helium on the bulk properties of fusion reactor structural materials, *Nuclear Fusion*, 24, (1984), 1039-1083.
- [14] Kashinath A., Misra A., Demkowicz M.J., Stable storage of helium in nanoscale platelets at semicoherent interfaces, *Physical Review Letters*, 110, (2013), 086101.

- [15] Li N., Nastasi M., Misra A., Defect structure and hardening mechanisms in high dose helium ion implanted Cu and Cu/Nb multilayer thin films, *International Journal of Plasticity*, 32-33, (2012), 1-16.
- [16] Wilson W.D., Bisson C.L., Baskes M.I., Self-trapping of helium in metals, *Physical Review B*, 24(10), (1981), 5616-5624.
- [17] Csiszár G., Evolution of the Burgers-vector population of Cu-Nb multilayers with 7 at% He-implantation determined by X-ray diffraction, *Materials Science and Engineering A*, 609, (2014), 185-194.
- [18] Adamson R.B., Bell W.L., Kelly P.C., Neutron irradiation effects on copper at 327 °C, *Journal of Nuclear Materials*, 92 (1980), 149-154.
- [19] Mao S., Shu S., Zhou J., Averback R.S., Dillon S.J., Quantitative comparison of sink efficiency of Cu-Nb, Cu-V and Cu-Ni interfaces for point defects, *Acta Materialia*, 82, (2015), 328-335.
- [20] Victoria M., Baluc N., Bailat C., Dai Y., Luppo M.I., Schaublin R., Singh B.N., The microstructure and associated tensile properties of irradiated fcc and bcc metals, *Journal of Nuclear Materials*, 276, (2000), 114-122.
- [21] Escobar Galindo R., van Veen A., Evans J.H., Schut H., de Hosson J. Th. M.. Protrusion formation and surface porosity development on thermally annealed helium implanted copper, *Nuclear Instruments and Methods in Physics Research B*, 217, (2004), 262-275.
- [22] Kaminsky M., Das S.K., Correlation of blister diameter and blister skin thickness for helium-bombarded V, *Journal of Applied Physics*, 49(11), (1978), 5673-5675.
- [23] Terreault B., Ross G., St. Jacques R.G., Veilleux G., Evidence that helium irradiation blisters contain high-pressure gas, *Journal of Applied Physics*, 51(3), (1980), 1491-1493.
- [24] Han W., Demkowicz M.J., Mara N.A., Fu E., Sinha S., Rollett A.D., Wang Y., Carpenter J.S., Beyerlein I.J., Misra A., Design of radiation tolerant materials via interface engineering, *Advanced Materials*, 25, (2013), 6975-6979.
- [25] Odette G.R., Alinger M.J., Wirth B.D., Recent developments in irradiation-resistant steels, *Annual Review of Materials Research*, 38, (2008), 471-503.
- [26] Zhang X., Li N., Anderoglu O., Wang H., Swadener J.G., Höchbauer T., Misra A., Hoagland R.G., Nanostructured Cu/Nb multilayers subjected to helium ion-irradiation, *Nuclear Instruments and Methods in Physics Research B*, 261, (2007), 1129-1132.
- [27] Thorsen P.A., Bilde-Sorensen J.B., Singh B.N., Bubble formation at grain boundaries in helium implanted copper, *Scripta Materialia*, 51, (2004), 557-560.

- [28] Zhang L., Demkowicz M.J., Morphological stability of Cu-Nb nanocomposites under high-energy collision cascades, *Applied Physics Letters*, 103, (2013), 061604.
- [29] Zinkle S.J., Horsewell A., Singh B.N., Sommer W.F., Dispersoid stability in a Cu-Al<sub>2</sub>O<sub>3</sub> alloy under energetic cascade damage conditions, *Journal of Nuclear Materials*, 195, (1992), 11-16.
- [30] Demkowicz M.J., Hoagland R.G., Hirth J.P., Interface structure and radiation damage resistance in Cu-Nb multilayer nanocomposites, *Physical Review Letters*, 100, (2008), 136102.
- [31] Zhang X., Vo N.Q., Bellon P., Averback R.S., Microstructural stability of nanostructured Cu-Nb-W alloys during high temperature annealing and irradiation, *Acta Materialia*, 59, (2011), 5332-5341.
- [32] Chimi Y., Iwase A., Ishikawa N., Kobiyama M., Inami T., Okuda S., Accumulation and recovery of defects in ion-irradiated nanocrystalline gold, *Journal of Nuclear Materials*, 297 (2001), 355-357.
- [33] Ames M., Markmann J., Karos R., Michels A., Tschöpe A., Birringer R., Unraveling the nature of room temperature grain growth in nanocrystalline materials, *Acta Materialia*, 56, (2008), 4255-4266.
- [34] Höchbauer T., Misra A., Hattar K., Hoagland R.G., Influence of interfaces on the storage of ion-implanted He in multilayered metallic composites, *Journal of Applied Physics*, 98, (2005), 123516.
- [35] Koehler J.S., Attempt to design a strong solid, *Physical Review B*, 2(2), (1970), 547-551.
- [36] Lehoczy S.L., Strength enhancement in thin-layered Al-Cu laminates, *Journal of Applied Physics*, 49(11), (1978), 5479-5485.
- [37] Zhang X., Fu E.G., Misra A., Demkowicz M.J., Interface-enabled defect reduction in He ion irradiated metallic multilayers, *JOM*, 62(12), (2010), 75-78.
- [38] Fadda S., Locci A.M., Delogu F., Modeling of point defects annihilation in multilayered Cu/Nb composites under irradiation, *Advances in Materials Science and Engineering*, 2016 (2016), Article ID 9435431.
- [39] Was G.S., *Fundamentals of radiation materials science – Metals and alloys*, Springer, (2007).
- [40] Ortún-Palacios J., Locci A.M., Fadda S., Delogu F., Cuesta-López S., Role of interface in multilayered composites under irradiation: A mathematical investigation. Poster

presentation at Spring Meeting of the European Materials Research Society, 2016, May 2<sup>nd</sup> to 6<sup>th</sup>, Lille, France.

- [41] Demkowicz M.J., Hoagland R.G., Uberuaga B.P., Misra A., Influence of interface sink strength on the reduction of radiation-induced defect concentrations and fluxes in materials with large interface area per unit volume, *Physical Review B*, 84, (2011), Article ID 104102.
- [42] Ziegler J. F., Transport of Ions in matter (TRIM), IBM Corp. software, (1991).
- [43] Brailsford A.D., Bullough R., The rate theory of swelling due to void growth in irradiated metals, *Journal of Nuclear Materials*, 44, (1972), 121-135.
- [44] Zhao P., Shimomura Y., Molecular dynamics calculations of properties of the self-interstitials in copper and nickel, *Computational Materials Science*, 14, (1999), 84-90.
- [45] Dudarev S.L., Density functional theory models for radiation damage, *Annual Reviews of Materials Research*, 43 (2013), 35–61.
- [46] Suzuki A., Mishin Y., Atomistic Modeling of Point Defects and Diffusion in Copper Grain Boundaries, *Interface Science*, 11 (1), (2003), 131-148.
- [47] Nemirovich-Danchenko L. Yu., Lipnitskiĭ A. G., Kul'kova S. E., Vacancies and their Complexes in FCC metals, *Physics of the Solid State*, 49, (2017), 1079-1085.
- [48] Finkenstadt D., Bernstein N., Feldman J.L., Mehl M.J., Papaconstantopoulos D.A., Vibrational modes and diffusion of self-interstitial atoms in body-centered-cubic transition metals: A tight-binding molecular-dynamics study, *Physical Review B*, 74, (2006), art. no. 184118.
- [49] Chung-Ping C., The dislocation morphology in deformed and irradiated niobium, *Retrospective Theses and Dissertations*, (1977), Paper 5860.
- [50] Gutthoff F., Hennion B., Herzig C., Petry W., Schober H.R., Trampenau J., Lattice dynamics and self-diffusion in niobium at elevated temperatures, *Journal of Physics: Condensed Matter*, 6, (1994), 6211-6220.
- [51] Ramos de Debiaggi S., de Koning M., Monti A.M, Theoretical study of the thermodynamic and kinetic properties of self-interstitials in aluminum and nickel, *Physical Review B*, 73, (2006), 104103.
- [52] Debiaggi S.B., Decorte P.M., Monti A.M., Diffusion by vacancy mechanism in Ni, Al, and Ni<sub>3</sub>Al: Calculation Based on Many-Body Potentials, *Physica Status Solidi (b)*, 195, (1996), 37-54.

- [53] Shao S., Wang J., Misra A., Hoagland R.G., Spiral patterns of dislocations at nodes in (111) semi-coherent FCC interfaces, *Scientific Reports*, 3, (2013), Article number: 2448.
- [54] Chekhovskoi V. Ya., Tarasov V. D., Grigor'eva N. V., Contribution of equilibrium vacancies to vanadium caloric properties, *High Temperature*, 49, (2011), 826–831.
- [55] Peart R.F., Diffusion of  $V_{48}$  and  $Fe_{59}$  in vanadium, *Journal of Physics and Chemistry of Solids*, 26, (1965), 1853-1861.

## Tables and figures of Chapter 5

**Table 1** Dimensionless variables and parameters, and scaling and reference values.

Name	Expression
Dimensionless point-defect concentration	$\chi_j^{(\gamma)} = \frac{C_j^{(\gamma)} - {}^r C_j^{(\gamma)}}{{}^s C_j^{(\gamma)}} \quad j = i, v; \quad \gamma = \alpha, \beta;$
Dimensionless spatial coordinate	$\xi = \frac{x - {}^r x}{{}^s x};$
Dimensionless time	$\tau = \frac{t - {}^r t}{{}^s t};$
Dimensionless diffusion coefficient	$\delta_j^{(\gamma)} = \frac{4D_j^{(\gamma)}}{9D_i^{(\alpha)}} \quad j = i, v; \quad \gamma = \alpha, \beta;$
Dimensionless lattice spacing	$\varpi^{(\gamma)} = \frac{b^{(\gamma)}}{L} \quad \gamma = \alpha, \beta;$
-	$A^{(\gamma)} = \sqrt{\frac{L^4 K_0^{(\gamma)} \alpha_{iv}^{(\gamma)} \Omega^{(\gamma)} (D_i^{(\gamma)} + D_v^{(\gamma)})}{(a^{(\gamma)})^2 (D_i^{(\alpha)})^2}} \quad \gamma = \alpha, \beta;$
-	$E_j^{(\gamma)} = \sqrt{\frac{81L^2}{16({}^{tot} S_j^{(\alpha-\beta)})^2} \frac{K_0^{(\gamma)} (a^{(\gamma)})^2}{\alpha_{iv}^{(\gamma)} \Omega^{(\gamma)} (D_i^{(\gamma)} + D_v^{(\gamma)})}} \quad j = i, v; \quad \gamma = \alpha, \beta;$
-	$F_j = \frac{\alpha_s L^2}{{}^{tot} S_j^{(\alpha-\beta)} D_i^{(\alpha)}} \quad j = i, v;$
Reference concentration	${}^r C_j^{(\gamma)} = {}^* C_j^{(\gamma)} \quad j = i, v; \quad \gamma = \alpha, \beta;$
Reference spatial coordinate	${}^r x = 0;$
Reference time	${}^r t = 0;$
Scaling concentration	${}^s C_j^{(\gamma)} = \sqrt{\frac{K_0^{(\gamma)}}{K_{iv}^{(\gamma)}}} \quad j = i, v; \quad \gamma = \alpha, \beta;$
Scaling spatial coordinate	${}^s x = \frac{3L}{2};$
Scaling time	${}^s t = \frac{L^2}{D_i^{(\alpha)}};$

**Table 2. Model parameters for Copper.**

Parameters	Unit	Value	Reference
a	m	$3.615 \cdot 10^{-10}$	-
b	m	$2.556 \cdot 10^{-10}$	-
${}^F E_i$	J	$4.374 \cdot 10^{-19}$	[44]
${}^F E_v$	J	$1.666 \cdot 10^{-19}$	[45]
${}^M E_i$	J	$0.131 \cdot 10^{-19}$	[44]
${}^M E_v$	J	$1.154 \cdot 10^{-19}$	[45]
$k_B$	J K <sup>-1</sup>	$1.3806488 \cdot 10^{-23}$	-
$K_0$	m <sup>-3</sup> s <sup>-1</sup>	$2.05 \cdot 10^{25}$	This study
L	m	$300 \cdot 10^{-10}$	This study
${}^F S_i$	J K <sup>-1</sup>	$10.257 \cdot 10^{-23}$	[46]
${}^F S_v$	J K <sup>-1</sup>	$1.878 \cdot 10^{-23}$	[47]
${}^M v_i$	s <sup>-1</sup>	$0.20 \cdot 10^{13}$	[46]
${}^M v_v$	s <sup>-1</sup>	$0.76 \cdot 10^{13}$	[46]
${}^{tot} S_i^{(Cu-\beta)}$	m <sup>-2</sup>	$0.13-3.20 \cdot 10^{17}$	Tables 3-4-5
${}^{tot} S_v^{(Cu-\beta)}$	m <sup>-2</sup>	$0.13-3.20 \cdot 10^{17}$	Tables 3-4-5
T	K	573.15	This study
z	-	4	This study
$\alpha_i$	-	1	[39]
$\alpha_{iv}$	-	48	This study
$\alpha_s$	m <sup>-2</sup> s <sup>-1</sup>	0	This study
$\alpha_v$	-	1	[39]
$v_D$	s <sup>-1</sup>	$10^{13}$	[39]
$\Omega$	m <sup>3</sup>	$1.182 \cdot 10^{-29}$	-

**Table 3. Model parameters for Niobium.**

Parameters	Unit	Value	Reference
a	m	$3.303 \cdot 10^{-10}$	-
b	m	$2.861 \cdot 10^{-10}$	-
${}^F E_i$	J	$7.370 \cdot 10^{-19}$	[48]
${}^F E_v$	J	$4.791 \cdot 10^{-19}$	[45]
${}^M E_i$	J	$0.128 \cdot 10^{-19}$	[48]
${}^M E_v$	J	$1.458 \cdot 10^{-19}$	[45]
$k_B$	J K <sup>-1</sup>	$1.3806488 \cdot 10^{-23}$	-
$K_0$	m <sup>-3</sup> s <sup>-1</sup>	$1.37 \cdot 10^{25}$	This study
L	m	$300 \cdot 10^{-10}$	This study
${}^F S_i$	J K <sup>-1</sup>	0	This study, [49]
${}^F S_v$	J K <sup>-1</sup>	$2.899 \cdot 10^{-23}$	[50]
${}^M v_i$	s <sup>-1</sup>	$0.81 \cdot 10^{13}$	[48]
${}^M v_v$	s <sup>-1</sup>	$2.01 \cdot 10^{13}$	This study, [50]
${}^{tot} S_i^{(Cu-Nb)}$	m <sup>-2</sup>	$3.20 \cdot 10^{17}$	[5]
${}^{tot} S_v^{(Cu-Nb)}$	m <sup>-2</sup>	$3.20 \cdot 10^{17}$	[5]
T	K	573.15	This study
z	-	4	This study
$\alpha_i$	-	0.16667	[39]
$\alpha_{iv}$	-	144	This study
$\alpha_s$	m <sup>-2</sup> s <sup>-1</sup>	0	This study
$\alpha_v$	-	1	[39]
$v_D$	s <sup>-1</sup>	$10^{13}$	[39]
$\Omega$	m <sup>3</sup>	$1.802 \cdot 10^{-29}$	-

**Table 4. Model parameters for Nickel.**

Parameters	Unit	Value	Reference
a	m	$3.520 \cdot 10^{-10}$	-
b	m	$2.489 \cdot 10^{-10}$	-
${}^F E_i$	J	$7.899 \cdot 10^{-19}$	[44]
${}^F E_v$	J	$2.195 \cdot 10^{-19}$	[45]
${}^M E_i$	J	$0.256 \cdot 10^{-19}$	[44]
${}^M E_v$	J	$2.059 \cdot 10^{-19}$	[45]
$k_B$	J K <sup>-1</sup>	$1.3806488 \cdot 10^{-23}$	-
$K_0$	m <sup>-3</sup> s <sup>-1</sup>	$2.27 \cdot 10^{25}$	This study
L	m	$300 \cdot 10^{-10}$	This study
${}^F S_i$	J K <sup>-1</sup>	$20.561 \cdot 10^{-23}$	This study, [51]
${}^F S_v$	J K <sup>-1</sup>	$2.692 \cdot 10^{-23}$	[47]
${}^M v_i$	s <sup>-1</sup>	$0.79 \cdot 10^{13}$	This study, [51]
${}^M v_v$	s <sup>-1</sup>	$4.44 \cdot 10^{13}$	This study, [52]
${}^{tot} S_i^{(Cu-Ni)}$	m <sup>-2</sup>	$0.13 \cdot 10^{17}$	[53]
${}^{tot} S_v^{(Cu-Ni)}$	m <sup>-2</sup>	$0.13 \cdot 10^{17}$	[53]
T	K	573.15	This study
z	-	4	This study
$\alpha_i$	-	1	[39]
$\alpha_{iv}$	-	48	This study
$\alpha_s$	m <sup>-2</sup> s <sup>-1</sup>	0	This study
$\alpha_v$	-	1	[39]
$v_D$	s <sup>-1</sup>	$10^{13}$	[39]
$\Omega$	m <sup>3</sup>	$1.094 \cdot 10^{-29}$	-

**Table 5. Model parameters for Vanadium.**

Parameters	Unit	Value	Reference
a	m	$3.020 \cdot 10^{-10}$	-
b	m	$2.615 \cdot 10^{-10}$	-
${}^F E_i$	J	$6.809 \cdot 10^{-19}$	[48]
${}^F E_v$	J	$4.021 \cdot 10^{-19}$	[45]
${}^M E_i$	J	$0.160 \cdot 10^{-19}$	[48]
${}^M E_v$	J	$0.993 \cdot 10^{-19}$	[45]
$k_B$	$\text{J K}^{-1}$	$1.3806488 \cdot 10^{-23}$	-
$K_0$	$\text{m}^{-3} \text{s}^{-1}$	$0.89 \cdot 10^{25}$	This study
L	m	$300 \cdot 10^{-10}$	This study
${}^F S_i$	$\text{J K}^{-1}$	0	This study
${}^F S_v$	$\text{J K}^{-1}$	$4.446 \cdot 10^{-23}$	[54]
${}^M v_i$	$\text{s}^{-1}$	$1.40 \cdot 10^{13}$	[48]
${}^M v_v$	$\text{s}^{-1}$	$1.58 \cdot 10^{13}$	This study, [55]
${}^{tot} S_i^{(Cu-V)}$	$\text{m}^{-2}$	$0.50 \cdot 10^{17}$	[5]
${}^{tot} S_v^{(Cu-V)}$	$\text{m}^{-2}$	$0.50 \cdot 10^{17}$	[5]
T	K	573.15	This study
z	-	4	This study
$\alpha_i$	-	0.16667	[39]
$\alpha_{iv}$	-	144	This study
$\alpha_s$	$\text{m}^{-2} \text{s}^{-1}$	0	This study
$\alpha_v$	-	1	[39]
$v_D$	$\text{s}^{-1}$	$10^{13}$	[39]
$\Omega$	$\text{m}^3$	$1.458 \cdot 10^{-29}$	-

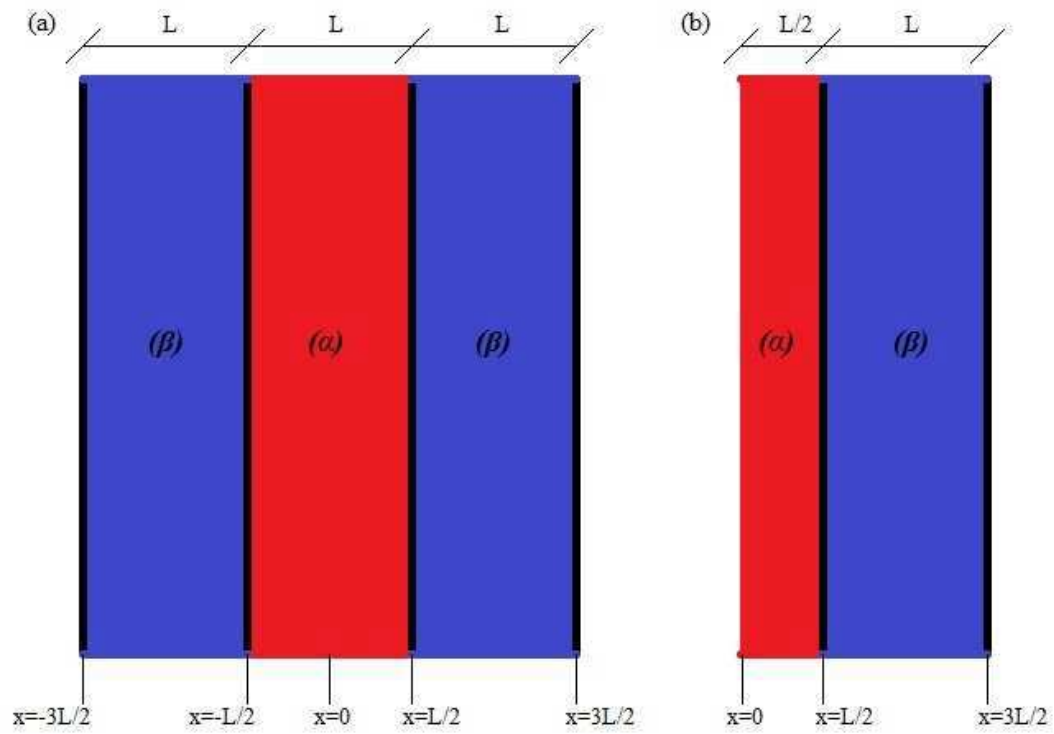


**Figure 1** Schematic of (a) the entire system and (b) the half-symmetric part modelled. Layer  $\alpha$  represents Copper while  $\beta$  indicates Niobium, Nickel, or Vanadium.

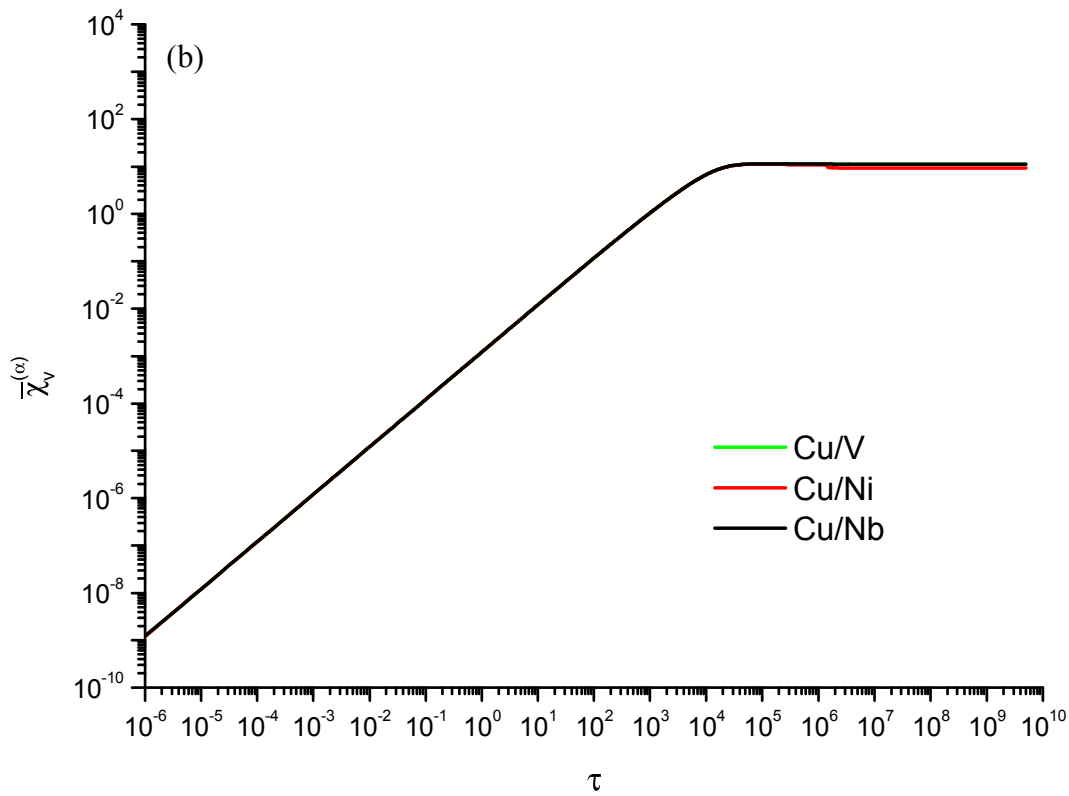
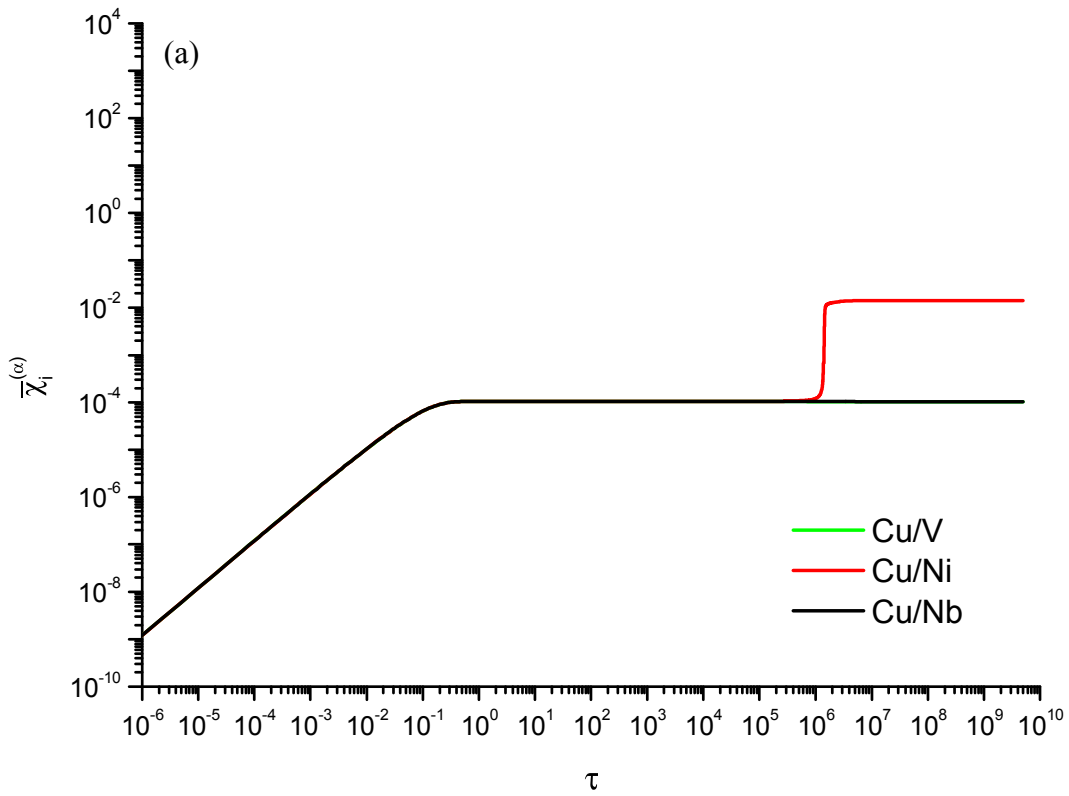


**Figure 2** Temporal profiles of average (a) SIA and (b) vacancy concentration in layer  $\alpha$ .

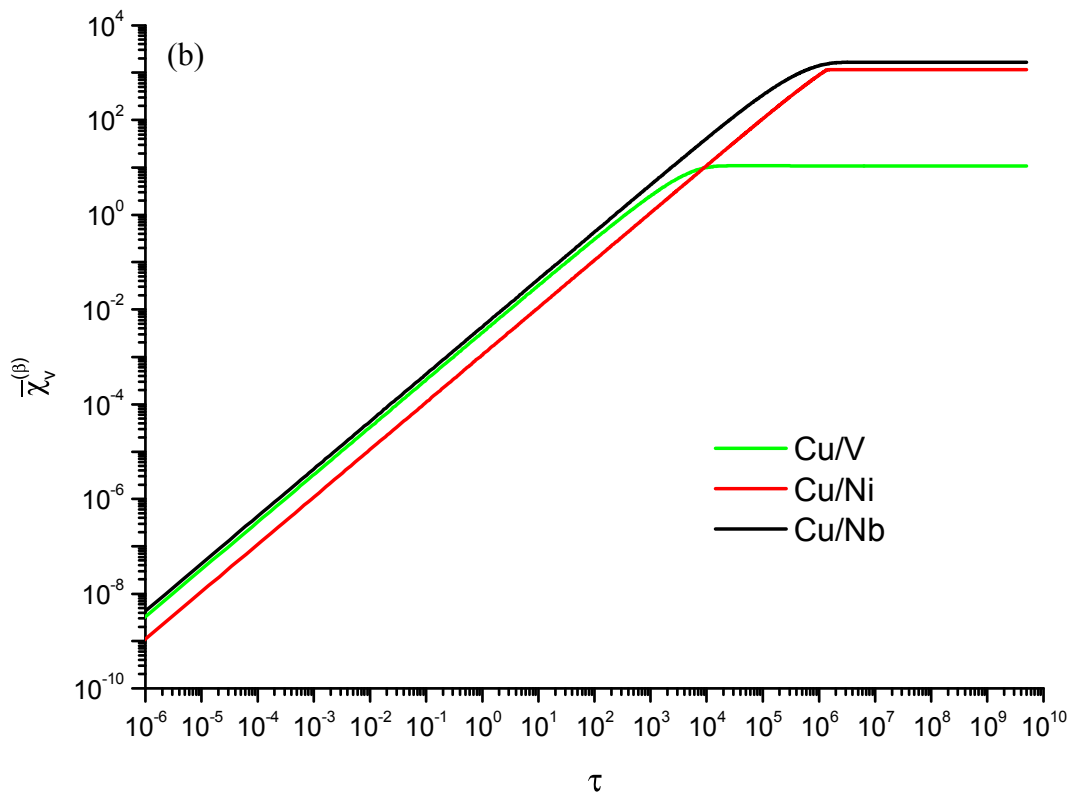
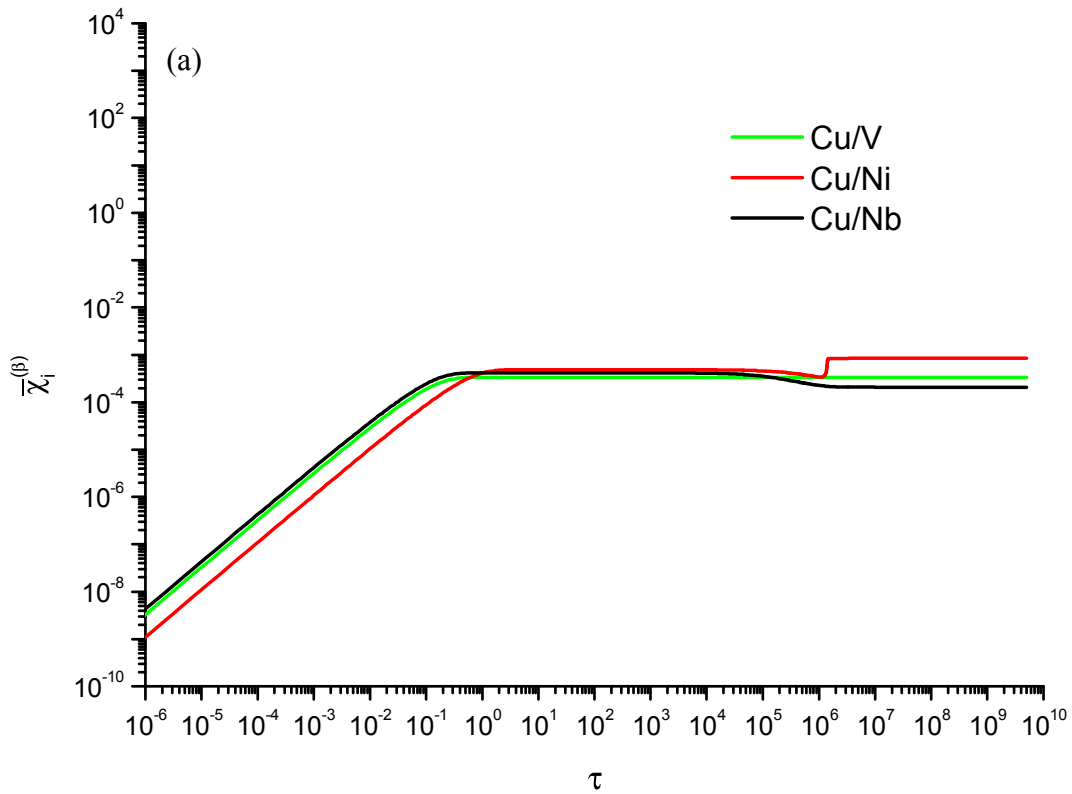


**Figure 3** Temporal profiles of average (a) SIA and (b) vacancy concentration in layer  $\beta$ .

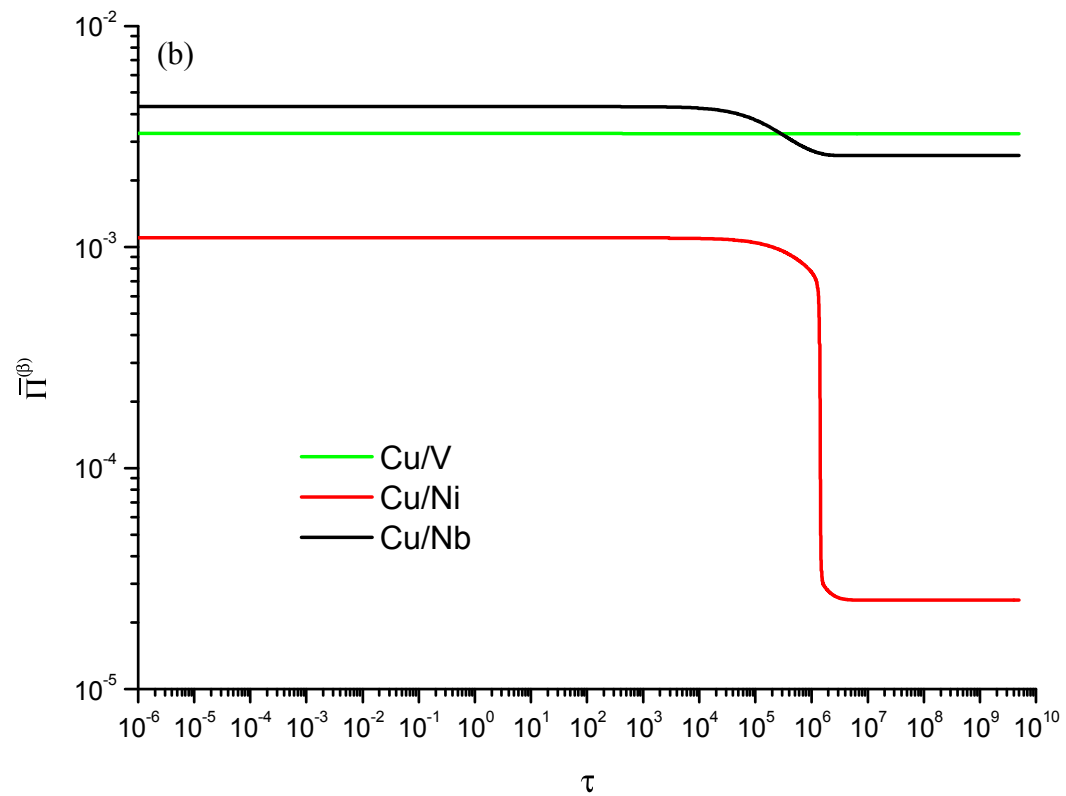
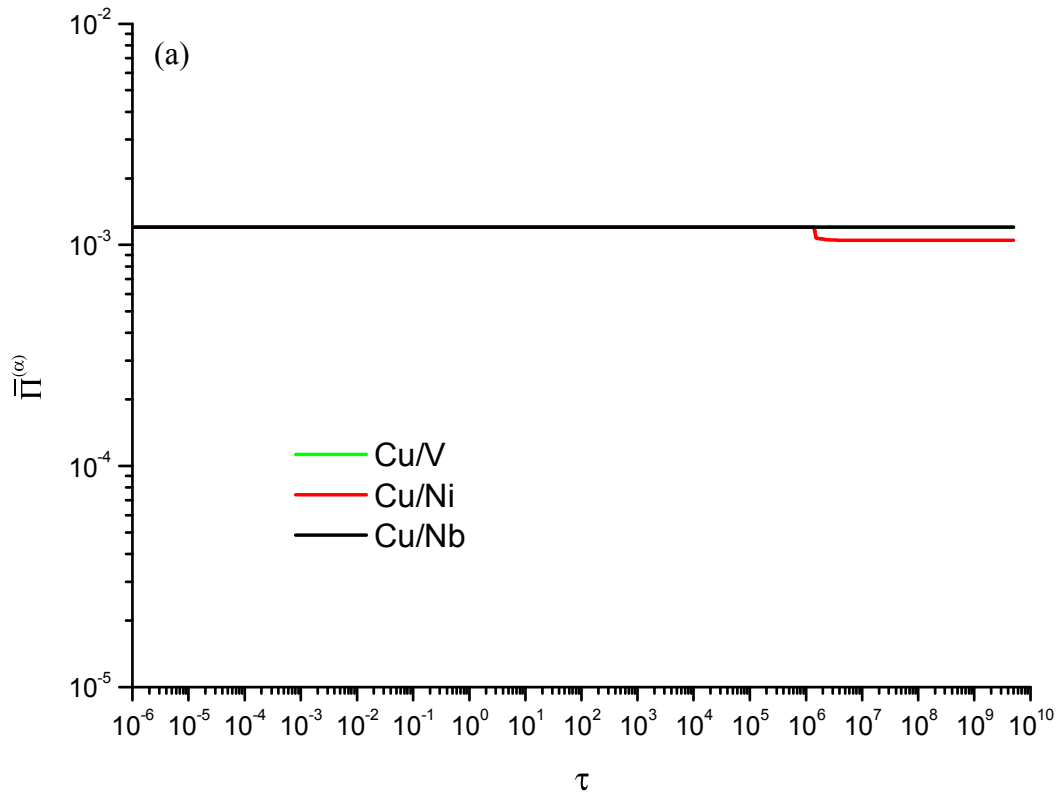


**Figure 4** Temporal profiles of average point-defect net-production rate in (a) layer  $\alpha$  and (b) layer  $\beta$ .

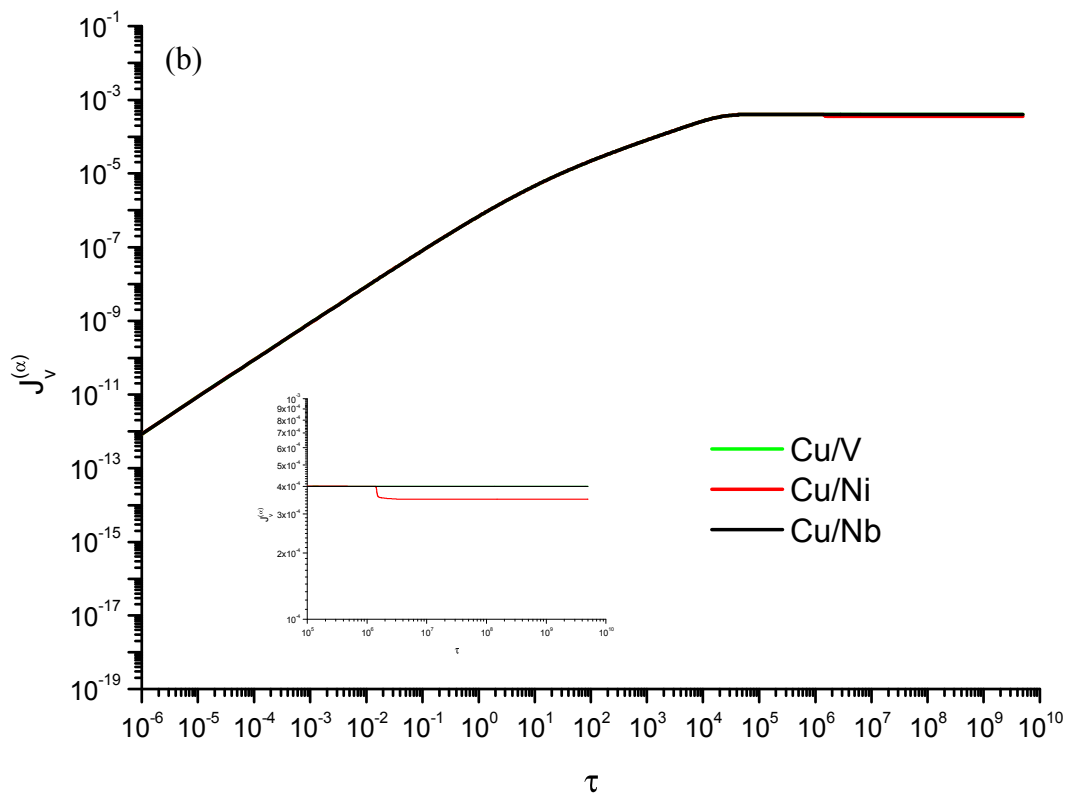
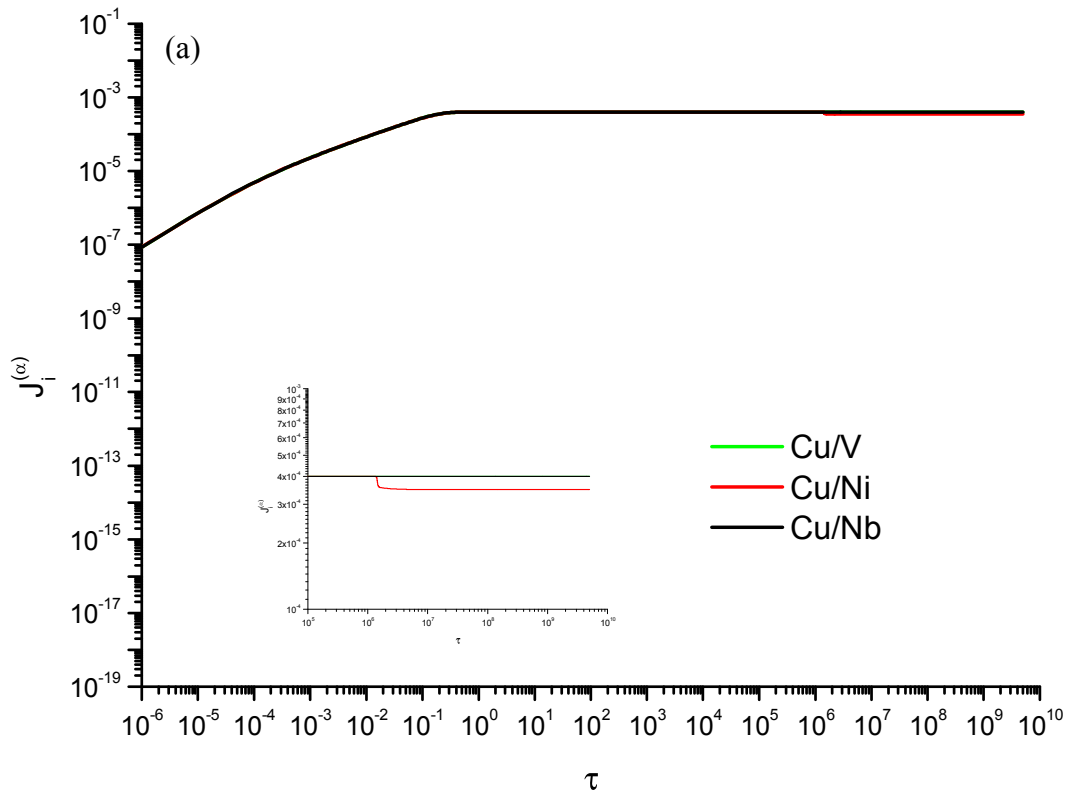


**Figure 5** Temporal profiles of (a) SIA and (b) vacancy flux from layer  $\alpha$  to the interface between metals  $\alpha$  and  $\beta$ .

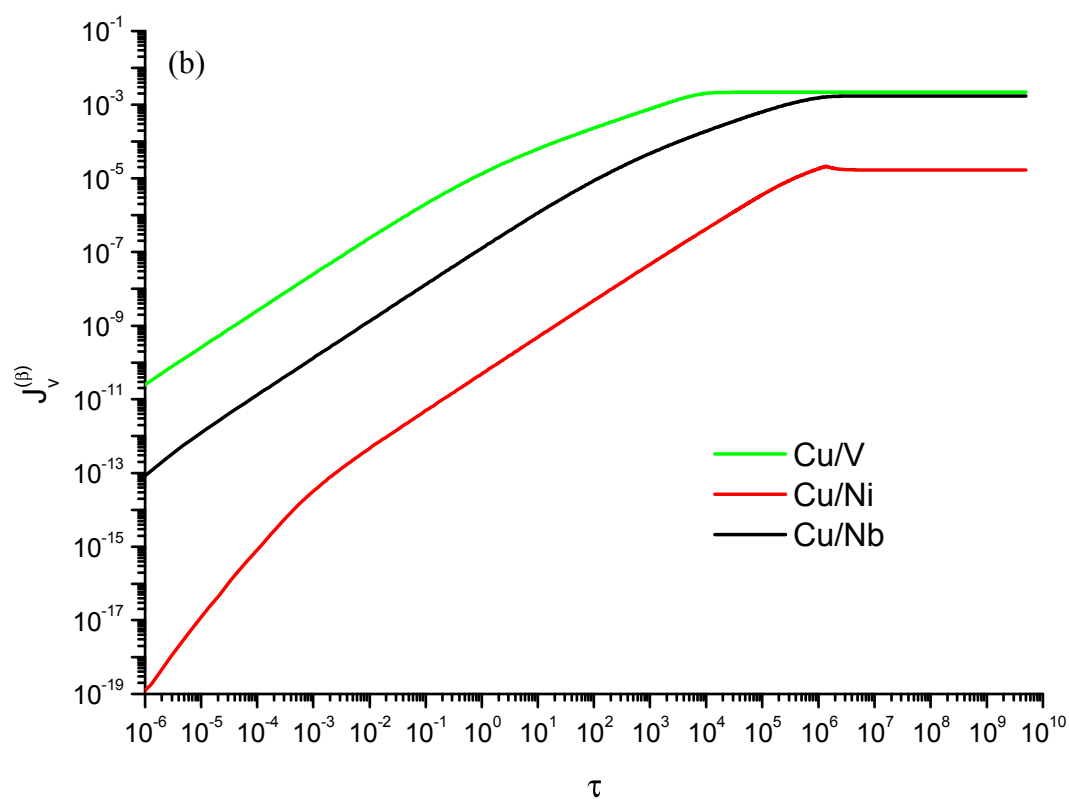
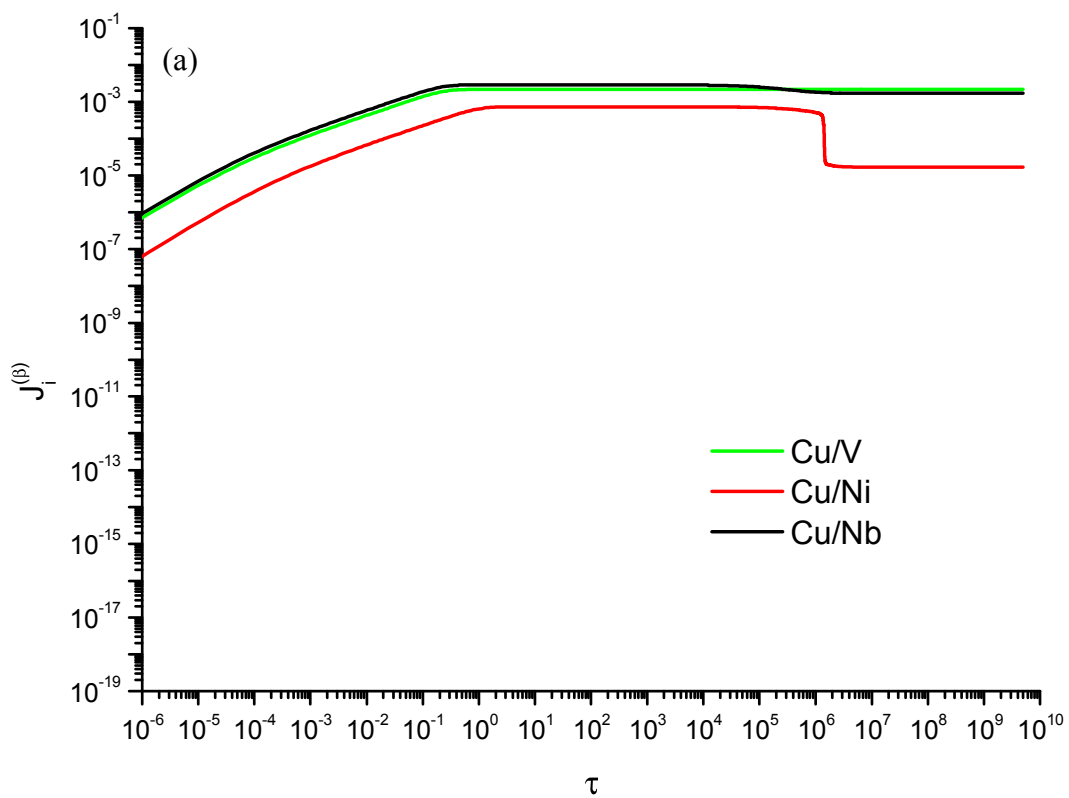


**Figure 6** Temporal profiles of (a) SIA and (b) vacancy flux from layer  $\beta$  to the interface between metals  $\alpha$  and  $\beta$ .

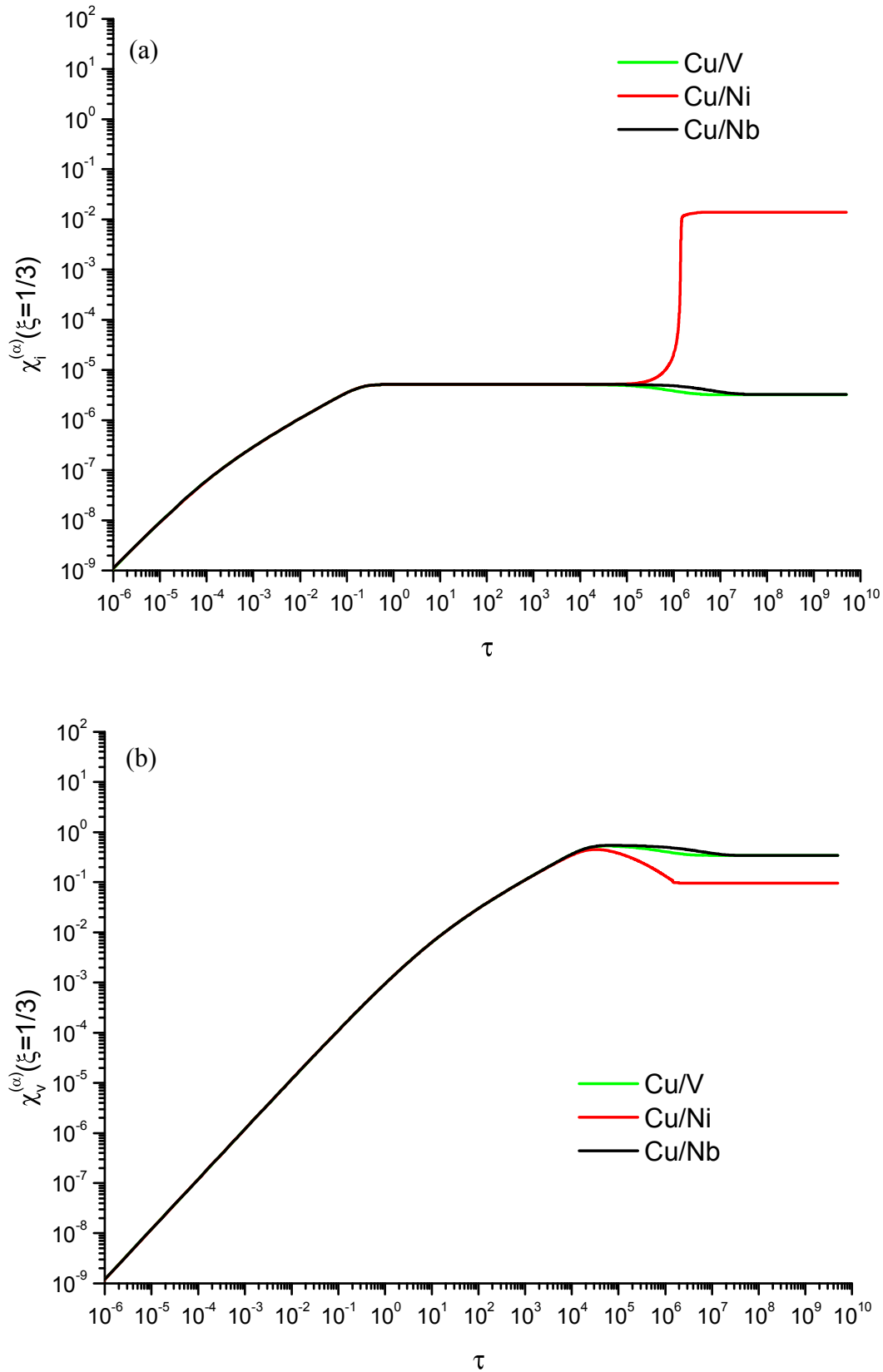


**Figure 7** Temporal profiles of (a) SIA and (b) vacancy concentration in layer  $\alpha$  at the interface between metals  $\alpha$  and  $\beta$ .

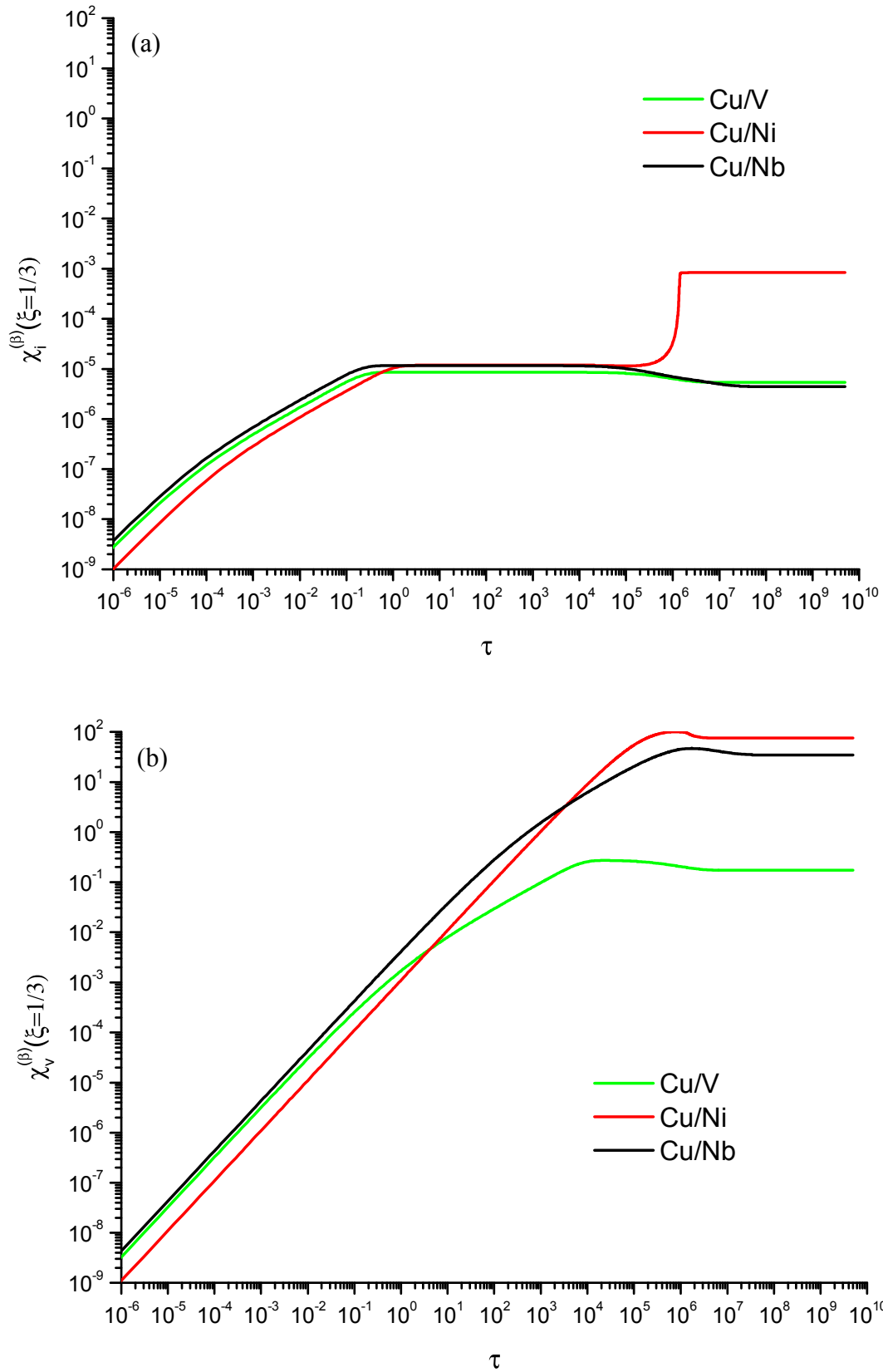


**Figure 8** Temporal profiles of (a) SIA and (b) vacancy concentration in layer  $\beta$  at the interface between metals  $\alpha$  and  $\beta$ .

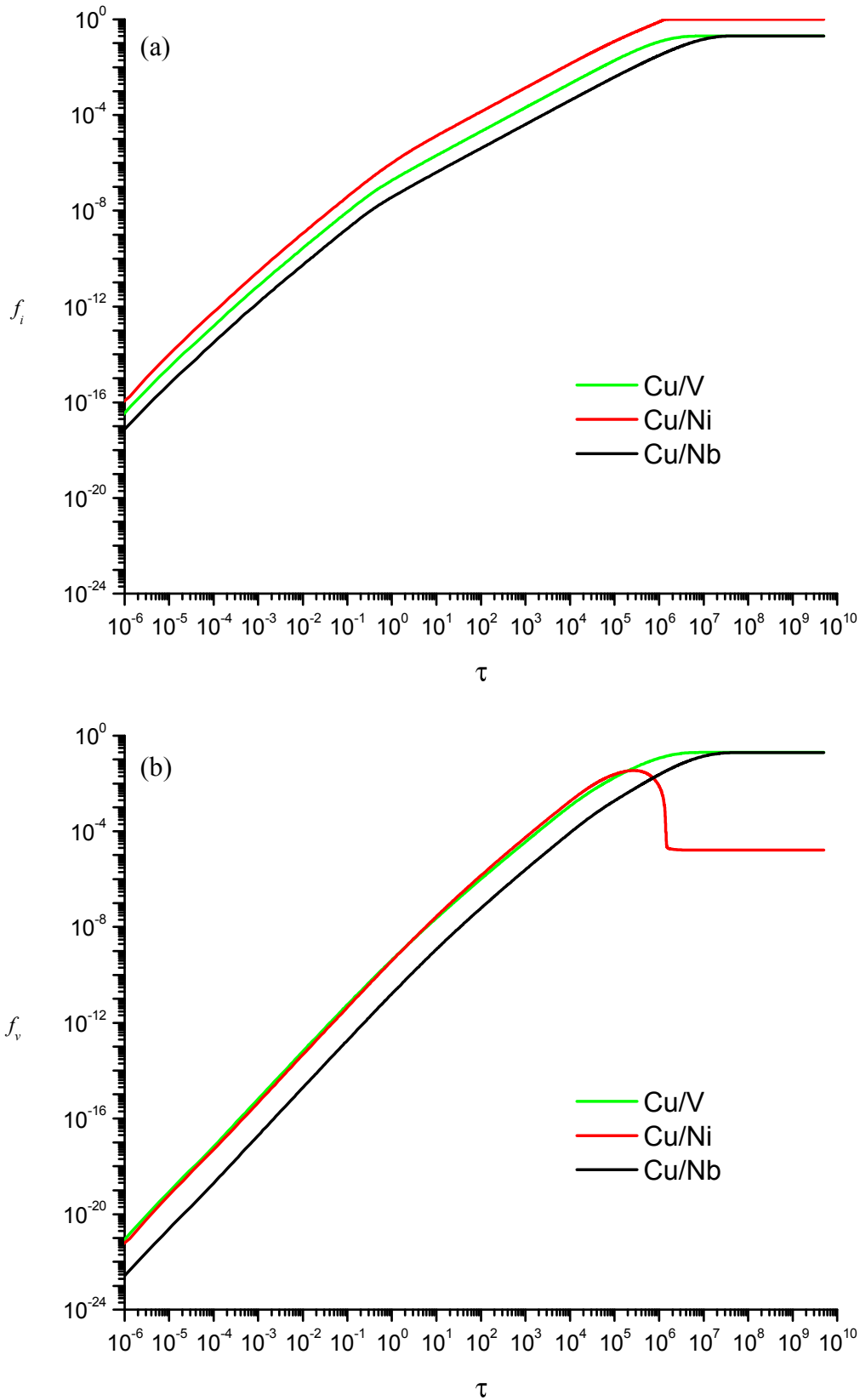


**Figure 9** Temporal profiles of (a) SIA and (b) vacancy trap occupation probability at the interface between metals  $\alpha$  and  $\beta$ .

## Chapter 6

### Self-healing ability assessment of irradiated multilayered composites: A continuum approach

#### 6.1. Introduction

Heterophase boundaries are interfaces with a great complexity between crystals of dissimilar chemistry, structure and orientation. The increase of interfacial area with respect to total volume can make material behavior to be influenced or even determined by these boundaries. Thus, nanoscale metallic multilayer composites (NMMCs) with ultra-high strengths and enhanced radiation damage tolerance could be designed tailoring layer thickness to take advantage of the atomic structure and energetics of the interfaces [1]. Nevertheless, the increase of interfaces number is not enough as they must be of the correct type [2]. In spite of their well-known importance, it has not been possible to study heterophase boundaries in detail until last years in which the situation has changed thanks to analyses with increased resolution and sensitivity besides to high-performance computational resources [3].

Variations in composition, stress or temperature may cause some interfaces to change easily from a metastable state to another one of almost the same energy which makes them affect a wide variety of processes [4]. Kurdjumov–Sachs (KS) [5] and Nishiyama–Wassermann (NW) [6,7] orientation relations are commonly found in close-packed fcc/bcc interfaces being the former the most studied. Despite their incommensurate character, a quasi-periodic pattern of patches may be present in these interfaces. This is the case of the interface atomic configuration termed  $KS_1$  in Cu/Nb multilayer composites which has been used as model system. While in  $KS_1$  there are patches of undercoordination, i.e., interface areas where a Cu and Nb atom are practically above each other, no patches of undercoordination exist in  $KS_2$  [8].  $KS_1$  is obtained joining Cu and Nb layers with the KS orientation relation. However, interfacial Cu plane in  $KS_2$  is homogeneously strained and rotated in such a way that makes this interface slightly favorable energetically with respect to  $KS_1$ . As a consequence,  $KS_2$  contains an extra interface between the strained interfacial Cu plane ( $Cu_\alpha$ ) and the rest of the Cu layer,  $Cu_\alpha/Cu$ , in addition to the  $Cu_\alpha/Nb$  one.

Lattice mismatch in heterophase interfaces may be accommodated by lattice strain, or by misfit dislocations injection which makes component crystals to return to the unstrained state. The existence of misfit dislocations can be proved by means of a disregistry analysis throughout the interface [4]. For such analysis, the relaxed structure and the correct reference

state [9,10], in which the interface is coherent, are needed. There are two sets of parallel misfit dislocation in Cu/Nb interface of  $KS_1$  and there is one set in each interface of  $KS_2$  ( $Cu_\alpha/Nb$  and  $Cu_\alpha/Cu$ ). Parameter values characterizing these sets of interfacial dislocations present in  $KS_1$  and  $KS_2$  can be found in **Ref. (4)** while their relative arrangement is illustrated in **Ref. (11)**.

Real Cu/Nb interfaces are not atomically flat even in multilayer composites synthesized by physical vapor deposition (PVD). Shear elastic constants of Cu/Nb interfaces have been demonstrated to be highly temperature dependent and easily influenced by the step density [12]. Therefore, interfaces with different atomistic roughnesses may have different shear stiffnesses. Severe plastic deformation (SPD) techniques allow to create Cu/Nb interfaces with different orientation of the habit planes to that of  $KS_1$  and  $KS_2$  [13]. This is the case of the interface studied in above work ( $Cu/Nb_{spd}$ ) and that has been compared with  $KS_1$  and  $KS_2$  ( $Cu/Nb_{pvd}$ ).  $Cu/Nb_{spd}$  contains three sets of parallel misfit dislocations. The dissimilarities found in the interface shear response of  $Cu/Nb_{pvd}$  and  $Cu/Nb_{spd}$  do not proceed from the difference of interface energy [14] but from the difference in misfit dislocation structure. Just one set of  $Cu/Nb_{spd}$  misfit dislocations has a Burgers vector within the interface plane which implies that the interface shears in that direction, i.e., the transverse direction along the interface, but not at all in the horizontal direction along the interface. The other two sets have Burgers vectors with non-zero component in the direction perpendicular to the interface. These misfit dislocations are not able to glide within the interface by themselves, they would need climb to occur. Nevertheless, misfit dislocation climb is unlikely to occur [13].

Light-ion beams are frequently used to study the effects of radiation on materials properties [15]. Such bombarding particles provoke atomic displacements that lead to the creation of self-interstitial atoms (SIAs) and vacancies mostly. These defects predominate in a region close to the irradiated surface where ion amount is negligible [16] and can be removed by means of recombination. One of the most promising strategies in the mitigation of radiation damage is the introduction of heterophase interfaces with enhanced ability to annihilate point defects [1]. An Embedded-Atom-Method (EAM) potential developed from Cu and Nb single-element potentials, and the Ziegler–Biersack–Littmark (ZBL) universal potential were joined to describe the interatomic and short range repulsive interactions respectively in Cu/Nb multilayer composites [17]. The resulting potential was used to simulate collision cascades nearby Cu/Nb- $KS_1$  interface as well as in single Cu and Nb crystals. The number of point defects produced per keV of primary knock-on atom (PKA)

energy in Cu/Nb multilayers was 50-70 % lower than in single Cu and Nb crystals [17]. This unique response of Cu/Nb NMMCs to irradiation arises from the extraordinary behavior of point defects in Cu/Nb interfaces. Indeed, void density and size in Cu layers of Cu/Nb NMMCs decrease when reducing the thickness [18].

Point-defect formation energies in Cu/Nb interfaces and bulk constituent metals were compared with the purpose of evaluating the point-defect trapping capacity of such interfaces. Molecular Dynamics (MD) simulations revealed similar and smaller point-defect formation energies away from Cu/Nb<sub>pvd</sub> interfaces and close to them respectively. Some Cu SIAs show similar formation energies to interfacial values at distances of up to 1 nm [4]. The relaxation process analysis of a Cu SIA located 1 nm from Cu/Nb interface showed a spontaneous migration to the interface without any energetic barrier or a very small one. The sites of lowest point-defect formation energies in Cu/Nb<sub>pvd</sub> interfaces are located in the regions of the quasi-periodic pattern commented previously that in turn coincide with the misfit dislocation intersections (MDIs). A Density Functional Theory (DFT)-based explanation was given in strain terms for vacancies [19]. A high corrugation exists in MDIs because a Cu atom is nearly on top of a Nb atom and they repulse each other. The introduction of a vacancy in these regions decreases the corrugation. The cost reduction of introducing a Cu vacancy is such that it ends up being energetically favorable unlike what happens outside of MDI regions. This means that a lower energy interface,  $KS_{\min}$ , can be found removing appropriate Cu atoms from  $KS_1$  and  $KS_2$  [4]. In addition, González *et al.* calculated the formation energy of a vacancy in the second plane of both sides of Cu/Nb interface near MDIs and the migration energy to the interfacial plane. Vacancy formation energies are between bulk and interface values, and vacancy migration energies are lower than in the bulk [20], so a successful vacancy trapping effect of Cu/Nb interface is expected.

A Cu atom removal or insertion in  $KS_1$  does not form compact point defects after relaxation but it changes the atomic volume in an extensive region and the interface reconstruction leads to the creation of 4- and 5-atom rings in the 3-atom ring network [4]. A point defect can be seen as a square edge dislocation loop of atomic dimensions [4,11]. If the two edge segments of the dislocation loop glide in contrary directions, a screw segment is created. This would be unfavorable energetically unless a screw dislocation with opposite Burgers vector already exists. The elimination of the screw segment between edge ones results in a screw dislocation with a jog and a kink pair. Thus, a small patch climbs one atomic plane from Cu/Nb interface converting it into  $KS_2$  [11]. On the other hand, the

insertion or removal of an atom in  $\text{Cu}_\alpha$  plane of  $\text{KS}_2$  provokes the shifting of a small patch from  $\text{Cu}_\alpha/\text{Cu}$  to  $\text{Cu}/\text{Nb}$  interface becoming  $\text{KS}_1$ .

Away from  $\text{Cu}/\text{Nb}_{\text{spd}}$  interfaces, point-defect formation energies are similar to the values obtained in single Cu and Nb crystals as it occurs in  $\text{Cu}/\text{Nb}$  multilayer composites synthesized by PVD, but highly variable in their vicinity for vacancies [13]. The sites of lowest point-defect formation energies in  $\text{Cu}/\text{Nb}_{\text{spd}}$  are located in MDI regions too. No constitutional vacancies are present in  $\text{Cu}/\text{Nb}_{\text{spd}}$  interfaces since all vacancy formation energies are positive. Furthermore, no point-defect delocalization occurs. The penalty energy associated to strained  $\text{Cu}_\alpha$  plane of  $\text{KS}_2$  is compensated with the energy gained by avoiding misfit dislocations from intersecting at the same interface plane ( $\text{KS}_1$ ). Hence, differences in the interaction of  $\text{Cu}/\text{Nb}_{\text{spd}}$  and  $\text{Cu}/\text{Nb}_{\text{pvd}}$  interfaces with point defects may be caused by the inability of  $\text{Cu}/\text{Nb}_{\text{spd}}$  misfit dislocations to shift one atomic plane.

In order to test the influence of thermodynamic properties and interface geometry on the atomic structure as well as on interface point-defect formation energies, EAM interaction potentials were fitted to different values of dilute heats of mixing [21] and lattice misfit [22] respectively keeping the rest of parameters unchanged. Variation of dilute heats of mixing, and therefore bonding strength, does not affect significantly the atomic structure or Cu vacancy formation energies, but it does affect Cu SIA formation ones. Variation of lattice misfit alters significantly the atomic structure due to changes in the misfit dislocation spacing and the dislocation character. All lattice misfits showed Cu point-defect formation energies lower than bulk values except in one case for vacancies. An increase of low vacancy formation energy sites is usually associated to an increase of MDI density so other semicoherent interfaces could be designed to trap point defects effectively.

$\text{Cu}/\text{Nb}_{\text{pvd}}$  interfaces not only act as sinks for point defects, they are catalysts for point-defect recombination too. Kink-jog pairs formed after a Cu atom insertion or removal, have dipolar elastic fields that allow long-range interactions between them. This causes a significant increase of the critical distance for Frenkel-pair recombination compared to Cu single crystal [11]. On the contrary, the critical distance for Frenkel pair recombination in the interfacial Nb plane is not increased as markedly as in the Cu one because Nb point defects remain compact. But, despite this, Frenkel pairs formed in Nb layer can also take advantage of the mechanism that aid rapid point-defect recombination in Cu layer if they migrate to the interfacial Cu plane [4]. In addition, the emission of SIAs from the interfaces may play an important role in the annihilation of radiation damage. MD simulations demonstrated that Cu SIAs are loaded in  $\text{Cu}/\text{Nb}$  interfaces during the collision cascades [23]. Next, such SIAs

interact with the remaining vacancies in Cu layer even if the latter are some planes away from the interface. A SIA is emitted from the interface causing an organized movement of adjacent Cu planes atoms that ends with the annihilation of a vacancy. The creation of low vacancy formation energy sites in Cu layer as a result of SIAs loading confirms the existence of long-range SIA-vacancy interactions. The SIA emission mechanism can be seen both in Cu/Nb<sub>pvd</sub> and Cu/Nb<sub>spd</sub> interfaces but it has a greater range of interaction in the last ones.

Point-defect clusters delocalize forming 4- and 5-atom rings in Cu/Nb<sub>pvd</sub> interfaces as single SIAs and vacancies [24]. Either single point defects or SIA clusters extend along set 1 of misfit dislocations while vacancy clusters extend along set 2. Taking as reference ground-state interface,  $KS_{\min}$ , point-defect cluster formation energy increases linearly with the number of point defects in the cluster unlike in single Cu crystal. The lack of thermodynamic driving forces for clustering besides the higher configurational entropy of isolated point defects than when forming a cluster suggest a tendency of point-defect clusters to divide into smaller ones and occupy different MDIs which may be beneficial due to the reduction of void formation.

MD simulations revealed that delocalized point defects migrate along set 1 of misfit dislocations from a MDI to a neighboring one in Cu/Nb<sub>pvd</sub> interfaces [24]. In between, the delocalized point defect extends and resides on both MDIs at the same time. The transition from delocalized state to extended one and vice versa requires the nucleation of thermal kink pairs at neighboring MDI and between both MDIs, respectively. Then, a kink-jog of the delocalized point defect annihilates with a kink-jog of the thermal kink pair permitting the transition between states. Thermal kinks nucleation or annihilation determines the energy barriers in the migration path which are smaller than in the bulk. On the contrary, DFT calculations suggest that vacancies stabilize at MDIs once they get trapped [19]. Nevertheless, supercell size limitations do not allow considering delocalized vacancies in the last work. In Cu/Nb<sub>spd</sub> interfaces, point defects are expected to migrate in a conventional way due to the predominant edge character of the three misfit dislocation sets and the incapacity of point defects to delocalize [13]. Formation, migration and dissociation of point-defect clusters in Cu/Nb<sub>pvd</sub> interfaces are governed by a multistage process with similar mechanisms to single point-defect migration ones [24]. Either delocalized point defects or thermal kink pairs can be represented by dislocation segments and saddle points in the migration path of point defects correspond to dislocation nucleation or annihilation. Hence, minimum energy paths may be analytically calculated with dislocation mechanics models [25].

The reduction of layer thickness decreases point-defect concentrations and fluxes to the interface. Nevertheless, point-defect concentrations are very sensitive to sink efficiency [26]. Indeed, different atomic configurations result in different misfit dislocation structures that interact in turn differently with point defects. Different void denuded zones (VDZ) widths were seen near Cu/Nb interfaces depending on their crystallographic character [18]. Sink efficiency of Cu/Nb<sub>spd</sub> interfaces is higher than Cu/Nb<sub>pvd</sub> one but none of them get decorated with voids unlike grain boundaries in nanocrystalline Cu [27]. Thus, synthesizing multilayer composites that remain free of voids is possible if layer thickness is reduced until VDZs near neighboring interfaces overlap.

He-irradiated Cu/Nb NMMCs are thermally stable in contrast with grains in nanocrystalline Cu that significantly coarsen [28]. Nevertheless, while He ions only transfer a small fraction of their kinetic energy to Cu and Nb atoms, morphological stability of Cu/Nb NMMCs may be compromised if they are irradiated with energetic neutrons or heavy ions [29]. Neutrons or heavy ions collide with Cu and Nb atoms initiating a ballistic phase followed by the formation of a thermal spike. The temperature reached is much higher than the melting one so a transient liquid phase forms until the energy is dissipated to surrounding atoms. Thermal spikes lead to the formation of point-defect clusters and, due to mixing across heterophase interfaces, an interfacial amorphous layer whose thickness is proportional to the square root of dose. Radiation-induced mixing is independent of interface crystallography and may be reduced by choosing low solubility metals with minimal liquid interdiffusivity as multilayer composite constituents [30,31]. In addition, the interdiffusion region of one interface should not overlap with the interdiffusion region of an adjacent interface to avoid layer pinchoff and, therefore, minimum layer thickness of Cu/Nb NMMCs should be between 2 and 4 nm [29].

The mechanisms underlying point-defect annihilation at NMMC interfaces have been covered in enough detail at atomistic scale. Nevertheless, they are subject to time-scale limitations so a continuum approach that describes long-term evolution of point-defects in irradiated NMMCs is highly desirable. In order to provide a contribution along this line, Fadda *et al.* validated a mathematical model to study the dynamic behavior of vacancies and interstitials in nanostructured metallic monolayers of Cu and Nb [32]. Layer boundaries were described as a continuum spatial distribution of sinks either neutral or variable-biased [33]. The effect of variation in layer thickness, temperature, point-defects production rate, and surface recombination coefficient on annihilation processes at interfaces was also addressed. In the previous chapter, their model was modified to take into account interface characteristics

deriving from coupling different metals and to allow metal layers influence each other's behavior through the evolution of interfacial variable-bias sink occupation.

The investigation presented in this chapter goes one step further and compares, quantitatively, model predictions with experimental results in Cu/Nb and Cu/V NMMCs [34]. In such experiments, both multilayer composites were synthesized by PVD. Hence, we have focused on  $\alpha/\beta$ -KS<sub>min</sub> and -KS<sub>1</sub> interfaces ( $\alpha = \text{Cu}$  and  $\beta = \text{Nb}$  or  $\text{V}$ ). These interfaces correspond to ground-state and defect-free KS structures respectively. The former contains constitutional vacancies, whose concentration is higher in Cu/Nb interface than in Cu/V one, and, according to Mao *et al.*, they seem to play a key role in Cu vacancy concentration dissimilarities between the two systems at the steady state. They believe that interface constitutional vacancies trap interstitials and facilitate vacancy recombination. Moreover, the unconventional behavior of point defects in these interfaces has to be considered. Accordingly, boundary equations and initial conditions have been adapted. Point-defect interactions with damaged and pristine boundaries tend to be different [35]. KS<sub>1</sub> may be seen as KS<sub>min</sub> loaded with SIAs [36]. Thus, we have investigated the effect of interface SIA loading [23] and constitutional vacancies [37] on the long-term point-defect evolution. Cu/Nb- and Cu/V-KS<sub>min</sub> interfaces have the same number of constitutional vacancies per MDI, however, the areal MDI density is different. Therefore, the effect of trap concentration has been analyzed too.

## 6.2. Mathematical model

We consider the same system described in the previous chapter, where a layer of metal  $\alpha$  is in between two layers of metal  $\beta$  (cf. **Figure 1a**). Therefore, some points explained in detail there will not be commented again and the reader should refer to above-mentioned chapter. However, all the necessary equations that allow the model resolution will be presented here for the sake of clarity. The evolution of point defects, i.e., self-interstitial atoms (SIA) ( $i$ ) and vacancies ( $v$ ) concentration in layers  $\alpha$  and  $\beta$  is described by the following one-dimensional spatial reaction-diffusion equations:

$$\frac{\partial C_j^{(\gamma)}}{\partial t} - D_j^{(\gamma)} \frac{\partial^2 C_j^{(\gamma)}}{\partial x^2} = K_0^{(\gamma)} - R_C^{(\gamma)} \quad j = i, v; \quad \gamma = \alpha, \beta; \quad (1)$$

along with their initial conditions

$$t = 0; \forall x \quad C_j^{(\gamma)} = {}^*C_j^{(\gamma)} \quad j = i, v; \quad \gamma = \alpha, \beta. \quad (2)$$

$C_j^{(\gamma)}$  is the concentration of the point defect of type  $j$  in layer  $\gamma$ ,  $D_j^{(\gamma)}$  is the diffusion coefficient of the point defect of type  $j$  in layer  $\gamma$  [26], while  $K_0^{(\gamma)}$  and  $R_C^{(\gamma)}$  are the production and the recombination rates of point defects per unit volume in layer  $\gamma$ , respectively.  ${}^*C_j^{(\gamma)}$  is the concentration of the point defect of type  $j$  in layer  $\gamma$  at thermodynamic equilibrium [33]. As the production rate of point defects is assumed time- and spatial-independent in each layer (see previous chapter), the recombination rate of point defects is expressed as a second order reaction [33]:

$$R_C^{(\gamma)}(x, t) = K_{iv}^{(\gamma)} (C_i^{(\gamma)} - {}^*C_i^{(\gamma)}) (C_v^{(\gamma)} - {}^*C_v^{(\gamma)}) \quad \gamma = \alpha, \beta; \quad (3)$$

where  $K_{iv}^{(\gamma)}$  is the kinetic constant.

Point defects tend to get trapped in MDI regions of NMMCs interfaces [21,22]. In the previous chapter, interfaces between metals  $\alpha$  and  $\beta$  were assumed to have a surface concentration of traps for interstitials,  ${}^{tot}S_i^{(\alpha-\beta)}$ , and a surface concentration of traps for vacancies,  ${}^{tot}S_v^{(\alpha-\beta)}$ , as in Brailsford and Bullough's original work [38]. This means that traps for SIAs and vacancies are treated as different physical entities, which is appropriate when point defects remain compact and well localized [13]. However, trapped SIAs and vacancies at interfaces of multilayer composites synthesized by PVD delocalize in a similar way and form kink-jog pairs [4]. Thus, only one trap typology is considered in this study which is capable of accommodating both SIAs and vacancies. Moreover, point-defect delocalization significantly increases the critical distance for Frenkel-pair recombination [11]. So, if a point defect jumps to an interface site close to a trapped opposite point defect, they recombine. Therefore, boundary conditions at the interface between metals  $\alpha$  and  $\beta$  may be expressed as:

$$x = \frac{L}{2}; \quad \forall t \quad D_j^{(\gamma)} \frac{\partial C_j^{(\gamma)}}{\partial x} = (1 - f_j - f_k + z f_k) K_j^{(\gamma)} (C_j^{(\gamma)} - {}^*C_j^{(\gamma)}) \quad (4)$$

$$j = i, v; \quad k \neq j = i, v; \quad \gamma = \alpha, \beta;$$

where  $L$  is the thickness of layer  $\gamma$  and  $K_j^{(\gamma)}$  is the transfer velocity of the point defect of type  $j$  from layer  $\gamma$  to the interface. A point defect may go into an unoccupied trap site, either by a SIA or a vacancy, or recombine with the nearest trapped opposite point defect, jumping there from  $z$  possible adjacent sites in the matrix. In the previous chapter,  $z$  was set equal to 4 for any material structure according to Brailsford and Bullough's work. Thus, the two interface annihilation mechanisms consisting of a point defect jumping to an unoccupied trap and to an occupied trap by the opposite point defect can be considered to have a prefactor of 1 and 4 respectively. As point defects do not remain compact in PVD multilayer composites interfaces, the original physical meaning of giving  $z$  a value of 4 may be lost. Nonetheless, the effect of  $z$  value in point-defect annihilation at the interface between metals  $\alpha$  and  $\beta$  will be evaluated in the next section.

Point-defect trap occupation probabilities are obtained by solving the following balance equations:

$$\begin{aligned} \frac{df_j}{dt} = & (1 - f_j - f_k) \frac{K_j^{(\alpha)}}{{}_{tot}S^{(\alpha-\beta)}} (C_j^{(\alpha)} - {}^*C_j^{(\alpha)}) - z f_j \frac{K_k^{(\alpha)}}{{}_{tot}S^{(\alpha-\beta)}} (C_k^{(\alpha)} - {}^*C_k^{(\alpha)}) \\ & + (1 - f_j - f_k) \frac{K_j^{(\beta)}}{{}_{tot}S^{(\alpha-\beta)}} (C_j^{(\beta)} - {}^*C_j^{(\beta)}) - z f_j \frac{K_k^{(\beta)}}{{}_{tot}S^{(\alpha-\beta)}} (C_k^{(\beta)} - {}^*C_k^{(\beta)}) \\ & - \frac{\alpha_s}{{}_{tot}S^{(\alpha-\beta)}} f_j f_k \end{aligned} \quad (5)$$

$$j = i, v; \quad k \neq j = i, v;$$

along with their initial conditions

$$t = 0, \quad f_j = f_j^0 \quad j = i, v; \quad (6)$$

where  ${}_{tot}S^{(\alpha-\beta)}$  is the surface concentration of traps for point defects and  $\alpha_s$  is the surface recombination coefficient. Temporal evolution of trap occupation probability by a point defect of type  $j$  depends on the fluxes of SIAs and vacancies to the interface arriving from both metal layers,  $\alpha$  and  $\beta$ , and the recombination of trapped SIAs with trapped vacancies. Fadda *et al.* [32] demonstrated that point-defect evolution in a metal monolayer did not depend on  $\alpha_s$  value. Hence,  $\alpha_s$  has been set equal to 0 in the same way that in the previous chapter where

we also studied metallic multilayer composites. The present investigation focuses on  $KS_{\min}$  and  $KS_1$  interfaces [4]. While the latter does not possess constitutional vacancies, the former has 2-3 vacancies per MDI [37]. Neither  $KS_{\min}$  nor  $KS_1$  possess constitutional SIAs. For a temperature similar to the one of this study, it was seen that a cluster of 5-6 SIAs or vacancies added to  $KS_1$ , i.e., defect-free interface, dissociated into smaller clusters and occupied different MDIs [24]. Moreover, according to that work too, if a SIA or vacancy cluster is added to  $KS_{\min}$ , i.e., the ground state structure, the SIAs or vacancies constituting the cluster are likely to evaporate from it and remain isolated thereafter. Therefore, it is assumed that each MDI is capable of accommodating 2-3 SIAs or vacancies.  $KS_{\min}$  and  $KS_1$  differ in the initial conditions of point-defect trap occupation probabilities,  $f_j^0$ , which may be in the range [0,1].  $f_i^0$  takes a nil value for both interface structures. However,  $f_v^0$  takes a nil value for  $KS_1$  and a unity value for  $KS_{\min}$ .

By referring to **Figure 1b**, boundary conditions can be completed. In the case of the symmetric surface of the entire system, boundary conditions may be expressed as:

$$x = 0; \quad \forall t \quad \frac{\partial C_j^{(\alpha)}}{\partial x} = 0 \quad j = i, v; \quad (7)$$

while in the case of the free surface on layer  $\beta$ , boundary conditions may be expressed as:

$$x = \frac{3L}{2}; \quad \forall t \quad \frac{\partial C_j^{(\beta)}}{\partial x} = 0 \quad j = i, v. \quad (8)$$

The model consisting of the balance Eqs. (1) along with their initial conditions, Eqs. (2), and their boundary conditions, i.e., Eqs. (4) in the case of the interface between metals  $\alpha$  and  $\beta$  modelled as variable-biased sinks, Eqs. (7) in the case of the symmetric surface of the entire system, or Eqs. (8) in the case of the free surface, allows to describe the spatial-temporal evolution of point-defect concentrations inside layers  $\alpha$  and  $\beta$  undergoing radiation.

In order to obtain dimensionless and normalized equations and parameters, a change of variables has been used in this study following the same procedure reported in the previous chapter. Dimensionless variables and parameters, as well as scaling and reference values can be found also there. According to this change of variables, the evolution of dimensionless

point-defect concentrations in layer  $\gamma$  as a function of the dimensionless time is described by the following equations:

$$\frac{\partial \chi_j^{(\gamma)}}{\partial \tau} - \delta_j^{(\gamma)} \frac{\partial^2 \chi_j^{(\gamma)}}{\partial \xi^2} = A^{(\gamma)} (1 - \chi_i^{(\gamma)} \chi_v^{(\gamma)}) \quad j = i, v; \quad \gamma = \alpha, \beta; \quad (9)$$

along with the initial conditions

$$\tau = 0; \quad \forall \xi \quad \chi_j^{(\gamma)} = 0 \quad j = i, v; \quad \gamma = \alpha, \beta. \quad (10)$$

At the interface between metals  $\alpha$  and  $\beta$  modelled as variable biased sinks, dimensionless boundary conditions may be expressed as:

$$\xi = \frac{1}{3}; \quad \forall \tau \quad \delta_j^{(\gamma)} \frac{\partial \chi_j^{(\gamma)}}{\partial \xi} = \frac{3}{2} (1 - f_j - f_k + z f_k) \frac{\delta_j^{(\gamma)}}{\varpi^{(\gamma)}} \chi_j^{(\gamma)} \quad (11)$$

$$j = i, v; \quad k \neq j = i, v; \quad \gamma = \alpha, \beta.$$

The dimensionless balance equations of trap occupation probabilities appear as follows:

$$\begin{aligned} \frac{df_j}{d\tau} = & E_j^{(\alpha)} \left[ (1 - f_j - f_k) \frac{\delta_j^{(\alpha)}}{\varpi^{(\alpha)}} \chi_j^{(\alpha)} - z f_j \frac{\delta_k^{(\alpha)}}{\varpi^{(\alpha)}} \chi_k^{(\alpha)} \right] \\ & + E_j^{(\beta)} \left[ (1 - f_j - f_k) \frac{\delta_j^{(\beta)}}{\varpi^{(\beta)}} \chi_j^{(\beta)} - z f_j \frac{\delta_k^{(\beta)}}{\varpi^{(\beta)}} \chi_k^{(\beta)} \right] \quad j = i, v; \quad k \neq j = i, v; \\ & - F_j f_j f_k \end{aligned} \quad (12)$$

along with their initial conditions

$$\tau = 0, \quad f_j = f_j^0 \quad j = i, v. \quad (13)$$

Dimensionless boundary conditions for the symmetric surface of the entire system may be expressed as:

$$\xi = 0; \quad \forall \tau \quad \frac{\partial \chi_j^{(\alpha)}}{\partial \xi} = 0 \quad j = i, v; \quad (14)$$

while dimensionless boundary conditions representing the free surface on layer  $\beta$  may be written as:

$$\xi = 1; \quad \forall \tau \quad \frac{\partial \chi_j^{(\beta)}}{\partial \xi} = 0 \quad j = i, v. \quad (15)$$

Average dimensionless concentration and net-production rate of the point defect of type  $j$  in layer  $\gamma$ ,  $\bar{\chi}_j^{(\gamma)}$  and  $\bar{\Pi}^{(\gamma)}$  respectively, as well as dimensionless flux of the point defect of type  $j$  from layer  $\gamma$  to the interface between metals  $\alpha$  and  $\beta$ ,  $J_j^{(\gamma)}$ , have been defined as in the previous chapter with the aim of illustrating and discussing model results. Model equations are solved by using the commercial software COMSOL Multiphysics 3.4, along with the parameters for Cu, Nb and V reported in the previous chapter except the value of parameter  $z$ , which has been evaluated in the next section before setting it, and  ${}^{tot}S^{(\alpha-\beta)}$ , which has been set equal to 2.5 times the values of  ${}^{tot}S_j^{(\alpha-\beta)}$ . The latter is due to  $KS_{\min}$  and  $KS_1$  capacity to accommodate 2-3 SIAs or vacancies in each MDI as it has been previously explained.

### 6.3. Results

In what follows, copper is represented by metal  $\alpha$  while metal  $\beta$  is niobium, or vanadium. Results are shown in a double-log plot (**Figures 2-9**) and they are obtained by solving the dimensionless version of the model illustrated in the previous section. All the results belong to the half-symmetric part of the layered system depicted in **Figure 1**. Firstly, the effect of parameter  $z$  value in point-defect evolution is evaluated as it has been indicated previously. This parametric sensitivity is performed in Cu/Nb NMMCs for either  $KS_{\min}$  or  $KS_1$  interface configuration. Three  $z$  values are considered, 0, 1 and 4. It should be noted that a nil value of parameter  $z$  for  $KS_1$  permits point defects in the matrix to jump only to unoccupied traps, canceling the mechanism consisting in the recombination of a point defect jumping from the matrix with the nearest trapped opposite point defect (cf. Eq. (4)). For  $KS_{\min}$ , a nil value of parameter  $z$  cancels both interface annihilation mechanisms and

suppresses point-defect fluxes. This last case represents the absence of point-defect traps.

The corresponding temporal profiles of average point-defect concentrations in Cu and Nb layers of Cu/Nb system for the different values of  $z$  are shown in **Figures 2** and **3**, respectively. It can be seen in **Figure 2a** that  $\bar{\chi}_i^{(\alpha)}$  constantly increases from the equilibrium concentration until  $\tau \approx 0.2$ . This behavior can be observed for all  $z$  values and for both interface configurations except for  $\text{KS}_{\min}$  with  $z=0$ . In this case,  $\bar{\chi}_i^{(\alpha)}$  continues increasing until  $\tau \approx 10^3$ . Then, average concentration of SIAs remains constant up to  $\tau \approx 10^7$  in Cu layer. However, there is a different evolution for  $\text{KS}_1$  with  $z=0$ . Indeed,  $\bar{\chi}_i^{(\alpha)}$  abruptly increases to reach a stationary SIA average concentration. **Figure 2b** shows the temporal evolution of vacancy average concentration in Cu layer. Initially,  $\bar{\chi}_v^{(\alpha)}$  increases until longer times than  $\bar{\chi}_i^{(\alpha)}$  except for  $\text{KS}_{\min}$  with  $z=0$ . In this case, vacancy and SIA average concentration in Cu layer show the same behavior. Similarly to  $\bar{\chi}_i^{(\alpha)}$ , no differences can be observed for  $\text{KS}_1$  between the three values of  $z$  until  $\tau \approx 10^7$ . Then,  $\bar{\chi}_v^{(\alpha)}$  also increases abruptly for  $z=0$  to reach a stationary vacancy average concentration. In contrast,  $\bar{\chi}_v^{(\alpha)}$  achieves a maximum for  $\text{KS}_{\min}$  with  $z$  equal to 1 and 4, to then decrease until steady state is reached. In all cases, the stationary value of  $\bar{\chi}_v^{(\alpha)}$  is higher compared to the stationary value of  $\bar{\chi}_i^{(\alpha)}$  except for  $\text{KS}_{\min}$  with  $z=0$  when it is equal.

**Figures 3a** and **3b** show the temporal profiles of SIA and vacancy average concentrations in Nb layer respectively for the different values of  $z$ . A similar behavior of  $\bar{\chi}_i^{(\beta)}$  compared to  $\bar{\chi}_i^{(\alpha)}$  can be seen for both interface configurations with the different values of  $z$ . The same occurs with  $\bar{\chi}_v^{(\beta)}$  with respect to  $\bar{\chi}_v^{(\alpha)}$ , although, some differences can be observed either in SIA or vacancy average concentrations. Firstly,  $\bar{\chi}_i^{(\beta)}$  decreases between  $\tau \approx 10^5$  and  $\tau \approx 10^7$  for all the cases studied except for  $\text{KS}_{\min}$  with  $z=0$ . Secondly,  $\bar{\chi}_v^{(\beta)}$  does not reach a maximum and decreases before steady state as  $\bar{\chi}_v^{(\alpha)}$  for  $\text{KS}_{\min}$  with  $z$  equal to 1 and 4. Instead, a stationary vacancy average concentration is reached in Nb layer after the initial increase. So, according to the results of **Figures 2** and **3** for the different values of parameter  $z$ , the overweighting of the mechanism consisting in the recombination of a point defect jumping from the matrix with the nearest trapped opposite point defect seems not to be effective. Indeed, point-defect evolution is not affected by the increase of  $z$  value from 1 to 4 either for  $\text{KS}_{\min}$  or  $\text{KS}_1$ . Therefore, the value of parameter  $z$  is set equal to 1 and the following results correspond to this value. The effect of no interface recombination ( $\text{KS}_1$  with

$z=0$ ) and point-defect traps absence ( $KS_{\min}$  with  $z=0$ ) is analyzed more extensively in the discussion section.

Now, a comparison between the response of Cu/Nb and Cu/V systems to irradiation for  $KS_{\min}$  and  $KS_1$  interface configurations is performed. Some details commented previously for Cu/Nb system would not be analyzed again and the reader should refer to previous paragraphs. The corresponding temporal profiles of average point-defect concentrations in layers  $\alpha$  (Cu) and  $\beta$  (Nb, or V) are depicted in **Figures 4** and **5**, respectively. It can be seen in **Figure 4a** that  $\bar{\chi}_i^{(\alpha)}$  does not show any difference between Cu/Nb and Cu/V systems and neither does it between  $KS_{\min}$  and  $KS_1$ . Similarly,  $\bar{\chi}_v^{(\alpha)}$  exhibits the same behavior for  $KS_1$  in both systems (**Figure 4b**). On the contrary, there is a different evolution of  $\bar{\chi}_v^{(\alpha)}$  depending on the interface configuration for each system, Cu/Nb or Cu/V. This can be seen too when comparing Cu/Nb to Cu/V for  $KS_{\min}$ .

**Figures 5a** and **5b** show the temporal profiles of SIA and vacancy average concentrations in layer  $\beta$  respectively. In contrast to  $\bar{\chi}_i^{(\beta)}$  in Cu/Nb system that decreases before reaching steady state, SIA average concentration in V layer maintains the stationary value reached after the initial increase during the rest of irradiation time. Furthermore, there are no differences in the evolution of  $\bar{\chi}_i^{(\beta)}$  between  $KS_{\min}$  and  $KS_1$  in Cu/V system unlike in Cu/Nb one. Even though  $\bar{\chi}_v^{(\beta)}$  initially increases to reach a stationary value in all the cases studied except for Cu/V- $KS_{\min}$  system, where  $\bar{\chi}_v^{(\beta)}$  reaches a maximum and decreases before reaching steady state, significant dissimilarities can be observed in the temporal profiles of vacancy average concentration in layer  $\beta$ .

The investigation of point-defect production, transport and annihilation phenomena may help to explain differences and similarities shown in the temporal evolution of point-defect average concentrations between the systems studied. Point-defect production rates in layers  $\alpha$  and  $\beta$  are constant temporally and spatially but, they have a different value for each metal (see previous chapter). On the contrary, point-defect recombination rates in layers  $\alpha$  and  $\beta$  depend upon SIA and vacancy concentrations in layer  $\alpha$  and  $\beta$  respectively. Thus, the corresponding temporal profiles of the average point-defect net-production rate in layers  $\alpha$  and  $\beta$ , which are the result of combining point-defect production phenomena with recombination one, are shown in **Figures 6a** and **6b**, respectively. It can be seen in **Figure 6a** that  $\bar{\Pi}^{(\alpha)}$  keeps constant at any time for both systems investigated, Cu/Nb and Cu/V, and both interface configuration considered,  $KS_{\min}$  and  $KS_1$ . This can be considered to occur too in

$\bar{\Pi}^{(\beta)}$  (**Figure 6b**) for Cu/V system as the decrease observed for  $KS_{\min}$  is very small. On the other hand, average point-defect net-production rate in Nb layer shows a significant decrease, which is more notable for  $KS_{\min}$  than for  $KS_1$ , before steady-state is reached.

Point-defect flux to the interface between the two metals represents the other mechanism affecting point-defect annihilation in addition to bulk recombination. The corresponding temporal profiles of point-defect fluxes from layer  $\alpha$  and layer  $\beta$  to the interface between the two metals are reported in **Figures 7** and **8**, respectively. It can be seen in **Figure 7a** that  $J_i^{(\alpha)}$  shows the same behavior for all the systems investigated. The higher diffusivity of SIAs allows them to get the interface between metals faster than vacancies. Consequently, SIA flux achieves a maximum earlier than vacancy one (cf. **Figures 7a** and **7b**). There are no differences in the evolution of  $J_v^{(\alpha)}$  between both systems, Cu/Nb and Cu/V, but only for  $KS_1$ , not for  $KS_{\min}$ .

It can be seen in **Figure 8a** that  $J_i^{(\beta)}$  increases to reach a stationary value for all the cases considered. Only SIA flux from layer  $\beta$  in Cu/V- $KS_1$  system maintains this value during the whole irradiation exposure. For the rest of cases,  $J_i^{(\beta)}$  decreases before reaching steady state. The significance of the decrease is very small in Cu/V system for  $KS_{\min}$ . In Cu/Nb system, the decrease is more notable for  $KS_{\min}$  than for  $KS_1$ . **Figure 8b** shows that vacancy flux from layer  $\beta$  strongly depends upon the system investigated and the interface configuration. It should be noted that, once the steady state is reached, the fluxes of SIAs and vacancies from layer  $\alpha$ , or layer  $\beta$ , to the interface have the same value for each particular system and interface configuration.

Besides the transfer velocity of point defects to the interface, which does not generate differences in layer  $\alpha$  since it is the same metal (Cu) for all the systems investigated, point-defect flux relies on point-defect concentration at the interface and point-defect trap occupation probability (cf. Eq. (4)). Despite the differences between the values of point-defect concentration at the interface and point-defect average concentration, their temporal profiles show a very similar behavior. So, the former are not shown here. On the other hand, and lastly, temporal profiles of trap occupation probabilities by point defects are depicted in **Figure 9**. Trap occupation probability by SIAs (**Figure 9a**) increases and then it reaches a stationary state for all the cases studied. It can be also seen that the stationary value is higher for  $KS_1$  than for  $KS_{\min}$  in both systems, Cu/Nb and Cu/V. Steady state is reached sooner by Cu/V system than by Cu/Nb one either for  $KS_1$  or  $KS_{\min}$ . The stationary value of  $f_i$  is the same in the two systems for  $KS_1$  but not for  $KS_{\min}$ . For this case, the steady-state value of  $f_i$  is

higher for Cu/Nb system than for Cu/V one. Vacancy trap occupation probability shows a similar behavior to SIA one for  $KS_1$  in both systems (cf. **Figure 9a** and **9b**). Nevertheless,  $f_v$  behaves very different for  $KS_{\min}$  due to the initial condition.

#### 6.4. Discussion

Thin layered systems are designed with the aim to increase interfaces density. The higher the available surface for annihilation of point defects, the lower their concentration within the system. This was demonstrated at very different time scales [17,26]. Cu/Nb interfaces synthesized by PVD are virtually inexhaustible sinks for radiation-induced point defects [4,11]. SIA and vacancy delocalization allow for long-range interactions between them which facilitates Frenkel-pair recombination. Cu SIAs are loaded at Cu/Nb interfaces during the collision cascades and their subsequent emission promotes enhanced recombination near the interface [23]. However, the effect of interface point-defect trapping and recombination mechanisms on the long-term evolution of point defects has not been investigated. So, before comparing model predictions in Cu/Nb and Cu/V NMMCs, it is worth discussing the influence of these mechanisms on point-defect concentrations.

Temporal profiles of average SIA and vacancy concentrations in Cu and Nb layers of Cu/Nb system for the different values of  $z$  are shown in **Figures 2** and **3**, respectively. In the previous section, it has been stated that point-defect evolution is not affected by the increase of  $z$  value from 1 to 4 either for  $KS_{\min}$  or  $KS_1$ .  $KS_{\min}$ , i.e., ground state structure, along a value of  $z$  equal to 1, can be considered the reference case among the cases studied as it is the one that most accurately represents reality in multilayer composites synthesized by PVD. On the other hand,  $KS_1$ , i.e., defect-free structure, can be seen as  $KS_{\min}$  loaded with SIAs. Thus, interface SIA loading ( $KS_1$  with  $z=1$ ) decreases steady-state values of vacancy average concentration in Cu and Nb layers with respect to the reference case (cf. **Figures 2b** and **3b** respectively) while, on the contrary, the stationary SIA average concentration value does not show any difference in Cu layer (cf. **Figure 2a**) or increases slightly in Nb one (cf. **Figure 3a**). These value differences are caused by dissimilarities on the evolution of average point-defect net-production rate and/or point-defect flux to the interface between metals. Either in Cu or Nb layer, the higher flux of vacancies for  $KS_1$  (cf. **Figures 7b** and **8b** respectively) results in the lower value of vacancy average concentration. On the contrary, the higher point-defect net-production rate for  $KS_1$  (cf. **Figure 6b**) is responsible of the higher SIA average concentration value in Nb layer.

For  $KS_1$ , temporal profiles of point-defect average concentrations are independent of

$z$  value up to  $\tau \approx 10^7$ . But then, if point-defect trapping is allowed but point-defect recombination at the interface is not (KS<sub>1</sub> with  $z=0$ ), point-defect average concentrations increase (cf. **Figures 2 and 3**) until bulk recombination compensates the suppression of point-defect flux to the interface due to the saturation of traps by SIAs and vacancies, i.e.,  $f_i + f_v = 1$  (results not shown). So, with respect to the equivalent case in which interface recombination is allowed (KS<sub>1</sub> with  $z=1$ ), it can be concluded that both SIA and vacancy average concentration at steady state increase when no recombination of point defects occurs at the interface. If neither point-defect trapping nor point-defect recombination at the interface are allowed (KS<sub>min</sub> with  $z=0$ ), steady-state value of SIA and vacancy average concentration increases and decreases, respectively, in comparison to the rest of cases studied (cf. **Figures 2 and 3**). This case represents the absence of traps for point defects. Since there is no point-defect flux to the interface between metals, the only annihilation mechanism of point defects is the bulk recombination and, consequently, evolution of SIA and vacancy average concentration show the same behavior.

Now, a comparison between point-defect concentrations within the systems investigated is performed. Special attention is paid to the behavior of the same metal Cu (layer  $\alpha$ ), when it is surrounded by diverse metals  $\beta$  (Nb, or V). Cu/V<sub>pvd</sub> interfaces are capable of accommodating 2-3 SIAs or vacancies per MDI as Cu/Nb<sub>pvd</sub> ones but their areal MDI density is different [37]. According to Mao *et al.* [34], constitutional vacancies seem to play an important role in Cu vacancy concentration dissimilarities between the two systems studied at the steady state. So, numerical simulation results for KS<sub>min</sub> and KS<sub>1</sub> interface configurations are compared too. Temporal profiles of average SIA and vacancy concentrations in layers  $\alpha$  and  $\beta$  are represented in **Figures 4 and 5**, respectively. SIA average concentrations in layer  $\alpha$  show the same behavior for all the cases studied (cf. **Figure 4a**). This is due to the absence of differences in  $\bar{\Pi}^{(\alpha)}$  (cf. **Figure 6a**) and  $J_i^{(\alpha)}$  (cf. **Figure 7a**). On the other hand, a general comparison of the results reveals that vacancy average concentration in layer  $\alpha$  group by interface configurations, KS<sub>min</sub> or KS<sub>1</sub> (cf. **Figure 4b**), while in layer  $\beta$ , SIA and vacancy average concentration group by system, Cu/Nb or Cu/V (cf. **Figures 5a and 5b** respectively). However, differences can be found between the cases that belong to each group except in  $\bar{\chi}_v^{(\alpha)}$  for KS<sub>1</sub>. The lower steady-state values of  $\bar{\chi}_v^{(\alpha)}$  correspond to Cu/Nb- and Cu/V-KS<sub>1</sub> systems (cf. **Figure 4b**) and are the result of a higher  $J_v^{(\alpha)}$  before reaching a stationary state (cf. **Figure 7b**). For KS<sub>min</sub>, dissimilarities in  $\bar{\chi}_v^{(\alpha)}$  between Cu/Nb and Cu/V systems are caused by differences in vacancy flux from layer  $\alpha$  too.  $J_v^{(\alpha)}$  reaches steady state in Cu/V system but in

Cu/Nb one vacancy flux from layer  $\alpha$  continues increasing for a while (cf. inset of **Figure 7b**) because  $f_v$  decreases (recall boundary condition (11) and cf. inset of **Figure 9b**). This causes that between  $\tau \approx 3 \cdot 10^5$  and  $\tau \approx 2 \cdot 10^6$  the vacancies annihilated at the interface are more than the vacancies produced in layer  $\alpha$  which makes  $\bar{\chi}_v^{(\alpha)}$  lower in Cu/Nb system (cf. **Figure 4b**). Consequently, steady-state value of  $\bar{\chi}_v^{(\alpha)}$  is lower in Cu/Nb system than in Cu/V one for  $\text{KS}_{\min}$ . Before comparing vacancy-concentration results in layer  $\alpha$  to results reported in **Ref. (34)**, point-defect concentrations in layer  $\beta$  are analyzed too. Differences in the steady-state value of  $\bar{\chi}_i^{(\beta)}$  and  $\bar{\chi}_v^{(\beta)}$  between the four cases investigated can be explained by means of the evolution of  $\bar{\Pi}^{(\beta)}$  and  $J_v^{(\beta)}$  respectively. Thus, the higher the average point-defect net-production rate in layer  $\beta$  at longer times (cf. **Figure 6b**), the higher the stationary value of SIA average concentration (cf. **Figure 5a**). And, the higher the vacancy flux from layer  $\beta$  to the interface at longer times (cf. **Figure 8b**), the lower the stationary value of vacancy average concentration (cf. **Figure 5b**). As in  $\bar{\chi}_v^{(\alpha)}$  for Cu/Nb- $\text{KS}_{\min}$  system, there is an interval in which  $\bar{\chi}_v^{(\beta)}$  decreases for Cu/V- $\text{KS}_{\min}$  system (cf. **Figures 4b** and **5b**). Mechanisms illustrated above are also responsible of this effect in this case. This confirms that the decrease of vacancy average concentration seen before reaching steady state in the Cu layer of Cu/Nb system and V layer of Cu/V one for  $\text{KS}_{\min}$  is due to the lower diffusion coefficient of vacancies in the other metal, niobium and copper respectively. So, in short, the response to irradiation of the systems investigated here depends on both, interface characteristics and bulk properties. The presence of interface constitutional vacancies decreases the concentration of SIAs slightly, if at all, and increases the concentration of vacancies significantly in each system.

Lastly, vacancy-concentration results in layer  $\alpha$  are compared to results reported in **Ref. (34)**. According to experimental results, vacancy concentration at the center of a 30-nm Cu layer was 1.9 times lower in Cu/Nb system than in Cu/V one. Similar predictions, a factor of 2 instead of 1.9, were obtained for vacancy average concentration in kinetic Monte Carlo simulations. As commented previously, the case that most accurately represents reality in multilayer composites synthesized by PVD corresponds to  $\text{KS}_{\min}$  interface configuration along a  $z$  value equal to 1. For this case, vacancy concentration at the center of the Cu layer (results not shown here due to the similitudes with vacancy average concentration) and  $\bar{\chi}_v^{(\alpha)}$  (cf. **Figure 4b**) are approximately 1.8 and 1.9 times lower respectively in Cu/Nb system than in Cu/V one. Mao *et al.* associated the lower Cu vacancy concentration in Cu/Nb- $\text{KS}_{\min}$

system to its higher probability of absorbing a vacancy at the interface. Either Cu/Nb<sub>pvd</sub> or Cu/V<sub>pvd</sub> interfaces are capable of accommodating 2-3 SIAs or vacancies per MDI but the areal MDI density is ~6.4 times higher in Cu/Nb<sub>pvd</sub> interface than in Cu/V<sub>pvd</sub> one. However, the lower the point-defect trap concentration, the lower the vacancy average concentration according to our results ( $KS_{\min}$  with  $z=0$ ). So, the explanation for above factor values, ~1.8 and ~1.9, points to the diffusivity of vacancies that is lower in copper than in niobium and makes Cu vacancy concentration decrease in Cu/Nb system before reaching the steady state. This results in a stationary value which is lower than in Cu/V system. In spite of the very good qualitative agreement between experimental results and our model predictions, it is worth to discuss some details. The production rate of Frenkel pairs has been calculated for copper, niobium, and vanadium layers with the irradiation conditions reported in **Ref. (34)** using Transport of Ions in Matter (TRIM) [39]. Then, a factor of  $10^{-2}$  has been applied. According to Mao *et al.*, this normalization achieved a perfect agreement between the absolute concentrations of Cu vacancies calculated in their rate-theory model and the experimental data. Nevertheless, a factor of  $\sim 2.41 \cdot 10^{-4}$  and  $\sim 1.17 \cdot 10^{-4}$  is needed in Cu/Nb and Cu/V system respectively with our model which is quite smaller than  $10^{-2}$ . Experimental results are given only in Cu layer (layer  $\alpha$ ) so it would be recommendable to have vacancy concentration in layer  $\beta$  (Nb, or V) too. Thus, a factor for each metal layer could be estimated.

## 6.5. Conclusions

A continuum model of point-defect evolution in multilayer composites is presented in this chapter. In order to compare quantitatively model predictions with experimental results in multilayer composites synthesized by PVD [34], previous chapter boundary equations and initial conditions have had to be adapted. Firstly, the effect of interface annihilation mechanisms on the long-term evolution of point defects has been studied. If SIAs and vacancies can be trapped but cannot recombine with the opposite point defect at the interface between metals, SIA and vacancy concentrations within the system increase. However, if none of the two mechanisms is operative, i.e., absence of traps for point defects, SIAs and vacancies behave similarly which leads to a rise and a drop in the concentration of SIAs and vacancies respectively. In addition, the effect of interface SIA loading and constitutional vacancies has been investigated too by comparing the results corresponding to  $KS_{\min}$  and  $KS_1$  interface configurations. The presence of interface constitutional vacancies decreases the concentration of SIAs slightly, if at all, and increases the concentration of vacancies significantly. The latter is in agreement with VDZ measurements [18] that reveal a higher sink

efficiency in Cu/Nb<sub>spd</sub> interfaces [13] than in Cu/Nb<sub>pvd</sub> ones [4] for vacancies. On the contrary, interface SIA loading has the reverse effect to the presence of constitutional vacancies at the interface. The emission of SIAs loaded at the interface promotes enhanced recombination near the interface according to Liu *et al.* [23]. So, this agrees too with our results that predict a significant decrease of vacancy concentration when SIAs are loaded at the interface.

The response to irradiation of the systems investigated here, Cu/Nb and Cu/V, depends on both interface characteristics and bulk properties. It is worth highlighting that point-defect flux to the interface depends upon the value of point-defect trap concentration, which is characteristic of each metal couple  $\alpha$ - $\beta$ , and the properties of the two adjacent layers (recalling boundary condition (4)). However, the influence of the properties of one metal in the point-defect evolution of the other metal is only effective if there are constitutional vacancies at the interface, i.e., for  $KS_{\min}$ . This can be seen in the temporal evolution of vacancies. The concentration of vacancies decreases before reaching the steady state in the Cu layer of Cu/Nb system because the diffusivity of vacancies is lower in niobium than in copper. It occurs similarly in the V layer of the Cu/V system. A comparison of model results for  $KS_{\min}$  shows no differences between Cu/Nb and Cu/V systems regarding SIA temporal evolution in copper (layer  $\alpha$ ), while in layer  $\beta$ , SIA concentration at steady state is lower in niobium than in vanadium. On the other hand, the lower steady-state value of vacancy concentration in layer  $\alpha$  and  $\beta$  correspond to Cu/Nb and Cu/V systems respectively for  $KS_{\min}$ . Irradiated Cu/Nb NMMCs had numerous voids in Cu layers at the end of the experiment but no voids were seen in Nb layers due to the high and low mobility of vacancies, respectively, in these metal layers [18]. Hence, the high concentration of vacancies in Nb layer should not be an issue in terms of damage.

As a final conclusion, there is a very good qualitative agreement between our model predictions and results reported in Ref. (34). Indeed, vacancy concentration at the center of the Cu layer and average one are approximately 1.8 and 1.9 times lower, respectively, in Cu/Nb system than in Cu/V one for  $KS_{\min}$ . So that the agreement is quantitative too, a factor of  $\sim 2.41 \cdot 10^{-4}$  and  $\sim 1.17 \cdot 10^{-4}$  should be applied in Cu/Nb and Cu/V system respectively to the production rate of Frenkel pairs calculated using TRIM for each layer (Cu, Nb, or V) instead the factor of  $10^{-2}$  suggested by Mao *et al.* and used in the present study. The small value of these factors could mean that, although Cu vacancy concentration differences between Cu/Nb- and Cu/V- $KS_{\min}$  systems are determined at longer time scales, multilayer composites designed at the nanometric scale may be governed by mechanisms that occurs in lower time

scales. In the case of having also experimental vacancy concentration in layer  $\beta$  (Nb, or V) too and not only in Cu (layer  $\alpha$ ), it could be estimated a factor for each metal layer that in turn may allow relating interface characteristics and bulk properties with the magnitude of the factor. After validation with data of experiments carried out in other systems, point-defect concentrations may be calculated for any NMMC whose properties were known without the need of further experiments or atomistic simulations.

## Nomenclature of Chapter 6

$A$	dimensionless production rate of point defects, -;
$C$	concentration of point defects, $\text{m}^{-3}$ ;
$D$	diffusivity, $\text{m}^2 \text{s}^{-1}$ ;
$E$	dimensionless parameter of point-defect jumps from the matrix, -;
$F$	dimensionless parameter of point-defect surface recombination, -;
$f$	trap occupation probability, -;
$K$	transfer velocity, $\text{m s}^{-1}$ ;
$K_{iv}$	recombination factor of the anti-defects, $\text{m}^3 \text{s}^{-1}$ ;
$K_0$	production rate of point defects, $\text{m}^{-3} \text{s}^{-1}$ ;
$L$	layer thickness, $\text{m}$ ;
$R_C$	removal rate of point defects due to recombination, $\text{m}^{-3} \text{s}^{-1}$ ;
${}^{tot}S$	concentration of traps for point defects, $\text{m}^{-2}$ ;
$t$	time, $\text{s}$ ;
$x$	spatial coordinate, $\text{m}$ ;
$z$	number of jumps, -;

### *Greek letters*

$\alpha_s$	surface recombination coefficient, $\text{m}^{-2} \text{s}^{-1}$ ;
$\chi$	dimensionless concentration of point defects, -;
$\delta$	dimensionless diffusivity, -;
$\tau$	dimensionless time, -;
$\varpi$	dimensionless lattice spacing, -;
$\xi$	dimensionless spatial coordinate, -;

### *Superscripts*

*	equilibrium;
$(\alpha)$	layer of element $\alpha$ ;
$(\gamma)$	layer of element $\gamma$ ;
$(\beta)$	layer of element $\beta$ ;

$(\alpha\text{-}\beta)$  system formed by elements  $\alpha$  and  $\beta$ ;

*Subscripts*

$i$  self-interstitial atom;

$j$  point defect of the type  $j$ ;

$v$  vacancy.

## References of Chapter 6

- [1] A. Misra, M. J. Demkowicz, X. Zhang, and R. G. Hoagland, "The radiation damage tolerance of ultra-high strength nanolayered composites", *JOM: Journal of the Minerals, Metals and Materials Society*, vol. 59, no. 9, pp. 62-65, 2007.
- [2] M. J. Demkowicz, P. Bellon, and B. D. Wirth, "Atomic-scale design of radiation-tolerant nanocomposites", *MRS bulletin*, vol. 35, no. 12, pp. 992-998, 2010.
- [3] D. L. Medlin, M. J. Demkowicz, and E. A. Marquis, "Solid State interfaces: Toward an atomistic-scale understanding of structure, properties, and behavior", *JOM: Journal of the Minerals, Metals and Materials Society*, vol. 62, no. 12, pp. 52-52, 2010.
- [4] M. J. Demkowicz, J. I. A. N. Wang, and R. G. Hoagland, "Interfaces between dissimilar crystalline solids", *Dislocations in solids*, vol. 14, pp. 141-207, 2008.
- [5] G. Kurdjumow and G. Sachs, "Über den mechanismus der stahlhärtung", *Zeitschrift für Physik*, vol. 64, no. 5-6, pp. 325-343, 1930.
- [6] Z. Nishiyama, "X-ray investigation of the mechanism of the transformation from face centered cubic lattice to body centered cubic", *Science Reports of the Tohoku Imperial University*, vol. 23, pp. 637-664, 1934.
- [7] G. Wassermann, "Über den Mechanismus der  $\alpha$ - $\gamma$ -Umwandlung des Eisens", *Mitteilungen aus dem Kaiser Wilhelm-Institut für Eisenforschung zu Düsseldorf*, Verlag Stahleisen, 1935.
- [8] M. J. Demkowicz and R. G. Hoagland, "Structure of Kurdjumov–Sachs interfaces in simulations of a copper–niobium bilayer", *Journal of Nuclear Materials*, vol. 372, no. 1, pp. 45-52, 2008.
- [9] A. J. Vattré and M. J. Demkowicz, "Determining the Burgers vectors and elastic strain energies of interface dislocation arrays using anisotropic elasticity theory", *Acta Materialia*, vol. 61, no. 14, pp. 5172-5187, 2013.
- [10] A. J. Vattré and M. J. Demkowicz, "Partitioning of elastic distortions at a semicoherent heterophase interface between anisotropic crystals", *Acta Materialia*, vol. 82, pp. 234-243, 2015.
- [11] M. J. Demkowicz, R. G. Hoagland, and J. P. Hirth, "Interface structure and radiation damage resistance in Cu-Nb multilayer nanocomposites", *Physical Review Letters*, vol. 100, no. 13, article 136102, 2008.
- [12] S. A. Skirlo and M. J. Demkowicz, "Viscoelasticity of stepped interfaces", *Applied Physics Letters*, vol. 103, no. 17, article 171908, 2013.

- [13] M. J. Demkowicz and L. Thilly, "Structure, shear resistance and interaction with point defects of interfaces in Cu–Nb nanocomposites synthesized by severe plastic deformation", *Acta Materialia*, vol. 59, no. 20, pp. 7744-7756, 2011.
- [14] J. Wang, R. G. Hoagland, X. Y. Liu, and A. Misra, "The influence of interface shear strength on the glide dislocation–interface interactions", *Acta Materialia*, vol. 59, no. 8, pp. 3164-3173, 2011.
- [15] A. A. Sagüés and J. Auer, "Mechanical behavior of Nb-1% Zr implanted with He at various temperatures", no. CONF-750989-P2, 1976.
- [16] N. Li, M. J. Demkowicz, and N. A. Mara, "Microstructure Evolution and Mechanical Response of Nanolaminate Composites Irradiated with Helium at Elevated Temperatures", *JOM: Journal of the Minerals, Metals and Materials Society*, vol. 69, no. 11, pp. 2206-2213, 2017.
- [17] M. J. Demkowicz and R. G. Hoagland, "Simulations of collision cascades in Cu–Nb layered composites using an EAM interatomic potential", *International Journal of Applied Mechanics*, vol. 1, no. 3, pp. 421-442, 2009.
- [18] W. Han, M. J. Demkowicz, N. A. Mara, E. Fu, S. Sinha, A. D. Rollett, Y. Wang, J. S. Carpenter, I. J. Beyerlein, and A. Misra, "Design of radiation tolerant materials via interface engineering", *Advanced Materials*, vol. 25, no. 48, pp. 6975-6979, 2013.
- [19] C. González, R. Iglesias, and M. J. Demkowicz, "Point defect stability in a semicoherent metallic interface", *Physical Review B*, vol. 91, no. 6, article 064103, 2015.
- [20] S. L. Dudarev, "Density functional theory models for radiation damage", *Annual Review of Materials Research*, vol. 43, pp. 35-61, 2013.
- [21] X. Y. Liu, R. G. Hoagland, J. Wang, T. C. Germann, and A. Misra, "The influence of dilute heats of mixing on the atomic structures, defect energetics and mechanical properties of fcc–bcc interfaces", *Acta Materialia*, vol. 58, no. 13, pp. 4549-4557, 2010.
- [22] X. Y. Liu, R. G. Hoagland, M. J. Demkowicz, Michael Nastasi, and A. Misra, "The influence of lattice misfit on the atomic structures and defect energetics of face centered cubic–body centered cubic interfaces", *Journal of Engineering Materials and Technology*, vol. 134, no. 2, article 021012, 2012.
- [23] X. Y. Liu, B. P. Uberuaga, M. J. Demkowicz, T. C. Germann, A. Misra, and M. Nastasi, "Mechanism for recombination of radiation-induced point defects at interphase boundaries", *Physical Review B*, vol. 85, no. 1, article 012103, 2012.

- [24] K. Kolluri and M. J. Demkowicz, "Formation, migration, and clustering of delocalized vacancies and interstitials at a solid-state semicoherent interface", *Physical Review B*, vol. 85, no. 20, article 205416, 2012.
- [25] K. Kolluri and M. J. Demkowicz, "Dislocation mechanism of interface point defect migration", *Physical Review B*, vol. 82, no. 19, article 193404, 2010.
- [26] M. J. Demkowicz, R. G. Hoagland, B. P. Uberuaga, and A. Misra, "Influence of interface sink strength on the reduction of radiation-induced defect concentrations and fluxes in materials with large interface area per unit volume", *Physical Review B*, vol. 84, no. 10, article 104102, 2011.
- [27] W. Z. Han, M. J. Demkowicz, E. G. Fu, Y. Q. Wang, and A. Misra, "Effect of grain boundary character on sink efficiency", *Acta Materialia*, vol. 60, no. 18, pp. 6341-6351, 2012.
- [28] W. Han, E. G. Fu, M. J. Demkowicz, Y. Wang, and A. Misra, "Irradiation damage of single crystal, coarse-grained, and nanograined copper under helium bombardment at 450 C", *Journal of Materials Research*, vol. 28, no. 20, pp. 2763-2770, 2013.
- [29] L. Zhang and M. J. Demkowicz, "Morphological stability of Cu-Nb nanocomposites under high-energy collision cascades", *Applied Physics Letters*, vol. 103, no. 6, article 061604, 2013.
- [30] L. Zhang, E. Martinez, A. Caro, X. Y. Liu, and M. J. Demkowicz, "Liquid-phase thermodynamics and structures in the Cu–Nb binary system", *Modelling and Simulation in Materials Science and Engineering*, vol. 21, no. 2, article 025005, 2013.
- [31] L. Zhang and M. J. Demkowicz, "Radiation-induced mixing between metals of low solid solubility", *Acta Materialia*, vol. 76, pp. 135-150, 2014.
- [32] S. Fadda, A. M. Locci, and F. Delogu, "Modeling of point defects annihilation in multilayered Cu/Nb composites under irradiation", *Advances in Materials Science and Engineering*, vol. 2016, Article ID 9435431, 17 pages, 2016.
- [33] G. S. Was, *Fundamentals of radiation materials science – Metals and alloys*, Springer, 2007.
- [34] S. Mao, S. Shu, J. Zhou, R. S. Averback, and S. J. Dillon, "Quantitative comparison of sink efficiency of Cu-Nb, Cu-V and Cu-Ni interfaces for point defects", *Acta Materialia*, vol. 82, pp. 328-335, 2015.
- [35] I. J. Beyerlein, A. Caro, M. J. Demkowicz, N. A. Mara, A. Misra, and B. P. Uberuaga, "Radiation damage tolerant nanomaterials", *Materials Today*, vol. 16, no. 11, pp. 443-449, 2013.

- [36] M. G. McPhie, L. Capolungo, A. Y. Dunn, and M. Cherkaoui, "Interfacial trapping mechanism of He in Cu–Nb multilayer materials", *Journal of Nuclear Materials*, vol. 437, no. 1-3, pp. 222-228, 2013.
- [37] M. J. Demkowicz, A. Misra, and A. Caro, "The role of interface structure in controlling high helium concentrations", *Current Opinion in Solid State and Materials Science*, vol. 16, no. 3, pp. 101-108, 2012.
- [38] A. D. Brailsford and R. Bullough, "The rate theory of swelling due to void growth in irradiated metals", *Journal of Nuclear Materials*, vol. 44, no. 2, pp. 121-135, 1972.
- [39] J. F. Ziegler, *Transport of Ions in Matter* (TRIM), IBM Corp. Software, 1991.

## Figures of Chapter 6

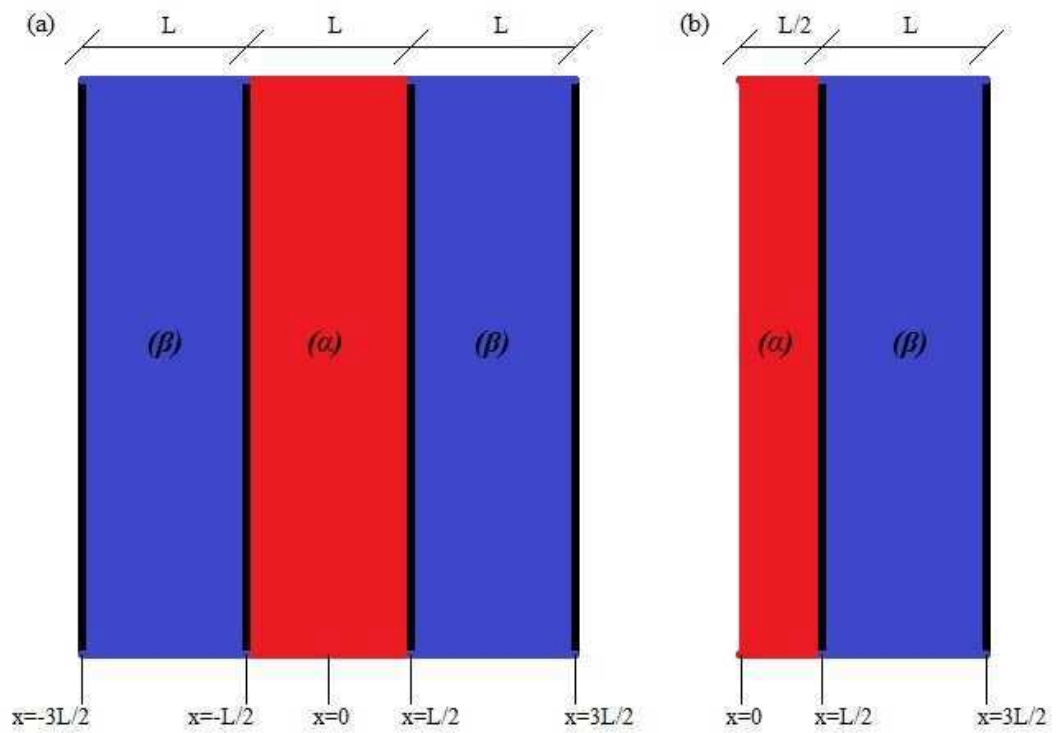


**Figure 1** Schematic of (a) the entire system and (b) the half-symmetric part modelled. Layer  $\alpha$  represents Copper while  $\beta$  indicates Niobium, or Vanadium.

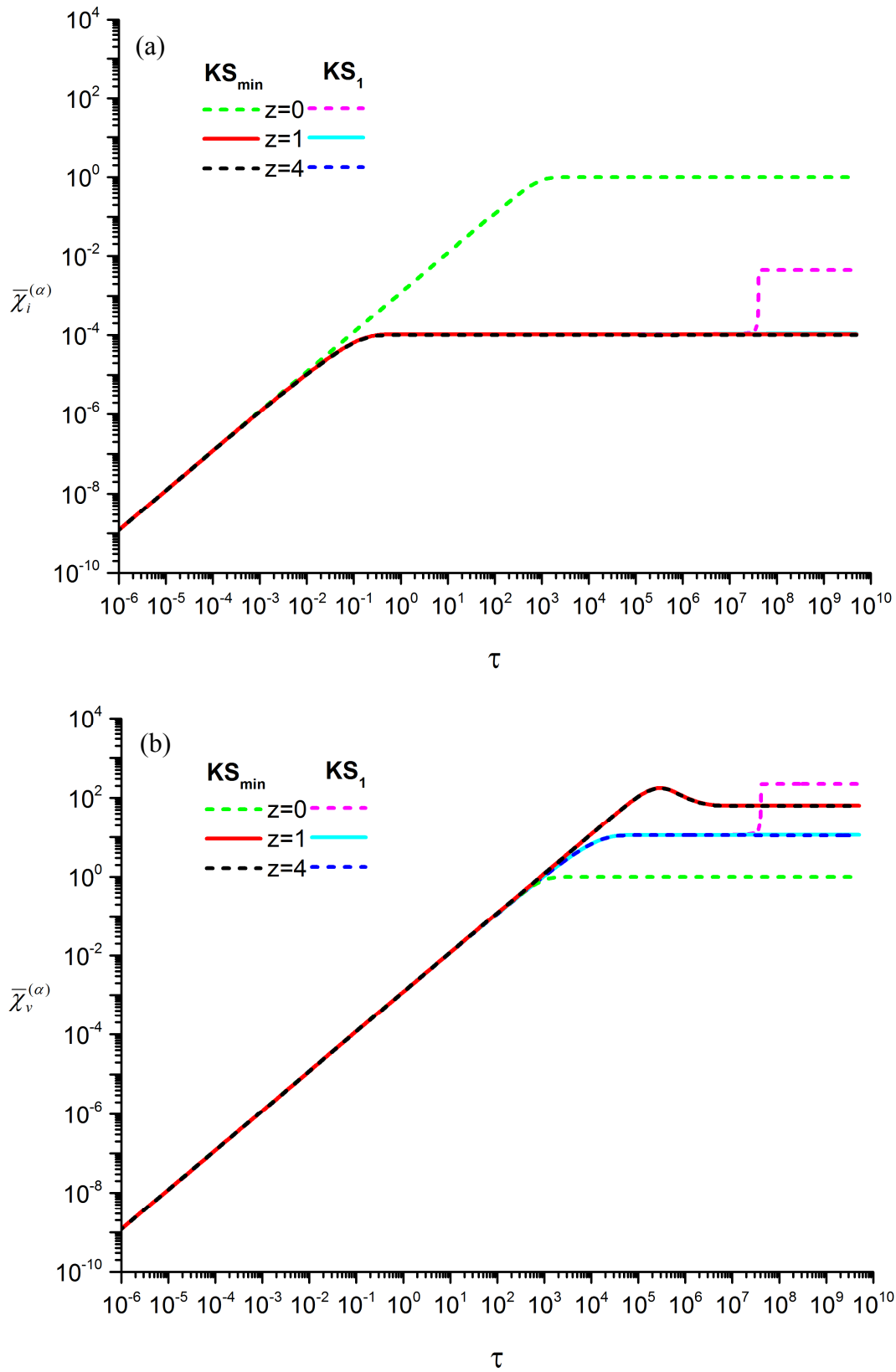


**Figure 2** Temporal profiles of average (a) SIA and (b) vacancy concentration in the Cu layer of Cu/Nb system for different values of parameter  $z$ .

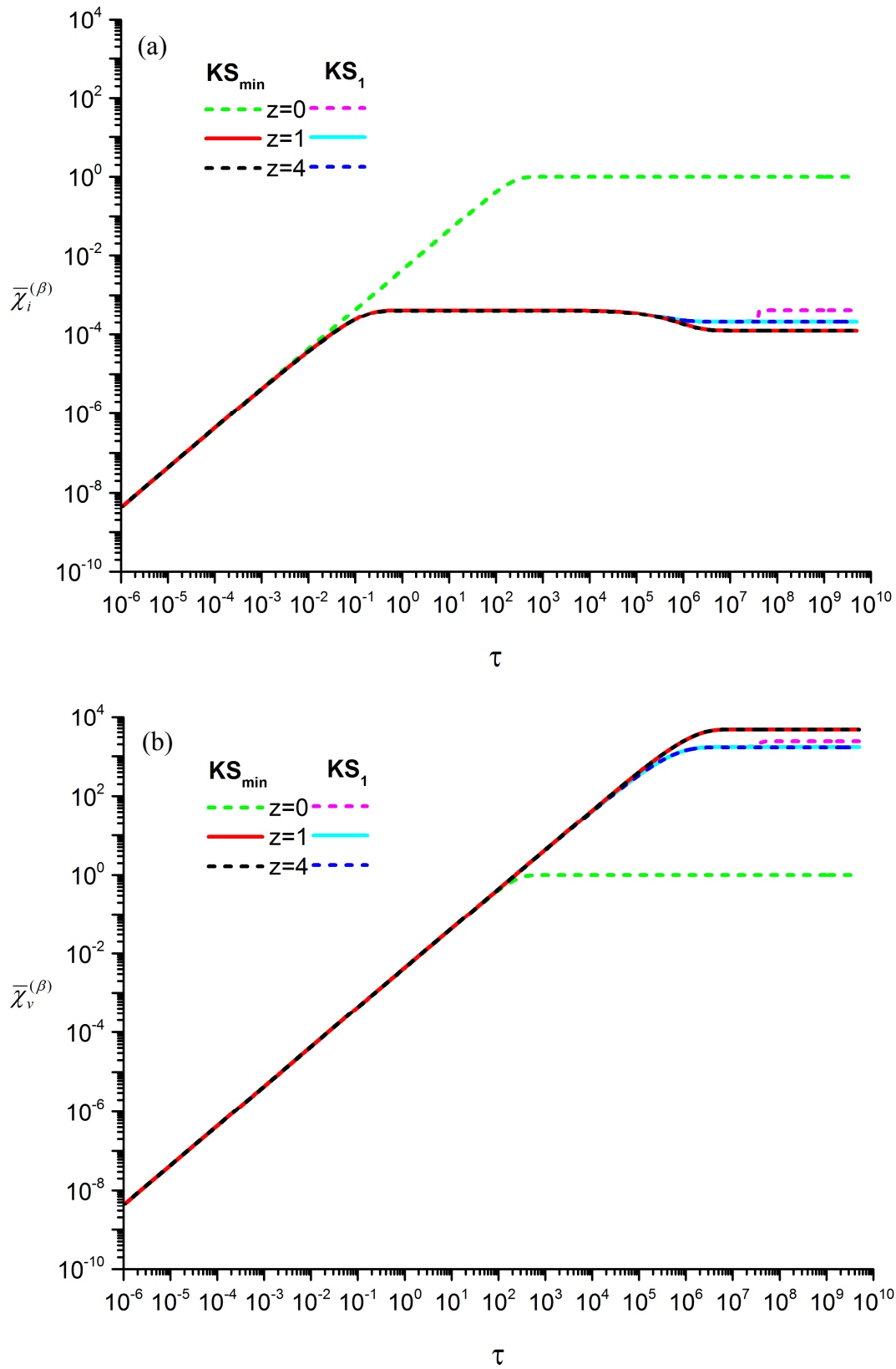


**Figure 3** Temporal profiles of average (a) SIA and (b) vacancy concentration in the Nb layer of Cu/Nb system for different values of parameter  $z$ .

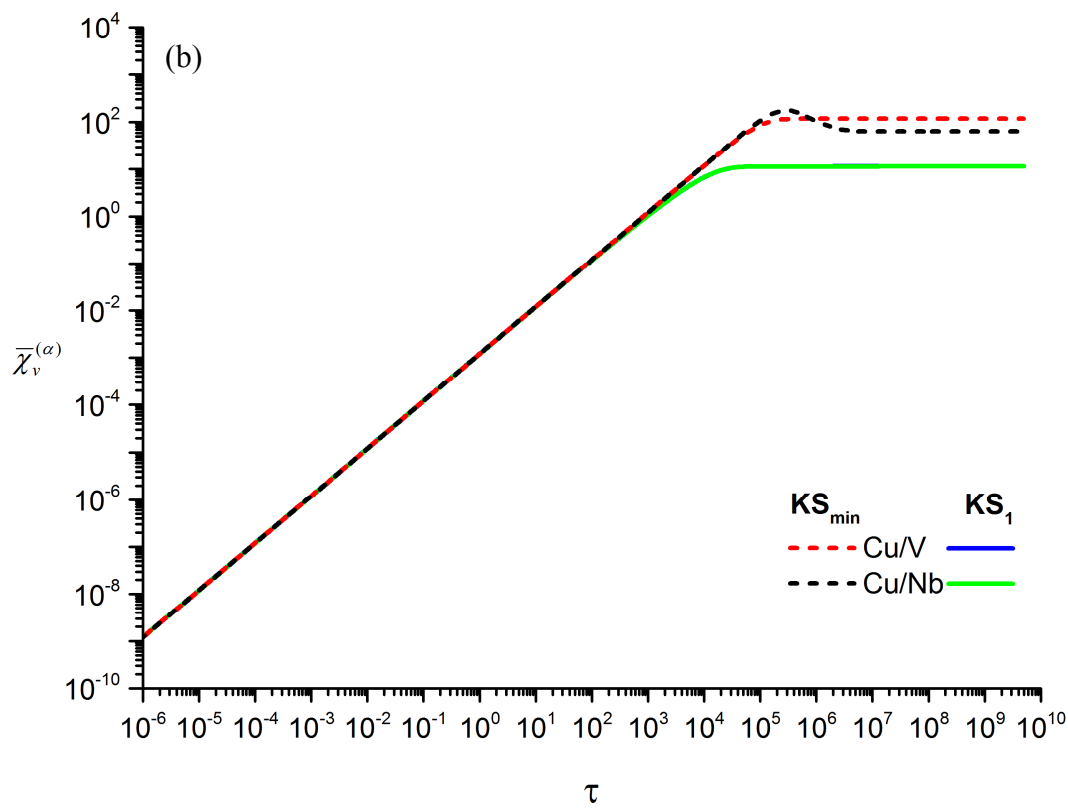
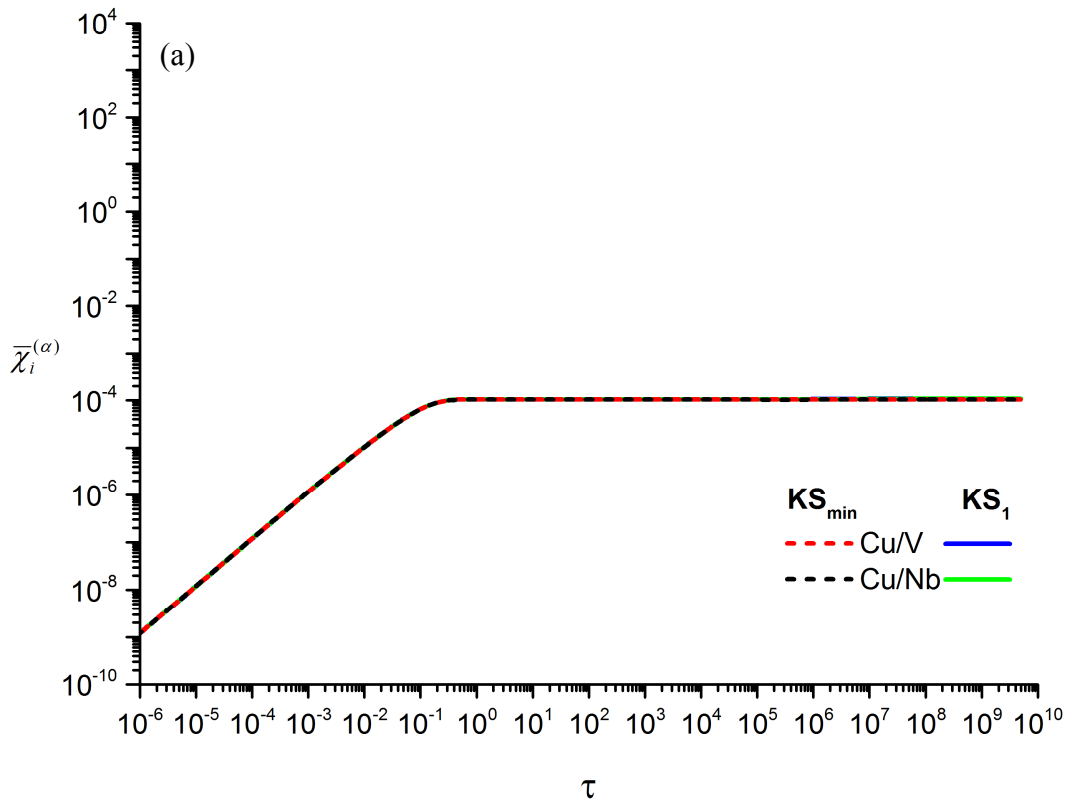


**Figure 4** Temporal profiles of average (a) SIA and (b) vacancy concentration in layer  $\alpha$  ( $z = 1$ ).

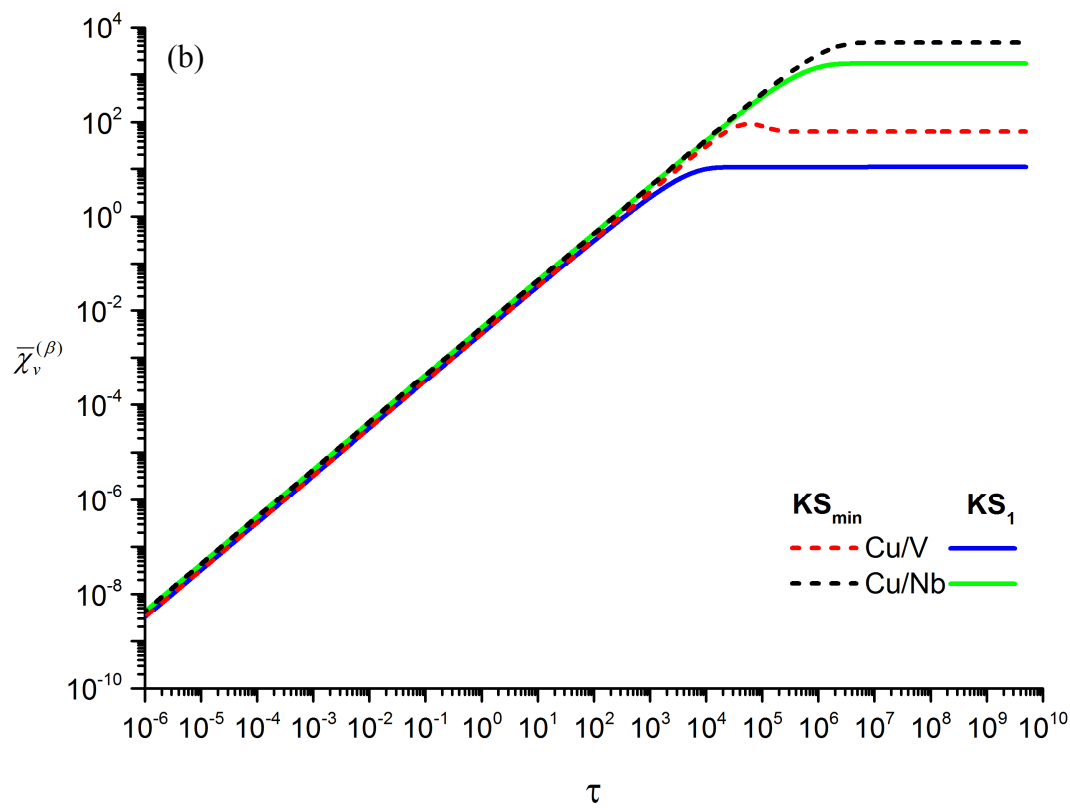
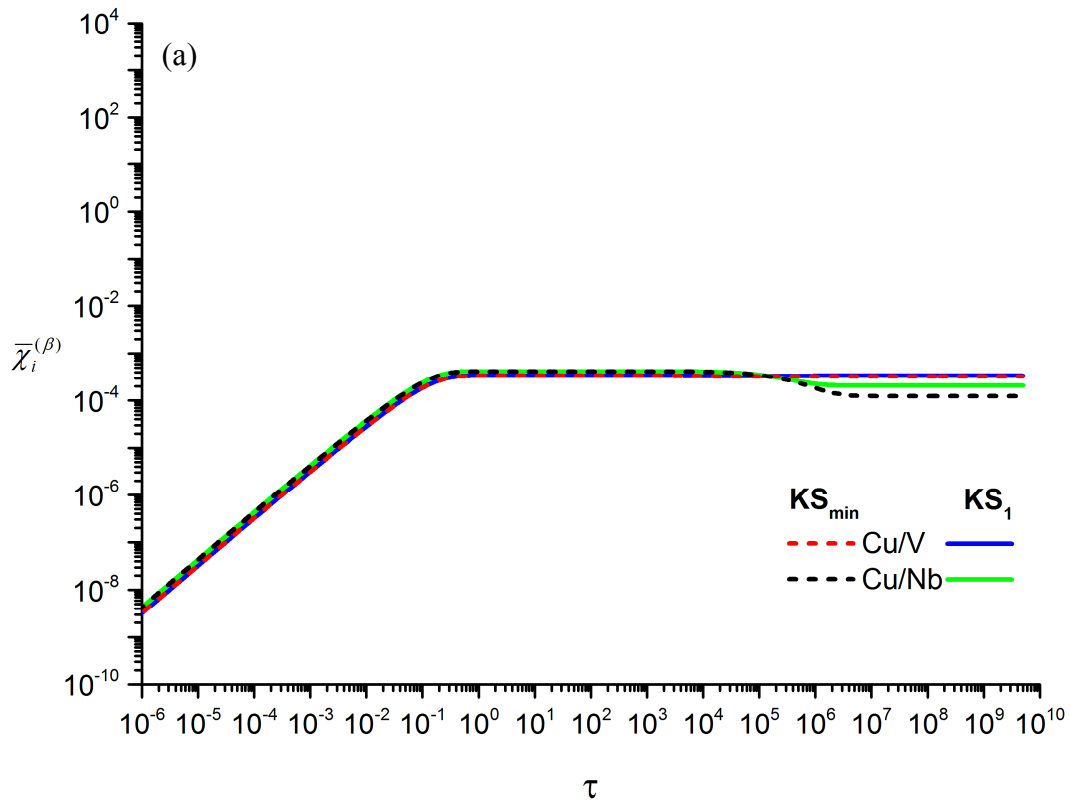


**Figure 5** Temporal profiles of average (a) SIA and (b) vacancy concentration in layer  $\beta$  ( $z = 1$ ).

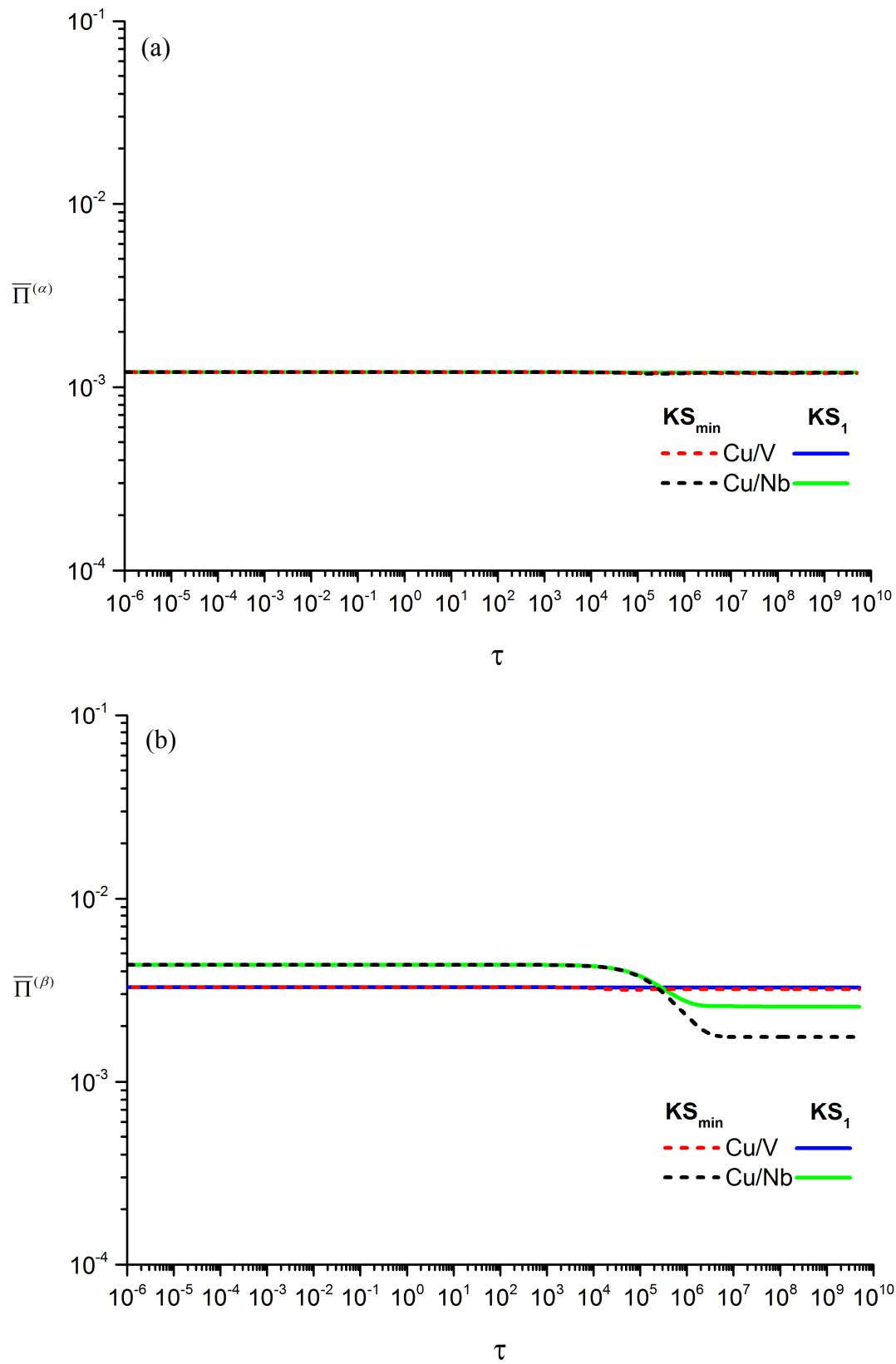


**Figure 6** Temporal profiles of average point-defect net-production rate in (a) layer  $\alpha$  and (b) layer  $\beta$  ( $z = 1$ ).

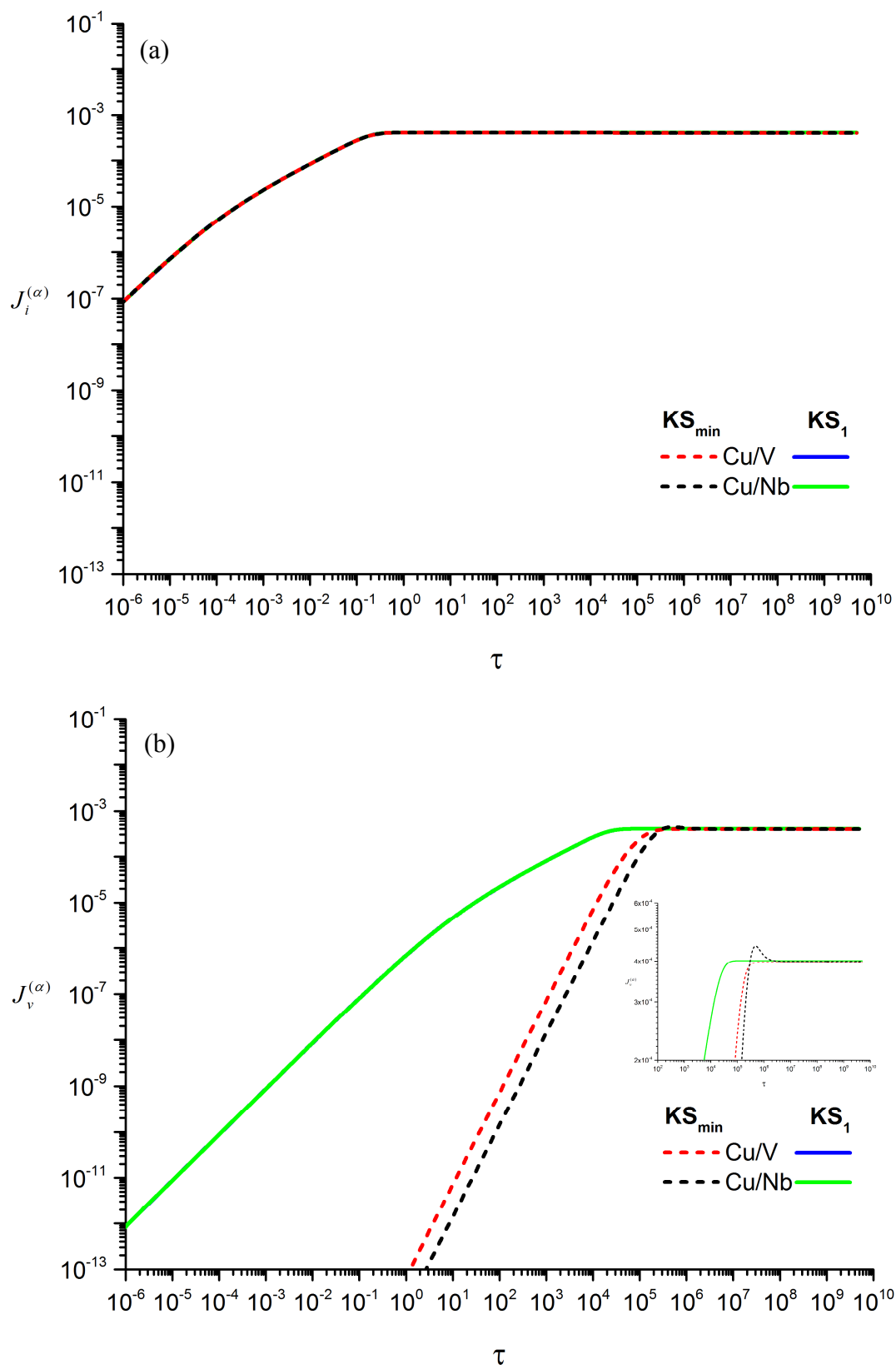


**Figure 7** Temporal profiles of (a) SIA and (b) vacancy flux from layer  $\alpha$  to the interface between metals  $\alpha$  and  $\beta$  ( $z=1$ ).

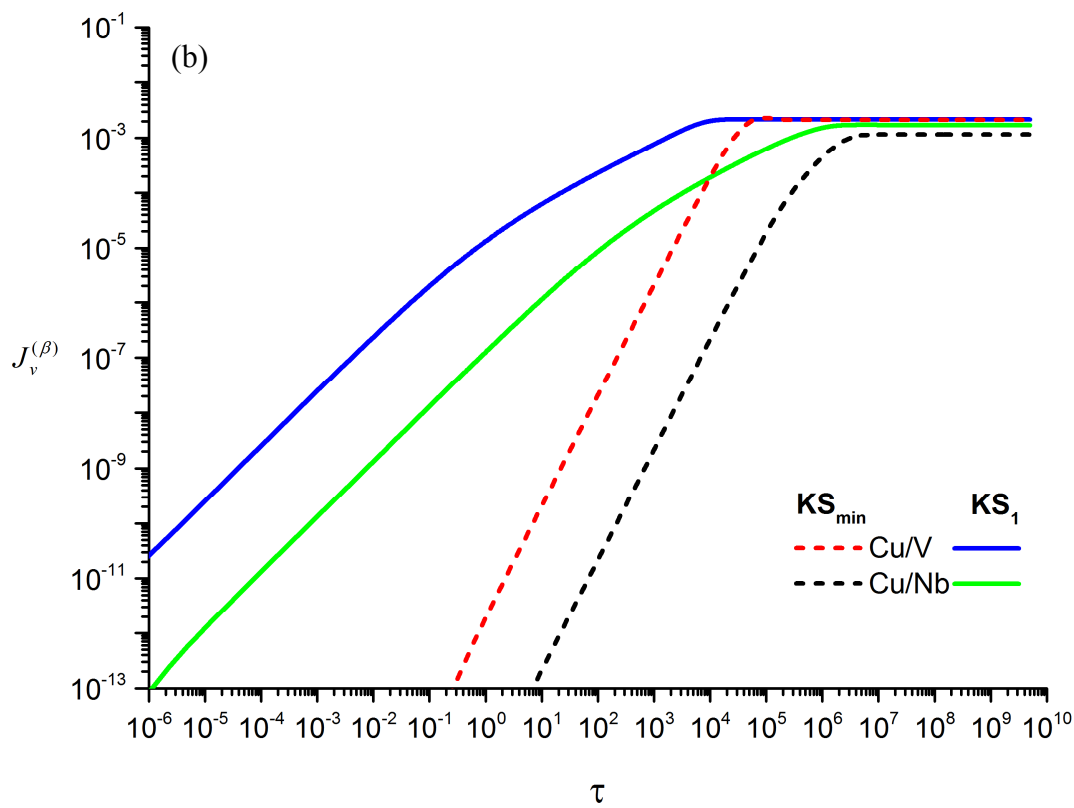
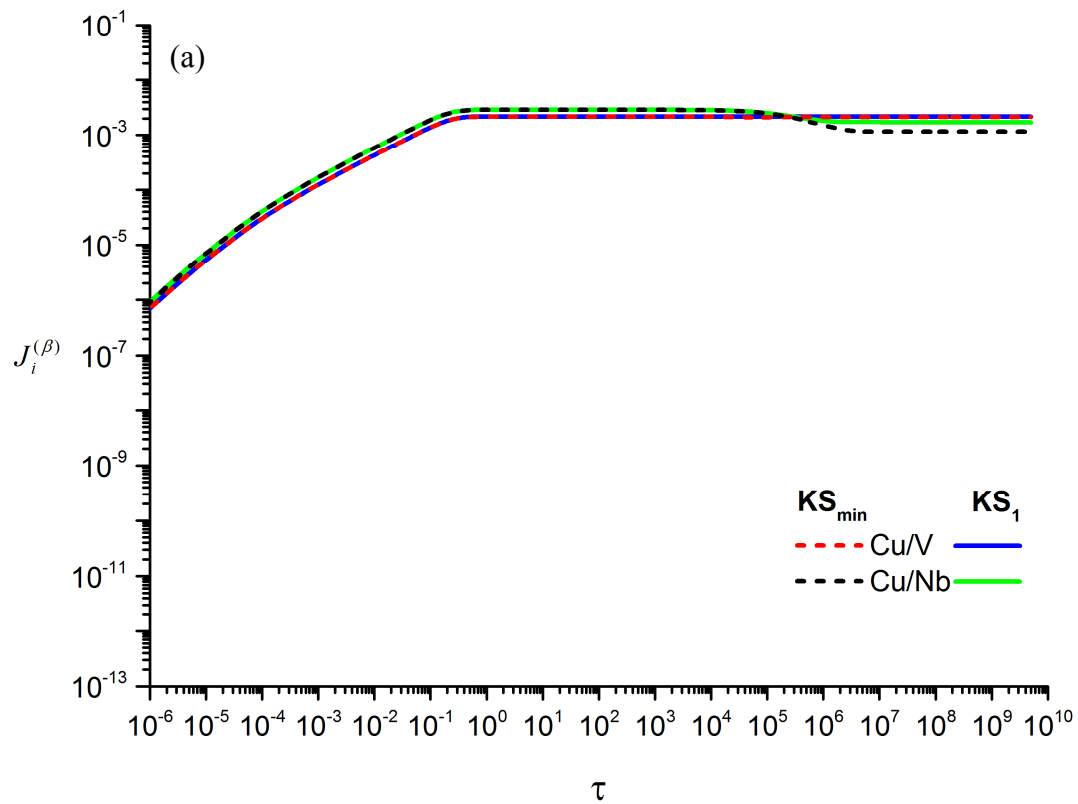


**Figure 8** Temporal profiles of (a) SIA and (b) vacancy flux from layer  $\beta$  to the interface between metals  $\alpha$  and  $\beta$  ( $z = 1$ ).

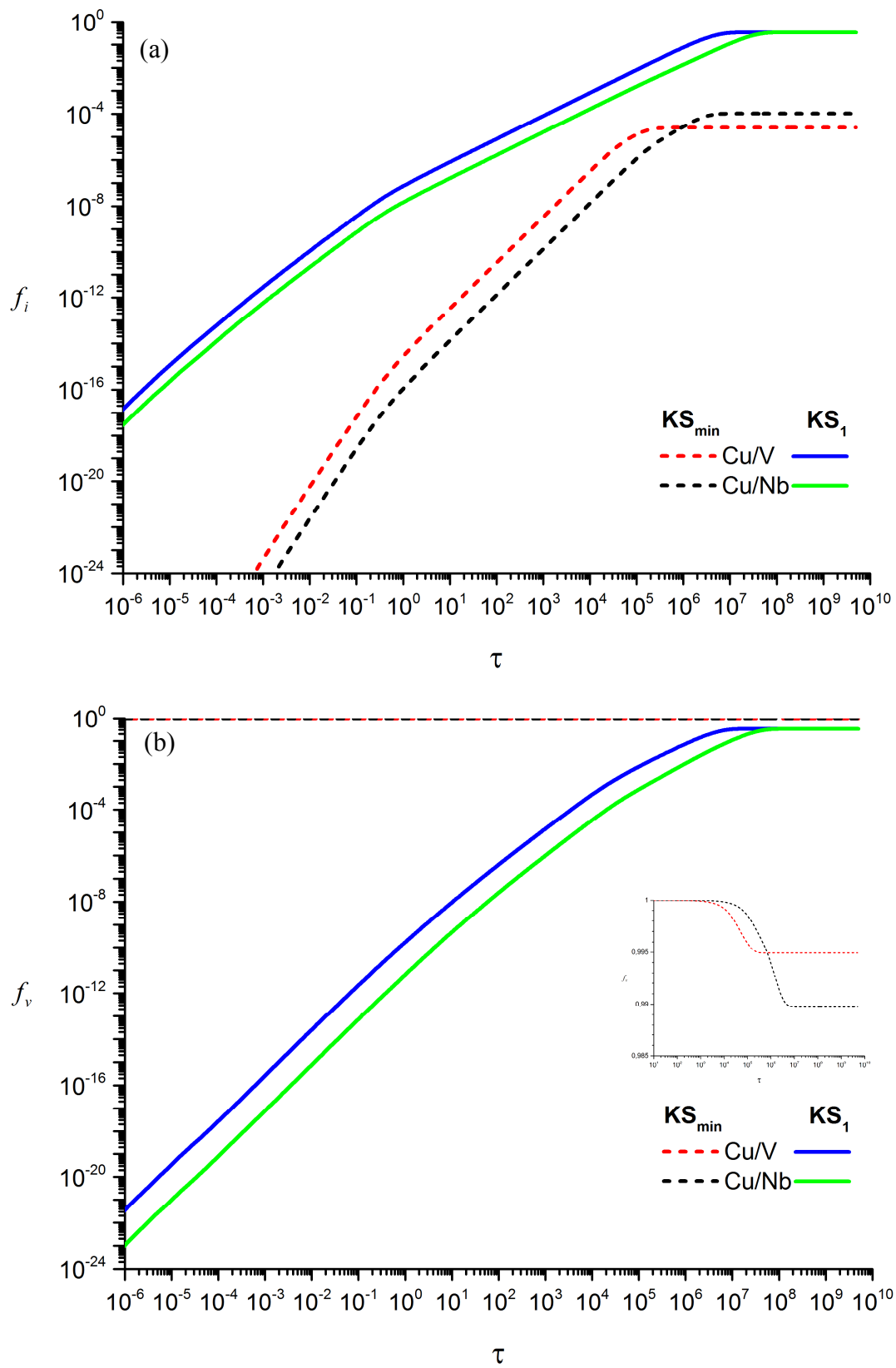


**Figure 9** Temporal profiles of (a) SIA and (b) vacancy trap occupation probability at the interface between metals  $\alpha$  and  $\beta$  ( $z = 1$ ).

## Chapter 7

### Concluding remarks

The objective of this thesis was to develop a framework of multiscale predictive modeling to optimize the design of nanostructured materials that exhibit improved resistance to damage and exceptional mechanical properties for application in advanced engineering systems.

Structural materials within first-generation fusion nuclear reactors based on a deuterium-tritium reaction will have to manage and remove large amounts of helium coming from alpha-particle radiation, tritium decay and neutron transmutation reactions. In addition, bombarding particles provoke atomic displacements that lead to the creation of point defects. Therefore, finding a material capable of minimizing the damage induced by radiation is very desirable.

The DFT study of the interaction between a He atom and graphene (Chapter 2) has revealed that stable non-defective graphene penetration by helium is tremendously complicated even for the most favorable trajectory, that is, vertical permeation towards graphene hexagon center. Moreover, helium can diffuse over graphene on any direction at nearly any temperature. The saturation process of helium on graphene has been investigated too by means of DFT calculations (Chapter 3). We have successively added helium atoms over highly symmetric graphene points (hexagon center C, midpoint of hexagon side, or bridge B, and hexagon vertex V) and relaxed the system in a step-by-step procedure. The atomic structure with the lowest total energy in each step is determined by the electron density distribution corresponding to the system of previous step. Last added helium atoms are located in zones with negligible variations of charge density, forming bonds with previously added helium atoms. Helium atoms form a multilayered system with hcp structure that grows epitaxially on graphene. The atoms of the first helium layer are physisorbed on graphene. Nevertheless, the interactions of helium atoms in the second and third layer with the graphene sheet are very small and negligible respectively. Thus, the binding energy of each single helium atom in the second layer or successive ones to the rest of the system can be approximated as the binding energy of the helium dimer multiplied by the number of nearest neighboring helium atoms. For a helium atom in the first layer, its adsorption energy to graphene has to be also considered.

With the aim of studying the temperature effects on helium trapping and storage in Cu/Nb-KS<sub>1</sub> interface, we have performed MD simulations at different temperatures (300, 500 and 700 K) on Cu/Nb bilayer composites in presence of an increasing amount of helium (Chapter 4). Interstitial diffusion is the dominant migration mechanism of He atoms to the interface. Consequently, a similar number of He atoms gets to the Cu/Nb interface for the three temperatures studied. Incoming He atoms contribute to increase the number of interfacial clusters and their size in the first stages but, after that, they basically contribute to increase interfacial He-clusters size. Many of these clusters, which are similar in number for the three temperatures studied, partially occupy the central part of the misfit dislocation intersections or are near them. The capacity to accommodate interfacial helium is enhanced for lower temperatures in terms of lattice distortion because Cu and Nb atoms are less compressed. Helium clusters grow on both sides of Cu/Nb interface by self-interstitial atoms emission and dislocation loop punching in the absence of displacement damage. The pressure exerted by these clusters on Cu and Nb atoms increases as long as vacancies are thermally emitted from the cavities for 500 and 700 K, or until this mechanism ceases to be effective for 300 K. Due to the higher He atoms/vacancies ratios of the interfacial precipitates, a greater and lower degree of hardening and swelling is expected respectively for higher temperatures except for low helium concentrations in the interface.

A mathematical model that describes long-term evolution of point defects in multilayer composite materials under irradiation is presented in this thesis (Chapter 5). Then, boundary equations and initial conditions of this continuum model have been adapted to consider the unconventional behavior of point defects at  $\alpha/\beta$ -KS<sub>min</sub> and -KS<sub>1</sub> interfaces ( $\alpha$  = Cu and  $\beta$  = Nb or V). The response to irradiation of the systems investigated, Cu/Nb and Cu/V, depends on both interface characteristics and bulk properties. Nonetheless, the influence of the properties of one metal on the point-defect evolution of the other metal is only effective if there are constitutional vacancies at the interface, i.e., for KS<sub>min</sub>. The lower concentration of vacancies in the Cu layer of the Cu/Nb system at steady state is due to the low mobility of vacancies in niobium. Quantitative comparison of our model predictions with experimental results in the literature has revealed that, although Cu vacancy concentration differences between Cu/Nb and Cu/V systems are determined at longer time scales, multilayer composites designed at the nanometric scale may be governed by mechanisms happening in lower time scales. For instance, SIAs are loaded at interfaces during the collision cascades and their subsequent emission promotes enhanced recombination with vacancies near the interface. SIA temporal evolution in copper (layer  $\alpha$ ) shows no differences between Cu/Nb

and Cu/V system while in layer  $\beta$ , SIA concentration at steady state is lower in niobium than in vanadium. The lower steady-state value of vacancy concentration in layer  $\beta$  corresponds to Cu/V system.

Ground-state KS interface configuration, i.e.,  $KS_{\min}$ , has 2-3 vacancies per MDI either in Cu/Nb or Cu/V multilayer composites. Since areal MDI density is higher in Cu/Nb interface than in Cu/V one, the former exhibits a higher He solubility than the latter for the same layer thickness. In addition, before transforming into bubbles, helium precipitates may form platelets at MDIs which storage helium nearly three times more efficiently than bubbles. To control helium bubble nucleation and growth, it is not only recommended to maximize the areal MDI density but also to minimize the concentration of vacancies in the matrix. The concentration of vacancies in Cu and Nb layer of Cu/Nb- $KS_{\min}$  system has been predicted to be lower and higher than in Cu and V layer of Cu/V- $KS_{\min}$  one, respectively. The high concentration of vacancies in the Nb layer should not be an issue as rapid formation of voids is prevented from occurring due to the low mobility of vacancies in this metal. Hence, Cu/Nb NMMCs seem to be more promising for reducing the damage provoked by bombarding particles and retarding the appearance of the eventual deleterious effects caused by helium. Graphene can act as a nanomembrane for the retention and storage of helium, as well as a vehicle for its management. So, nanocomposite structures containing graphene might be an excellent solution to definitively avoid helium issues in future nuclear reactors.

Severe plastic deformation techniques allow to create an interface different from those found in Cu/Nb multilayer composites synthesized by physical vapor deposition as  $KS_{\min}$ . No point-defect delocalization occurs and no constitutional vacancies are present in that interface obtained via severe plastic deformation. However, its vacancy sink efficiency is higher. Therefore, which technique produces more radiation-resistant nanocomposites remains an open question and further investigation is required in this regard. An important advantage of severe plastic deformation techniques to be considered is their capacity to fabricate large volumes of material, which offers the possibility of using these advanced materials commercially.

The multiscale methodology of this work gives access to information that would not be available otherwise, predicts material performance at different working conditions and interprets experimental results. It also gives insight on how material processing, nanostructure, microstructure and properties interact. Several models are used and linked to cover all scales. A He-graphene interaction potential based in DFT calculations is provided to model helium behavior on graphene at a larger scale. Continuum mechanical response of

Cu/Nb interface in the presence of different amounts of helium is estimated by averaging the MD stress values of the atoms in that region. Furthermore, results obtained at atomistic scale are integrated in continuum models that study point-defect annihilation mechanisms at NMMC interfaces either through the constitutive equations or the parameters. Thus, this thesis proves that multiscale computational modeling is a powerful tool kit to achieve relevant findings in materials science and engineering.